

AD-A259 781



**Solar Flares and Magnetospheric Particles:  
Investigations Based Upon the ONR-602  
and ONR-604 Experiments**

2

**Technical Report**

ONR Grant

N00014-90-J-1466

**DTIC**  
**ELECTE**  
**DEC 29 1992**  
**S A D**

**John P. Wefel and T. Gregory Guzik**

Department of Physics and Astronomy  
Louisiana State University  
Baton Rouge, LA 70803-4001

Phone: 504-388-8696  
FAX: 504-388-1222

This document has been approved  
for public release and sale; its  
distribution is unlimited.

**92-32890**



13108

15 October 1992

92 12 28 065

## CONTENTS

I.	Introduction.....	1
II.	The Instruments and Missions.....	3
III.	ONR-602: Particle Access Over the Poles.....	7
	A. Introduction.....	7
	B. Instrument Parameters.....	8
	C. Cross-Calibration with IMP-8.....	9
	D. Charge States.....	14
	E. Polar Access Regions.....	17
IV.	ONR-604 Performance.....	25
	A. Instrument Description and Operation.....	25
	B. Pre-launch Calibration.....	30
	C. Launch and On-Orbit Checkout.....	38
	D. Post-Launch Performance.....	45
V.	Data System, Databases and ONR-604 Analysis.....	48
	A. Reduction and Processing.....	48
	B. Ancillary Databases.....	50
	C. ONR-604 Analysis.....	57
VI.	Summary of Preliminary Results.....	79
	A. March 91 Solar Flare.....	79
	B. Quiet-time Helium.....	91
	C. Particle Access and Charge States.....	97
VII.	Modeling the Environment: Single Event Upsets.....	108
	A. Overview.....	108
	B. The CRRES Environment.....	109
	C. Solar Modulation.....	112
	D. Galactic Cosmic Rays.....	119
	E. LET Spectra.....	124
VIII.	Bibliography.....	127

Accession For	
NTIS CRA&I	<input checked="" type="checkbox"/>
DTIC TAB	<input type="checkbox"/>
Unannounced	<input type="checkbox"/>
Justification .....	
By .....	
Distribution /	
Availability Codes	
Dist	Avail and/or Special
A-1	

## I. Introduction

The work reported here has been performed at Louisiana State University under Office of Naval Research Grant N00014-90-J-1466, entitled "Solar Flares and Magnetospheric Particles: Investigations Based Upon the ONR-602 and ONR-604 Experiments." The objective of this project has been to gain a better understanding of the energetic particle environment in near-Earth space (Geospace) using data provided by the two experiments ONR-602 and ONR-604. These instruments were designed and built by the Laboratory for Astrophysics and Space Research at the University of Chicago under the CRIE project (J. A. Simpson, P.I., M. Garcia-Munoz and J. P. Wefel, Co-I) and were sponsored for flight in the Air Force STP program by The Office of Naval Research. ONR-602 flew on the S81-1 Pallet Mission in 1982 in a low-altitude polar orbit, while ONR-604 was part of the CRRES mission of 1990-91 in a Geostationary Transfer Orbit (GTO). These missions each sampled a different region of Geospace at different times in the solar cycle, and together provide a database that can address a range of fundamental problems. The overall goal of the program is to understand the radiation environment in Geospace well enough to make predictions of the effects to Space Systems (and, eventually, humans) that must function in the Geospace environment.

The study of solar flares, and the interaction of solar flare radiations with the geospace environment, is one of the most fundamental investigations in space science. Involved are basic questions about the mechanism for energy generation in the flare region, the conversion of this energy into high energy charged particles, neutrons, x-rays and gamma rays, the interplanetary propagation of the particles to Earth, the access of these particles to the magnetosphere and the changes initiated in our local environment due to the solar flare. In the latter case, the solar particles are superposed upon an existing background of geomagnetically trapped and pseudo-trapped charged particles, which are themselves of fundamental importance in the dynamics of the geospace environment.

While these questions are quite compelling scientifically, they also have important practical applications. The influence of solar activity and the consequent geomagnetic disturbances on the availability and quality of long range, short wave radio communication is perhaps the best known of the solar effects. With the advent of the space program and the ever increasing use of the space environment for both civilian and military applications, the consequences of space radiations are becoming a major operational concern since possible effects of such radiations include: the long-term degradation of hardware in the space environment, the abrupt failure of space systems due to a short-term event or even a single, intensely ionizing particle, and limitations imposed by the radiation environment on the human presence in orbit. Our ability to assess the resulting operational limitations depends both on detailed knowledge of the geospace environment and its spatial and temporal variability and on the degree of sophistication of the space systems that are required to operate there. As this sophistication increases, so does the need for more detailed knowledge of the environment and for development of a capability for predicting its characteristics over a given orbit.

The large fluences of protons and electrons encountered in Geospace combined with the solar ultraviolet flux are responsible for the degradation of exterior spacecraft components (e.g. solar panels) while induced potentials from the space environment can lead to major electrical discharges between different parts of a spacecraft. For electronic components located within the spacecraft, the overall radiation dose can be large (depending upon the orbit), requiring spacecraft designers to employ radiation-hardened parts and, often, passive shielding which is costly in the form of increased weight.

There is, however, another source of radiation damage -- single particle induced effects -- which has been recognized for the past several decades as a major problem (Binder et al., 1975). There are two types of such single particle effects whose relative importance depends upon the

character of the radiation environment and the type of electronic parts employed in a space system. First, protons or alpha particles can interact with the silicon substrate in an integrated circuit device and produce low velocity fragments that lose energy by ionization at a rate sufficient to interfere with the operation of the device (May and Woods, 1980; McNulty et al., 1980; Guenzer et al., 1980; Petersen, 1980). Fortunately, the interaction rate for protons and alphas is relatively small, but as the packing density of electronic circuits increases, these interactions may become a problem. Second, there is now ample evidence for a direct effect caused by heavy ions ( $Z \geq 2$ ) traversing integrated circuit devices, particularly low power memory chips (Kolasinski et al., 1979; Ziegler and Lanford 1979; Hamm et al., 1979; Bruckner et al., 1980; Pickel and Blandford, 1980). Since the rate of ionization energy loss scales as the square of the particle's charge, the heavy ions deposit considerably more energy than protons and alphas, producing enough charge carriers within the sensitive region of the device to upset its logical state. Generically, such effects are called Single Event Upsets (SEU's).

Although the relative abundance of heavy ions is small compared to that of protons, the damage efficiency is high since the effects are caused directly by the passage of the particle through the device. In addition, the damage potential increases with the particle charge, making an energetic iron nucleus, for example, much more potentially damaging than an oxygen ion. The major concern for the future lies in the fact that as the sophistication level and device density of the electronic systems increases, the number of charge carriers involved per device decreases. This makes a device sensitive to effects caused by incident particles from a wider range of the charge spectrum and thereby increases the overall sensitivity of these systems to disruption by individual particles. The importance of this problem is such that a concerted effort is now underway to understand both the device sensitivity and the radiation environment in sufficient detail to aid in spacecraft design and operational planning. This was one of the main goals of the CRRES mission.

The heavy ion component of the geospace particle environment is particularly important but has not been studied in sufficient detail. Adams et al. (1981) reviewed and summarized present knowledge of heavy charged particles in the galactic cosmic radiation, in solar flares (at varying levels of enhancement) and in the magnetosphere. The composition of the galactic cosmic rays is the best known, followed by that of solar energetic particles. The presence of heavy ions at relatively high energies in the magnetosphere remains a controversial question (see Adams and Partridge, 1982), to which ONR-602 and ONR-604 are contributing.

Astrophysically, the heavy ion component is particularly important since the relative abundance of elements and isotopes in this component contains a characteristic "signature", which provides much of the information necessary to unravel the questions of the origin, acceleration and history of the particles. Thus, detailed investigation of the heavy ion component combines both scientific and practical goals and this is the motivation behind the ONR-602 and ONR-604 experiments and the investigations described here.

In subsequent sections, we briefly review the instrumentation and the missions and then describe the results obtained from the ONR-602 analysis. The CRRES spacecraft was launched during this grant, and much of our effort has been devoted to the processing and analysis of this new data. The ONR-604 instrument is described in detail, including the pre-launch accelerator calibrations and the post-launch initial on-orbit check-out activities. The data handling system developed at LSU is detailed along with the analysis procedures that have been employed. The science analysis has focused on questions of particle access, flare analysis, cosmic ray levels, environment modeling and comparisons between ONR-602 and ONR-604 results. These are described in Section VI. Finally, we present some initial results on predicting the effects of the CRRES environment on micro-electronic devices.

## II. The Instruments and Missions

The ONR-602 and ONR-604 instruments were conceived in the 1970's expressly for the purpose of studying the heavy ion component in Geospace. The instruments were designed and built at the University of Chicago, under the leadership of Professor John A. Simpson, assisted by scientists M. Garcia-Munoz, G. Mason, K. Pyle, J. Wefel and R. Zamow and the engineering and technical staff of the Laboratory for Astrophysics and Space Research. The ONR-602 instrument, consisting of a main telescope and a smaller flux monitoring telescope, was designed to study the lowest energy flare and magnetospheric particles. The ONR-604 instrument was designed to extend the measurements to higher particles energies and to have sufficient collecting power to study the rarer species.

Originally, the two instruments were to be flown together on a single mission. However, when mission scheduling precluded this possibility, the two instruments were separately manifested. The ONR-602 experiment, also called Phoenix-1, was launched into a low-altitude polar orbit on the S81-1 Pallet mission and was active for seven months in 1982. This provided an opportunity to space test some of the new technology employed in the instruments, to reexamine the earth's low altitude magnetosphere during the 1982 epoch and to study low energy solar energetic particles. The S81-1 spacecraft was three-axis stabilized in an 85.5° inclination orbit, sun-synchronized from 1030 to 2230 local time. The satellite altitude varied from 170 to 290 km over the mission. Low energy particles were detected during the polar passes as well as in the region of the South Atlantic Anomaly.

Figure II.1 shows schematic diagrams of the Low Energy Telescope (or Main telescope) and the Monitor telescope, the two instruments included as part of the ONR-602 package on the S81-1 mission, and the ONR-604 telescope for CRRES. A unique feature of the Main telescope and the ONR-604 High Energy Telescope is the inclusion of solid state position-sensing detectors (PSD's), which were developed and fabricated at The University of Chicago, and are used to determine the trajectory of each particle within the instrument. Such trajectory data allows the measurements in the other detectors to be corrected for the exact angle of incidence of the particle, and, combined with the spacecraft ephemeris, gives the arrival direction from space for each event. The ONR-602 experiment was the first use in the space environment of this new technology, and the PSD's performed exceptionally well.

By combining the particle trajectory measured by the PSD's with the energy deposited in the stack of solid state detectors, each particle triggering the event logic and coming to rest in the instrument has its charge, mass and energy measured. This allows the element distribution, the energy spectrum and the isotopic distribution of the recorded events to be studied in detail. Moreover, by using a measured or modeled magnetic field direction, the trajectory information can be used to derive the incident particles' pitch angle distribution.

The Monitor telescope consists of a single, thin (40 micron thick) solid state detector surrounded by passive shielding, sufficient to absorb protons with energies up to about 40 MeV. There is no pulse height analysis for this telescope, but low energy particles are monitored by three counting rates, ML, MM and MH whose corresponding thresholds are adjusted so that they respond to  $Z \geq 1$ ,  $Z \geq 2$  and  $Z \geq 4$  particles, respectively. The thin detector and the selected thresholds make the Monitor insensitive to electrons. The Monitor rates are available for studying particles at energies, typically around 1 MeV/nucleon, below those needed to trigger the Main telescope.

The ONR-602 package was in nearly polar, 90 minute period, dawn-dusk orbit. The instrument, therefore, alternated between low counting rates near the equator and high counting rates in the polar regions. In addition, there were data gaps, due to the power limitations imposed by the spacecraft, which complicated the analysis.

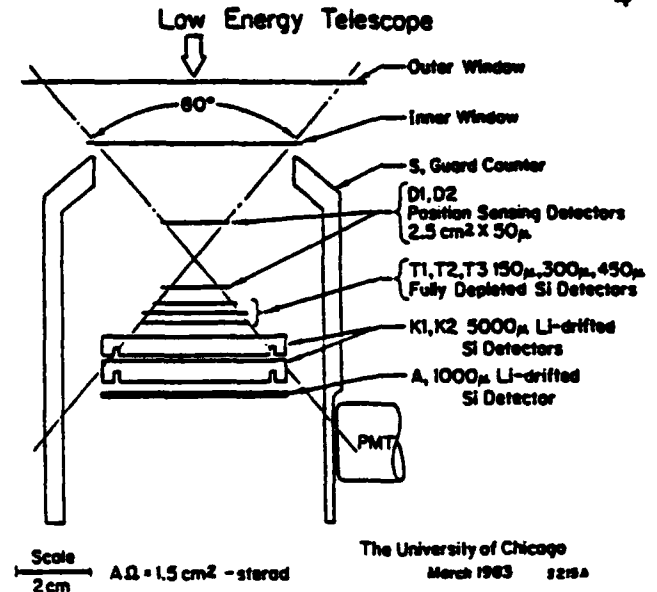
ONR - 602 ( on S 81-1 )

SEP ELEMENTS/ISOTOPES

Z: He - Ni

E:  $\sim 4 - 230$  MeV/N

GEOM:  $1.5 - 1.0$  cm<sup>2</sup>-SR



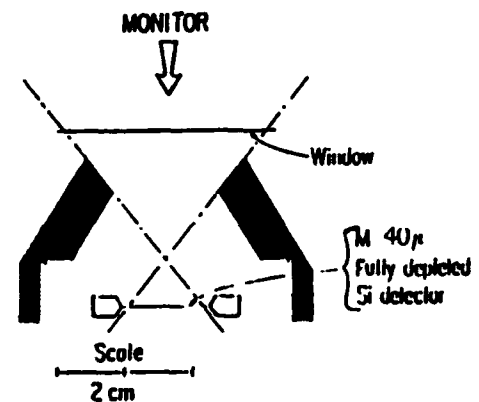
ONR - 602 ( on S 81-1 )

SEP & MAGNETOSPHERIC PARTICLE  
FLUX MONITORING

Z: P, He, Z > 2

E:  $\sim 0.6 - 10$  MeV/N

GEOM:  $0.5$  cm<sup>2</sup>-SR



ONR - 604 ( on CRRES )

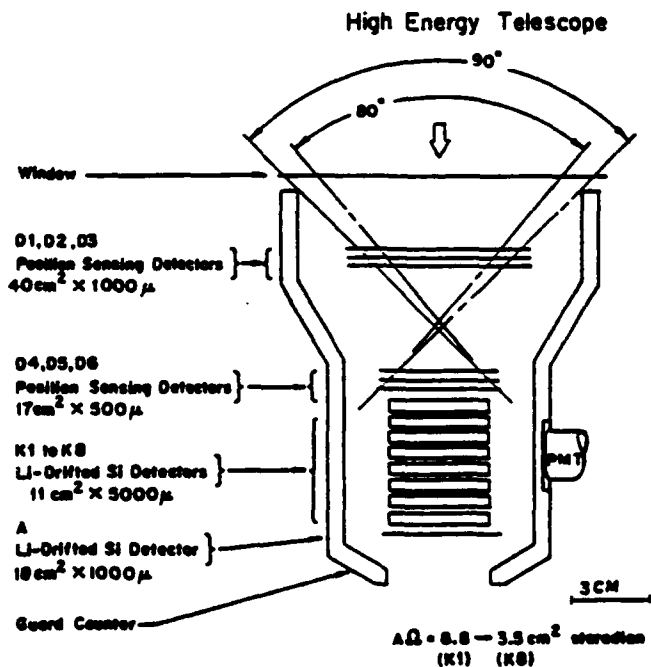
SEP & GCR ELEMENTS/ISOTOPES

MAGNETOSPHERIC HEAVY IONS

Z: H - Ni

E:  $\sim 25 - 570$  MeV/N

GEOM:  $8.8 - 3.5$  cm<sup>2</sup>-SR



BUILT BY THE UNIVERSITY OF CHICAGO

Figure II.1. Schematic Diagram of the ONR Telescopes.

In addition to ONR-602, the S81-1 pallet included the SEEP (Stimulated Emission of Energetic Particles) experiment from the Lockheed Palo Alto Research Laboratory. This experiment measured very low energy electrons and protons, as well as atmospheric x-rays, and was designed to look for magnetospheric particle precipitation events.

With the initiation of the CRRES mission for space radiation studies and the inclusion of ONR-604 as one of the major instruments on the mission, an additional opportunity for magnetospheric and solar flare science was established. As part of that program, the SPACERAD Science Team was formed to provide scientific planning in support of the overall mission objectives, and LSU joined the science team both to represent and support the ONR-604 experiment and its vital role in the mission and to help incorporate the ONR-602 data into the overall picture of the magnetosphere which is emerging from the CRRES/SPACERAD program.

The Challenger disaster delayed the launch of CRRES until mid-1990 and converted the program from a shuttle launch to an expendable launch vehicle (ATLAS). CRRES (Combined Release and Radiation Effects Satellite) is a joint NASA/DoD mission designed to both study/monitor the particles and fields in Geospace and to stimulate the magnetosphere through chemical releases (Barium and Lithium). The releases took place during different parts of the CRRES orbit and were monitored both by CRRES instruments and by other, cooperative, experiments.

CRRES was launched on July 25, 1990 and achieved a near Geosynchronous Transfer Orbit with apogee of 33,580 km and perigee of 350 km. The orbital period is 9 hours 51.5 minutes with an orbital inclination of 18.2° and an eccentricity of 0.711. This orbit takes CRRES through the heart of the inner (proton) and outer (electron) trapped radiation regions as well as providing measurements of interplanetary particles near apogee. Thus, many of the magnetospheric phenomena studied by ONR-602 from low altitude in polar orbit can be studied in more detail by CRRES, as well as maintaining the capability for measuring solar flare particles and their access to the magnetosphere. In addition, the GTO provides access to regions of the magnetosphere unavailable to ONR-602 and thereby permits an expanded range of investigations.

In addition to the ONR-604 experiment, CRRES includes a large number of other "environment" sensors focused upon the magnetospheric electrons and protons. Table 2.1 lists some of these instruments and the measurement performed. Note that only ONR-604 provides information on the energetic heavy ions. More details on the operation of each of these instruments may be found in Gussenhaven, Mullen and Sagalyn (1985), while the ONR-604 instrument performance is described in detail in a subsequent section of this report. The important point is that on-board CRRES is sufficient environment monitoring to provide correlative data for the analysis of the ONR-604 experiment.

In addition to the environment monitoring instruments, CRRES includes a Microelectronics Package (MEP) whose purpose is a direct "in situ" test of a wide variety of microelectronic devices. These are mounted behind different amounts of shielding and include devices ranging from "rad-hard" to very radiation sensitive. Thus, CRRES provides an "on-board" monitor of SEU effects and part of our work has been directed to modeling the particle environment in order to predict the expected SEU rate.

**TABLE 2.1: CRRES "Environment" Instruments**

<b>Instrument Number</b>	<b>Measurement</b>
604	ions: 20 - >500 MeV/nucleon
701-11A	ions: 1 - 425 keV/Q
701-11B	ions: 40 ev/Q - 40 keV/Q
701-11C	ions: 100 keV/nucleon - 15 MeV/ion
307-8-3	ions: 4 - 2000 keV/Q
701-7A	p: 20 - 80 MeV
701-7B	p: >320 MeV, >440 MeV
701-8/9	p: 1 - 100 MeV
702-2	e, p : dosimeter
701-3	e, p : MOS dosimeter
701-4	e: 1 - 10 MeV
307-3	e : 20 - 5000 keV, p : 0.5 - 100 MeV
701-5A	e: 30 keV - 2 MeV
701-5B	e: 20 - 250 keV, p: 0.04 - 2 MeV

Analysis of the data from the ONR-602 and ONR-604 instruments is being conducted jointly by The University of Chicago and Louisiana State University. For the ONR-602 analysis, LSU has responsibility for: (1) correlative studies on solar flares, involving the collection of data from other spacecraft or ground-based observatories and the combination of this data with the ONR-602 results, and (2) magnetospheric particle investigations focusing on spatial and temporal variations and their relationship to solar flare/interplanetary conditions. Chicago has principal responsibility for first phase data processing, instrument functioning, and analysis of solar flare elemental and isotopic composition. For ONR-604, LSU is working on the magnetospheric particles, solar flares, and correlative studies. Chicago is focused upon the elemental and isotopic composition questions. Of course there is considerable overlap, and both groups work on the access problem and on the heavy ion modeling.



### III. ONR-602: Particle Access Over the Poles

#### A. Introduction

Our previous work with the ONR-602 dataset involved a detailed analysis of low-energy ( $\sim 1$  MeV) proton precipitation from the ring current as a diagnostic of the state of the magnetosphere. Observed over the equatorial parts of the orbit, these low energy particles exhibited an altitude dependence, energy spectrum and latitudinal profile that was described by the charge exchange model for a ring current source (Guzik et al., 1989). This work was the subject of a Ph.D. dissertation.

We have also been analyzing the solar energetic particle events that were observed during the S81-1 mission, illustrated in Figure III.1.

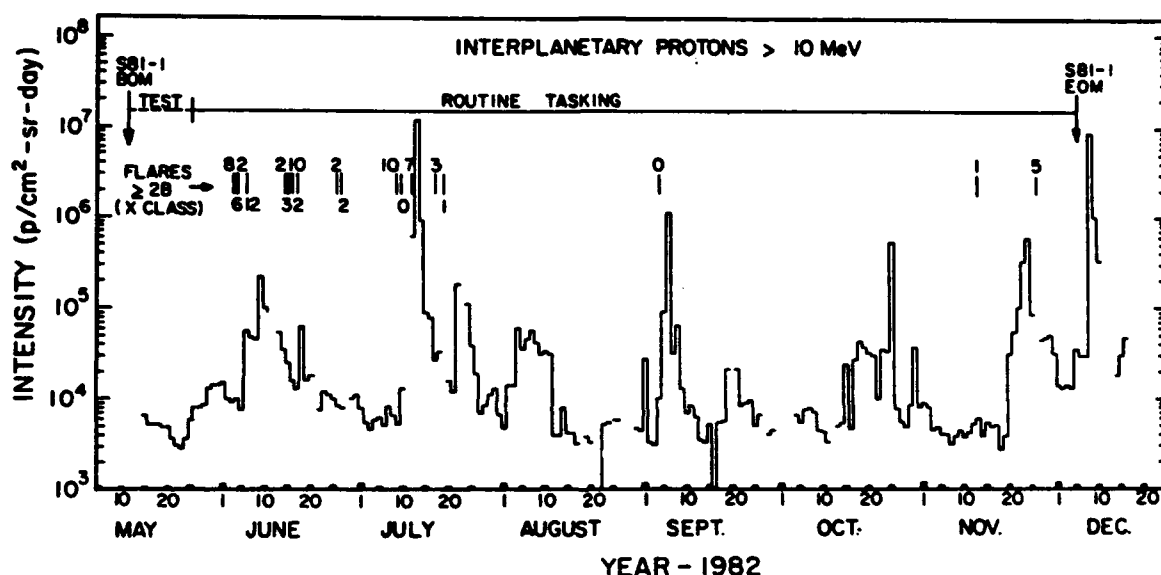


Figure III.1. Solar Energetic Particle Events observed by ONR-602.

Plotted is the intensity of interplanetary protons  $> 10$  MeV as recorded by the GOES monitoring satellites along with an indication (top) of the flare classification. Both individual flare analyses and aggregate solar particle studies have been carried out on these 1982 flares. There were five major flare periods June, mid-July extending into August, early September, October and late November, 1982. An additional flare in early December 1982 erupted just after the S81-1 End of Mission (EOM) and could not be studied. None of these flares are of the very large (c.f. August 72) type and are mostly impulsive in character. The total heavy ion yield varies from event to event, but the statistics are limited.

An analysis was performed for the combined flare periods of June, July and November, 1982 which yielded the overall elemental composition and the isotopic distribution for C, N, O, Ne Mg and Si (Simpson, Wefel and Zamow, 1983; Guzik, 1988). No appreciable secondary spallation component was observed, and the agreement of the measured isotope composition with standard solar system material indicated that particle rigidity was not a dominant effect in the solar flare acceleration process. A first ionization potential (FIP) bias was found in the elemental ratios which agrees with other flare results and with gamma ray derived abundances. This indicated that

the FIP selection was not due to the acceleration process but is pre-existing in the matter that is accelerated as Solar Energetic Particles (SEP).

## B. Instrumental Parameters

For the particle access questions discussed below, we will employ both pulse height analyzed results and counting rate data, the latter from both the Monitor Telescope and the Main Telescope (c.f. Figure II.1). Here we review briefly some of the relevant characteristics of the two telescopes.

The monitor telescope was a passively shielded unit with a single, 40- $\mu\text{m}$ -thick, fully depleted silicon detector. It had an opening angle of  $75^\circ$ , a geometrical factor of  $0.5 \text{ cm}^2\text{-sr}$  and was mounted on the spacecraft with the telescope axis tilted at an angle of  $2.35^\circ$  to the local vertical in a plane perpendicular to the orbital plane. The monitor telescope returned three counting rates, ML, MM, and MH, all with an accumulation time of 4.096 s, corresponding to three different threshold settings for the pulse height from the detector. Rate ML had a threshold value of 0.36 MeV and could be triggered by protons in the energy range 0.6-9.1 MeV, by alpha particles in the energy range  $\sim 0.4$ -80 MeV/nucleon, and by  $Z > 2$  particles of energy  $> 0.7$  MeV/nucleon ( $^{12}\text{C}$ ). The threshold setting for MM was 2.8 MeV, corresponding to alpha particles of 0.8-4.5 MeV/nucleon and to  $Z > 2$  particles  $\sim 0.5$ -80 MeV/nucleon ( $^{12}\text{C}$ ). Rate MH had a threshold of 10.5 MeV and could be triggered only by  $Z > 2$  particles in the interval 1.2-11 MeV/nucleon ( $^{12}\text{C}$ ). Within the equatorial part of the orbit, the ratios of the observed counting rates were  $\text{MM/ML} \sim 10^{-3}$ ,  $\text{MH/ML} \sim 10^{-4}$ , and  $\text{MH/MM} \sim 10^{-1}$ , which reflect published values for the composition and indicate that the ML counting rate was almost entirely due to protons. An investigation of the ML background was carried out by analysis of data from regions between the equator and the mid-latitude zones and showed a negligible background, less than 4% of the average peak rate.

The main telescope (CRIE-LO) used 50  $\mu\text{m}$  thick two-dimensional position-sensing detectors (PSDs) developed by the University of Chicago (Lamport et al., 1980) to determine the incidence trajectories of the particles. These PSD's are followed by thicker detectors T1, T2, T3 -- fully depleted silicon detectors of thickness 150, 300 and 450  $\mu\text{m}$  -- and K1, K2 -- Lithium drifted silicon detectors of 5000  $\mu\text{m}$  thickness. Particles penetrating the entire stack are detected by the anti-coincidence detector A, and side penetrating particles are observed in the surrounding anti-coincidence scintillator, S. For an identified "event", we require the particle to stop within the detector stack (A not fired) and not to show any signal in the scintillator guard counter. For the lowest energies, we require particles stopping in T2 or T3 and use T1 as the energy loss detector. This corresponds to energy ranges of, for example, 11-24 MeV/nucleon for  $^{12}\text{C}$  and 17-38 MeV/nucleon for  $^{28}\text{Si}$ . For higher energies, events stopping in K1 and K2 are included, and this extends the energy range to beyond 200 MeV/nucleon for the heaviest nuclei (Ni). Most SEP events studied, however, have energies of about 10-50 MeV/nucleon.

The CRIE-LO telescope also returns counting rates of different types. The coincidence counting rates (RD1-RA) measure the penetration of particles into the stack. For example, RT2 requires a logic condition  $\text{D1} \cdot \text{D2} \cdot \text{T1} \cdot \text{T2} \cdot \text{T3}$  where the terms refer to the discriminators attached to each of the detectors. With the nominal detector thresholds ( $\text{D1}, \text{D2} = 2 \text{ MeV}$ ;  $\text{T1}, \text{T2}, \text{T3} = 4 \text{ MeV}$ ;  $\text{K1}, \text{K2} = 1 \text{ MeV}$ ;  $\text{A} = 0.25 \text{ MeV}$ ;  $\text{S} = 0.5 \text{ MeV}$ ), the particle species and approximate energy ranges (at  $15^\circ$  incidence angle) sampled by the different rates are given in Table 3.1. In addition, the single detector counting rates (D2S-SS) are also recorded, and the characteristics of these rates are included in Table 3.1.

The energy ranges quoted in the Table are approximate and do not include any indication of background effects. The main telescope contained a radioactive source, an in-flight calibrator, which was utilized to monitor the operation of detectors D1, D2 and T1. This calibrator provides a fixed background level for the singles rates from these detectors (and rate RD1). In addition, the

singles rates involve particles incident from many different angles and therefore show a large background counting rate. Note that the coincidence rates are relatively insensitive to low energy protons, except for large angle particles incident upon D1. Helium nuclei and heavy ions are studied from energies of  $\sim 1$  MeV/nucleon upward. The scintillator singles rate SS is ascribed to electrons as the primary particle but also has sensitivity to protons and to multiple particle events.

**Table 3.1: Counting Rates from the ONR-602 Experiment**

<u>Counting Rate</u>	<u>Particle Species</u>	<u>Energy (MeV/nucleon)</u>
ML	$\geq p$	0.5 - 9
MM	$\geq \text{He}$	0.8 - 4.5
MH	Hi-Z( $^{12}\text{C}$ )	1.1 - 11
<hr/>		
RD1	Calibrator	
	He	$\sim 0.5 - 8$
	p(large angles)	$\sim 2 - 2.5$
RD2	He	$\sim 2.5 - 8$
RT1	He	$\sim 3.5 - 8$
RT2	He	$\sim 5.5 - 8$
RT3,RK1,RK2,RA	Z $>2$	varies with Z
<hr/>		
D2S	Calibrator	
	He	$\sim 2 - 8.5$
T1S	Calibrator	
	He	$\sim 3.5 - 14$
T2S	p	$\sim 7 - 9.5$
	He	$\sim 6 - 33.5$
T3S	p	$\sim 10 - 15$
	He	$\sim 9 - 60$
K1S	p,He	$\geq 12.5$
K2S	p,He	$\geq 34.0$
AS	p,He	$\geq 48.0$
SS	electrons	$> 0.85$

### C. Cross-Calibration with IMP-8

One of the unanswered questions in the analysis has been the degree (if any) of geomagnetic shielding experienced by ONR-602 in the polar regions. This question can be investigated by comparing measurements from an interplanetary spacecraft with the polar cap data from ONR-602. Fortunately, IMP-8 is still operating and contains a Low Energy Telescope that has a proton channel identical in threshold and geometric factor and with a detector similar to the Monitor Telescope. (In fact, the Monitor design was copied from the IMP-8 LET.) IMP-8 is outside the magnetosphere at 14-23  $R_E$ .

Figure III.2 shows the individual rates where IMP-8 represents hourly averages of the L1NL2 rate and ONR-602 shows polar cap ( $>75^\circ$  latitude) averages. The correspondence between the two  $>0.5$  MeV rates is exceedingly good for the entire S81-1 mission. Figure III.3 shows a direct correlation of the IMP-8 and ONR-602 rates for the June 1982 flare period (c.f. Figure III.1), with IMP-8 represented by filled circles. The remarkable tracking of the two spacecraft

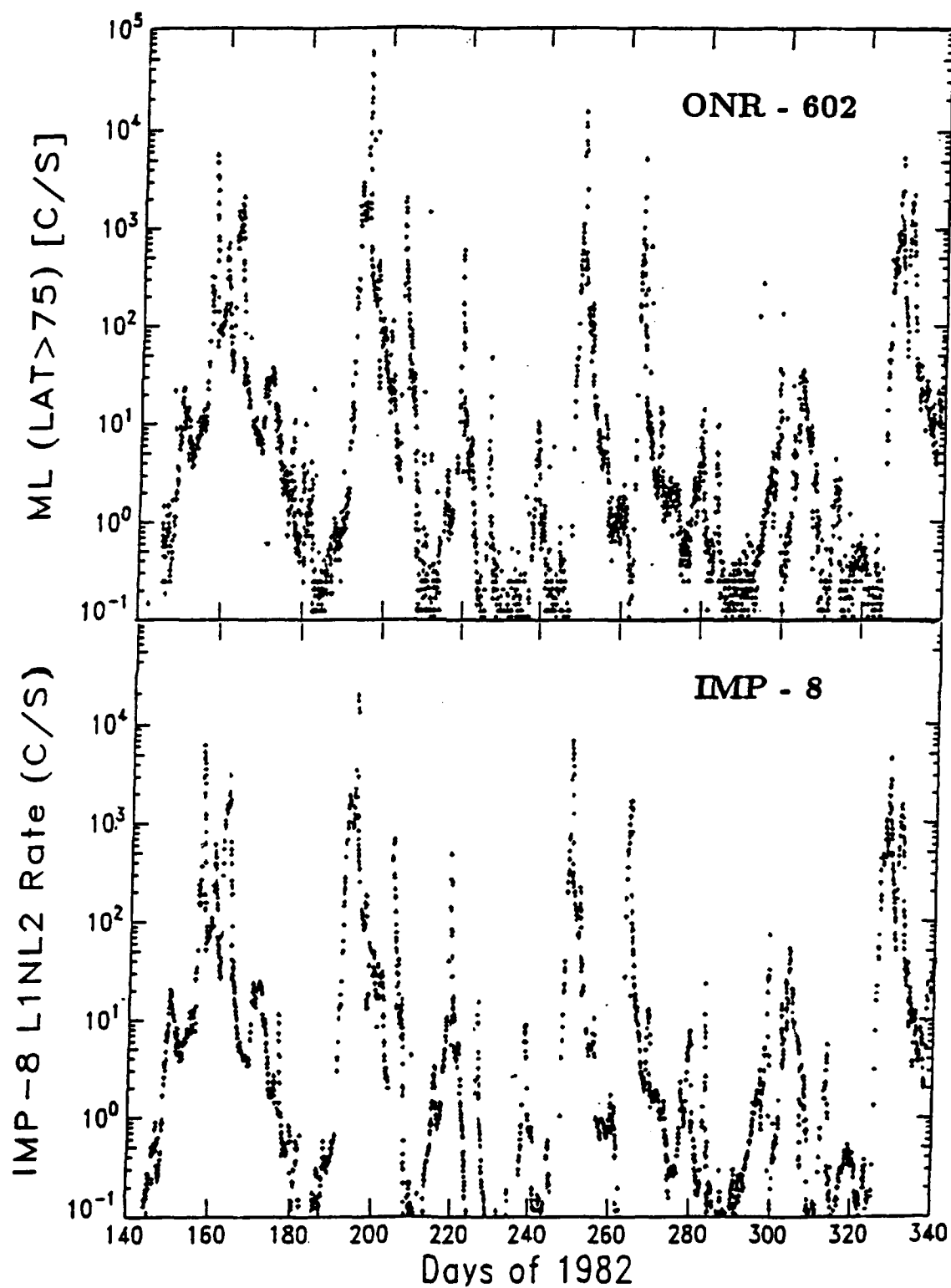


Figure III.2. The ONR-602 polar cap averaged ML rate (top) compared to the IMP-8 hourly averaged L1NL2 rate (bottom).

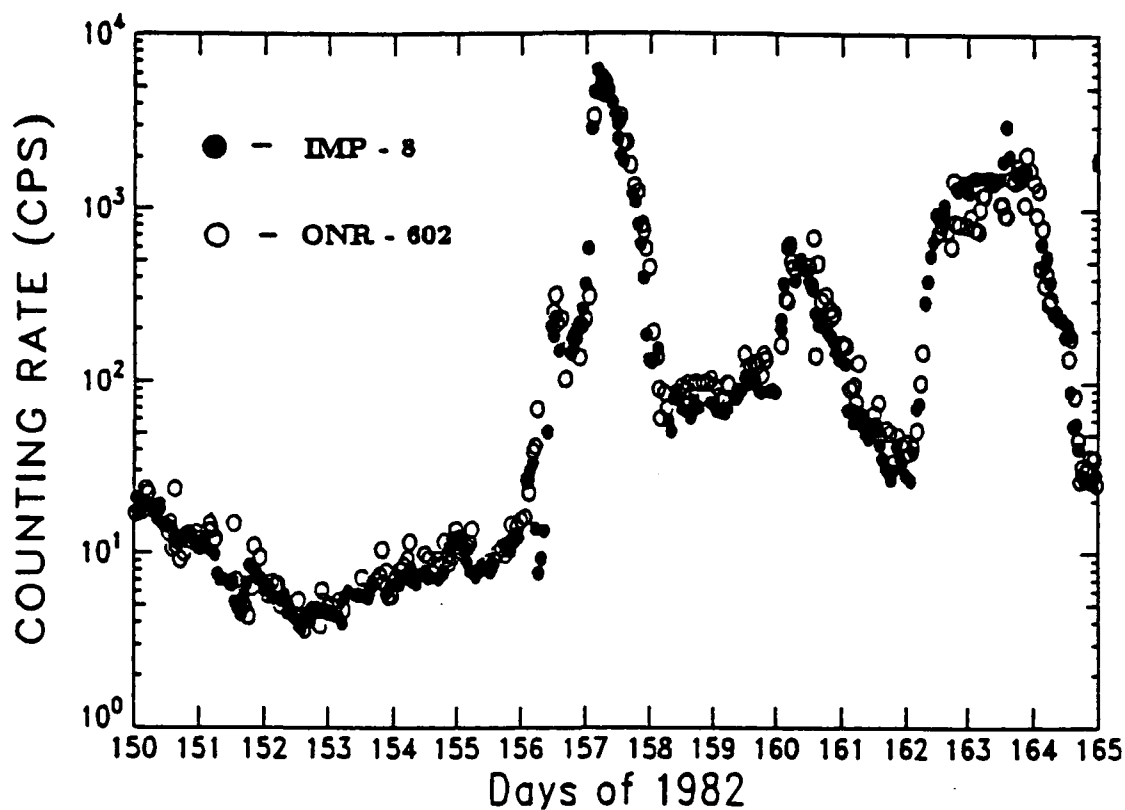


Figure III.3. Direct comparison of the IMP-8 and the ONR-602 proton counting rates ( $>0.5$  MeV) for the June, 1982 flare period.

S81-1, IMP-8, & ISEE-3 Protons in June 1982

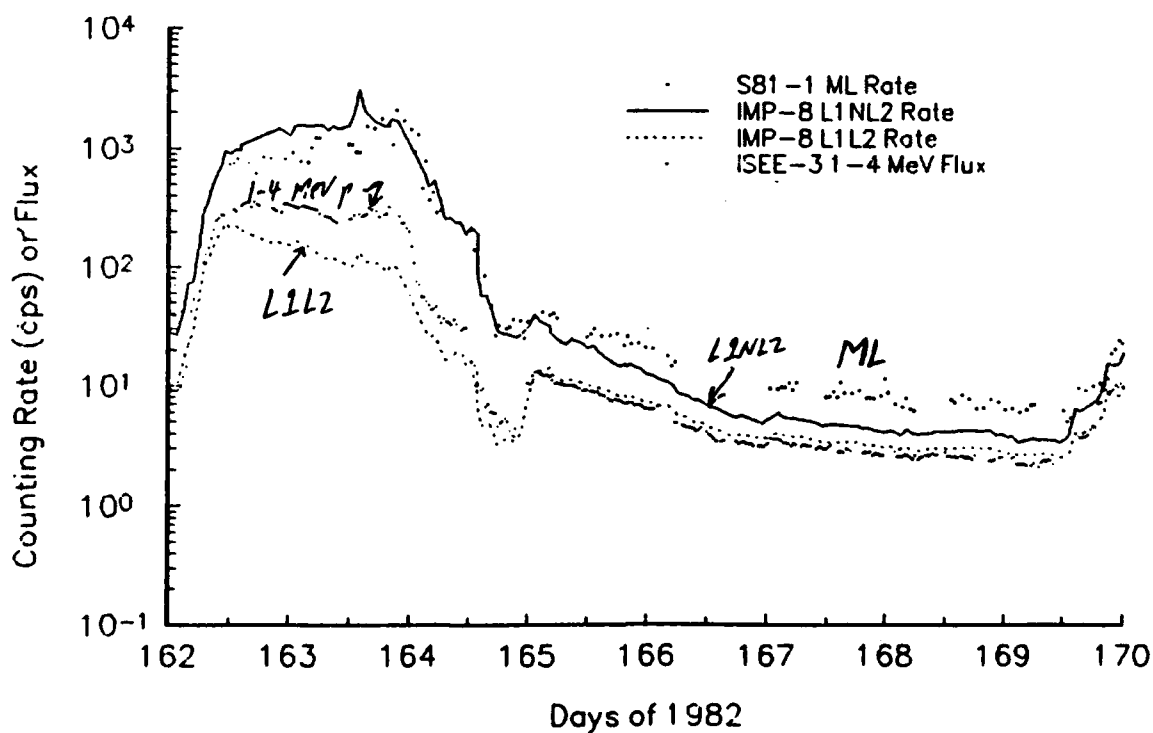


Figure III.4 Correlation of polar cap and interplanetary particle intensities for June, 1982.

indicates that the correlation time scale for these low energy particles from IMP to S81-1 is generally  $\leq$  few hours, i.e. there is no long diffusion or "storage" time between IMP-8 and the polar cap regions.

Note, however, that around days 160-164 the ONR-602 points are slightly shifted for the IMP-8 results. This could indicate longer correlation times (10-12 hours) as would be expected if access were from the extended geomagnetic tail. Figures III.2 and III.3 do, however, confirm that ONR-602 is observing interplanetary particles at low altitude over the polar caps.

An extension of this comparison to quiet times and to include the ISEE-3 spacecraft as well is shown in Figure III.4 where data are presented for the declining phase of the June flare period shown in the previous figure. The solid line and the large dots (ML) both refer to  $>0.5$  MeV protons. The L1L2 rate from IMP-8 records  $>2$  MeV protons while the small dots give the flux of 1-4 MeV protons from ISEE-3. During the flare and the declining phase, the ML and L1NL2 rates track well, while the 1-4 MeV rate is always above the L1L2 ( $>2$  MeV) rate. This indicates a soft spectrum with considerable numbers of particles in the 0.5-1 MeV range. However, at about day 165 the 1-4 and  $>2$  MeV rates begin to coalesce, and the IMP-8  $>0.5$  MeV rate declines to approach the other two rates. This coalescence indicates a hardening particle spectrum. The S81-1 ML rate, however, remains significantly above the other rates. Note that IMP-8 was located sunwards of the dayside magnetopause for days 161-169, which may have depressed the IMP-8 rate relative to the polar cap results. In any case, multi-spacecraft observations are a powerful tool in analyzing the morphology of solar particle events.

An example of a normal polar cap pass is shown in Figure III.5 for day 194 (13 July), during the onset of a solar flare. All three monitor rates are plotted as a function of magnetic latitude and show similar behavior. The dashed line indicates the location of the last closed magnetic field line at a magnetic latitude of  $59^\circ$ . The particle rates fall precipitously at the boundary within one accumulation period (4.096 seconds) which indicates the sharpness of the boundary layer. From the ONR-602 data, the thickness of the layer is  $\leq 30$  km, the highest spatial resolution we can achieve with the monitor counting rates.

In a simple Stormer model for the geomagnetic field, the cutoff rigidities at the last closed field line correspond to particle energies of  $\sim 13$  MeV for protons (c.f. ML = 0.5-9 MeV) and  $\sim 3$  MeV/nucleon for Helium (c.f. MM = 0.8-4.5 MeV/nucleon). Thus, the majority of the particles sampled by ML and MM do not have sufficient rigidity to penetrate the magnetic field and be observed at latitudes below the last field line. This forms an effective "edge" to the polar cap free access region. (This edge is located below the  $75^\circ$  latitude assumed in the previous comparisons.) As will be discussed below, the behavior observed in Figure III.5 is typical of undisturbed magnetic conditions. For other times, however, the free access zone can be modified drastically and extend to lower latitudes.

The free access zone shown on Figure III.5 is directly applicable to the July flare. This was the most intense proton flare during the S81-1 mission (c.f. Figure III.1). The CRIE-LO counting rates for pulse height analyzed events on July 11-15 are shown in Figure III.6. The helium and CNO rates reached their highest 1982 mission levels on July 13th, while minimal response was seen in the analysis channels for heavier ions. The gradual increase of the helium rates from July 11 reflects the arrival at Earth of ions from a series of 2B-3B flares on the sun's east limb during July 9-12. While other, more well-connected flares are known to show time-dependent variations in the relative abundances of oxygen through iron due to interplanetary propagation effects (Mason et al., 1983), the July flare measurements provide a better representation of "average" SEP abundances as reported by Simpson et al. (1983). No events in the iron range were observed. Note that the combined 1982 dataset used in our combined flare analysis was dominated by ions from the July period.

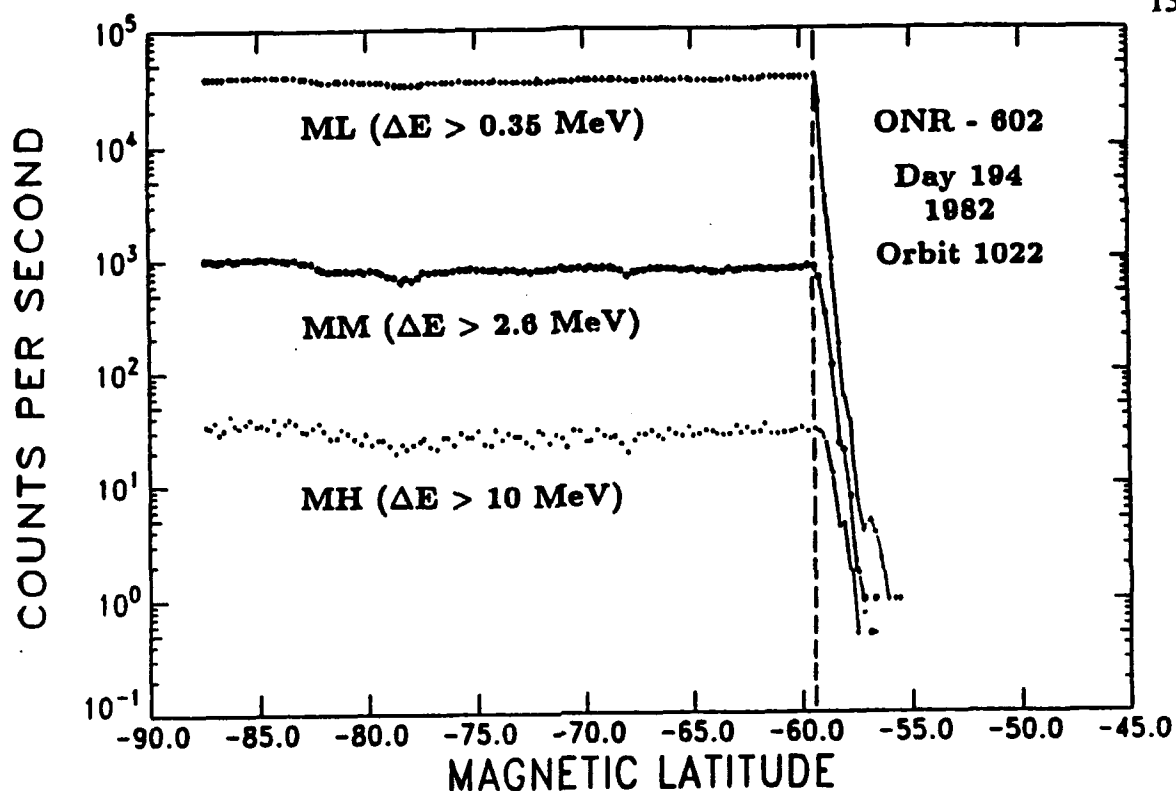


Figure III.5 The polar cap access zone for day 194. Shown are the three monitor telescope counting rates as a function of magnetic latitude.

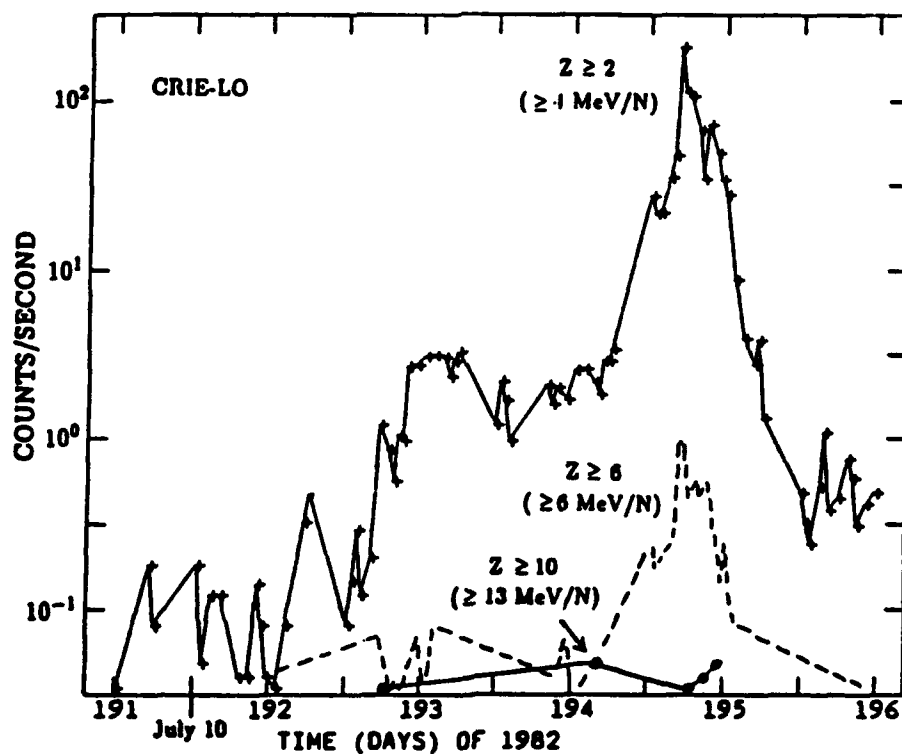


Figure III.6. Ion counting rates measured by the CRIE-LO telescope for the 11-15 July solar flare period.

Moving to higher energies, we can investigate the response of the CRIE-LO scintillator (SS) rate compared to IMP-8 data. Figure III.7 shows the SS rate (bottom) compared to high energy IMP-8 rates, again for the June 1982 flare period. The top two plots (note logarithmic scale) give 30-95 MeV proton and  $\sim 1$  MeV electron rates from IMP-8. The center plot shows the Cherenkov trigger rate in the IMP-8 main telescope corresponding to  $>100$  MeV penetrating protons. The peak at day 156-157 corresponds to the arrival of relativistic particles ( $>100$  MeV protons, electrons). This peak is also present in the SS rate indicating that SS is responding to relativistic particles. However, the SS rate does not fall after this peak as does the  $>100$  MeV proton plot. This indicates that SS is observing an additional component, either 50-100 MeV protons or electrons (with less than 100% efficiency) or, probably, some of both. In any case, it is clear that SS may be employed to monitor much higher energy particles than are possible with the monitor telescope and the CRIE-LO coincidence counting rates.

The above discussion demonstrates the importance and the utility of cross-calibration between two experiments exposed to the "same" environment. The conclusion from this cross-calibration is that the monitor telescope at the polar caps does indeed see interplanetary levels of particles. Thus, higher energy events have equally free access and provide valid measurements of the elemental and isotopic distributions of the SEP's. In addition, the SS rate is shown to be a valid monitor for relativistic particles from solar flares.

#### D. Charge States

For many years there have been reports of protons and heavy ions appearing in the magnetosphere at energies far below those required for a fully stripped particle to penetrate the Earth's magnetic field at the point of observation (Akasofu et al., 1963; Imhof et al., 1971; Oeschies et al., 1989; Biswas et al., 1990; Adams et al., 1991). These have been interpreted as non-fully stripped ions and attributed to the anomalous component, to solar flare particles or to a new cosmic ray component. The S81-1 orbit and the solar flare heavy ions recorded by the CRIE-LO instrument provides an opportunity to investigate the occurrence of such "sub-cutoff" heavy ions.

The advent of high precision computer codes for tracing charged particle trajectories through high-order multipole expansions of the internal field (e.g. Shea and Smart, 1975) has removed uncertainties inherent in theoretical calculations with simple dipole field models. However, a limitation of the trajectory tracing technique has been that, although the main cone regions of the rigidity spectrum can be used to determine rigidity cutoff values above which all particles have access to the observation point within the magnetosphere, finite computing time generally precludes the tracking of lower rigidity particles entering the magnetosphere via quasi-trapping and longitudinal drift modes. Such entry modes may be significantly affected or even facilitated by transient magnetospheric configurations associated with solar events.

One way of accounting for sub-cutoff events in an artificial manner is to assign an "effective" or "pseudo-" charge to each event, which presumes that the direct penetration of the magnetosphere by each such ion was made possible by a partially ionized state  $Q < Z$  where  $Z$  is the fully stripped ion charge. This approach has been used to estimate upper limits on charge states for ions arising from the anomalous component of cosmic rays at energies below 100 MeV/nucleon where such ions are thought to be singly ionized. Since low- $Z$  solar ions at keV-MeV energies are known to be "almost" fully stripped (i.e.,  $Z - Q < 2$ ) from direct charge state measurements, the deep penetration of such ions into the magnetosphere cannot be accounted for by charge state alone, but the effective charge distributions can still be calculated to characterize events with respect to proximity in rigidity to the nominal computed cutoffs.

Figure III.8 shows the low-L distribution of priority 1 (solid) and priority 2 (open) events that were pulse height analyzed during the S81-1 mission. The concentration of events at particular



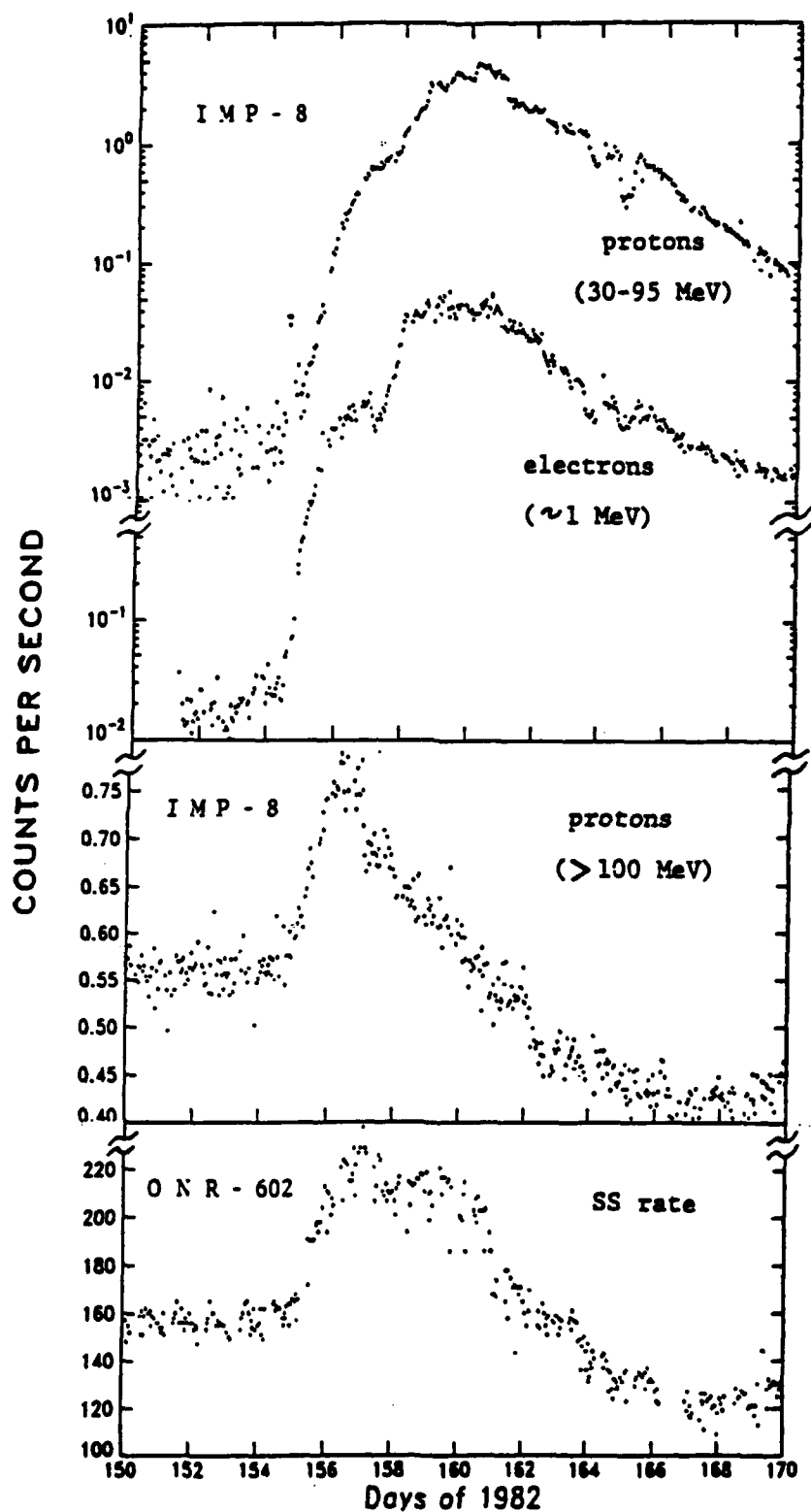


Figure III.7. Comparison of the time dependence of the ONR-602 scintillator rate (SS) with high energy proton and electron rates from IMP-8 for the June flare period.

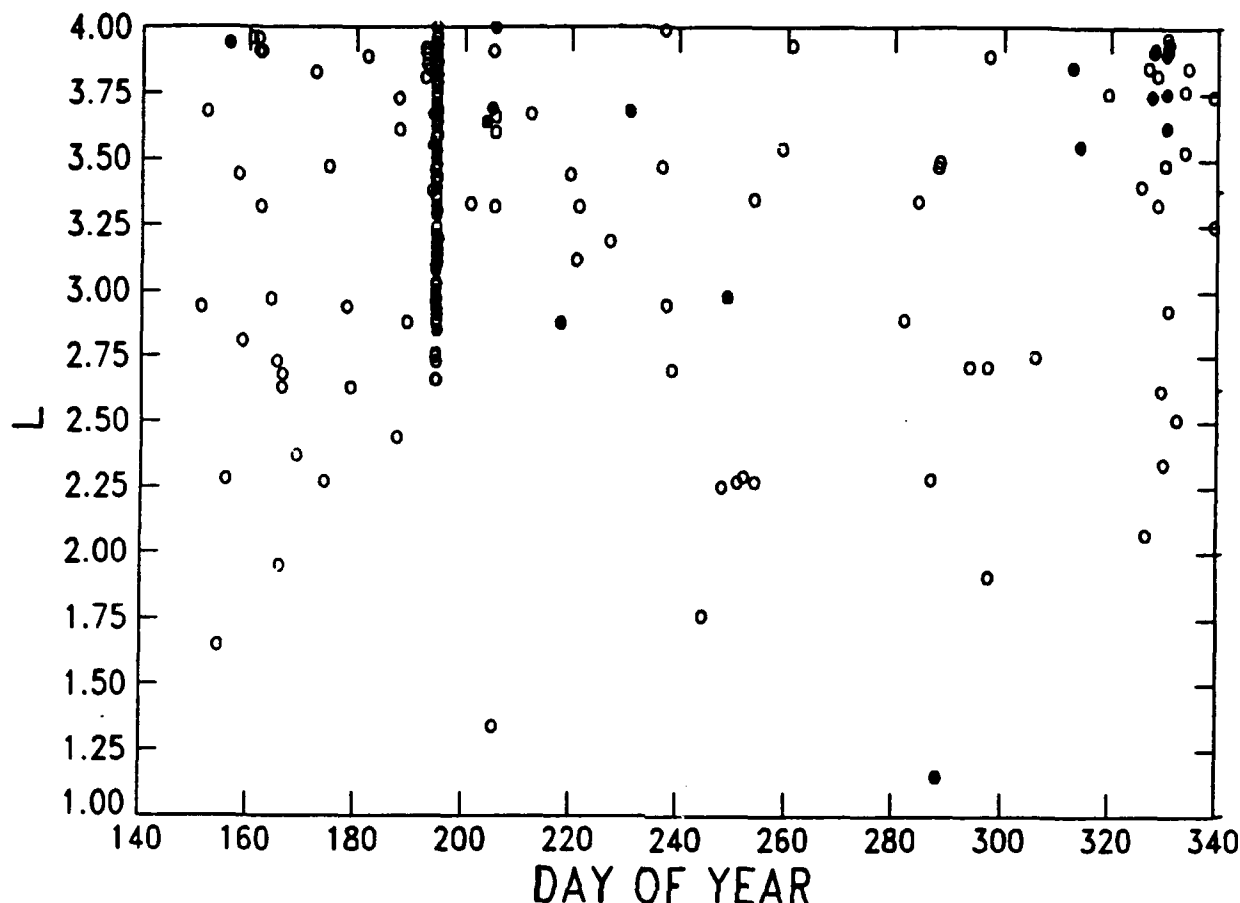


Figure III.8. The low-L distribution of P1 (solid) and P2 (open) events pulse-height analyzed by the CRIE-LO instrument.

days reflects the increased intensity during the large flares (see Figure III.1). The important point here is that these relatively low energy events are observed at quite low L values. For example, for  $L < 2.5$  in a simple dipole model, a fully stripped particle would need to have an energy  $> 0.5$  GeV/nucleon to penetrate to the S81-1 orbit.

We have developed a revised version of the Shea and Smart cutoff code incorporating the magnetic field model of the earth's magnetosphere of Tsyganenko (1987). This includes an internal component computed from the 1980 IGRF field model and an additional external field composed of several components arising from the ring current and other current systems in the magnetotail and magnetopause regions. Although local-time dependent cutoff variations are known to arise from longitudinally asymmetric ring current systems, the Tsyganenko model uses a symmetric ring current approximation which can lead to slight underestimates of day/night asymmetries in computed cutoffs. The general model is based on empirical fits to a long series of IMP and HEOS magnetic field measurements from 1963 onward. The fit parameters are determined for different Kp index levels (0-5) of geomagnetic disturbance.

Trajectory tracing is done for each particle to check whether the given ion event was detected on an allowed trajectory to the detection point from outside the magnetosphere. If the trajectory is not allowed for a fully stripped charge state  $Q = Z$ , we then decrement the charge state  $Q$  until an allowed trajectory is found, if any. Almost all ion events analyzed for  $Z > 2$  can be assigned a non-zero  $Q$  value, primarily since the assumed ion rigidity increases rapidly as  $Q$  approaches unity.

Figure III.9 shows the derived  $Q$  values for events identified as Carbon (top) and Oxygen (bottom) as a function of  $L$  for day 194 (orbit 1023) during the July flare. The circles and crosses show the result of assuming arrival from the West or the East, the two extremes in the cut-off calculations. In either case, there are a significant number of events with  $Q$  values less 6 (carbon) or 8 (oxygen) and the smaller  $Q$  values are found, as expected, at the lowest  $L$  values.

Figure III.10 (top) shows the ratio of  $Q/Z$  for the same Carbon events as a function of the particle energy (10-40 MeV/nucleon). It might be anticipated that the smallest values of  $Q$  would apply to the lowest energy events, but this does not appear to be the case. The energy distribution of the low  $Q/Z$  particles appears to reflect the distribution of the  $Q/Z = 1$  events to within the limited statistics. This indicates that there is no instrumental detection bias that is producing the low  $Q$  values.

The lower portion of Figure III.10 shows a summary of the  $Z$ - $Q$  values obtained for all of the events on day 194 as a function of the particle's actual charge  $Z$ . These "sub-cutoff" events are observed for all of the elements from Helium up to the Ne-Mg region of the charge spectrum.

Thus, our trajectory tracing technique also reveals particles, in this case SEP's, that have an "effective" charge well below their nuclear charge. These are not an artifact of the instrument or the analysis technique but represent valid charged particle events penetrating the geomagnetic field in regions that should be unallowed for a quiescent magnetic field. As described in the next section, we believe that these particles do not actually have  $Q < Z$  but are instead allowed to penetrate at low  $L$  values due to very disturbed conditions within the Earth's magnetosphere.

### E. Polar Access Regions

The question of particle penetration into the magnetosphere can be addressed quantitatively from a polar orbiting satellite such as S81-1. The presence of several large solar flares during the S81-1 mission allows both quiet and magnetically disturbed conditions to be investigated. Figures III.11 and III.12 show North (top) and South (bottom) polar pass profiles for two consecutive orbits near the onset of the flare increase on day 203. Shown are the time profiles for the ML rate ( $>0.5$  MeV protons) and for the P3 rate ( $>4$  MeV/nucleon helium + heavy ions + some proton pileup contamination) versus the fractional time phase of each 90-minute orbital period, for which the zero time corresponds to northward crossing of the nightside geographic equator. The north polar passage in orbit 1170 is closest to the onset time for P2 events at 1 AU and shows the strongest spatial variations and a nightside spike suggesting preferential SEP ion access on that side of the magnetosphere. Although statistics limited near onset, the P3 rate shows considerable structure at later times and conforms approximately to the ML profile.

The transient spatial variations indicate "windows" for SEP ion access which may persist in gross morphology from one orbit to the next but which can undergo smaller changes within 1-2 hours. It appears that the magnetospheric field lines threading the lower intensity regions in the polar cap structures suggest a potential link to processes also responsible for the theta aurorae and transpolar arcs in the same region. For example, field-aligned currents associated with such auroral phenomena may affect the linkage of polar cap field lines to interplanetary space through the magnetopause and thereby the access of interplanetary particles.

Turning next to the July, 1982 flare period, Figure III.13 shows the time profile of  $Z$ - $Q$  values (open circles in the range of 1-10 on the vertical axis) and magnetic  $L$  values for P2 ions events measured during the peak flare intensity period on day 194 (July 13). Also shown is the  $K_p$  index (top) and the product of solar wind velocity and the square of the interplanetary magnetic field magnitude (dashed line), the latter being a measure of the solar wind pressure on the dayside magnetopause. Although values of  $Z$ - $Q > 0$  are found all during the process of the flare, the

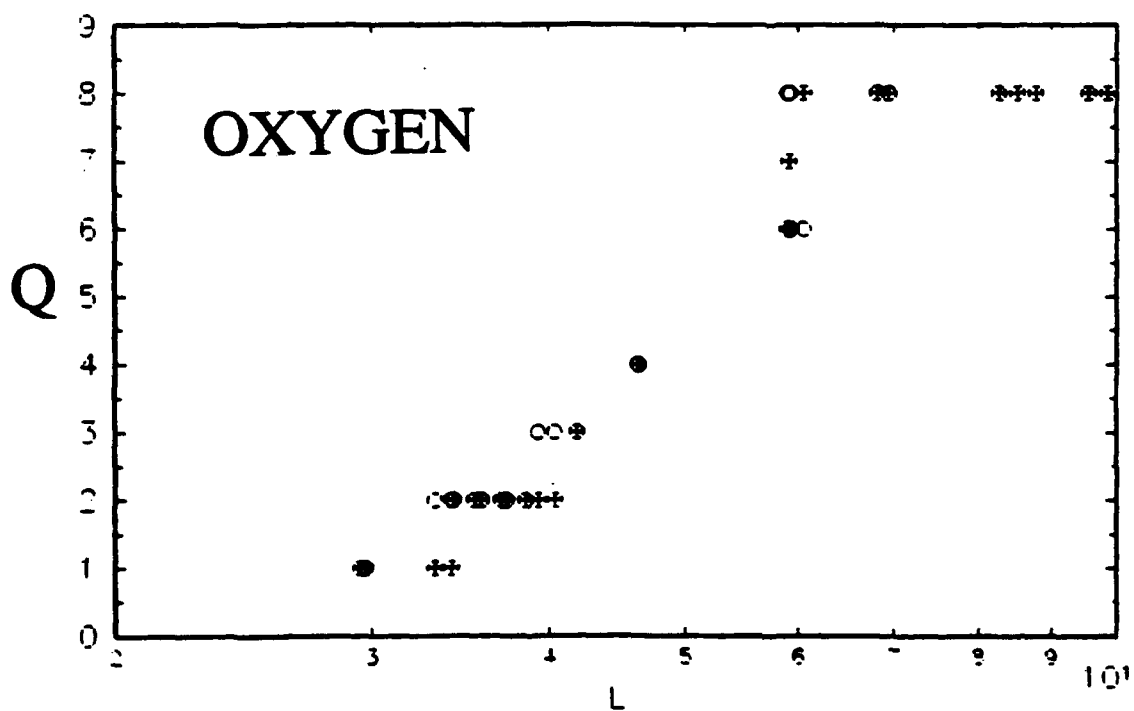
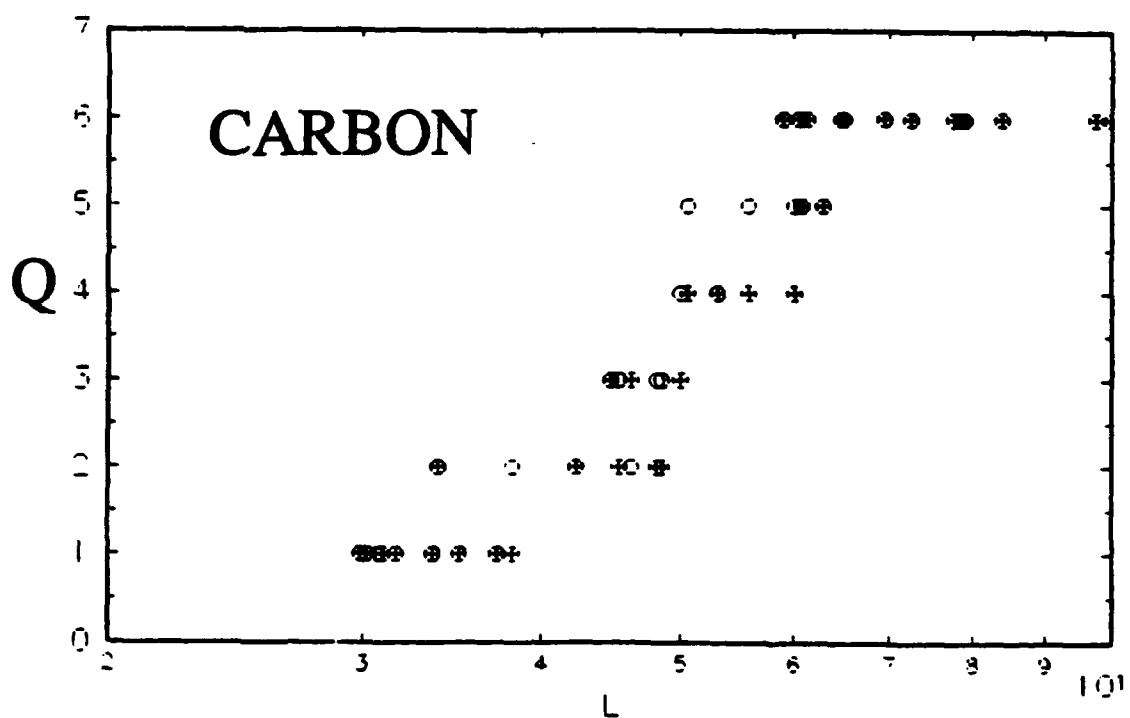


Figure III.9. "Effective" charge  $Q$  calculated for Carbon (top) and Oxygen ions (bottom) recorded on day 194.

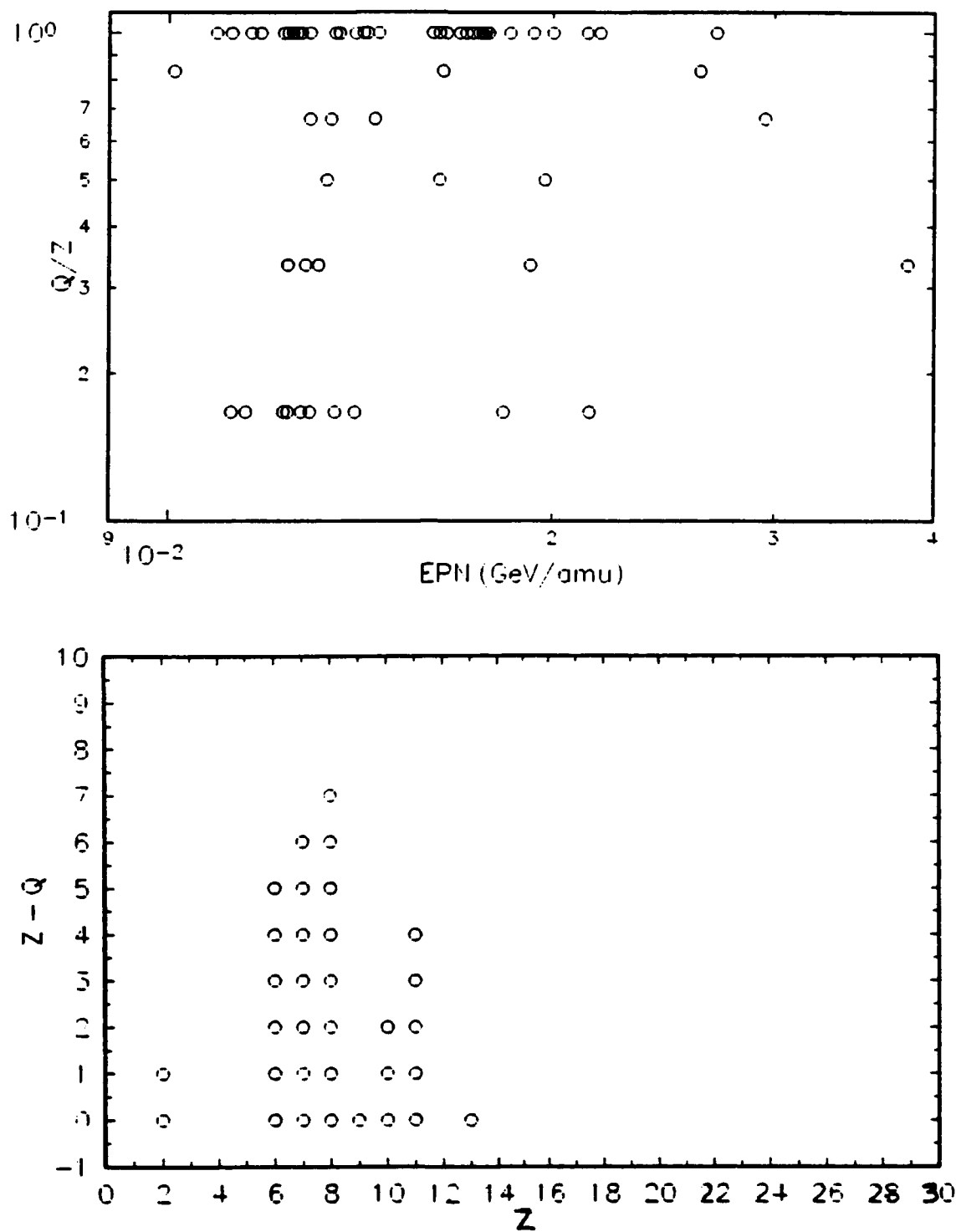


Figure III.10. The energy distribution of the fractional charge  $Q/Z$  for the Carbon events of Figure III.9 (top) and the  $Z-Q$  distribution for all of the events of day 194 as a function of the particle's nuclear charge (bottom).

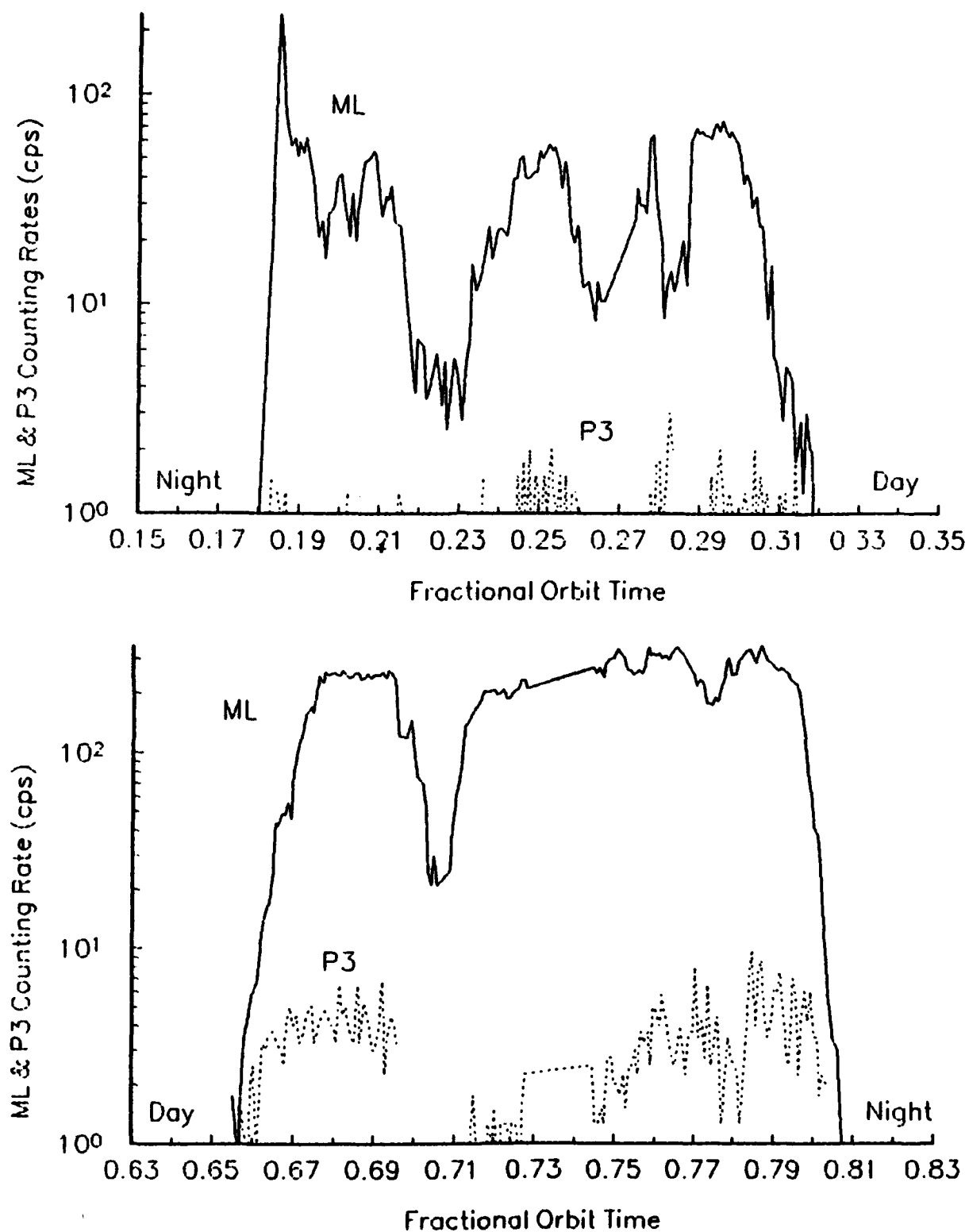


Figure III.11. The North (top) and South (bottom) polar pass for orbit 1170 on day 203 of 1982.

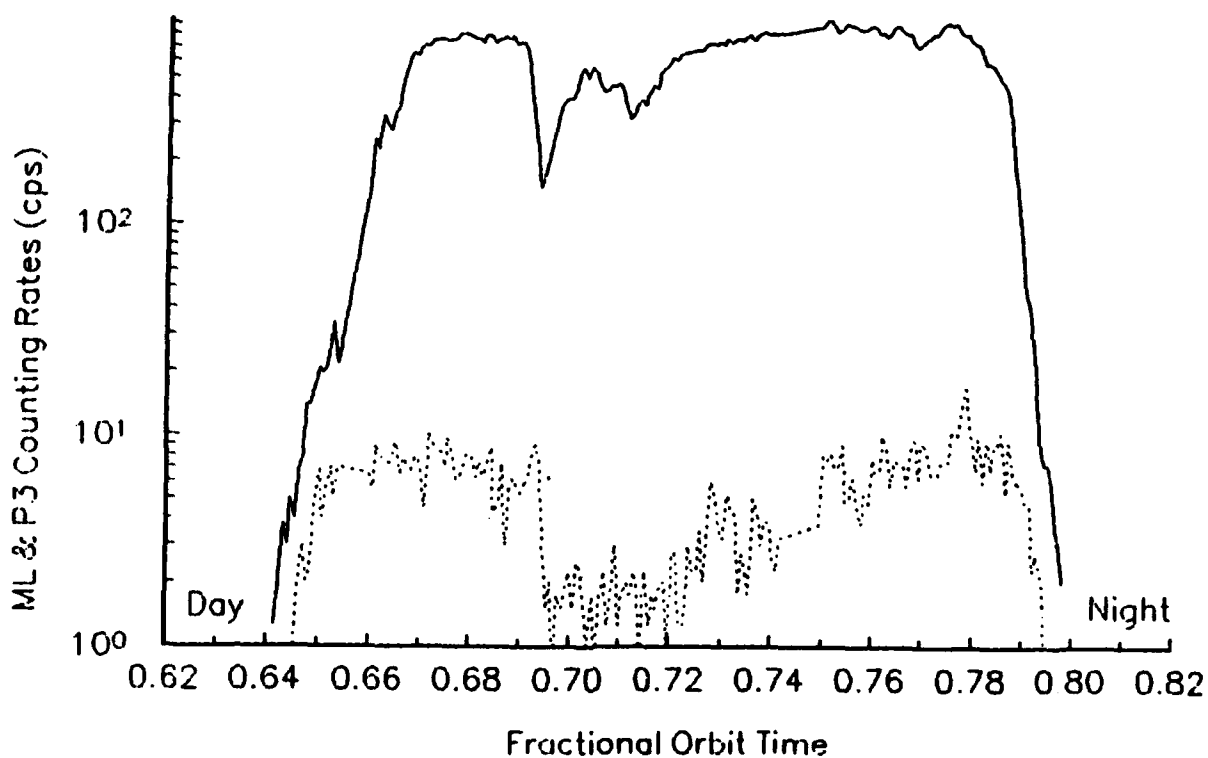
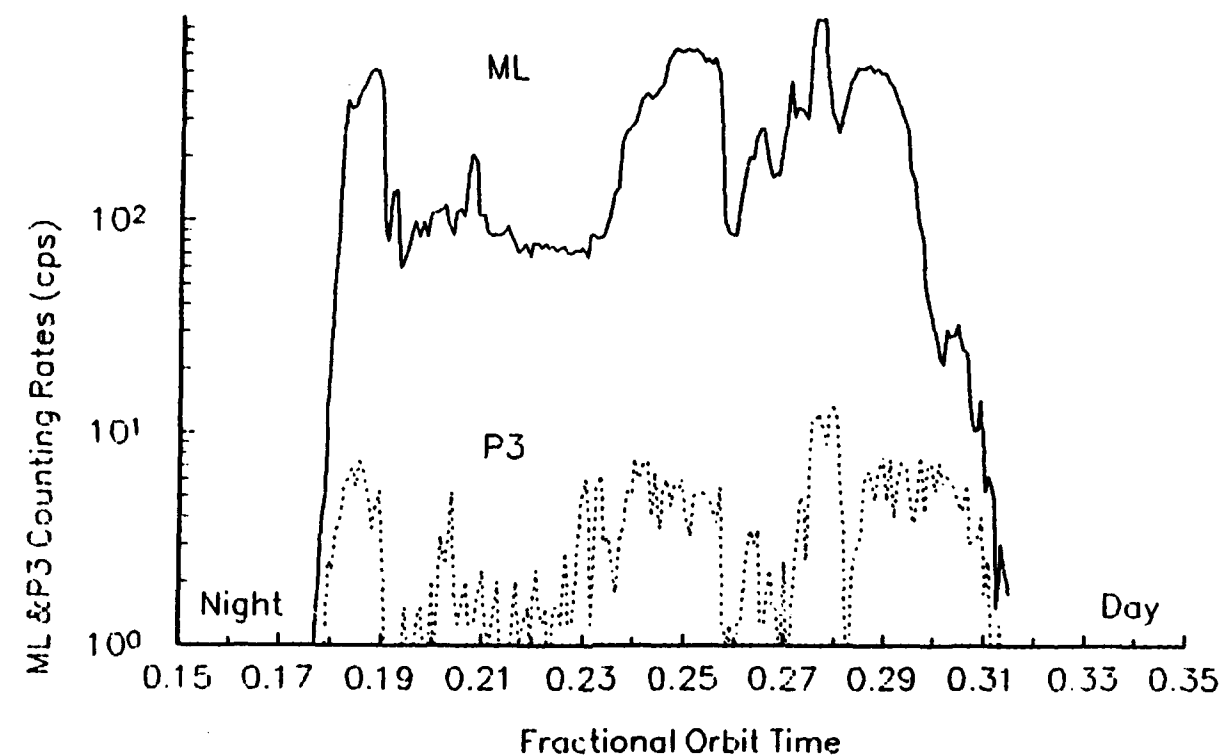


Figure III.12. Same as Figure III.11 except for the next orbit, 1171, on day 203.

# S81-1 P2 Events >10 MeV/amu for July 11-13 Flares

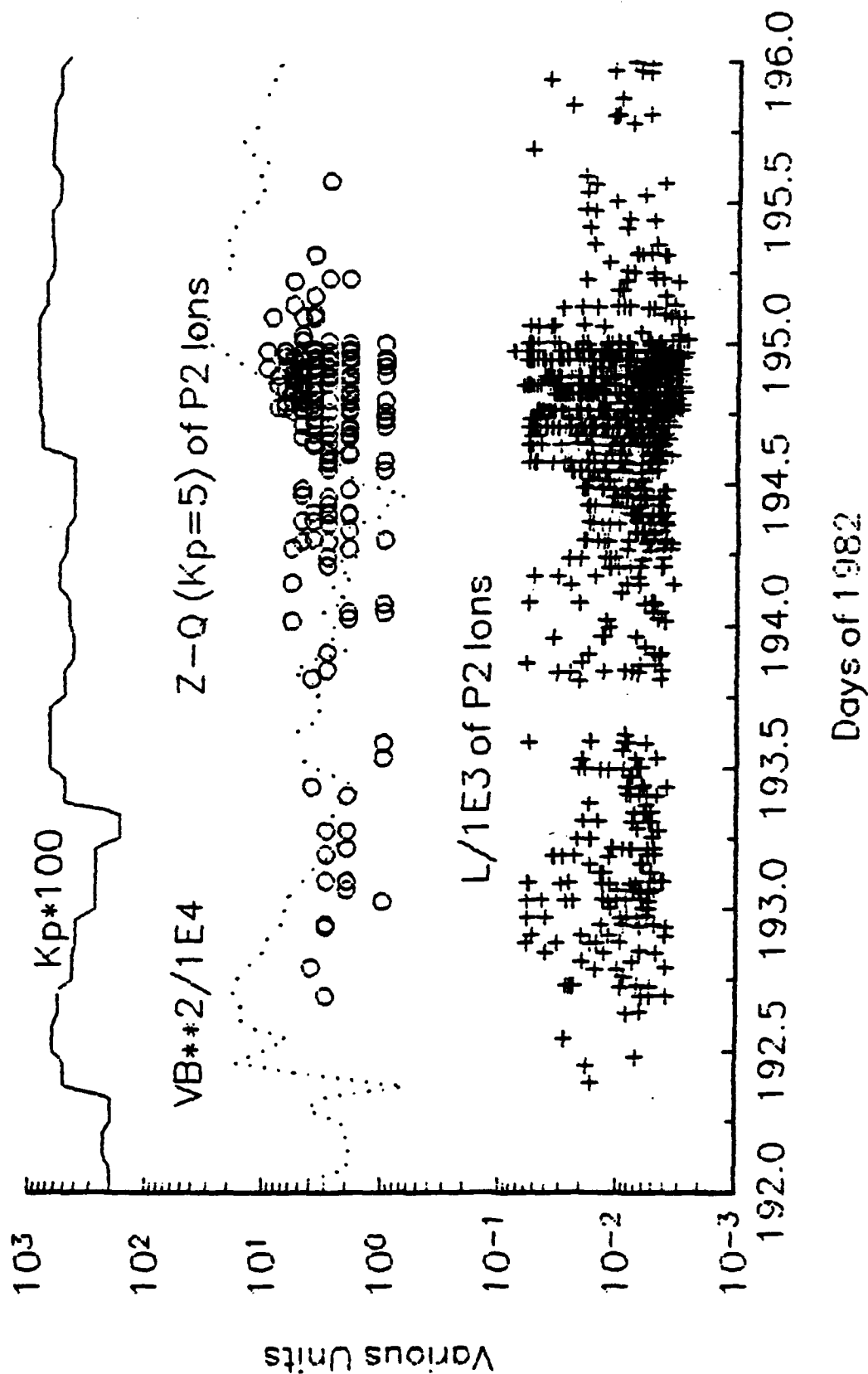


Figure III.13. The time history of the July, 1982 flare showing, from top, the  $K_p$  index, the solar wind pressure on the magnetosphere, the Z-Q values for the ions and the L position of the ion's arrival at the spacecraft.



largest values up to 10 (i.e., for ions with  $Z > 10$ ) are found in the most intense period at day 194.5-195.0 when the  $K_p$  and solar wind parameters show a sharp upturn in magnetospheric activity and solar wind pressure. The increase in large  $Z-Q$  is associated with more events being detected at lower  $L$  values where higher magnetic rigidities (e.g., lower  $Q$  for given momentum determined from the measurements) are required to account for the events as being of solar flare origin. Note that  $K_p=5$  was used as a worst case value for the magnetospheric disturbance level in the Tsyganenko field model. This value minimizes the number of  $Z-Q > 1$  events in the present analysis.

The implication of Figure III.13 is that the apparent presence of ions with  $Z-Q > 1$  is correlated with the level of disturbance in the geomagnetic field, as indicated by  $K_p$  and the solar wind pressure. Such effects should also be observable during the polar passes. As an illustration, Figure III.14 shows the calculated  $Z-Q$  values for the P2 events as functions of the satellite  $L$  value for events detected in two orbits, before and during the peak intensity of the flare. Events with  $Z-Q = 0$  are shown at the bottom of the figure, indicating detection in geographic local time on the dayside (open circles) and nightside (plus sign). Values of  $Z-Q \geq 1$  are plotted between 1 and 10 on the ordinate axis with the same symbols for dayside and nightside events. Also shown are the dayside (solid) and nightside (dotted) counting rate profiles for the  $>0.5$  MeV proton (ML) and the  $>4$  MeV/amu helium (P3) channels. Note the large changes in  $L$  position of the equatorward boundaries for the proton and helium profiles. For orbit 1023 the ML protons and the He + heavy ions counted by P3 had, on the nightside, essentially unimpeded access down to  $L < 3$ !

The most striking comparison, however, is the ion events with  $Z-Q > 0$ . These occur at or poleward of the low energy particle access boundary. None of the events are found at appreciably lower  $L$  values than the access "edge." Since the proton profile (ML) would not be affected by charge state differences, it seems that the protons and the associated ion events near the proton boundaries gain access into the magnetosphere well below the Stormer cutoffs in  $L$  for those particles ( $L = 10$  for  $\sim 10$  MeV/nucleon P3 ions). The strong correlation of observed cutoffs in the counting rate profiles and ion event locations to the increasing dayside/nightside asymmetry between the two orbital intervals argues that the solar flare particle access to low altitudes is not accurately modeled by the Stormer-type calculation. Also, the magnetospheric configuration at these times may be significantly different from that used in the Tsyganenko model (even with  $K_p=5$ ). It is also possible that the ions may gain access via quasi-trapped trajectories over the observational time resolution interval between consecutive crossings of the polar caps. Radial diffusion could account for some of the  $Z-Q > 0$  events, but the paucity of events in the mid- and low-latitude regions suggests that inward transport rates are only significant, if at all, in the outer magnetosphere near the nominal cutoff boundaries.

Thus, the presence of events whose calculated  $Q$  is less than the nuclear charge  $Z$ , should not be taken to imply non-fully stripped particles. The magnetic field models used to calculate these  $Q$  values are certainly not correct during the highly disturbed conditions surrounding a flare such as the July, 1982 period. The events could well be fully stripped and follow the same access routes that allow the low-energy ML and P3 ions to be observed at low  $L$  values. Thus, we suspect that the reported "sub-cutoff ions," at least those of solar flare origin, do not necessarily indicate an anomaly but may be the result of our inability to model the disturbed geomagnetic field and the corresponding particle access channels.

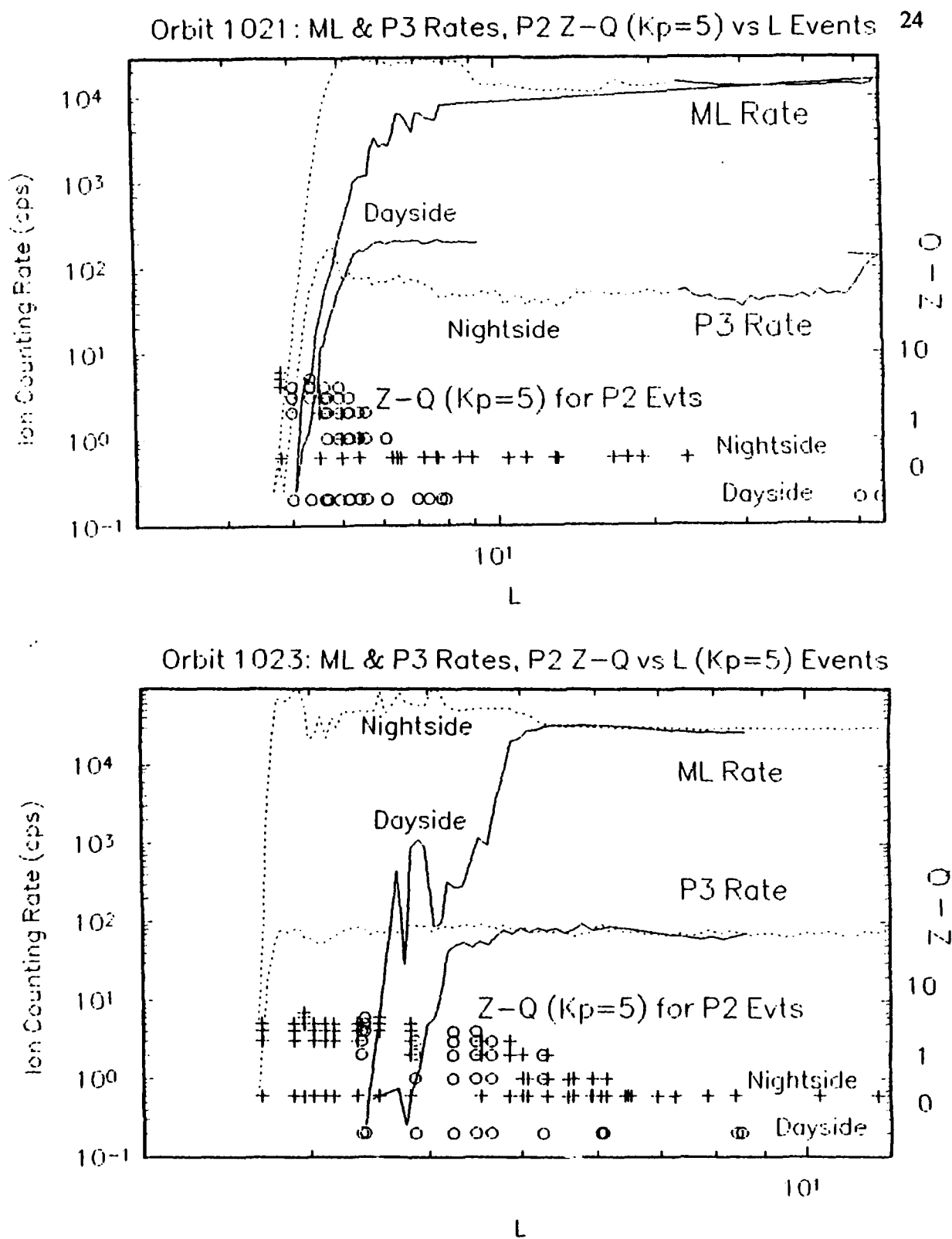


Figure III.14. North polar passes for orbits 1021 (top) and 1023 (bottom) showing the L dependence of the ML and P3 counting rates and the distribution of Z-Q for the P2 ions.

## IV. ONR-604 Performance

The "key" experiment for heavy ion analysis on CRRES is the ONR-604 instrument built by the Laboratory for Astrophysics and Space Research at The University of Chicago under the direction of John A. Simpson. The experiment was constructed with NASA support from the CRIE project under contract NAS-2-24430 and sponsored for flight on-board CRRES by the Office of Naval Research.

### A. Instrument Description and Operation

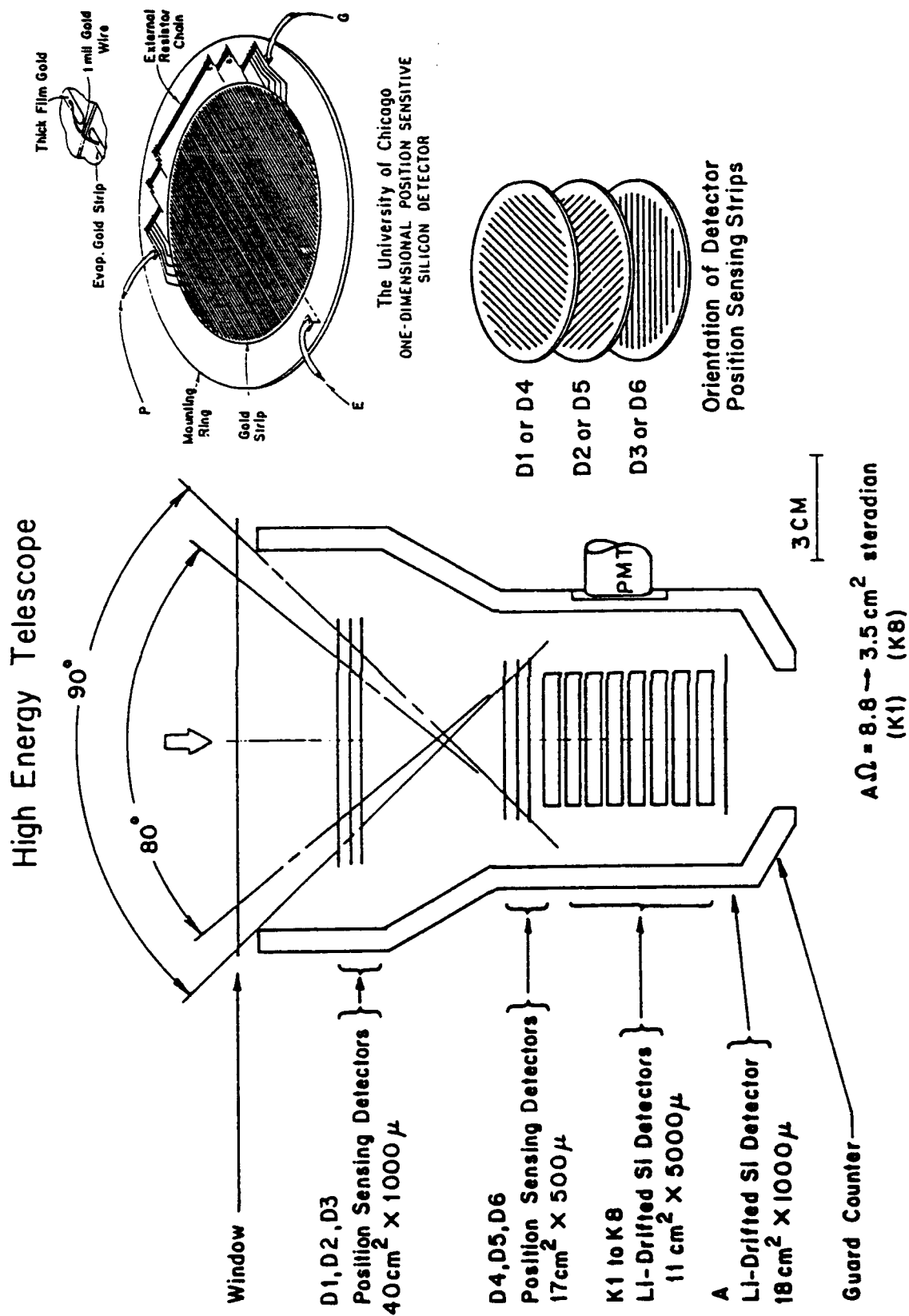
The ONR-604 investigation was designed to obtain new data on the elemental and isotopic composition of high energy, heavy ions to explore processes in solar flares, in the galaxy and within our Geospace environment. The instrument is optimized for studies of the heaviest ions, up through the iron peak. The single High Energy Telescope (HET), shown schematically in Figure IV.1 (Simpson et al., 1985), consists of a stack of fifteen silicon solid state detectors surrounded by a scintillation guard counter plus external passive shielding to reduce the effects of low energy background radiation. The stack contains six Position Sensitive Detectors (PSD) -- upper right -- used to determine the particle trajectory (Lamport et al., 1976) followed by eight 5 mm thick detectors which measure the particle energy loss and residual energy, allowing mass and charge identification by the  $\Delta E$ -E technique. A 1000 micron thick penetration detector (A) is located at the bottom of the stack.

A unique feature of the instrument is the six one-dimensional PSD's, for which ONR-604 is the first space exposure of this new technology developed at Chicago. A schematic view of a PSD is shown at the top right of the figure. The upper surface consists of many parallel strips of gold each connected via a wire bound to a resistive divider network. By comparing the signal from the resistive divider network (P) to the full energy signal measured at the stack surface (E), the strip nearest the point of incidence of the particle can be determined. From a fit to the positions in the six PSD's, the trajectory of the particle is determined with an angular accuracy of better than  $1^\circ$ , as validated by accelerator calibrations. The PSD's allow the incident trajectory of each event to be determined, providing corrections for the path length in the other detectors and point of incidence on the detector surface as well as allowing, for example, the particle pitch angle distribution to be studied.

For each event that is pulse height analyzed, the total energy deposited in each of the first 14 detectors is read out. This allows the particle range ("ID") to be used to subdivide the full energy interval. For high precision charge and mass identification, the particle must come to rest within the instrument, which determines the energy over which each type of particle can be studied. The entire stack is surrounded by a scintillator guard counter to eliminate out-of-geometry events and particles that exit from the side of the apparatus. The scintillator signal is not part of the trigger logic but is recorded (along with A) as a flag for each analyzed event. In addition, a ground-commandable operations mode is provided for the detailed analysis of proton and alpha particle flux levels.

Because the anti-coincidence scintillator guard subtends a large solid angle, it must be shielded from the high counting rates induced by electrons trapped in the magnetosphere. Passive shielding to eliminate  $<4$  MeV electrons is provided by a magnesium shield and Tantalum collar. The lower part of the scintillator is located well within the instrument package and is surrounded on five sides by electronic modules which offer additional shielding. The backward moving particles are shielding additionally by the spacecraft structure.

In order to protect further against accumulated radiation damage to the detectors D1, D2 and D3 (where the average geometrical factor is  $87 \text{ cm}^2\text{-sr}$ ), a 3 mm external aluminum window shield is placed over the telescope. This shield lowers the magnetospheric integrated proton and electron



The University of Chicago  
MAR. 2, 1977.

Figure IV.1. The ONR-604 telescope and its Position Sensing Detectors.

radiation doses for detectors D1, D2, and D3 below the tolerance threshold of these detectors while increasing, only slightly, the energy intervals for measurement of the heavy particles which are the main objective of the experiment.

Separating isotopes for elements as heavy as nickel, requires precision measurements of the energy deposits in the detectors. For this, exceptionally linear, highly stable electronic circuits to analyze the signals have been developed. Each analysis chain is individually calibrated preflight. The performance of each analysis chain is monitored during flight by an on-board calibrator which sends a sequence of 2000 pulses spanning the entire range of signal sizes. Further, in-flight calibration and normalization is provided by measurement of actual galactic cosmic ray events.

In addition to heavy particles, the instrument measures protons and alpha particles over the energy range 25-120 MeV/nucleon. In quiet regions of space, a priority system insures that the heavy nuclei are analyzed in preference to protons and alphas. In regions of high background radiation, a commandable heavy particle "normal mode" is invoked. This raises the thresholds on the detectors D1 through D6 to suppress the high firing rates induced by trapped protons and electrons while still permitting the rare heavy ions to be analyzed. In "normal mode", the "proton mode" thresholds of detectors D1 through D6 are increased by a factor of 5.8 and, as a consequence, the instrument becomes practically insensitive to single protons.

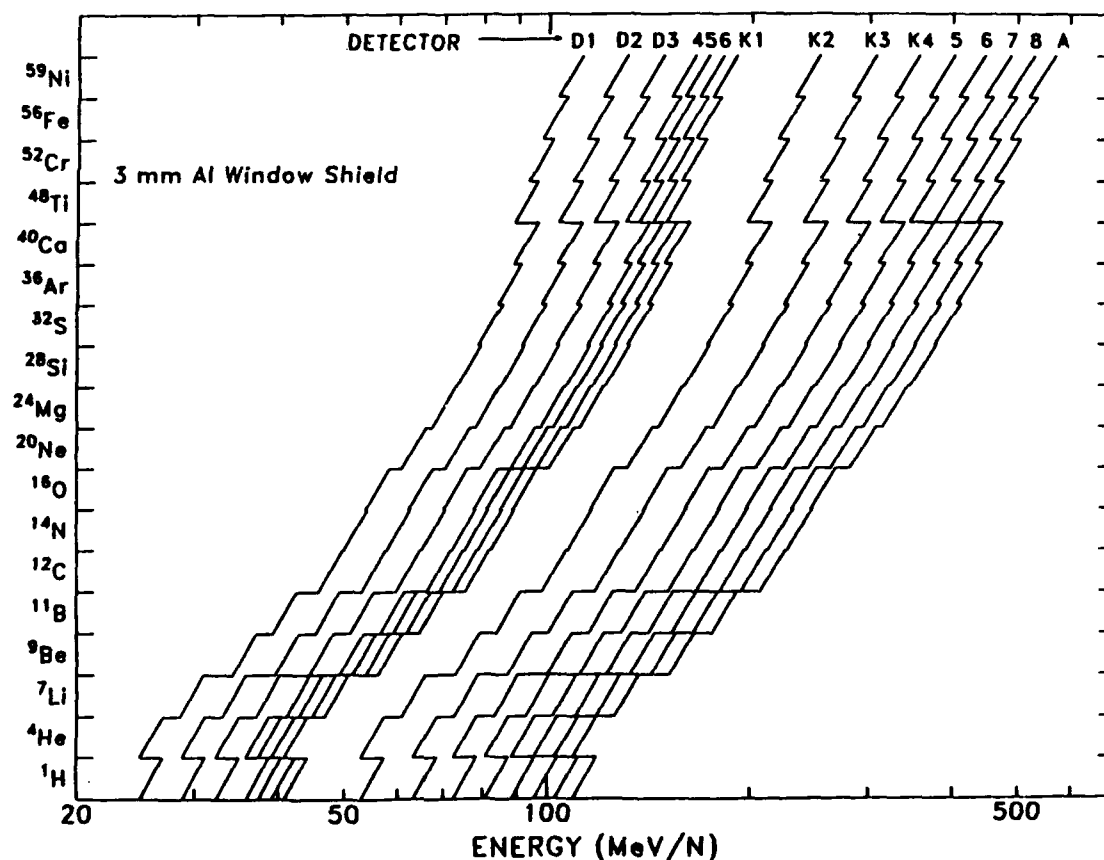


Figure IV.2 ONR-604 energy ranges for selected isotopes.

The energy ranges for triggering the different detectors for different species in the ONR-604 instrument are illustrated in Figure IV.2 for selected isotopes from H through Ni. The lines connect the incident energies for  $0^\circ$  and  $30^\circ$  angles of incident. Figure IV.2 indicates that H and He are studied over an approximate interval of 25-120 MeV/nucleon while Fe is measured over a range of ~100-550 MeV/nucleon.

The instrument acceptance is also a function of energy. For the lowest energy events, those that stop in D1 - D3, the geometrical factor is  $>80 \text{ cm}^2\text{-sr}$  while for the highest energies (stopping in K8) the geometrical factor is only  $\sim 3 \text{ cm}^2\text{-sr}$ . This changing acceptance provides one of the principal normalization problems in deriving particle spectra.

The highest quality data is obtained for particles stopping in K2-K8. However the HET also measures particles that (1) stop in K1, (2) stop in D2 - D6 and (3) penetrate K8. For (1) and (2), it is necessary to use the signal from the E contact of the PSDs to provide energy loss information. For events stopping in D2 or D3, the path length uncertainty is given by  $\sec \theta$  where  $\theta$  is the maximum angle through the window ( $\sim 69^\circ$  for D2) which gives a spread of a factor of 2.8. Thus, D1 D2 and D3 analysis can separate protons and helium, but no heavier elements. For particles stopping in D4, the  $\sec \theta$  spread is reduced to a factor of 1.44. Particles stopping in D5 - K1, have trajectory information available, and elemental separation is limited only by the quality of the E signals from the PSDs. Finally, the charge composition of events penetrating the entire stack can be studied over a limited energy interval.

The ONR-604 instrument incorporates a priority system for the pulse height analyzed events. Each particle is defined by the instrument logic hardware as either a P1, P2 or P3 event. P3 is the instrument trigger, defined by the logic condition

$$P3 = GC = D1D2D3\bar{S} + D1D2D3(K1 + K2).$$

Thus, allowed events must trigger the first three PSD's, and not go out the sides triggering the scintillator OR must trigger the first three detectors and one of either K1 or K2, independent of the scintillator. (Commands are available to allow any or all of detectors D1, D2, D3, K1, K2, S or A to be disabled in the logic.) P2 events add to P3 the requirement,  $(K1M + K2M) \bar{A}$ , i.e. the particle must stop in the stack and trigger the medium level discriminator threshold on detectors K1 or K2. Finally, P1 events add to P3 the requirement that one of the high discriminator thresholds on K1 - K8 must be triggered. Thus, considering the discriminator thresholds, P1 responds approximately to  $\geq \text{Ne}$  (stopping or penetrating); P2 records He to  $\sim \text{Ne}$  (stopping), and P3 encompasses everything else allowed by the trigger logic. When a high priority event is detected, it will cancel the pulse height analysis of a lower priority event. Thus a P1 will replace a P2 or P3 event, while a P2 will override a P3 event. (Discriminator patterns indicate when such an override has taken place.) This priority system ensures that a maximum number of P1 events will be analyzed and that the preponderance of H and He will not "swamp" the heavy ions. This is particularly important for obtaining heavy ion fluxes, since for Iron, for example, over the energy range 180-535 MeV/nucleon, corresponding to IDK1 through IDK8 in ONR-604, the expected number of nuclei is only about a dozen per day!

The ONR-604 instrument returns both pulse height and count rate data, the latter involving both singles and coincidence rates, including the P1, P2 and P3 priority rates. The counting rates are important in their own right, provide a diagnostic for instrument performance and are used to normalize the pulse height readouts to obtain particle flux. The rates are accumulated for a fixed time period of 4.096 seconds and their readout is controlled by a commutation system. Logic rates are output continuously while detector singles counting rates are sub-commutated so that singles rates are available less frequently. Table 4.1 gives the logic for the different rates as well as an indication of the approximate particle energy range sampled by the rate.

Table 4.1: ONR-604 Counting Rates

Rate No.	Detector Interval (Rate Name)	Rate Logic		Energy Interval of Rate in Proton Mode (MeV)	Particle Defining Energy Interval
1	D1	$D1\overline{D2}\overline{D3}$	$(\overline{S})a$	24.8 - 44.5	Protons
2	D2	$D1D2\overline{D3}\overline{D4}$	$(\overline{S})a$	28.3 - 48.2	"
3	D4	$D13D4\overline{D5}\overline{D6}$	$(\overline{S})a$	35.1 - 43.9	"
4	D5	$D13D5\overline{D6}\overline{K1}$	$(\overline{S})a$	36.6 - 45.5	"
5	K1	$D13K1\overline{K2}\overline{K3}$	$(\overline{S})a$	40.0 - 59.4	"
6	K2	$D13K1D2\overline{K3}$	$(\overline{S})a$	52.0 - 70.6	"
7	K3	$D13K1K3\overline{K4}$	$(\overline{S})a$	62.1 - 79.9	"
8	K4	$D13K1K4\overline{K5}$	$(\overline{S})a$	71.2 - 88.5	"
9	K5	$D13K1K5\overline{K6}$	$(\overline{S})a$	79.3 - 96.5	"
10	K6	$D13K1K6\overline{K7}$	$(\overline{S})a$	87.0 - 103.5	"
11	K7K8	$D13K1K7\overline{A}$	$(\overline{S})a$	94.0 - 116.9	"
12	A	$D13K1K8A$	$(\overline{S})a$	107.5 - 275	"
13	P3	$D13\overline{S}+D13(K1+K2)$		24.8 - 275	"
14	P2	$P3(K1M+K2M)\overline{A}$		42 - 105	$^4\text{He}$
15	P1	$P3 (K1H+K2H+K3H+K4H+K5H+K6H+K8H)$		127 - 352 (typical)	$^{24}\text{Mg}$
16		Single's Rate Sub-com			

Notes: M = Medium Threshold; H = High Threshold; (Low Threshold is indicated by detector symbol)

S Scintillation guard counter

$(\overline{S})a$   $\overline{S}$  term included in every alternate readout

P3 Pulse Height Analysis Gate Control (Priority No. 3 or low priority)

P2 Priority No. 2 or Medium Priority

P1 Priority No. 1 or High Priority

Figure IV.3 shows a sample plot of the rates for orbit 649, first part of day 108 of 1991. Figure IV.3a gives the three priority rates and the command state of the instrument. ONR-604 went into proton mode (PM) about 0615 and remained there until ~1115, corresponding to the apogee portion of the orbit. The P3 rate, for example, jumped about an order of magnitude when PM mode was on. Note the P1, P2 and P3 spike around 0900. This corresponds to a calibration period as indicated by the CAL (C) command, and must be removed from rate averages. There was also a data gap during this orbit from ~1145 - 1350. Just after the gap the P2 rate shows a tremendous "spike" for a single readout. These occur periodically and must also be eliminated to obtain clean data. Finally, one should note the P1 rate in which the individual particles can (almost) be counted, indicating the low intensity of the heavy ions.

Figure IV.3b displays the singles rates from the different detectors (~1 minute averages), and Figures IV.3c-e show the coincidence rates listed in Table 1. In each plot of Figure IV.3c-e, the rate logic with the  $\bar{S}$  term is plotted as the solid line, while the rate without this term is given as the dashed line. Rate D1 and D2 are shown as 33 second averages while the remainder are displayed as 3 minute averages. In all cases, the peak between 0400 and 0500 corresponds to low-L values ( $L = 1-3$ ) and shows the effect of magnetospheric particles on the ONR-604 counting rates. Note also that there is significant structure in the rates during a perigee pass (0400-0500) and into the "apogee" portion (0630,  $L > 5$ ) of the orbit. Understanding this structure is one of the challenges for the ONR-604 data analysis.

## B. Pre-launch Calibration

The ONR-604 instrument was calibrated in July, 1977, April, 1978, July, 1979, and again in February, 1989 with beams of He, C, Ne, Ar, and Fe particles (with energies such that the particles stopped in the telescope) at the Bevalac heavy ion accelerator at the Lawrence Berkeley Laboratory. These extensive calibrations demonstrated that ONR-604 can resolve isotopes of H to Ni, over the relevant energy ranges, and provided a means to check instrument operation, priorities, rates and thresholds. Finally, the use of a radioactive source during the Feb. 89 calibration provided a simulation of expected instrument performance in a high radiation background environment.

With the imminent launch of CRRES, a portion of our effort had to be devoted to finalizing the calibration data and looking for effects that would be observed in the flight data. In addition, we wanted to produce a calibration dataset close to what was expected on-orbit, in order to have a baseline to which the flight data could be compared.

For the accelerator work, special interface electronics were constructed. This interface eliminated the slow synchronous readout of the instrument and replaced it with a fast asynchronous readout which allowed the accumulation of significant statistical samples of events from the accelerator beam. For final confirmation of performance, the CRRES S/C interface was re-installed and data was recorded in spacecraft mode. Significantly more heavy ion events were recorded during these accelerator runs than will be seen during the entire CRRES mission!

For accelerator calibrations, the instrument was mounted in a gimbaled cradle that allowed it to be rotated in two axes. This permitted the beam to enter the telescope at a variety of zenith and azimuth angles. Such angular variations allowed the performance of the PSD trajectory system to be checked over the full range of allowed particle incidence angles and permitted the study of "edge effects" for particles incident at the maximum possible angles.

The accelerator beams were first focused at the instrument. Then, in front of the instrument was placed a polyethylene target (to fragment the beam into lower charge isotopes) and a rotatable aluminum wedge. The rotation of the wedge reduced the energy of the beam to provide events stopping throughout the detector stack. The beam was then defocused, which expanded it from about  $1 \text{ in}^2$  to  $\sim 4 \text{ in}^2$ , to cover the full size of the front three detectors (see Figure IV.1). Small



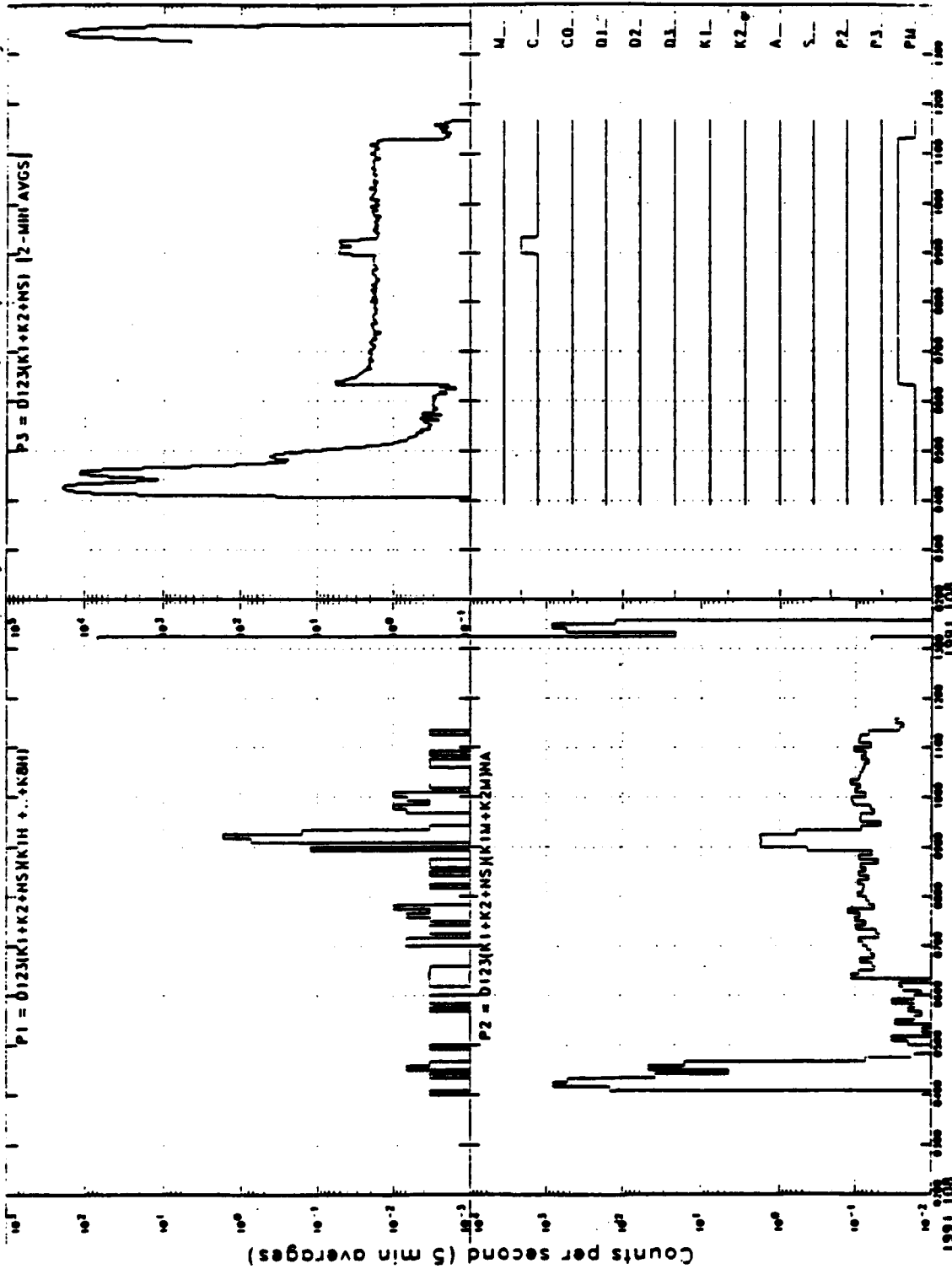


**Figure IV.3a. P1, P2 and P3 rates and ONR-604 command state for orbit 649, 18 April, 1991.**

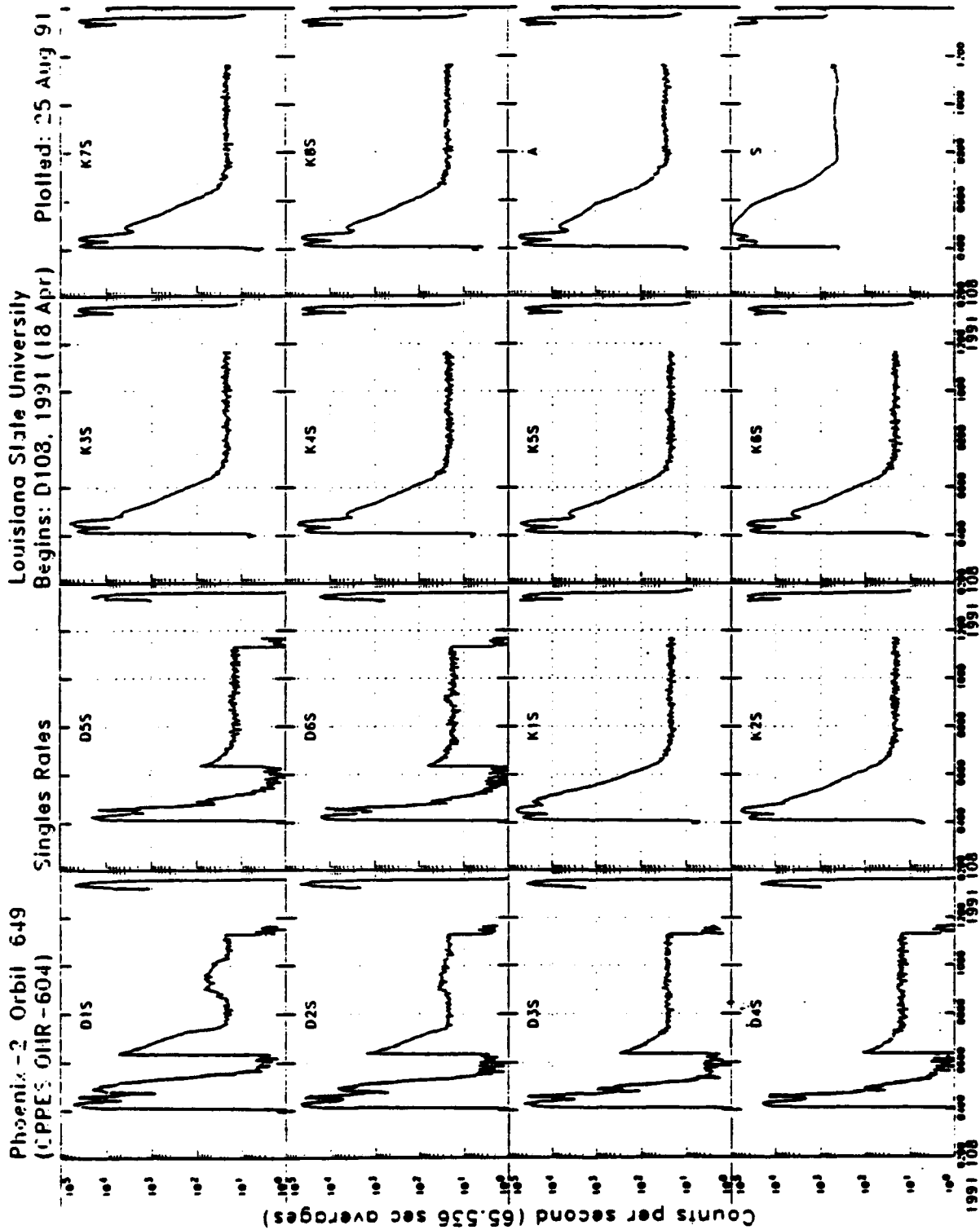


Figure IV.3b. Singles counting rates for orbit 649.

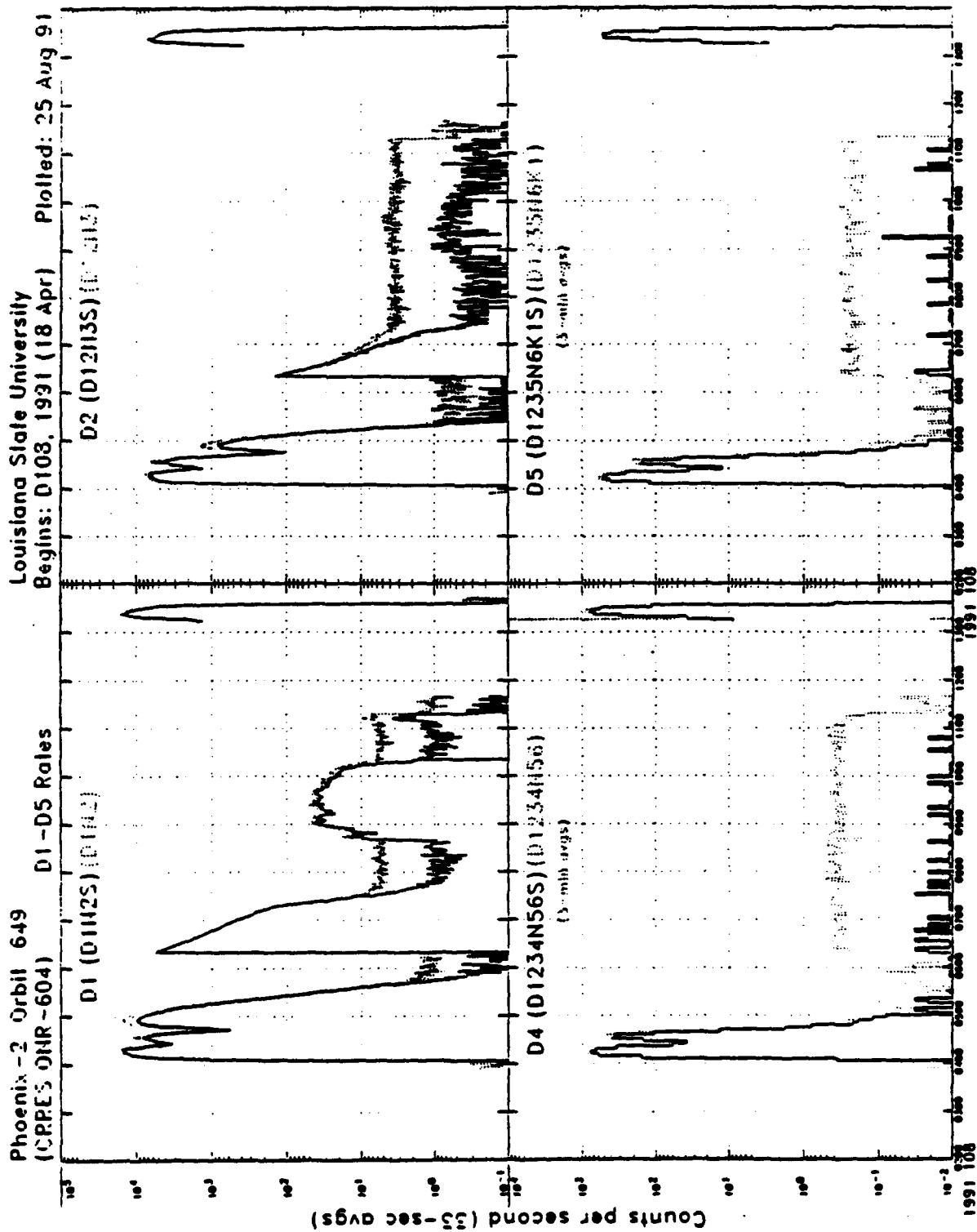


Figure IV.3c. Coincidence rates D1 - D5 for orbit 649.

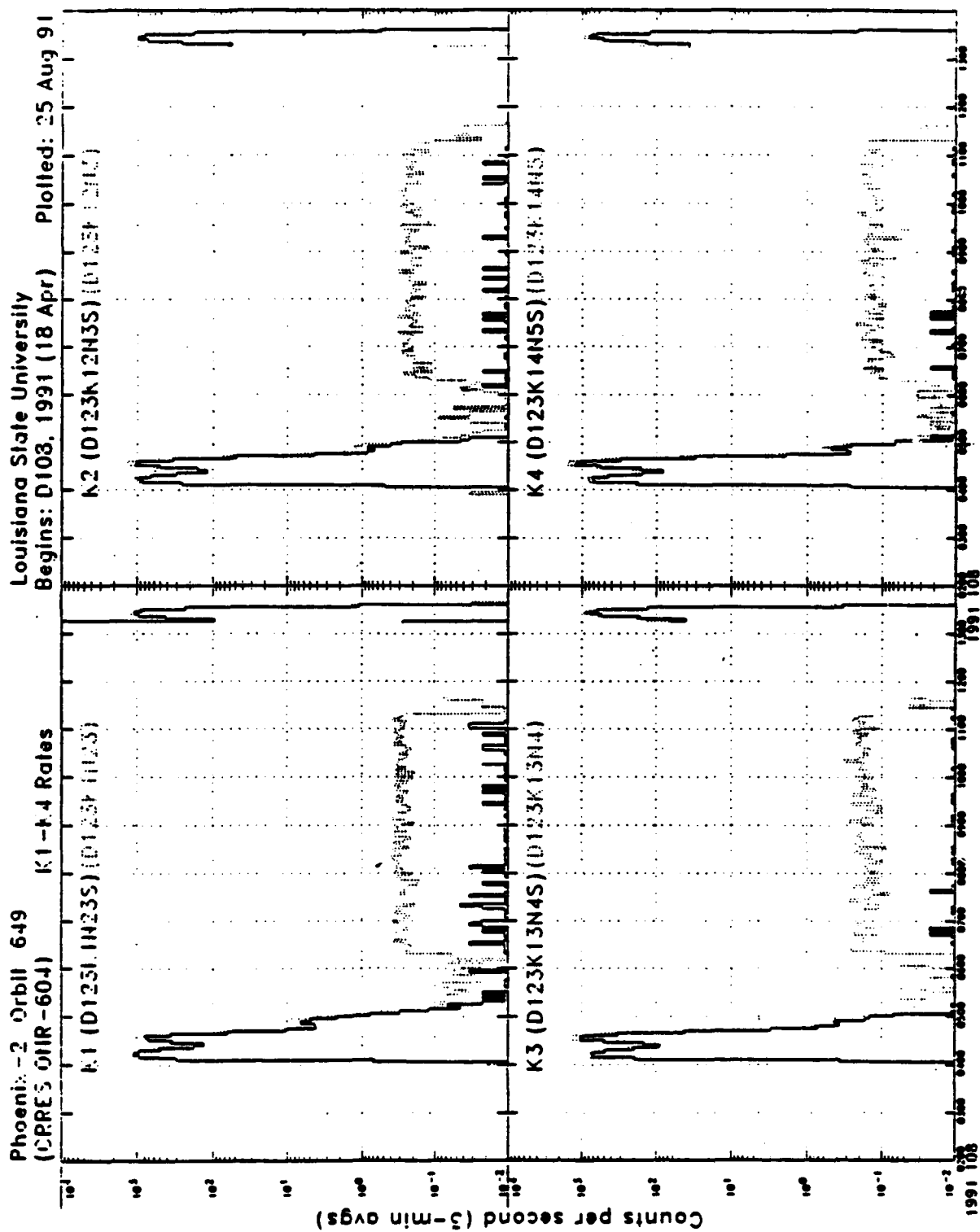


Figure IV.3d. Coincidence rates K1-K4 for orbit 649.

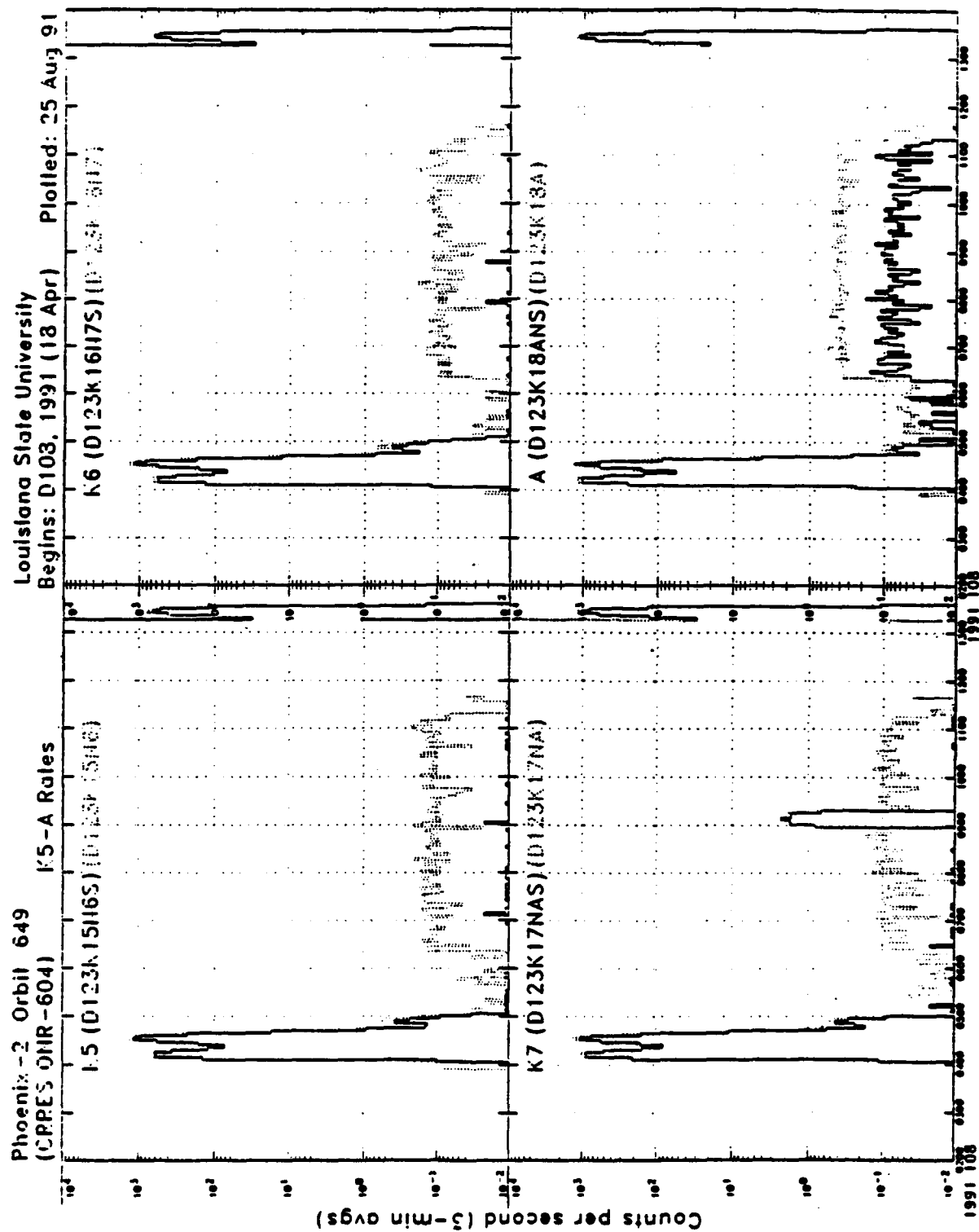


Figure IV.3e. Coincidence rates K5-A for orbit 649.

adjustments in beam energy were made by a remote controlled absorber system, in order to study events stopping in the PSD's or near the top and bottom surfaces of one of the K detectors.

For some runs it was necessary to generate the ion of interest, e.g. helium. This was done by putting a thick target in the beam upstream of the bending and focusing magnets. The beam (e.g. carbon) interacts in this target producing fragments. Then the isotope of interest (i.e. He) was focused by the magnets onto the telescope. (Of course, all isotopes with the same rigidity were focused as well, so these generated beams are not as clean as a pure accelerated beam). This allowed a specific charge range to be investigated in detail.

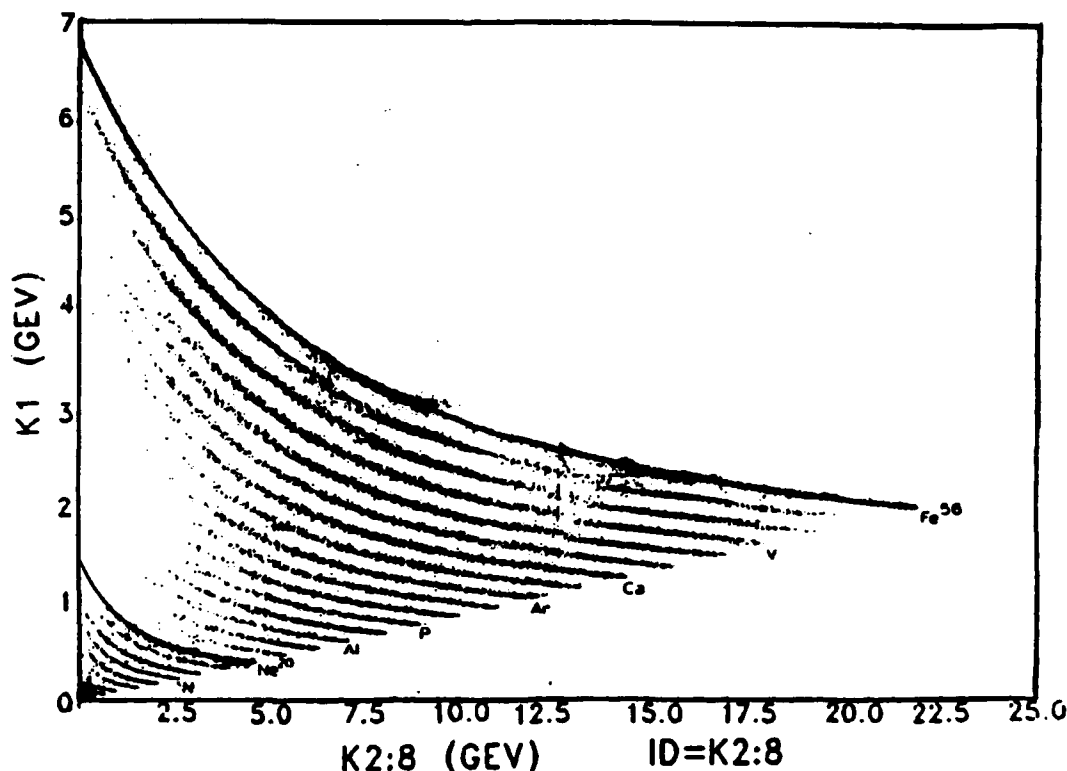


Figure IV.4. Raw Fe and Ne calibration data from the Bevalac showing the intensity variations with energy.

The energy coverage obtained with the wedge system was not uniform as shown in Figure IV.4 for Iron plus Neon data. The large black blobs correspond to concentrations of beam. Thus, in the analysis it was necessary to remove events to try to obtain as uniform a track coverage as possible, within the constraint of still maintaining ample statistics.

Figure IV.5 displays samples of the data from three separate "beams," Iron (top), Neon (center) and Helium (bottom). In all cases the plot shows the energy deposited in D1 + D2 vs the sum of the energy deposits in D3 through K8. For the Iron beam, only priority 1 events are shown. By combining data from several beams it has been possible to populate the element "tracks" over the full matrix. Note the tracks that are almost vertical, labeled "R" on the Neon plot. These correspond to events that passed through D1 D2 D3 but missed the edge of D4 or events that passed through D1-D6 but missed the edge of K1. Recalling the geometry of Figure IV.1, the detector radii decrease between D1-3, D4-6 and K1-8, so such events are allowed. Some will pass into the scintillator guard counter (S), but others will stop in the structural materials before S. This is one source of "background" that must be eliminated from the flight data.

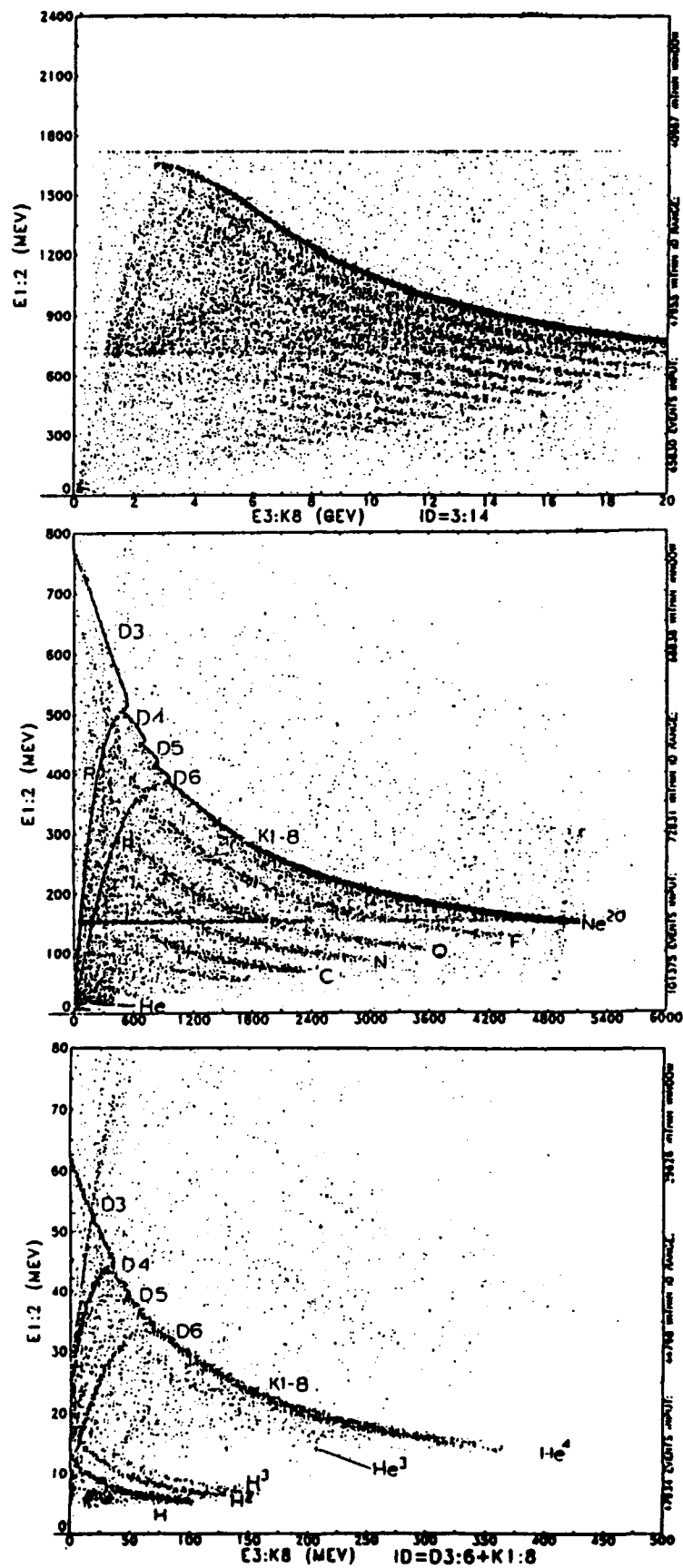


Figure IV.5. Accelerator calibration data from Iron (top), Neon (center) and Helium (bottom) runs.

There is also a black horizontal track on the Neon plot which corresponds to events leaving the edge of the stopping detector and not penetrating to S. Such events can be eliminated by using the instrument trajectory system to require the particle to be incident upon the central 2 cm of the last detector triggered. The result of such a "clean-up" is shown in the top panel of Figure IV.6, and has already been applied to the Fe and He parts of Figure IV.5. Note also that one can begin to see separated isotopes for H and He and the fragments of Ne.

Figure IV.6 shows the high resolution data, events that stop in detectors K2-K8, as the energy deposited in K1 versus the sum of energies in K2-K8, for the Neon calibration. Note that distinct isotope tracks for the fragments are visible. The lower portion of Figure IV.6 shows the data restricted to P2 and P3 events, i.e. P1 not triggered. The high discriminator thresholds on the K detectors (used to determine the P1-P2 division) cross the Neon energy deposit curve dividing this element between priority 1 and priority 2 as shown. Such a calibration allowed the KH discriminator thresholds to be checked and compared to the design values and calculated track structure.

Figure IV.7 shows a combination of the Ne and Fe datasets with the Iron track eliminated so that the fragment tracks can be observed. Over portions of the energy interval, separate isotope tracks can be discerned up into the sub-iron region. This demonstrates the intrinsic ability of the instrument to resolve heavy isotopes. In the lower portion of the figure, the data are restricted to only P1 events. The portions of the Neon track in high priority are apparent. Closer inspection shows that F and Na are also divided between P1 and P2 as predicted by the calculations.

Looking at the Helium events allows the P2-P3 transition to be investigated as well as the instrument command states. Figure IV.8 shows plots similar to Figure IV.5 (bottom). In the top panel the instrument is in "normal" mode (i.e. high D thresholds to eliminate protons and electrons) to be compared to the "proton" mode which was shown in Figure IV.5. Note that the hydrogen isotopes are eliminated by the "normal" (=heavy) mode command. Figure IV.8 (bottom) shows data restricted to P1 and P2 events (i.e. no P3 triggers). This indicates that the majority of the helium track lies in P2, but the lowest and highest energy helium events are found in priority P3. Thus, reconstructing the Helium energy spectrum will require normalizing the P3 priority readout to the P2 readout efficiency, just as reconstructing the Neon requires a P1-P2 normalization.

As part of the 1989 calibration, we investigated the operation of the instrument in a high radiation background provided by a specially purchased  $^{144}\text{Ce} - ^{144}\text{Pr}$  radioactive source of strength 100 milli-curies. This isotope, half-life of 284 days, decays by beta emission to excited states of  $^{144}\text{Pr}$  which transition to the ground state emitting gamma rays or decay by beta emission. The maximum beta energy is just under 3 MeV with a 2.2 MeV  $\gamma$ -ray as the highest energy photon. The source was prepared on a type-A mount and inserted into a machined aluminum holder equipped with removable brass shields, each of which had a different size hole machined into it. This allowed the intensity of the source to be varied with a minimum amount of handling and no direct exposure.

Data were taken with the source located at different distances from the instrument, using the full flight electronics. Individual electrons should not be able to trigger a P3 event, but 2 or 3-fold electron pile-up could. The observation of pulse height analyzed events produced with only the source near the instrument confirmed this prediction. Similar "events" will probably be observed in the inner magnetosphere or in the slot region.

A second question was what effect the presence of background radiation would have on heavy ions observed at the same time. To answer this question, the instrument was operated with the Iron beam on and with the radioactive source mounted at an angle exposing the front portion of the instrument. Figure IV.9 shows the result. Plotted is the energy deposit in D1-D6 versus the energy deposit in K1-K8 for an iron beam run without the source (top) and with the source (bottom). The bottom plot shows a second iron track, below the beam track, at an intensity  $\sim 1/3$  of the normal



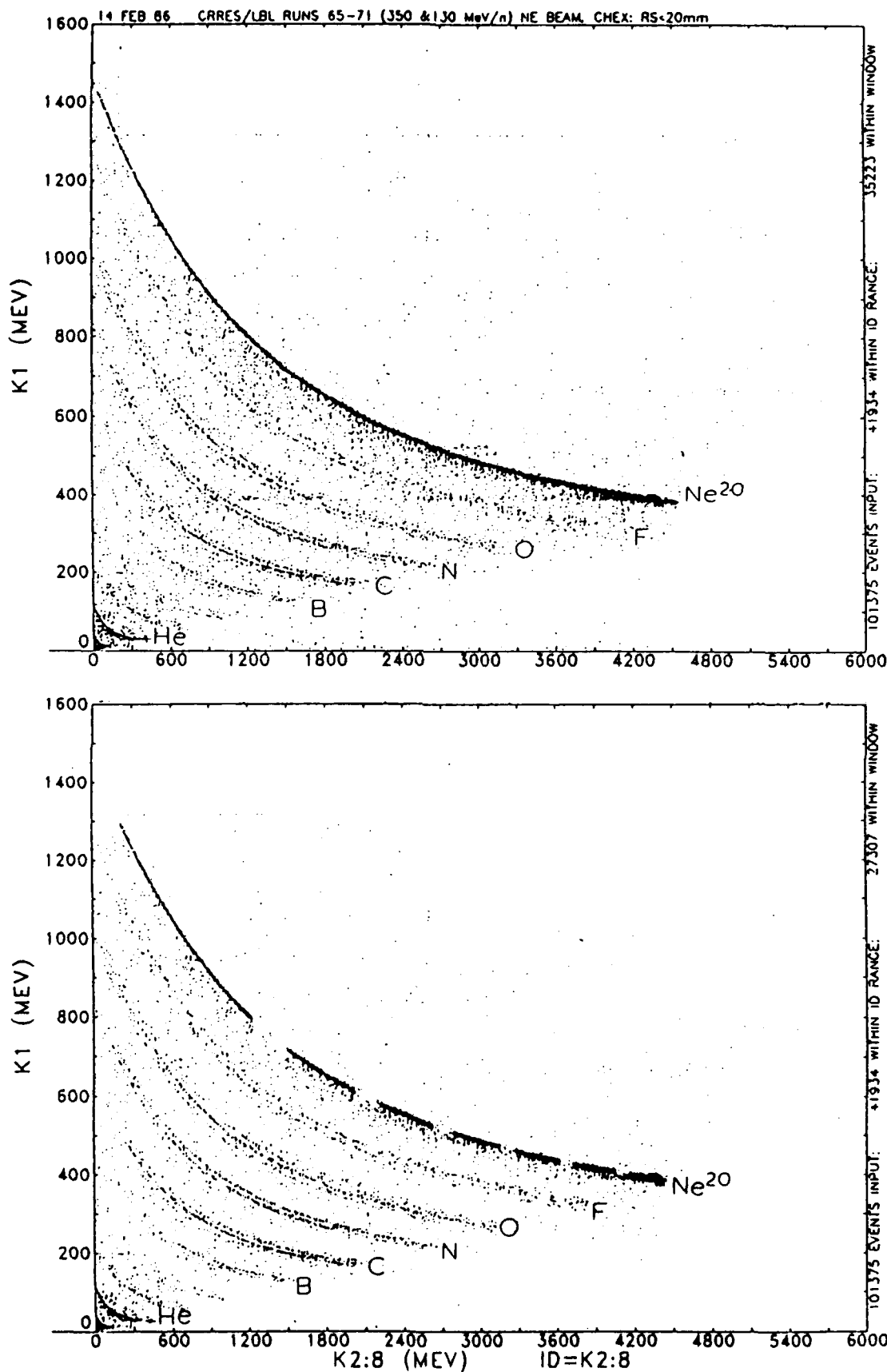


Figure IV.6. Bevalac Neon data showing all events (top) and priority 2+3 events only (bottom). A stopping radius cut has been applied to the data.

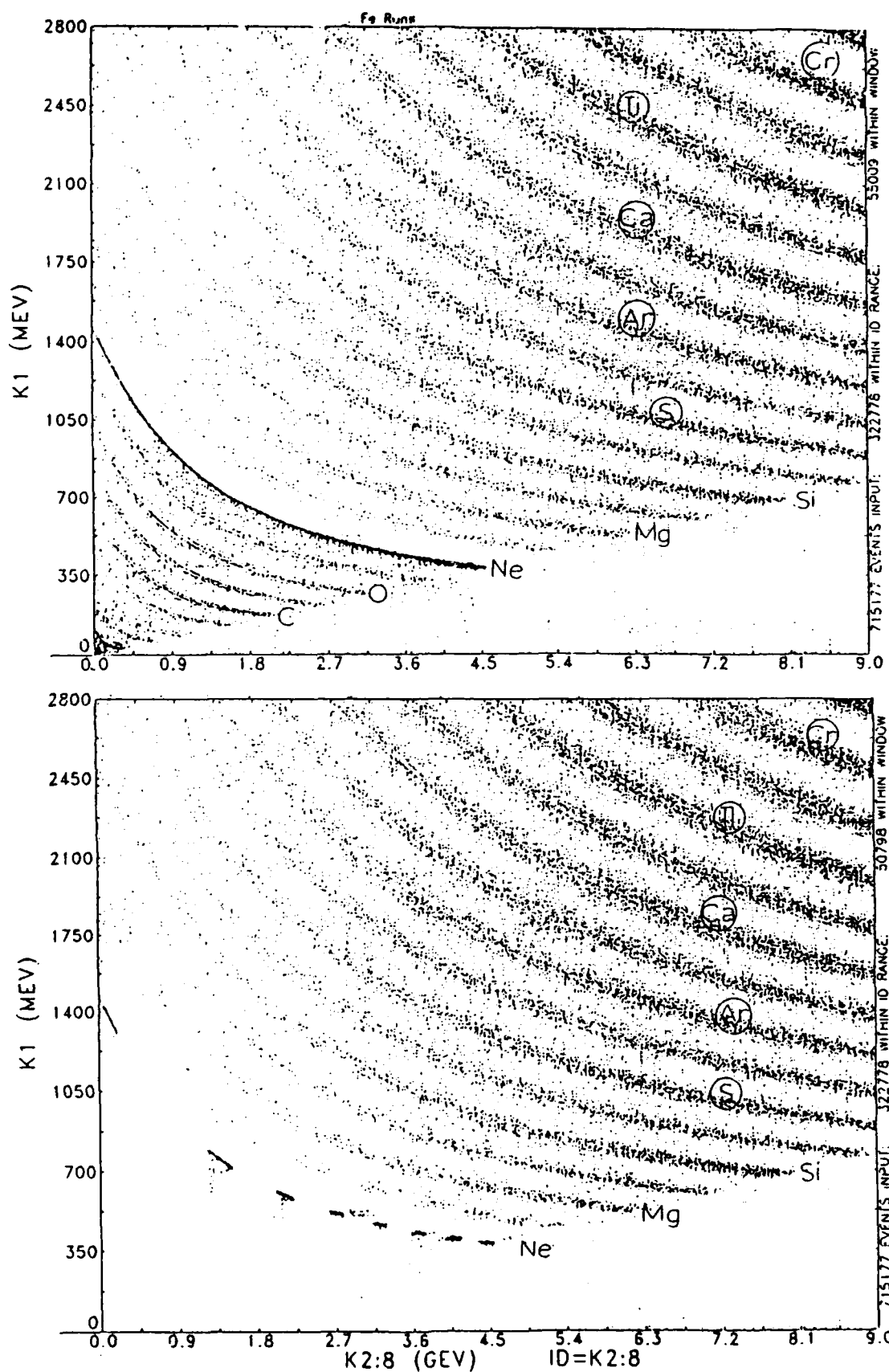


Figure IV.7. Iron + Neon data in K1 vs K2-8. The lower plot shows only P1 events.

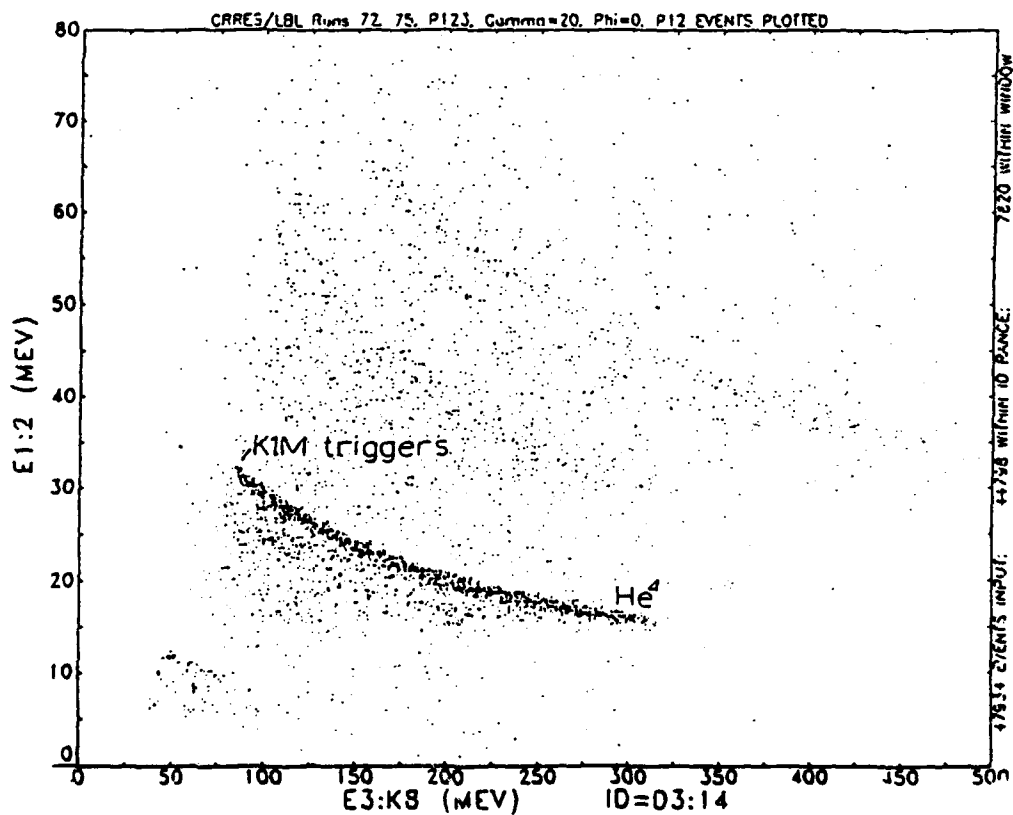
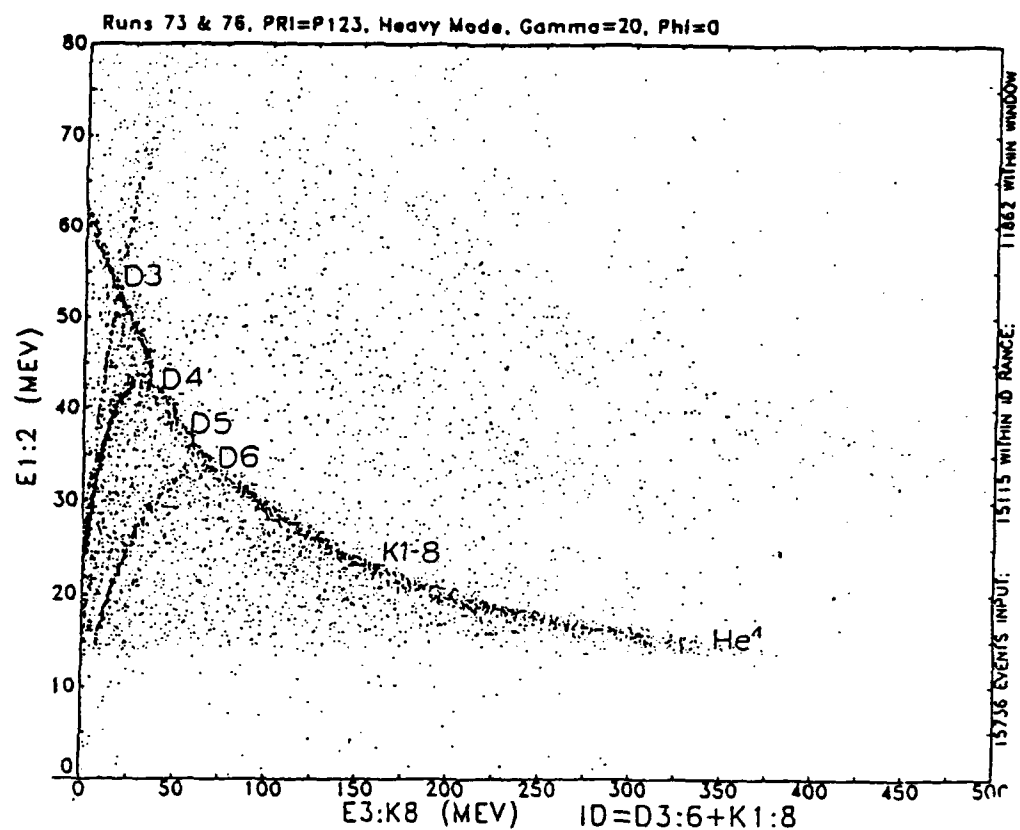


Figure IV.8. D1 + D2 versus D3-K8 for Helium events showing the effects of the normal mode command (top) and the P2-P3 division (bottom).

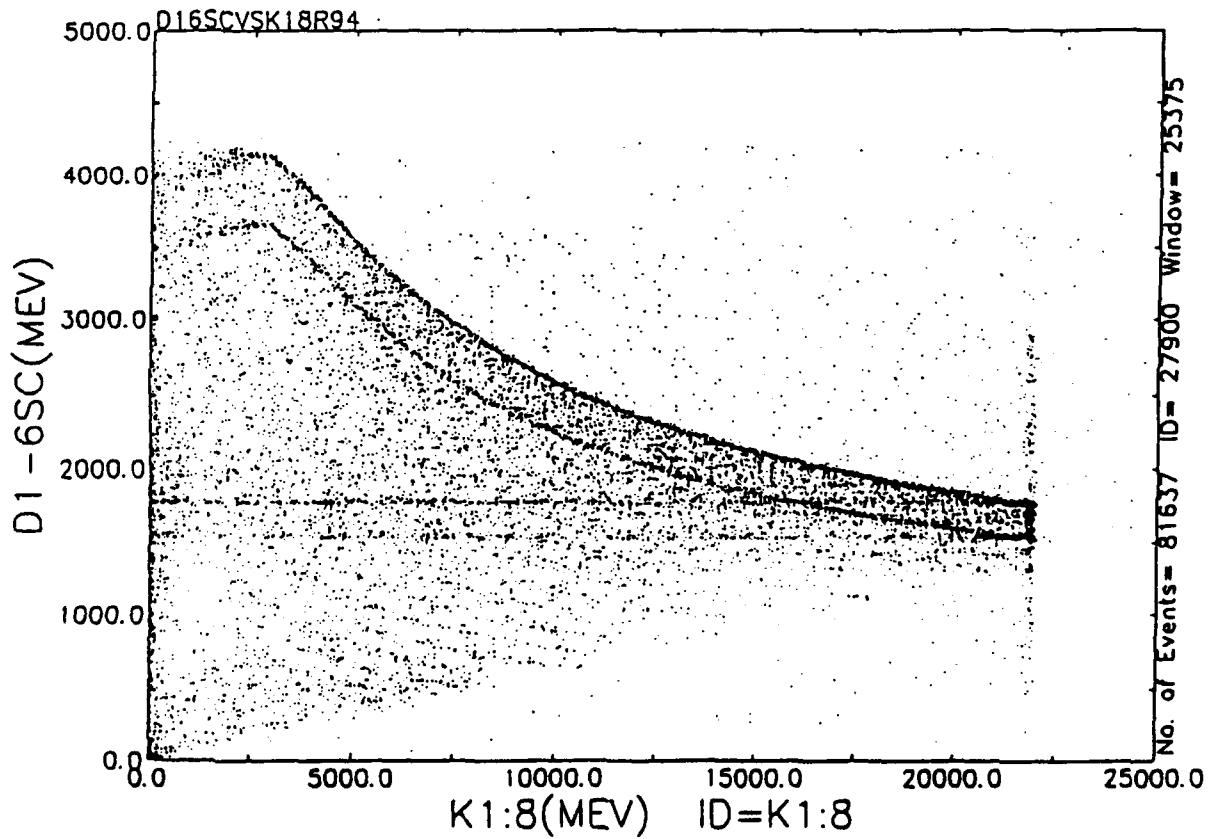
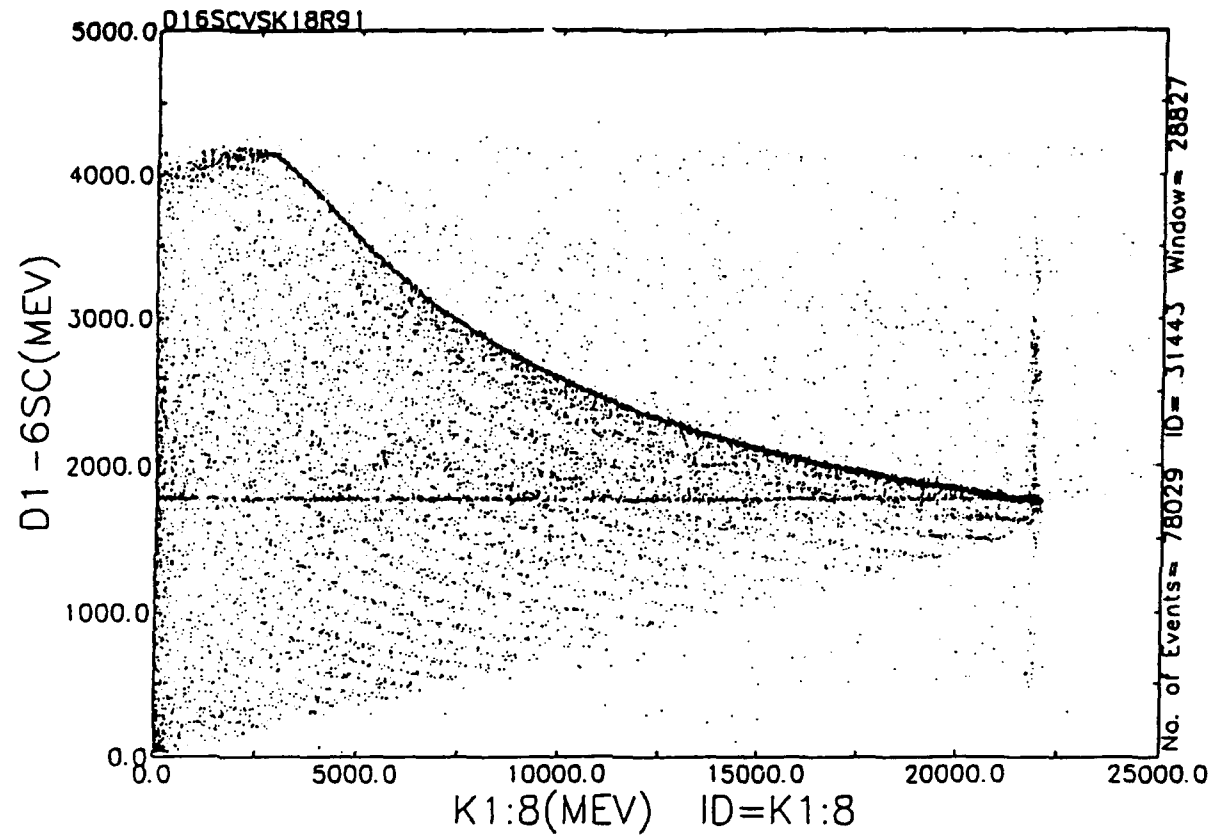


Figure IV.9. D1-D6 versus K1-K8 matrix for Iron beam events with NO source (top) and WITH source (bottom).

track. The lowered track results from the D detector amplifiers being below baseline when the iron event occurred, due to the high firing rate of the front detectors from the source radiation. That this effect is limited to the PSD's is demonstrated in Figure IV.10 where the K1 vs K2-K8 matrix is shown for the same data. No second track appears in the lower (source "on") plot in Figure IV.10. This is as expected since the energies of the source radiation are insufficient to cause rapid firing of the K detectors. Figure IV.11 shows the charge histograms for the two cases shown in Figure IV.10, and there appears to be no discernible degradation in the charge resolution nor a discernible shift in the position of the Iron track from the source.

The majority of the source effect is confined to the first detector D1. This is illustrated in Figure IV.12 which shows plots of the energy deposited in D1 (top), D2 (middle) and D3 (bottom) versus K1-K8. Only in the top plot is the "second track" noticeable. We expect such effects to occur during the CRRES mission, particularly near the outer belt. The flux and energy distribution of the background radiation in space will be different from that obtained in this source calibration, however the effects should be predictable. We expect that the K1-K8 events will be largely unaffected, but extracting the lower energies from the ONR-604 data will require very careful analysis.

### C. Launch and On-Orbit Checkout

Much of the effort in 1990 was devoted to pre-launch preparations, rehearsals and training at CSTC, launch operations and instrument turn-on and initial operations planning for the experiment. The important questions for ONR-604 were the instrument calibration, the performance in various parts of the orbit in different command states and the development of a plan for routine operations of ONR-604 on CRRES. In-flight calibration runs were scheduled over various parts of the CRRES orbit as well as while the instrument was in the different command states, i.e. proton mode and normal mode. These data were analyzed on a micro-computer system at CSTC before pronouncing the experiment "healthy" and implementing the routine operations plan.

Figure IV.13 shows the results of an In-Flight Calibration (IFC) run analyzed at CSTC. The instrument was in normal mode and the run was taken during a pass through the outer belt region. Plotted are the deviations of the IFC points from a best fit straight line. Of significance is the spread of the points which appears "bad" for P1, E1, P2 and E2, the amplifiers on the top two detectors in the telescope. For the other amplifier chains the deviations appear normal. When analyzed completely, the gains deduced from this run were all  $<0.15\%$  different compared to IFC run taken on the ground well before launch. Thus, it appears that the instrument maintained its absolute calibration through launch operations. Further, data taken in high background environments such as the outer belt may be subject to variations, at least in the top two PDS's.

Figure IV.14 shows the P3 counting rate as a function of time for a full orbit of data analyzed at CSTC. The instrument was in proton mode at the time. Note that P3 responds strongly to both the inner and outer belts but is relatively quiet under the belts at perigee and during this apogee pass. Figure IV.15 shows a comparison of the P3 and P2 rates for a later pass with the instrument still in proton mode. Two features (marked A and B) appear in the slot region and appear to have longitudinal symmetry. The surprise here is the lower plot in which P2 (nominally  $Z \geq 2$ ) shows a strong response in the inner belts but is insensitive to the outer belt particle population. The inner belt response may be to proton interactions or to event pile-up (such as observed during the accelerator calibration runs), but the exact nature of the response must be investigated further.

The data shown on Figure IV.14 and IV.15 indicate that (1) the P3 counting rate (and the D1, D2, D3 amplifiers) reach exceptionally high values in the inner magnetosphere, and (2) the P2 pulse height analysis will work only outside of the inner zone. Thus, it was prudent to protect the top detector systems by commanding the instrument into normal (=heavy) mode. However, this eliminates the measurements of protons at apogee. Therefore, an operational plan was developed

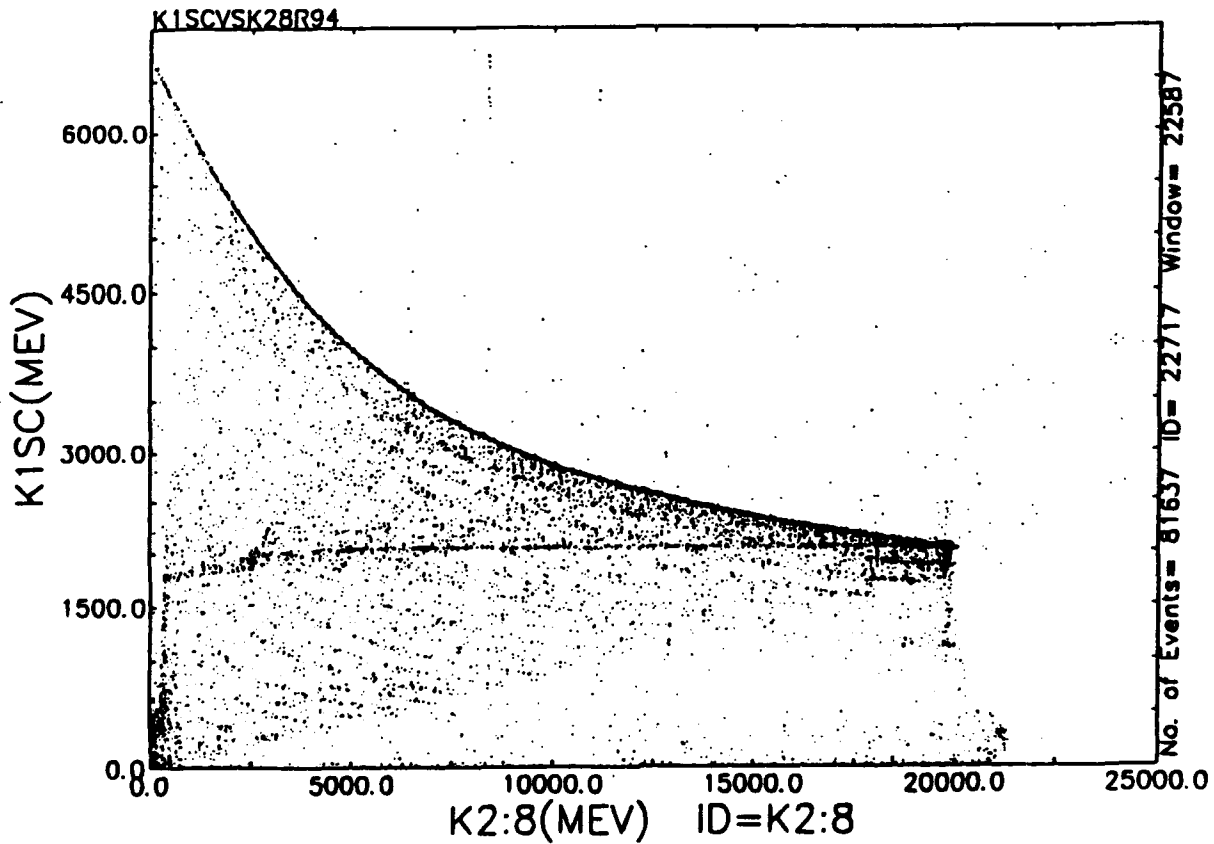
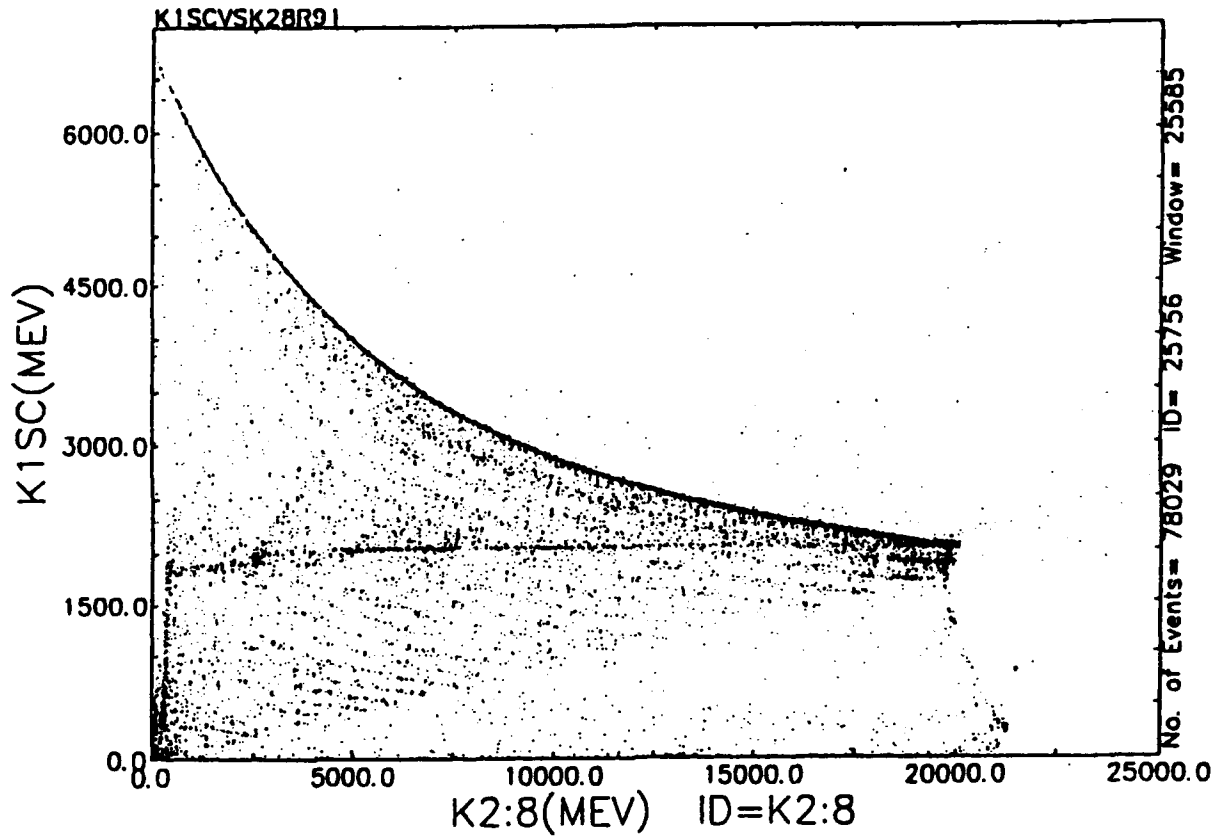


Figure IV.10. K1 versus K2-K8 matrix for Iron beam events with NO source (top) and WITH source (bottom).

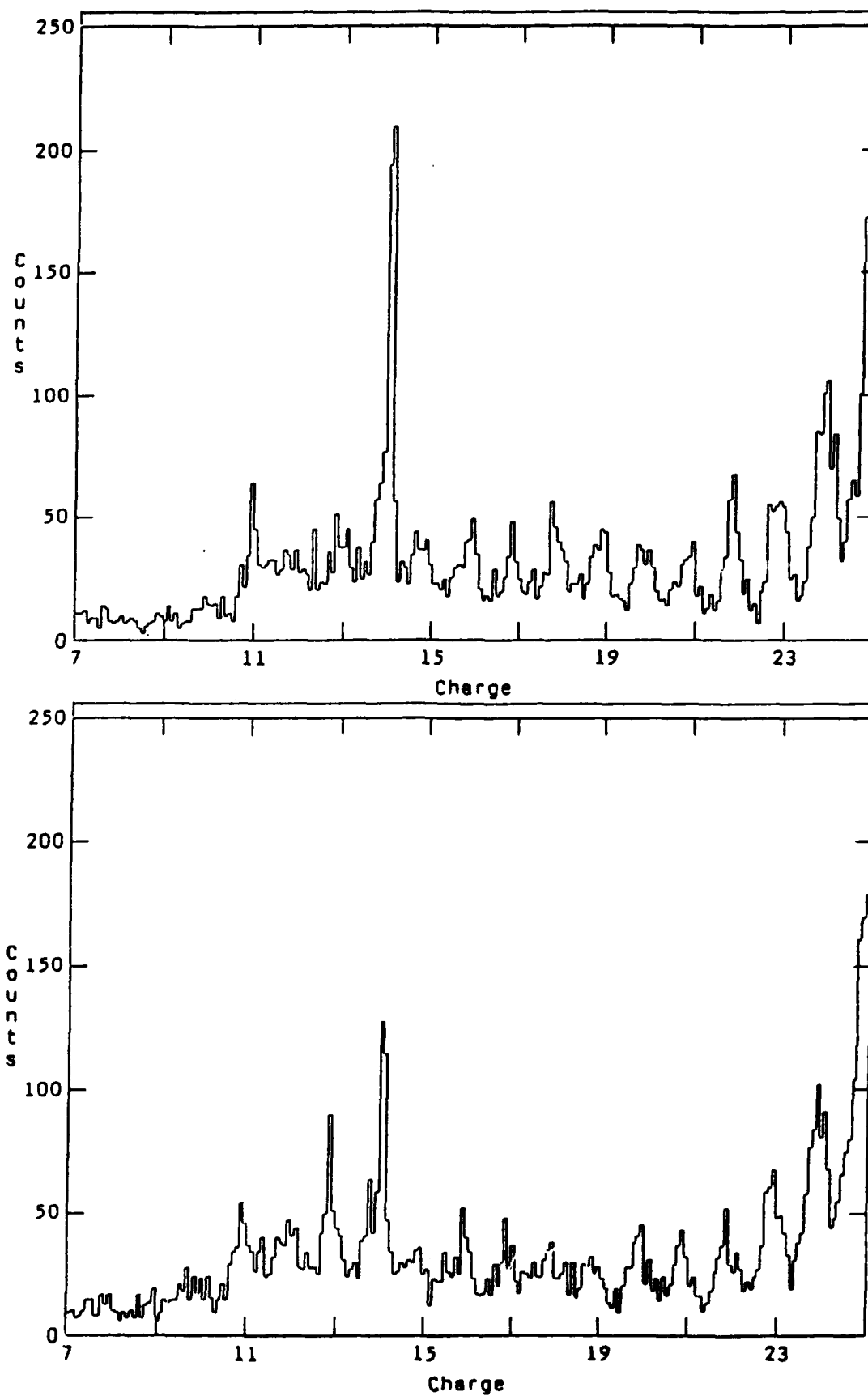


Figure IV.11. Charge histograms for events observed in iron runs with NO source (top) and WITH source (bottom).

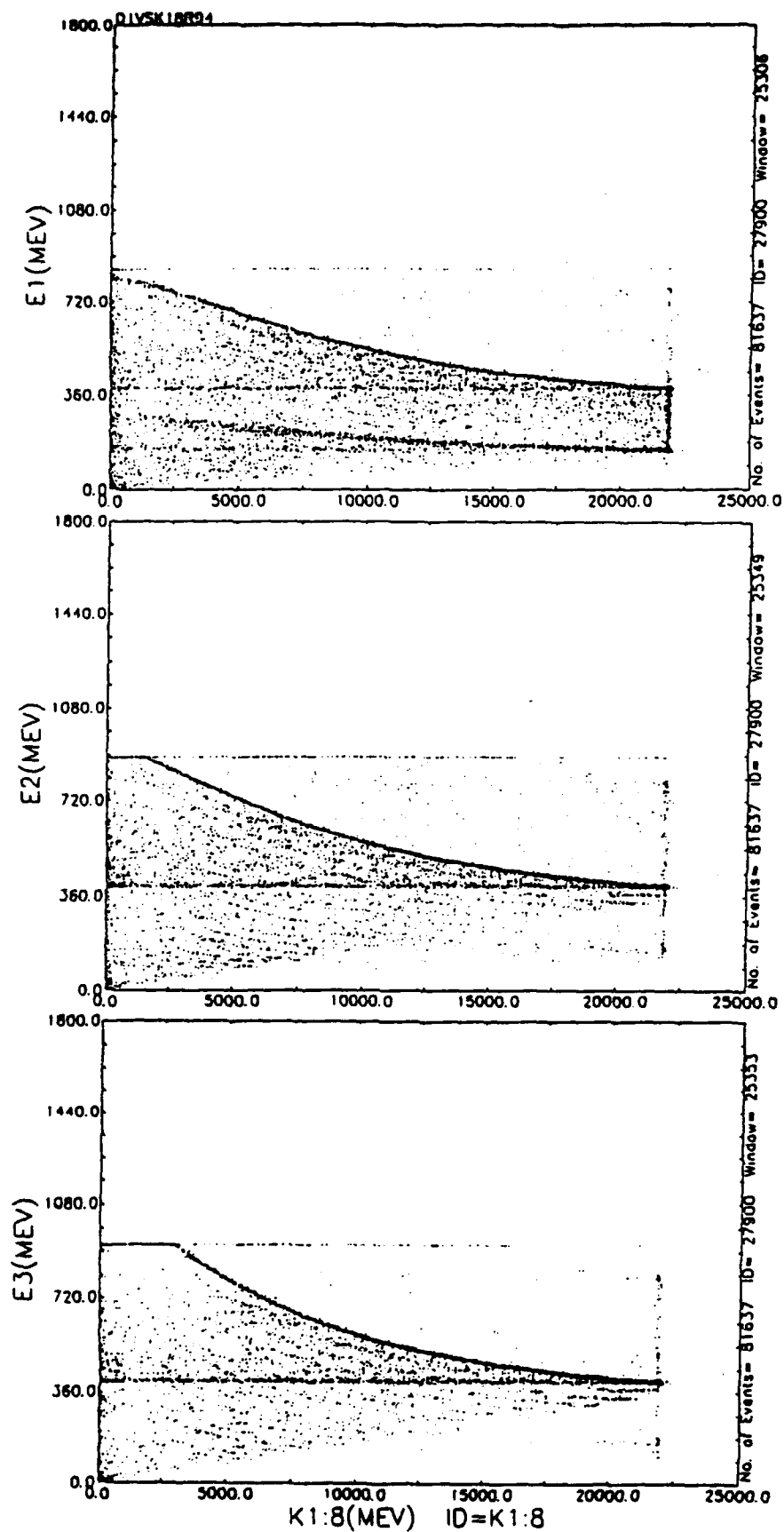


Figure IV.12. Energy deposits in D1 (top), D2 (middle) and D3 (bottom) versus K1-K8 for iron events taken WITH the radioactive source.



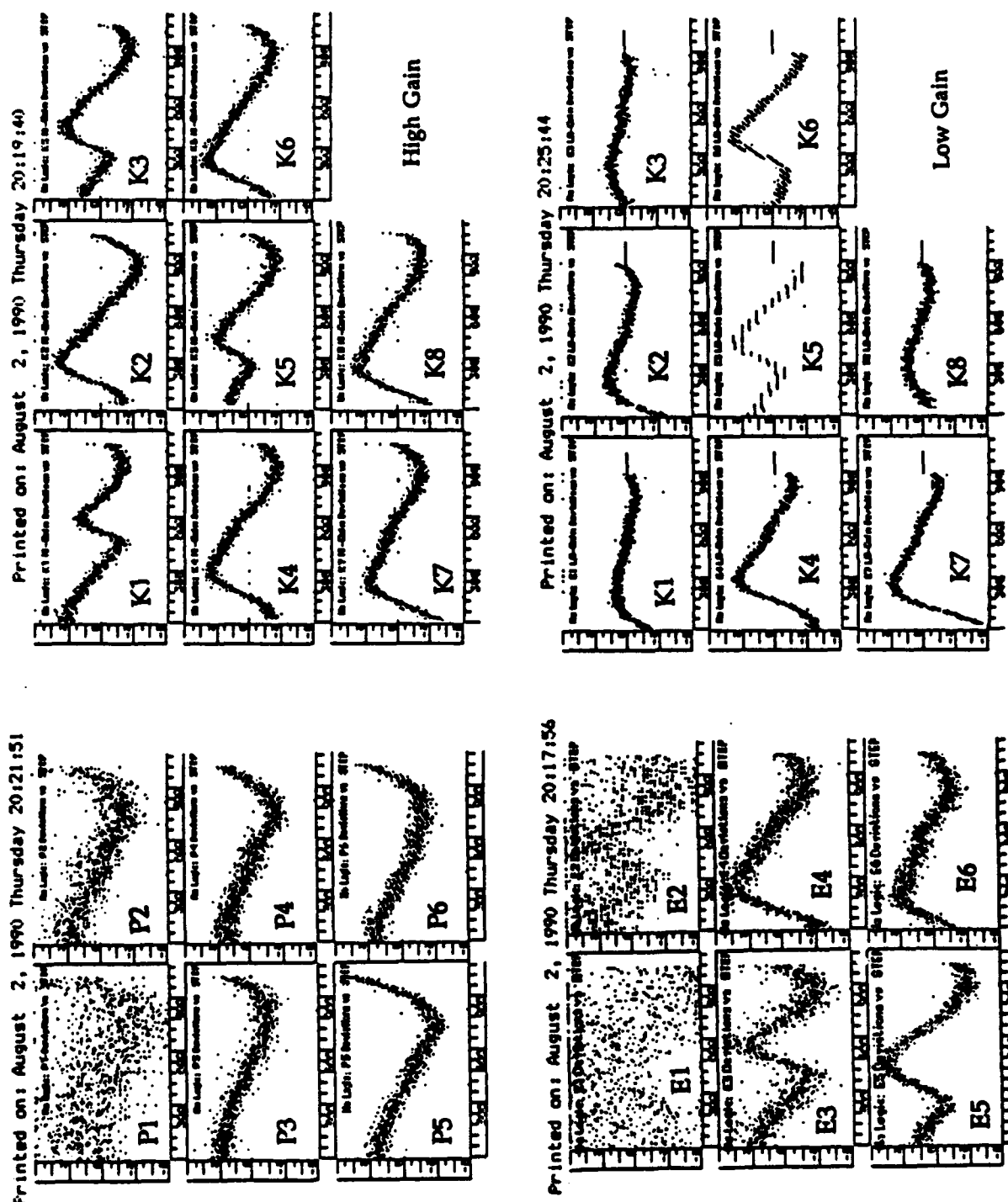


Figure IV.13. GSE Run 530, IFC Run at CSTC. Deviations of the points for each amplifier from a straight line.

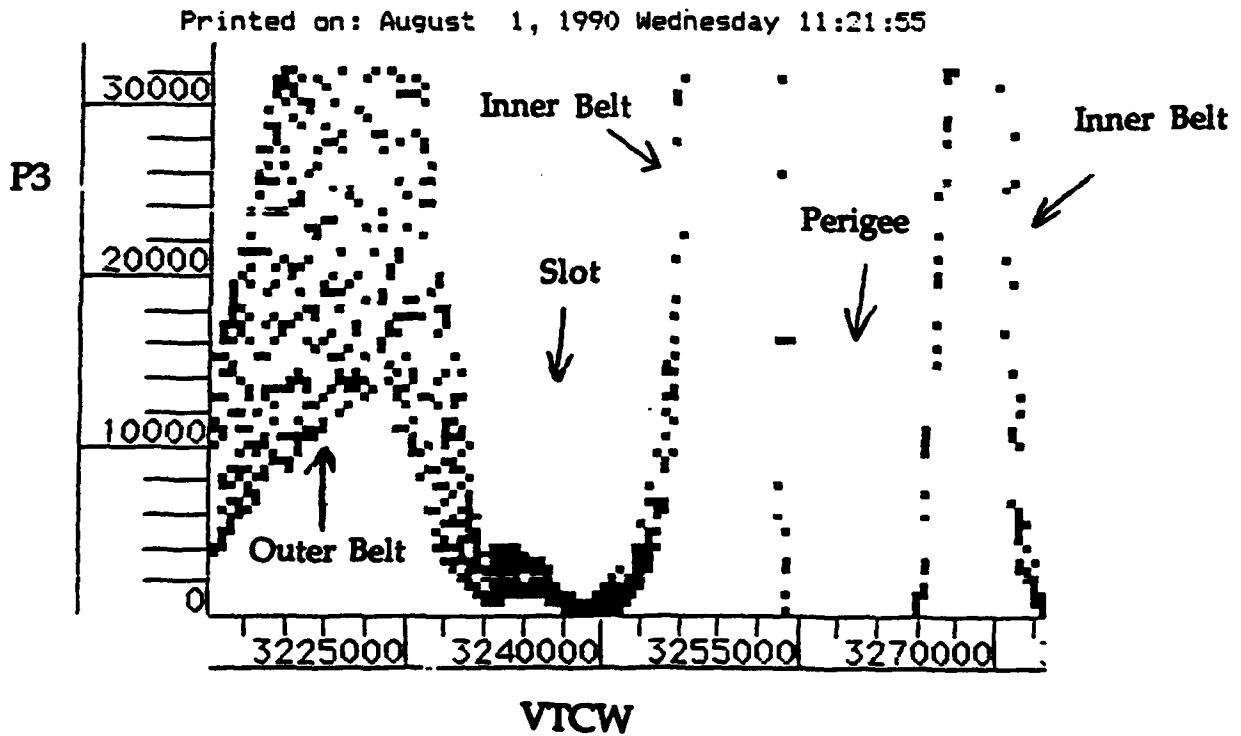
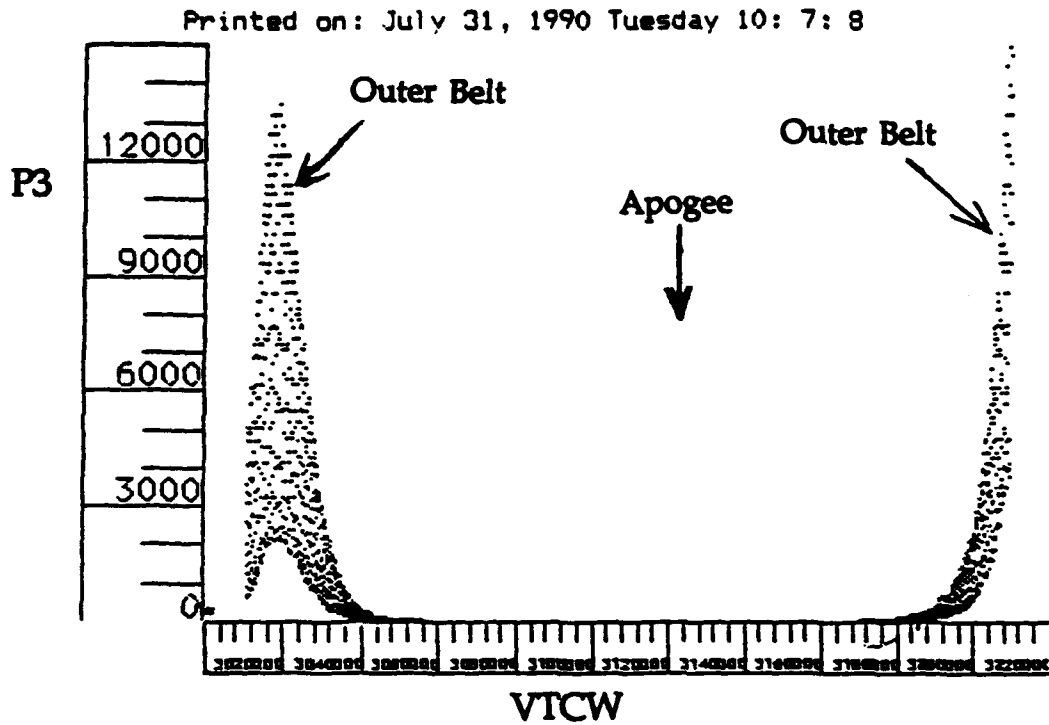


Figure IV.14. One of the first full orbits of data from ONR-604. Plotted is the P3 counting rate versus the Vehicle Time Code Word (VTCW) for the Apogee and Perigee portions of the orbit (GSE Run 515).

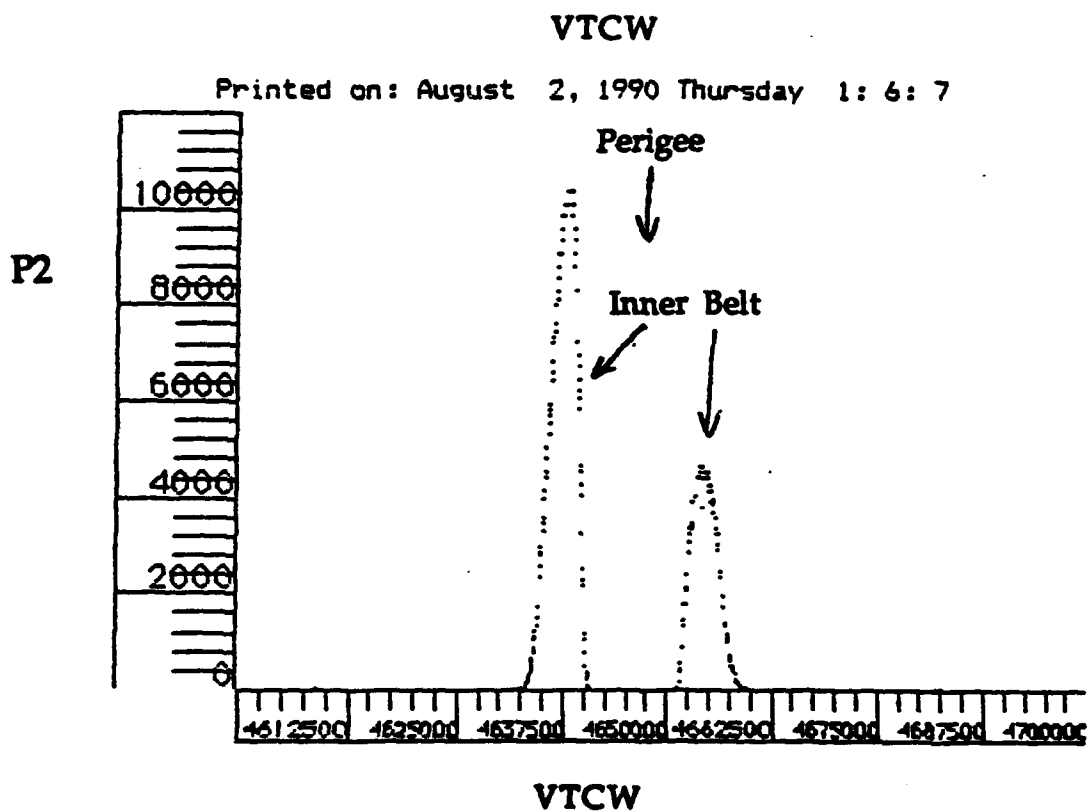
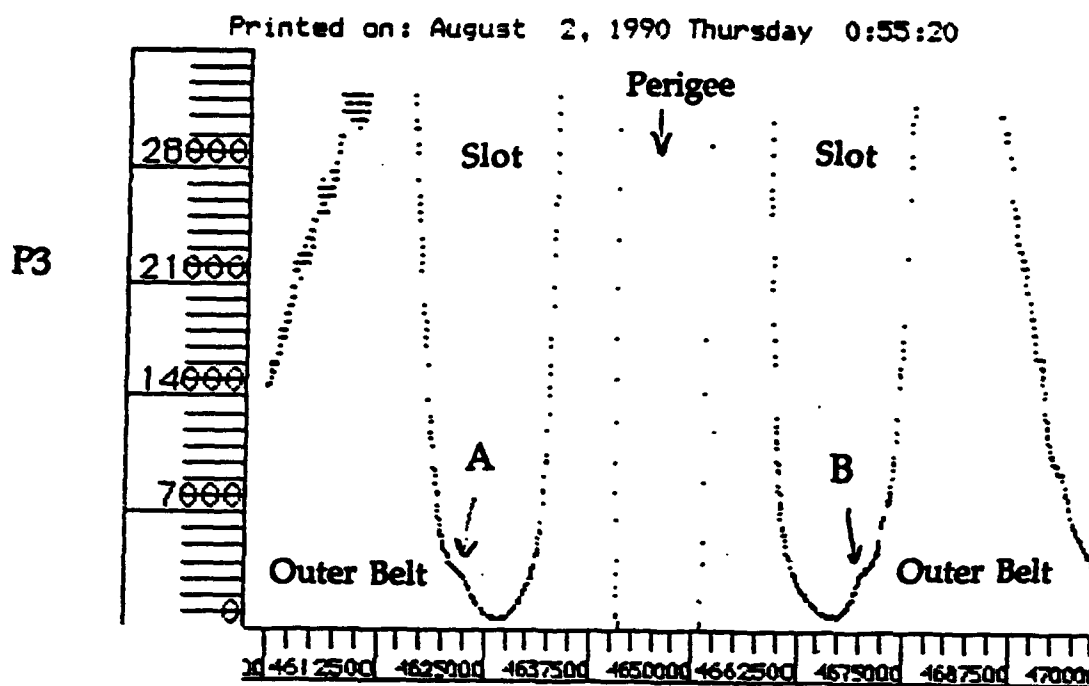


Figure IV.15. P3 and P2 rates versus VTCW for a full orbit on ONR-604 data in proton mode (GSE Run 521).

and implemented at CSTC whereby on every orbit the instrument is commanded into proton mode at an altitude of ~26,000 km outbound and is returned to normal mode at the same altitude on the inbound leg of the orbit. This is the operational sequence shown in Figure IV.3a and has been followed for essentially all of the mission.

Figure IV.16 shows an expanded view of the outer belt region as seen in the D2 and the P3 counting rates. Note the strong spin modulation in the rates (spin rate ~2.6 rpm at this time). Demodulating the rates, in order to look at data on short time scales (~4 seconds), will be necessary to understand the instrument response within the radiation belts.

#### D. Post-launch Performance

The ONR-604 experiment was monitored continuously through periodic IFC runs, through the singles and coincidence counting rates and through the pulse height analyzed events. With one exception (discussed below) the instrument continued to function nominally. The engineering parameters were also watched to ensure a constant temperature, and there was little or no short term variation and an acceptable long term drift.

ONR-604 suffered one minor degradation. It was noticed that in late October, 1990 the P1 amplifier failed to produce a full signal. The maximum output was a factor of 10 smaller than expected. The other amplifier on that detector (E1) continues to respond normally to both IFC runs and to particle events. Thus, we conclude that the problem is not in the detector itself, but is probably a component failure in the pre-amplifier circuit. In any case, the position information from D1 is degraded. Position is given by the ratio P1/E1 so that a P1 signal down by a factor of 10 will give a position always on one side of the detector. In fitting a trajectory to the PSD positions, this aberrant point will affect the fit and will show up as a large "fit residual," a parameter that is calculated for each trajectory. However, there are three PSD's (D1, D2, D3), for redundancy, in the top layer, so that the loss of position information from one of the three is not a significant degradation to the instrument's capability for reconstructing the particle trajectory.

The difficulty here was that the processing software (discussed below) had been constructed for six PSD signals. A new algorithm had to be implemented that used only five signals. This then had to be de-bugged and tested and incorporated into the processing software. This halted all processing until the algorithm was available, and required reprocessing of some of the affected orbits. However, when compared to the trajectories derived from six PSD's, the five PSD results are essentially identical. It is difficult to see any loss of precision in the trajectories. P1 was monitored continuously, but, did not return to good health.

Figure IV.17 shows a comparison of the P1 events that have been analyzed for the first ~9 months of the mission with the accelerator calibration data. Note that the segmented Neon track appears in both plots, Mg and Si are reasonably distinct and the iron track appears in the proper location. The flight statistics are still too meager to unambiguously identify many of the other elements, but preliminary charges can be assigned based upon calculated positions of the tracks. From this comparison, we conclude that the amplifiers have remained in calibration and that the detectors continue to function properly.

In October, 1991 CSTC controllers reported that they had lost all contact with the CRRES spacecraft on 10/12/91. Repeated attempts to contact the spacecraft continued for the next few weeks, but to no avail. It is theorized that the oneremaining battery on the spacecraft went into a short-circuit mode thereby disabling the power system including the transmitter and receiver. Thus, no commands were able to be received. In November, 1991, CRRES was officially declared non-operational. The full CRRES dataset, therefore, covers 14.5 months of on-orbit operations. The ONR-604 experiment performed well up to the last data received.

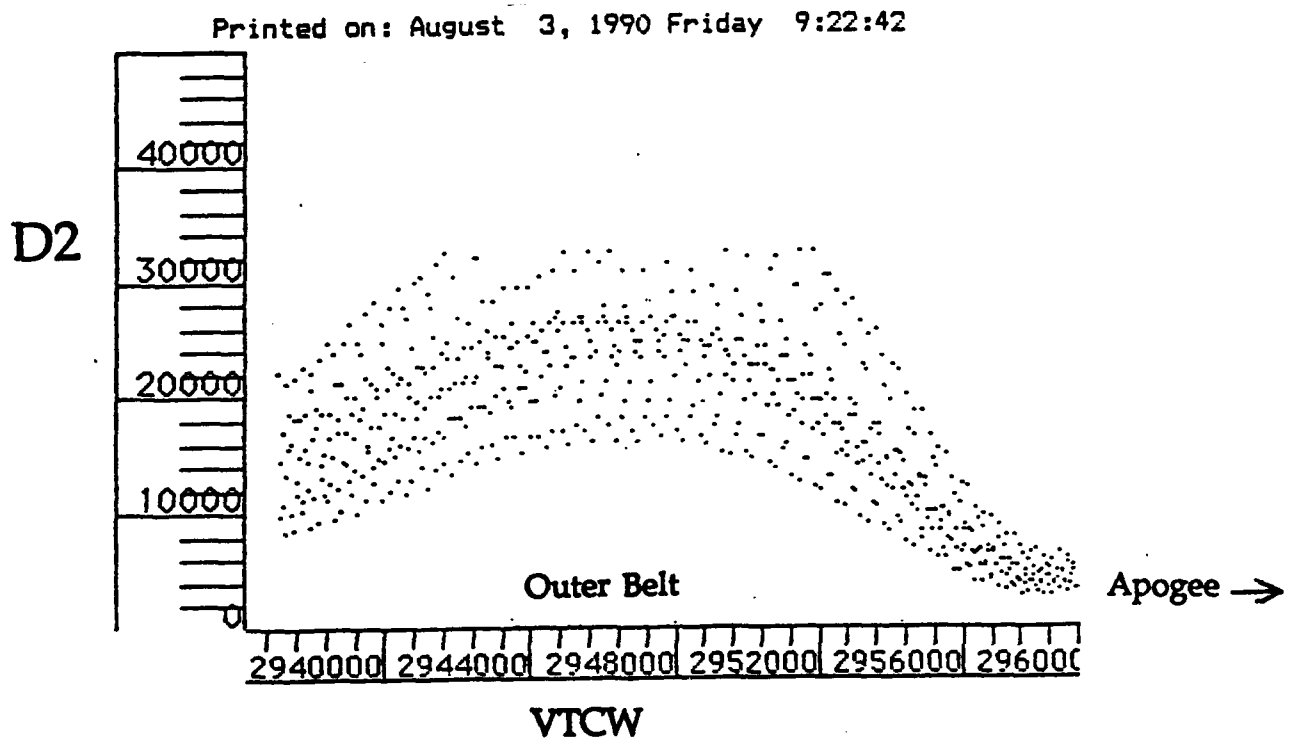
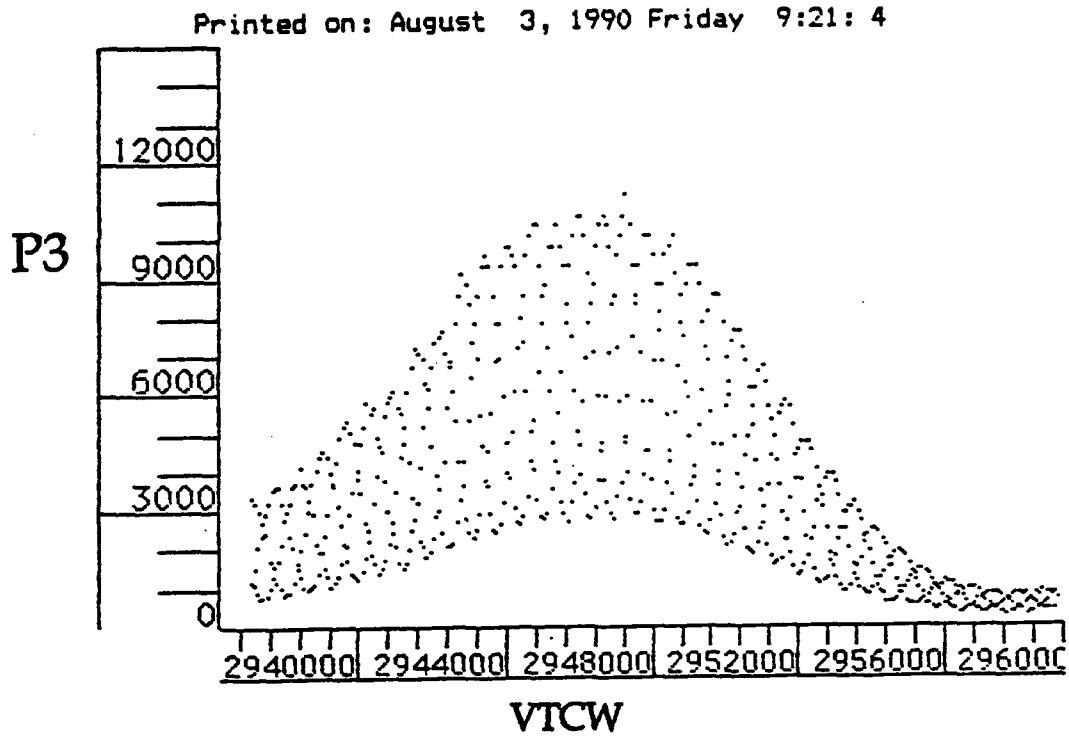


Figure IV.16. Expanded plot of the P3 and D2 counting rates for an outer belt pass approaching Apogee (GSE Run 508) showing the spin modulation in the rates.

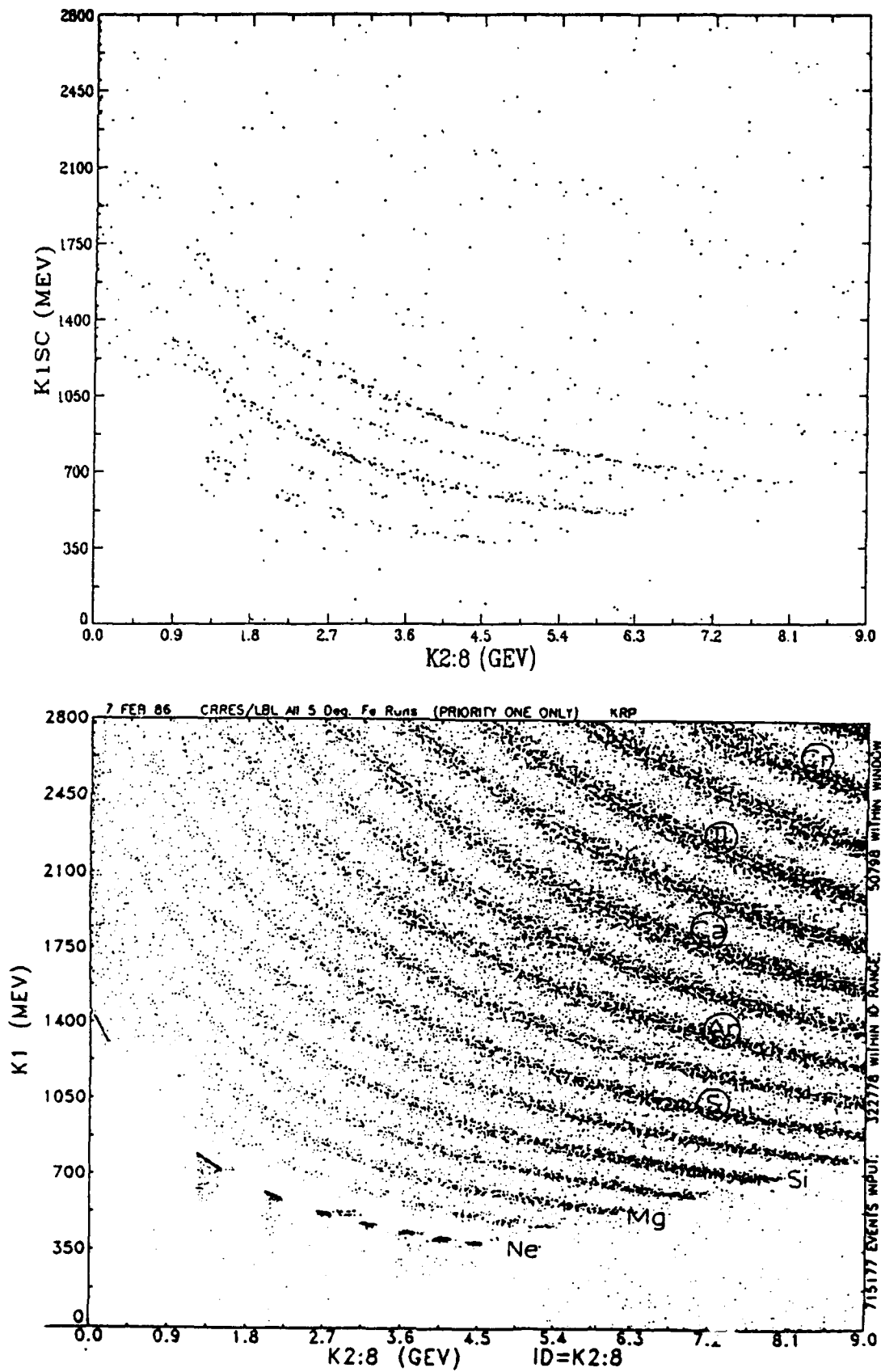


Figure IV.17. Comparison of the K1 versus K2-K8 matrix for P1 events from flight data (top) and accelerator calibration data (bottom).

## V. Data System, Databases and ONR-604 Analysis

In order to analyze the ONR-604 instrument and perform the science measurements, the raw data must be processed to (i) convert the data to "physics" units (e.g. particle trajectory angles in degrees, energy deposits in MeV), (ii) obtain auxiliary information necessary for monitoring the health and calibration of the instrument, and (iii) prepare the data for subsequent analysis. This processed data must then be further reduced to selected rates and elemental fluxes for particular geomagnetic environments and times before information on, for example, the level of solar modulation, active/quiet times and particle composition and spectra can be obtained. Much of the effort at LSU has been associated with implementing such a data system, including the correct procedures and software for data processing and reduction. To date, most of the fundamental processing activities have been established, but additional effort is still required to implement the higher level data reduction. In addition, the system must include ancillary data that will be employed for correlative studies and for model development.

### A. Reduction and Processing

The data flow through the current LSU processing and reduction software is shown in Figure V.1. Data from ONR-604 is received by LSU from the University of Chicago (UC) in the form of a processed C2ET data tape. These tapes contain the raw and processed PHA events, rate records, engineering/housekeeping data and associated magnetometer and ephemeris information for 5 consecutive orbits with a file for each orbit. Startup delays in generating Agency Tapes for UC and final debugging of the UC processing software delayed the beginning of routine production of C2ET tapes until the beginning of 1991. From then on, however LSU received 10-15 tapes from UC every 3 to 4 weeks. All data have now undergone initial processing. Initial on-orbit spacecraft and instrument checkout occurred during the first 60-70 orbits, and correct attitude information is not available for this period.

The initial step in the LSU processing was to use the COPY\_FILES program to generate a duplicate of the C2ET tape in a format compatible with the LSU VAX/VMS processing equipment. The program LIST\_FILES was then run on the LSU C2ET to validate the duplicate and generate an "overview" listing of the tape contents. Once the LSU C2ET tapes are verified the original tapes are returned to UC for reuse. Backup versions of the C2ET are archived at UC and only one copy of these tapes are kept at LSU.

The next major operation is to use the program RATE\_GEN to generate a Rate Parameter Tape. This tape is formatted specifically as input to the PIMPLOT production plotting program and contains data on the singles, coincidence and PHA priority rates as well as some ephemeris and housekeeping data. Time history plots (see Figure IV.3a-e) of these data are generated for each orbit on a pen plotter, are archived and are used to monitor instrument health and calibration, to monitor magnetospheric particle activity, and for the initial analysis of Solar Energetic Particle events.

The detailed analysis of the ONR-604 data usually requires only specific portions of the full dataset contained on the C2ET tape. Thus, as indicated in Figure V.1, the program SPLIT\_FILES is used to generate several data subsets which are then archived for later use. Processing and reduction software for the subsets has been developed and we concentrated, initially, on interpreting the instrument rates as these are the key to reliably selecting particle active/quiet times and to determining the absolute particle flux. As a result several programs now exist which process the Rates dataset into higher order information. The program SC\_Z provides information on the precise position and orientation of the instrument with respect to the geomagnetic field. This is needed for determining geomagnetic cutoffs and for tracing particle trajectories through the field in order to determine if the event is a trapped particle or has penetrated from interplanetary space. The program LIST\_TIMES identifies start and stop times for data gaps, orbits, IFC runs, gain changes and other special events.

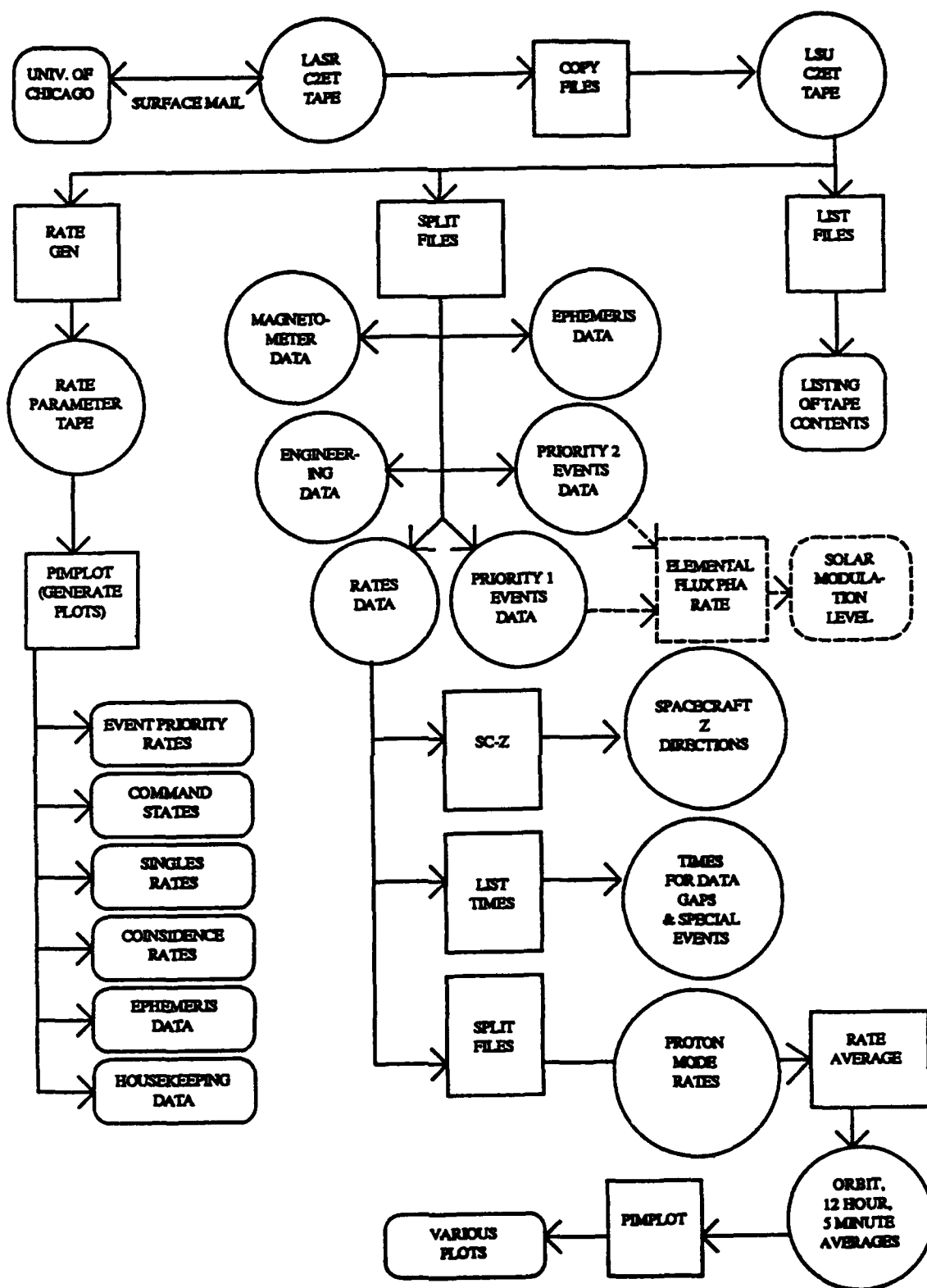


Figure V.1. Data flow through the current LSU Processing System.



This information is needed for correctly determining and evaluating rate averages. Using SPLIT\_FILES the Rates data is further selected for that portion of the spacecraft orbit which is nearest apogee, at the highest L shell values (generally greater than 4) and also when the instrument gain changes to "Proton Mode". Proton Mode allows ONR-604 to collect proton events which are normally excluded during passes through the intense radiation belts. Averages of these rates for 5 minute, 1/2 hour and orbit time periods are generated by the RATE\_AVERAGE program and time history plots are generated once again by PIMPLOT. These "Proton Mode Rates" are then used to examine the particle environment which is least affected by geomagnetic effects and which should be dominated by interplanetary particles.

Software to process the Event data subsets is still under development. Two such subsets are split from the C2ET tapes according to their assigned PHA analysis priority; Priority 1 is assigned to events which appears to be of charge  $\sim 10$  or above and Priority 2 is assigned for charge  $\sim 2$  and above. PHA events assigned to the remaining, lowest priority (3) can also be split from the C2ET tapes once methods for handling the electron and proton pile-up background evident in these low charge data are developed. Initial effort, however, was focused upon obtaining a measure of the Solar Modulation Level as a function of time from the Priority 1 and Priority 2 events. This involves converting the PHA counts into a "rate" for use in determining instrument live time and event collection efficiency; further subdividing the data into quiet and active times to separate the data associated with the cosmic rays from that associated with SEP; determining the event charge, energy and trajectory just outside of the spacecraft; isolating geomagnetically trapped and penetrating particles using trajectory tracing or cutoff calculations; and applying appropriate instrument geometry factors, collection efficiencies and live times to determine absolute elemental fluxes. An example of the derived rates is shown in Figure V.2 where the raw rate has been subdivided into a P2 Helium and a P2 CNO rate for comparison to the raw P1 (highest Z) rate. The major flares observed by ONR-604 are clearly revealed.

Analysis of the ONR-604 particle environment data is neither straight forward nor simple due to the complexity of both the instrument and the environment. It is likely that with improved understanding of both, the data processing and reduction requirements for ONR-604 will be altered. This can lead to unanticipated developments or simplifications to the processing scheme outlined in Figure V.1.

## B. Ancillary Databases

While the ONR-604 data is the major component in the LSU analysis effort, it can not provide all the information required for a complete understanding of the particle environment. Thus, LSU has established databases of auxiliary information which will be used to complement the ONR-604 analysis. Components of these databases which are maintained at LSU are shown in Figure V.3 and include IMP-8 proton and helium fluxes and quiet time selections in various energy bins and the Climax station neutron monitor data from the University of Chicago. These data are regularly downloaded to LSU over the NSI/DECnet network, and plotted for use in the selection of quiet and active time periods and, eventually, to aid in determining the solar modulation level. In addition, data from the McMurdo neutron monitor station has been provided to us by the Bartol Research Institute at the University of Delaware.

Figure V.4 shows the neutron monitor results from the two stations, and there is excellent agreement. The top plot shows the record for the past  $\sim 35$  years and indicates that in mid-1990 the conditions were those of solar maximum, the deepest solar maximum since  $\sim 1958$ . The lower plot shows an expansion of the plot for the first part of the CRRES mission. Note that the neutron monitor rates were gradually increasing (recovering) until the onset of the March 91 flare period.

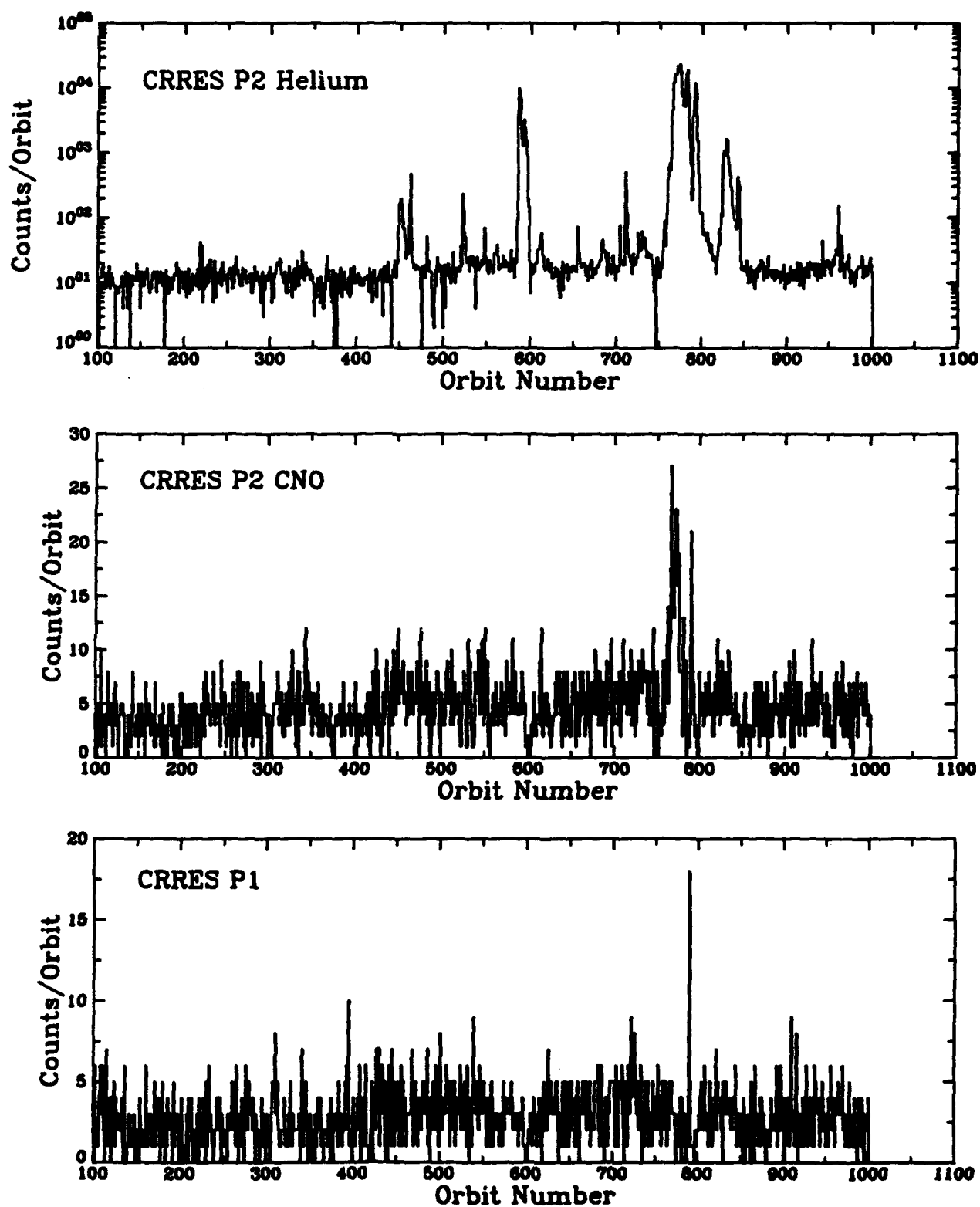


Figure V.2. Derived counting rate for P2 Helium, P2 CNO, and P1 as a function of orbit number during the CRRES mission.

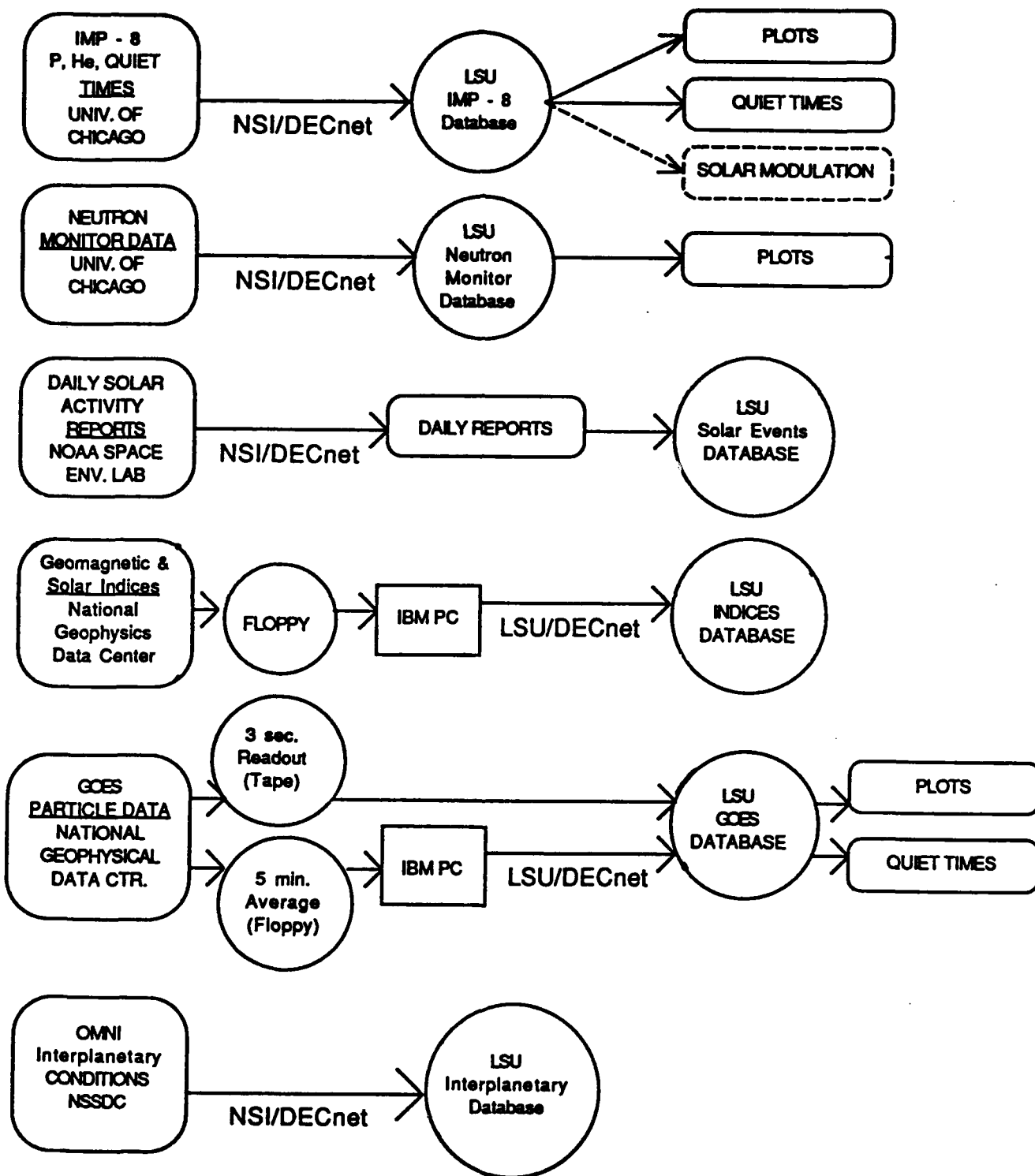


Figure V.3. Auxiliary databases established as part of the modeling effort.

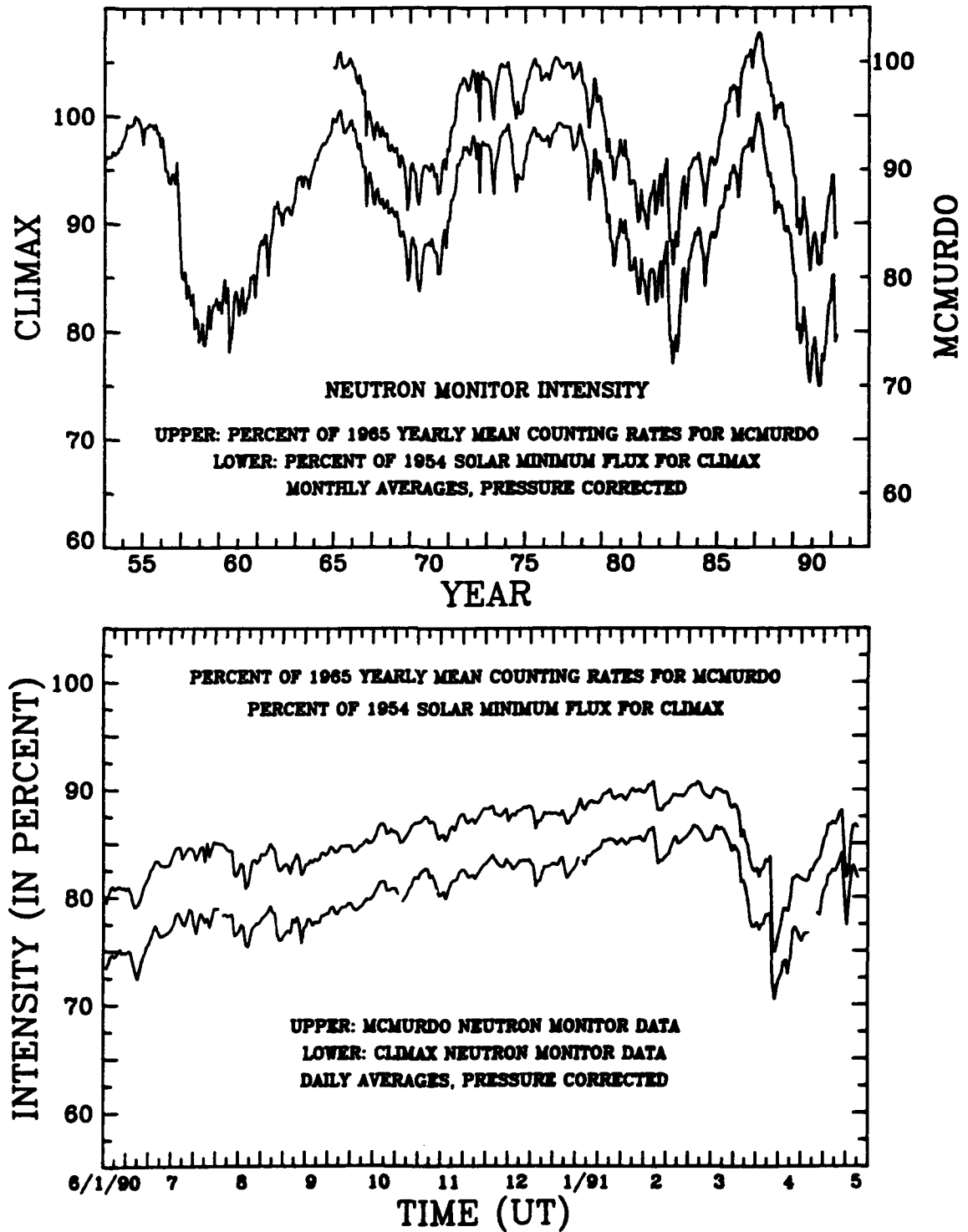


Figure V.4. Comparison of the Climax and McMurdo neutron monitor rates for the full time span of the measurements (top) and for a single year starting in June, 1990.

Daily reports of solar activity were obtained from the NOAA Space Environment Laboratory again using the NSI/DECnet network. These reports, which include x-ray fluence plots, geomagnetic storm and solar activity summaries and forecasts, and listing of recent solar events, are printed and archived. In addition, the event reports are stored online for later "real-time" access. Geomagnetic and Solar Indices such as Kp and D<sub>st</sub> are obtained from the National Geophysical Data Center on floppy disks. These are read on a IBM-PC and transferred to the online VAX database using the local DECnet network. These indices are used to correlate the active particle fluxes measured with ONR-604 to geomagnetic and solar disturbances.

Proton and electron particle data is also obtained from the geosynchronous GOES satellite from the National Geophysical Data Center. This data is received in the form of 5 minute averages on floppy disk and for the full time resolution (3 seconds) on magnetic tape. In addition, the 5 minute averages are received every month and are usually only a month or so off real time, while the full time resolution dataset can be delayed up to 8 months. Finally, the OMNI interplanetary conditions (e.g. solar wind velocity, interplanetary field) are obtained from the NSSDC over the NSI/DECnet network.

The GOES data consist of one electron channel (E1) and seven proton channels (P1-P7) covering the energy ranges:

E1	--	≥ 2 MeV electrons
P1	--	0.6 - 4.2 MeV
P2	--	4.2 - 8.7 MeV
P3	--	8.7 - 14.5 MeV
P4	--	15 - 44 MeV
P5	--	39 - 82 MeV
P6	--	84 - 200 MeV
P7	--	110 - 500 MeV

We have developed the interfaces to the plotting software so that GOES data can be compared to ONR-604 results on either long or short time scales. This provides for both mission summary analysis as well as cross calibration for the instrument.

An example of the latter is shown in Figure V.5 where the top four panels show ONR-604 rates while the bottom panels show the GOES fluxes for the period 14 Oct. - 6 Nov. 1990, near the beginning of the CRRES mission. The GOES results are plotted two to a panel, one with a solid line and the other with a dotted line. ONR-604 shows a large increase in the P3 and D2 coincidence rates around days 291-293 which is barely seen in the P2 and S rates. For GOES, none of the proton channels see such an increase, but the electrons (E1) do show it. This implies that the ONR-604 P3 and D1 D2D3S rates do have a large electron sensitivity, with less effect, but still a non-zero sensitivity, for P2 and the scintillator, S. This is consistent with the P3 performance observed within the magnetosphere (and with the pre-launch radioactive source calibration).

The reverse situation is also in evidence. GOES sees a low energy proton event at about day 297. The ONR-604 P3 and D2 rates barely see it; P2 does not see it; and S also does not see it. This validates the shielding calculations for S, in that S should be protected from low energy protons, and the logic for P2 which should not be triggerable by low energy protons.

As mentioned previously, the IMP-8 data provides another set for comparison with ONR-604. We have obtained IMP-8 proton and helium fluxes (3 energy ranges each) from the University of Chicago, as well as the quiet time selections that are commonly used for analyzing low energy data. A plot for the first part of the CRRES mission is illustrated in Figure V.6 where

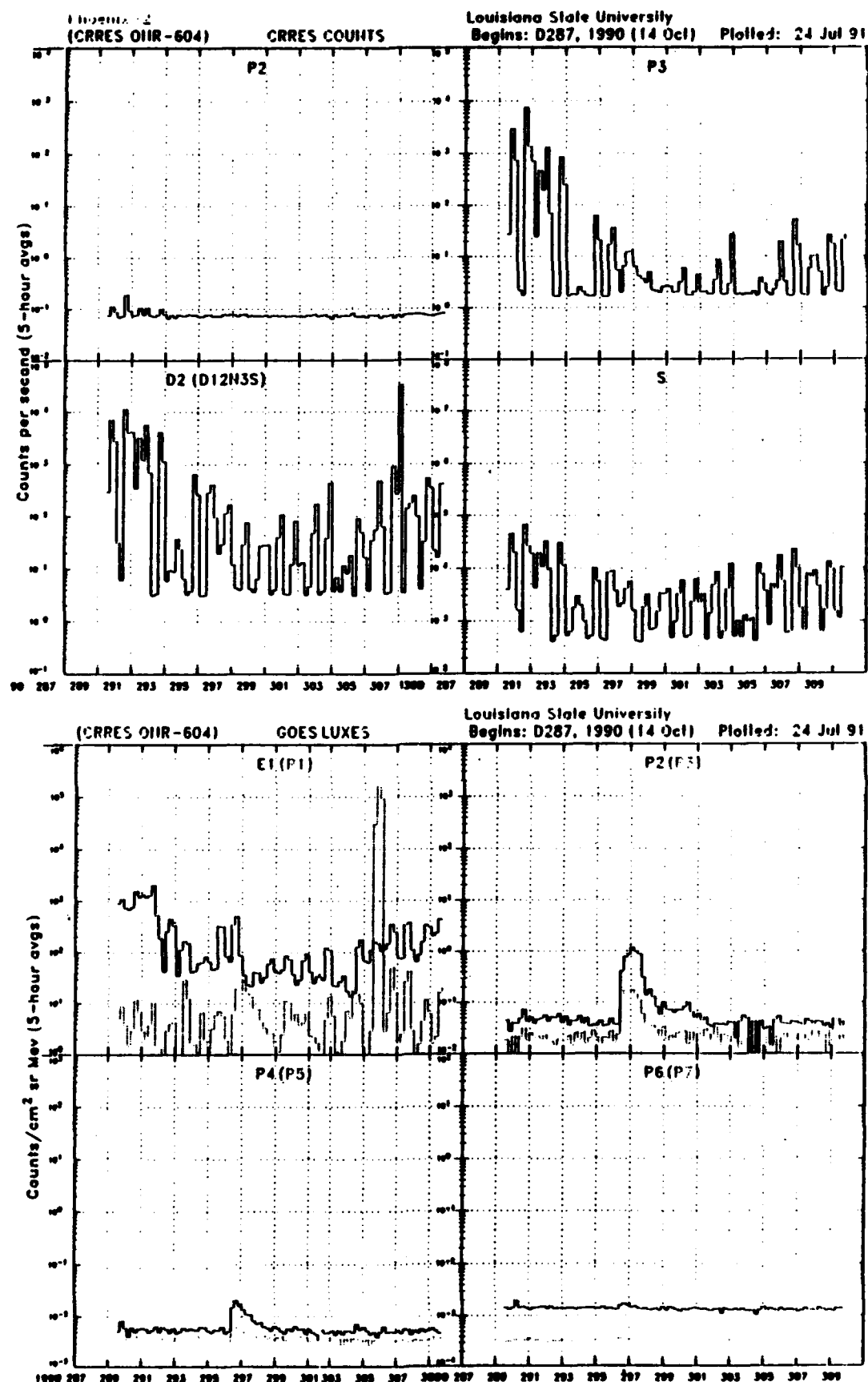


Figure V.5. Comparison of selected ONR-604 counting rates (top) with GOES fluxes for 10/14 - 11/6/90.

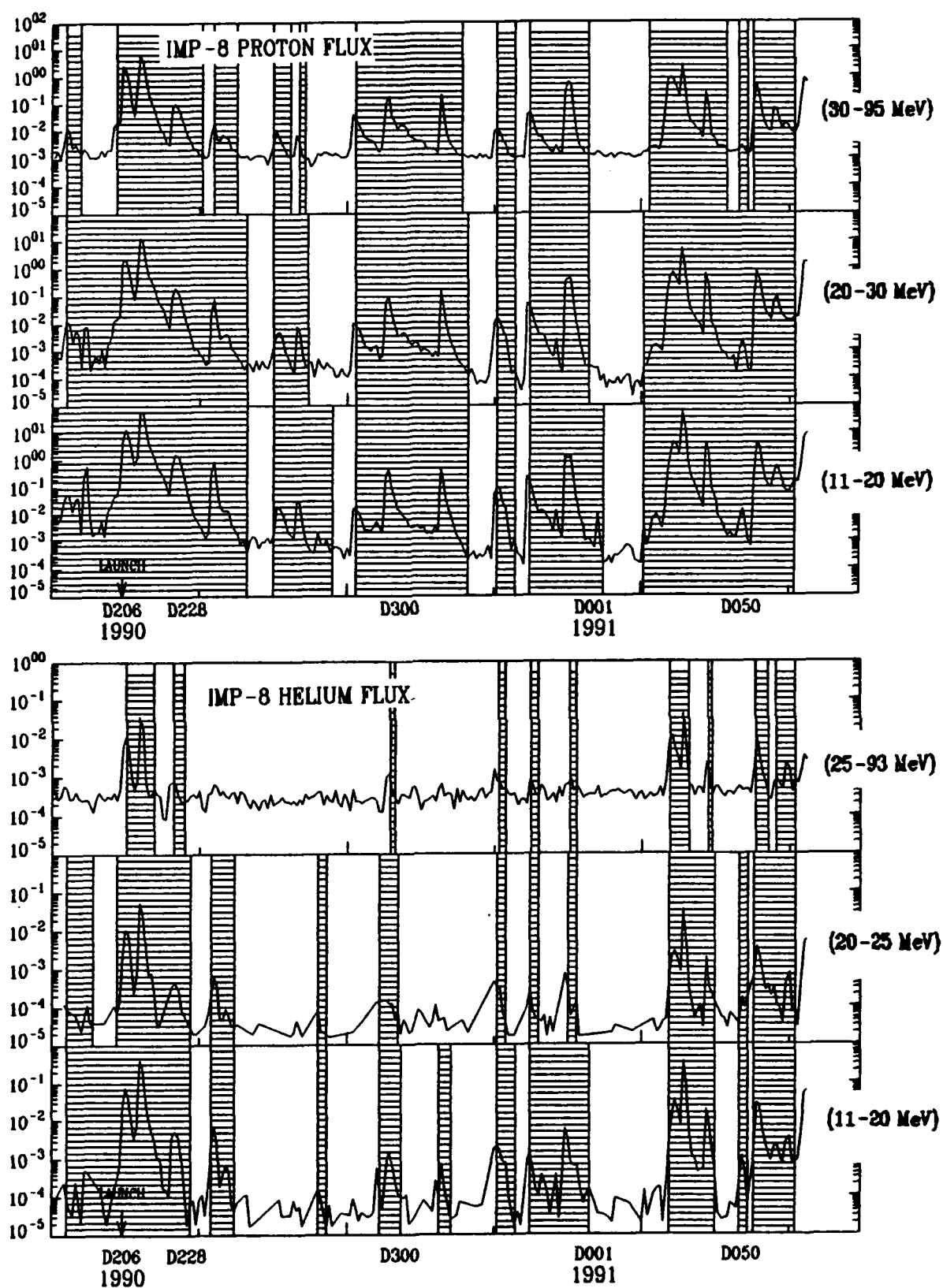


Figure V.6. IMP-8 selected quiet times (clear areas) shown over plots of the three proton and three helium counting rates for the first part of the CRRES mission.

the clear regions show the "quiet" intervals. One notes that CRRES launched into a moderate solar flare which had subsided by the time the S/C and instrument check-outs were finished and routine operations started. This period of time is extremely active for low energy particles, but for the energies most relevant to ONR-604, i.e. the 25-93 MeV/nucleon helium, the major flare periods can be easily identified.

An additional source of information is provided by the CRRES environment monitoring instruments described in Table 2.1. The CRRES project at Phillips Laboratory, Geophysics Directorate formed a Science Summary Database (SSD) as part of the first level reduction and processing of the data stream from the spacecraft. The selected data channels for this SSD are indicated in Table 5.1.

**Table 5.1. Data in Science Summary Database**

Species	Energy	Instrument	Units
e	4-5 MeV	701-4	Flux
e	>2.5 MeV	702-2	Counts/s
e	1-1.5 MeV	701-4	Flux
e	550-660 keV	701-5A	Flux
e	200-300 keV	701-5A	Flux
e	20-285 keV	701-5B	Counts/s
"He"	>45 MeV/n	604 (P2)	Counts/s
Star	>75 MeV	701-2	Counts/s
p	50 MeV	701-9	Flux
p	>35 MeV	701-2	Counts/s
p	3 MeV	701-8	Flux

The SSD has been down-loaded to LSU and formatted as another ancillary database to be used for comparison with ONR-604 and the other databases. Plotting software is available for the SSD, and a sample of the results is shown in Figure V.7a and V.7b for orbit 596 on day 86 of 1991. The proton channels are shown in Figure V.7a along with the L value and the magnetic field strength, both observed by the on-board magnetometer and calculated from a magnetic field model. The electron channels are summarized in Figure V.7b and show some interesting structure, particularly at apogee. Note that the fluxes of MeV electrons are relatively high over most of the CRRES orbit, which accounts for much of the background (discussed below) seen in the ONR-604 pulse height analysis and in the rate channels.

### C. ONR-604 Analysis

One of the difficulties in analyzing space data from a sensor system such as ONR-604 is the elimination of "background" events. One of the goals in the accelerator calibrations, discussed previously, was to identify potential sources of background and to develop procedures for handling such problems. Much of our work since CRRES launch has been devoted to "cleaning" the events, i.e. eliminating spurious or background events and checking the charge and energy assignment of the remaining events. We looked first at the P1 events, the heaviest, highest energy nuclei which are less affected by solar or geomagnetic disturbances. Figure V.8 shows two matrices for 20,000 raw P1 events as K1 versus K2-K8 (top) and ESL1SC versus ES (bottom), i.e. the energy in the preceding versus the energy in the stopping detector. In both cases, the iron track at the top of the figure is readily apparent, but there is an obvious "smear" of events in the center and at the bottom of the plots.



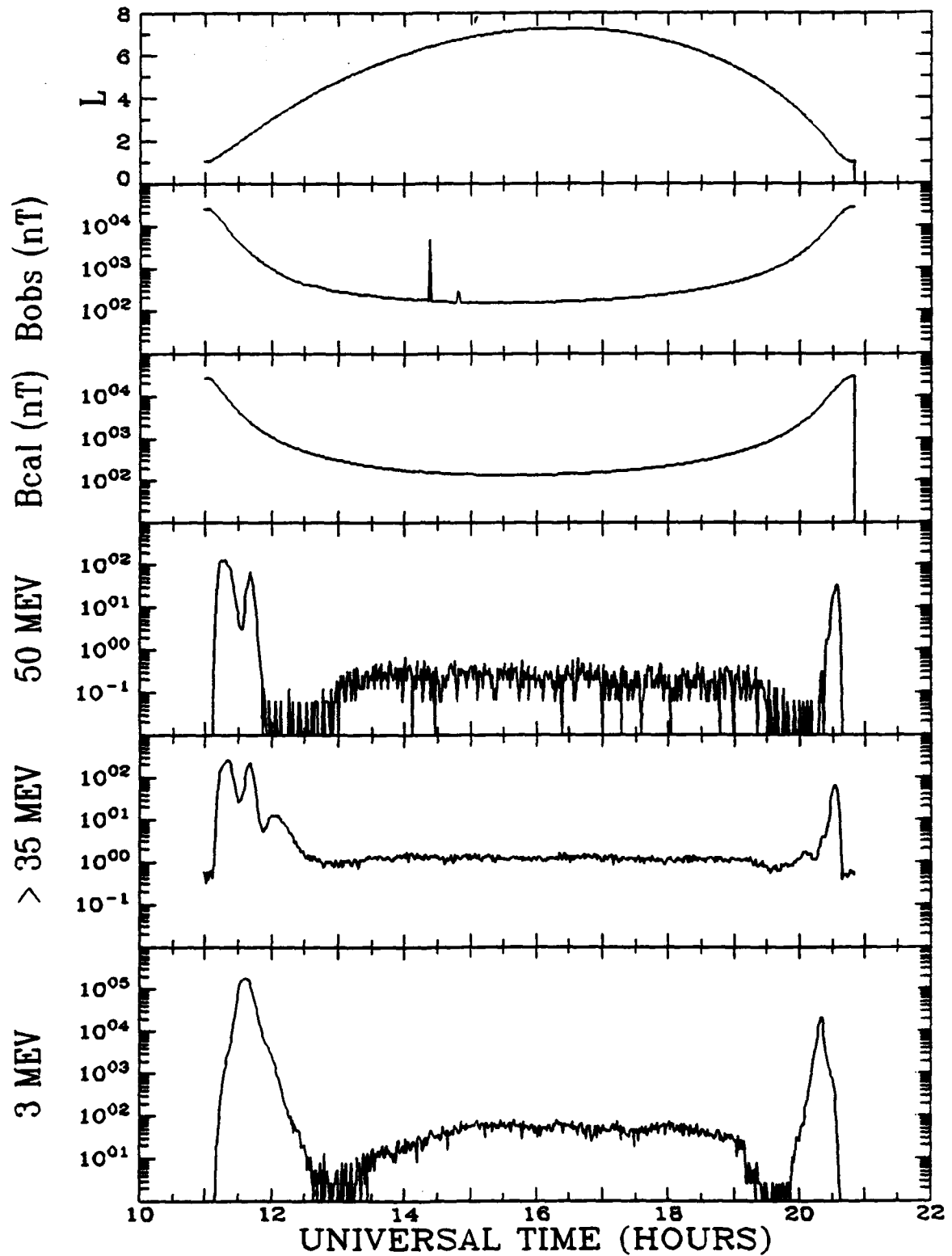


Figure V.7a. SSD plots for L, Magnetic Field and the proton channels for orbit 596.

06/91. ORBIT 596. PLOTTED: 1-2-91. LSU CRRES

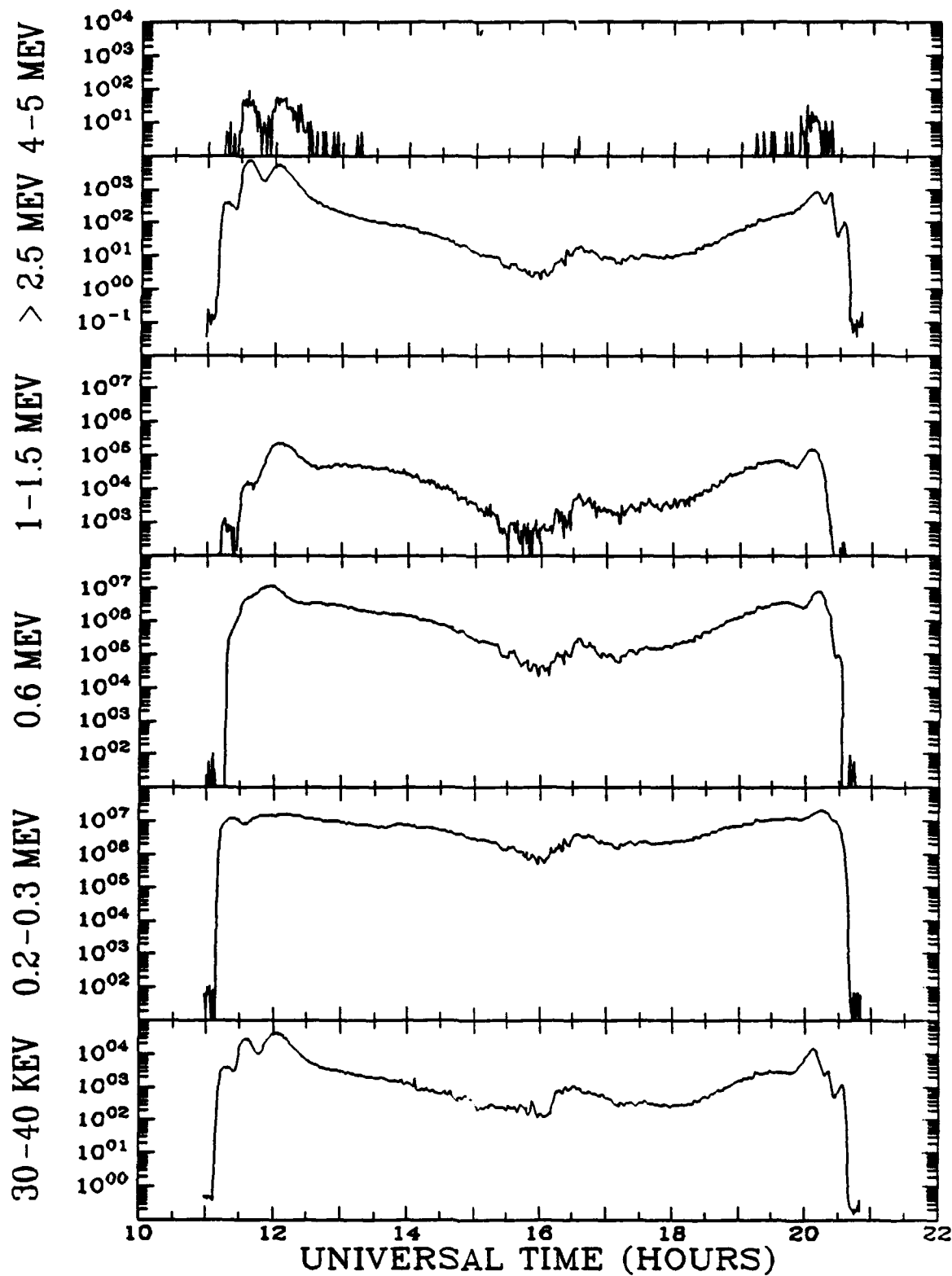


Figure V.7b. SSD plots for the electron channels for orbit 596.

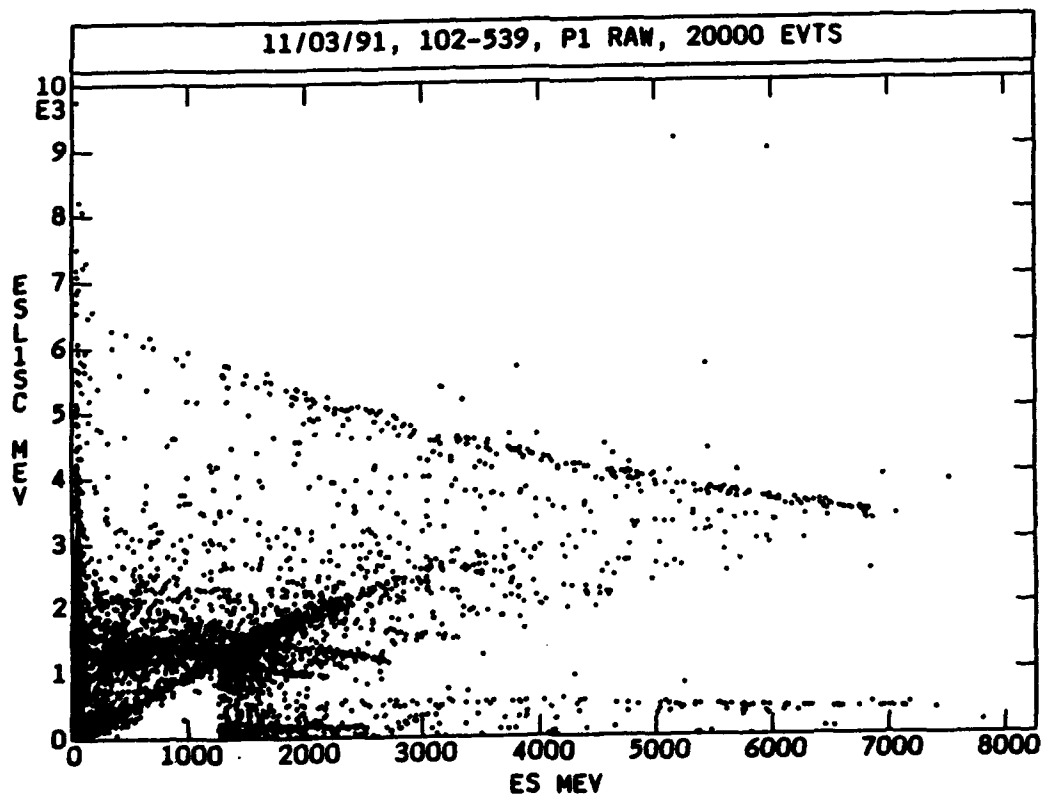
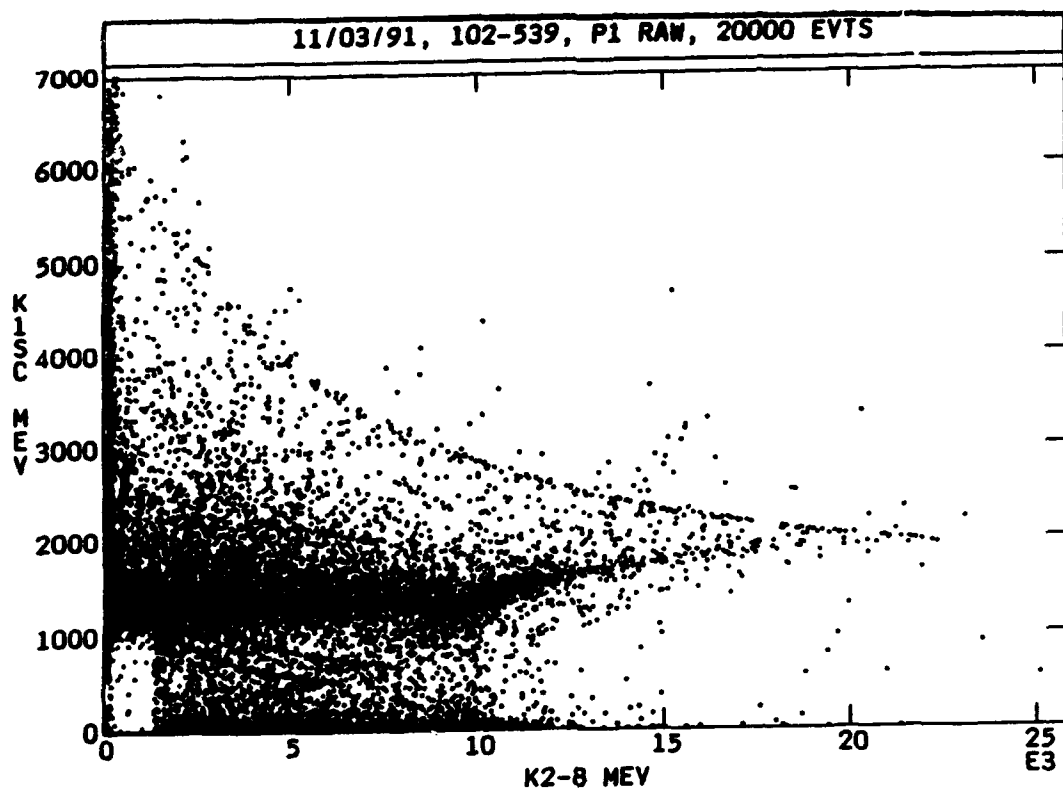


Figure V.8. Raw P1 events shown as (top) energy in K1 versus energy in K2-8 and (bottom) energy in the detector before versus the energy in the stopping detector.

The ID distribution for these 20,000 events is shown on the top of Figure V.9. A large fraction of the events are ID15, i.e. penetrating the anticoincidence detector at the bottom of the stack. The matrix for these penetrating events is shown at the bottom of Figure V.9 (c.f. Figure V.8 top). The penetrating particles account for much of the "smear" in the center and much of the pile-up near the x-axis. In addition, the negative ID's, indicating an unallowed discriminator bit pattern, must be eliminated.

A further cut is provided by the scintillator surrounding the instrument. Requiring  $S=0$ , i.e. no particle entering or leaving sides of the instrument, reduces the number of events from 20,000 to 3870, but also eliminates much of the "garbage" in the matrix. However,  $S=0$  is not sufficient. It is possible for a particle to leave the sides of an individual detector and stop in the ring holding the detector without triggering the scintillator. Such events were observed during the accelerator calibration of ONR-604. They can be eliminated by calculating the point of incidence of the particle on the stopping detector (using the information provided by the trajectory system) and restricting the analysis to only those events not near the edge of the detector.

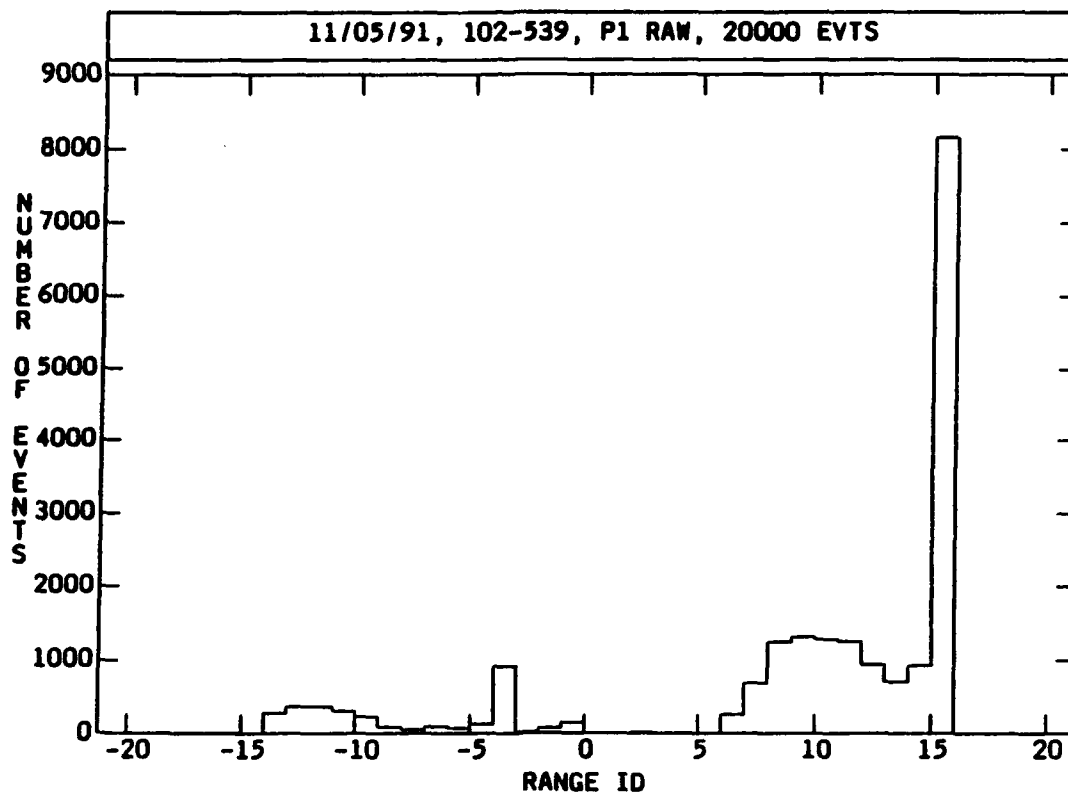
Putting all of these cuts together ( $P1B = \bar{S}$ ;  $\bar{A}$ ;  $ID < 15$ ;  $ID > 0$ ;  $RS < 20$  mm) and requiring that the calculated charge for the event be  $> 0$  gives the matrices shown in Figure V.10, to be compared with the raw matrices in Figure V.8. The improvement is tremendous; the individual element tracks are discernible; but the cost was in statistics. Only 7.4% of the original 20,000 events survive for further analysis. Note that not all of these are necessarily "good". Figure V.10 still shows events piled up near the x or y axes. Also, one event, nominally identified as Sr ( $Z=38$ ), shows up at very large signal levels. This is probably a non-real event whose origin must be analyzed.

Figure V.11 (top) shows the derived charge histogram for the "cleaned" events. While the resolution looks reasonable, there are a number of inconsistencies. First, events with  $Z < 9$  should not trigger P1, yet there are ~150 such events, mainly assigned  $Z = 1$  or 2. Second, there is a peak at  $Z = 27$ , Cobalt, which is a very rare element. Close inspection shows similar "spikes" just above some of the other main charge peaks. Finally, the peaks do not fall at the correct charge values.

Looking first at the 266 events assigned as  $25 \leq Z \leq 27$ , the lower portion of Figure V.11 shows the charge assignment as a function of ID. The majority of these events should be iron ( $Z = 26$ ), but the figure demonstrates a shift of a full charge unit between  $ID = 7$  and  $ID = 11$ . This indicates that a fine-tuning of the calibration of each detector is needed to obtain consistency. Another possible diagnostic is provided by the distribution of incident zenith angles, shown at the top of Figure V.12. The peak occurs at  $15-20^\circ$  as expected and shows no particular inconsistency.

Finally, we can look at the events with  $Z < 9$ , which are shown in the lower panel of Figure V.12, plotted as K1 versus K2-8 to facilitate comparison with Figure V.8 and V.10. These events account for some, but not all, of the events in Figure V.10 along the axes and in addition show a scatter throughout the matrix. The fact that these events are assigned a low charge while their position on the matrix of Figure V.12 would indicate a much larger charge indicates that there is something "funny" occurring near the stopping detector. Perhaps a nuclear interaction occurred in the stack or there are multiple particles traveling together (in time) but with different ranges. In principal, such events may be assigned higher charge values, so there could be such events among the rest of the particles as well.

To proceed further it is necessary to utilize the information from all of the detectors in the stack. We have developed a range-energy algorithm to predict the energy deposited in each detector given only the charge (ZCAL) and the energy in the stopping detector for each event. Figure V.13 (top) shows a cross plot of the energy deposited in detectors K1-K8 as calculated (y-axis) and measured (x-axis). Note that most of the events fall along the  $45^\circ$  line as anticipated, but that there are significant events off the line as well. It is these latter that are the potential background events. The lower plot of Figure V.13 shows the deviation of the observed and calculated energies. Note the



62

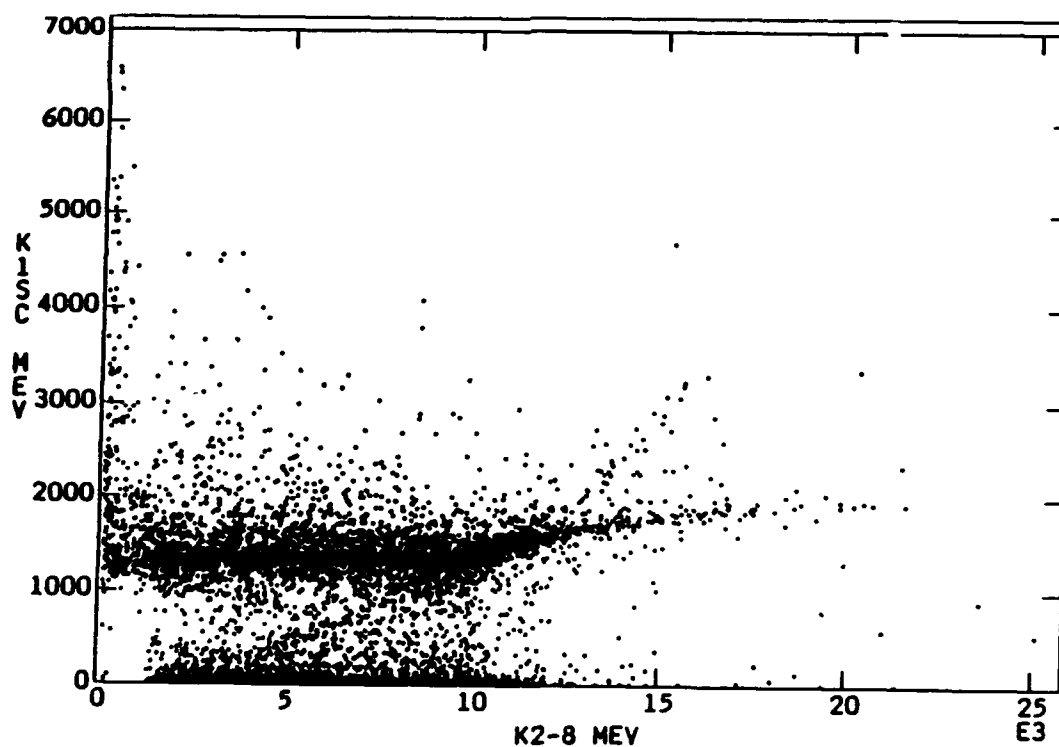


Figure V.9. The ID distribution for the raw P1 events (top) and the K1 versus K2-8 matrix for the penetrating (ID-15) events.

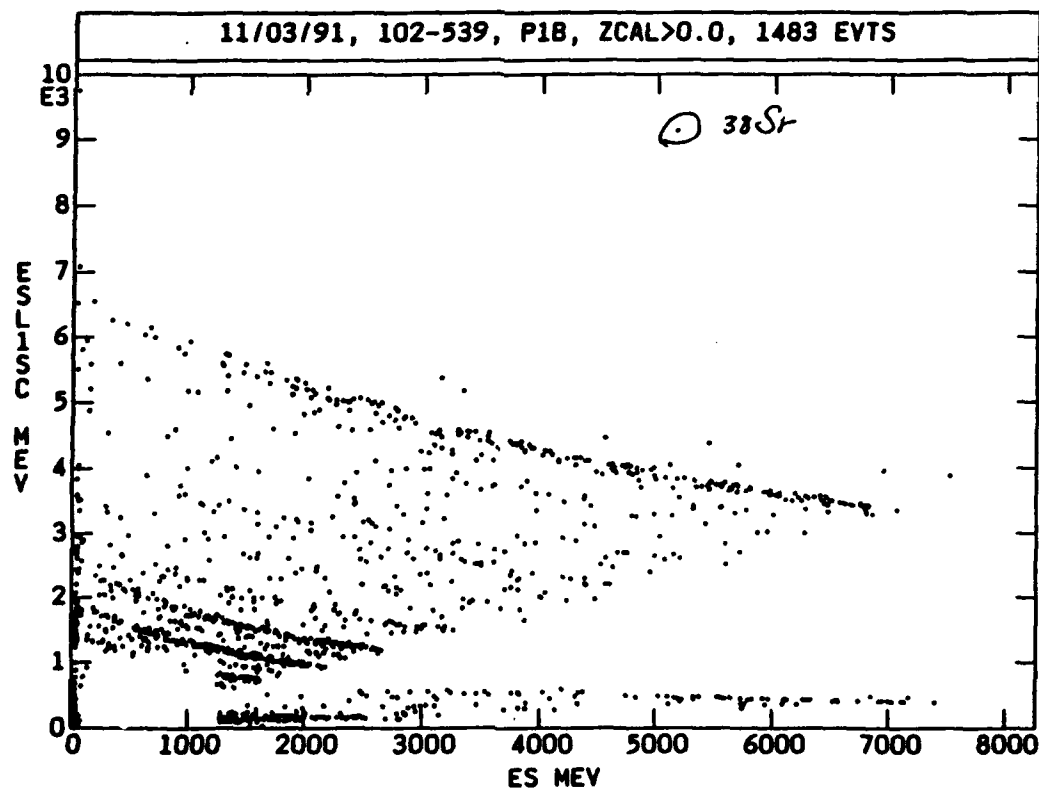
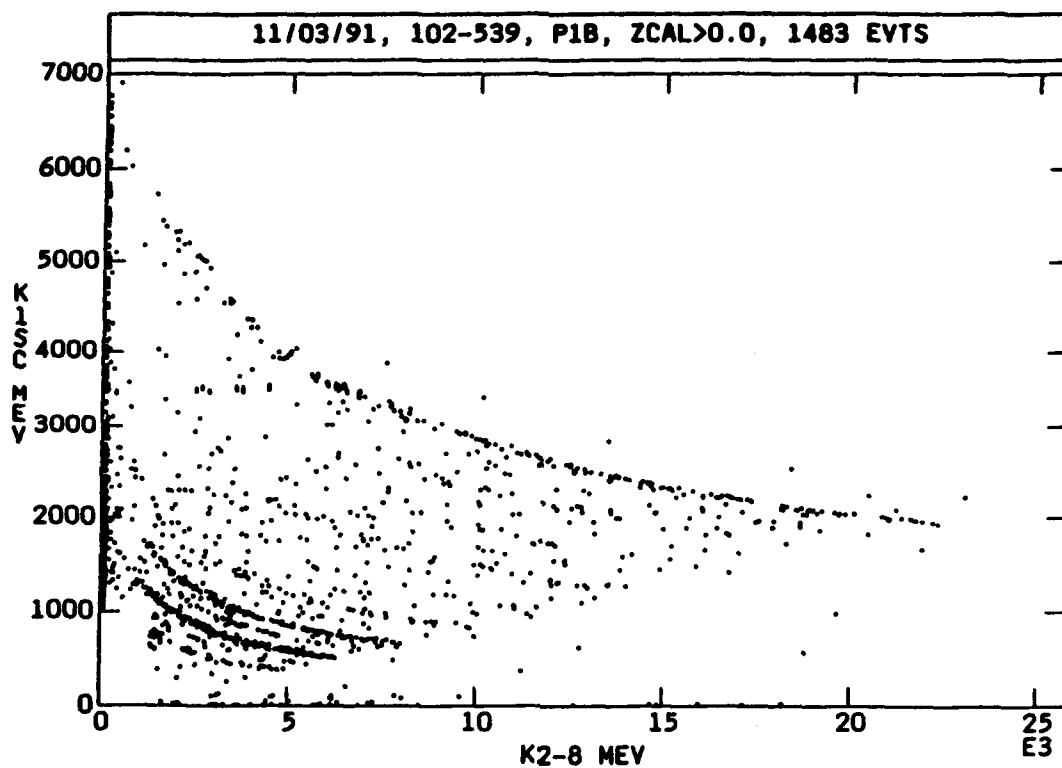


Figure V.10. The matrices of Figure 5 shown for first order "cleaned" events (P1B and  $Z>0$ ).

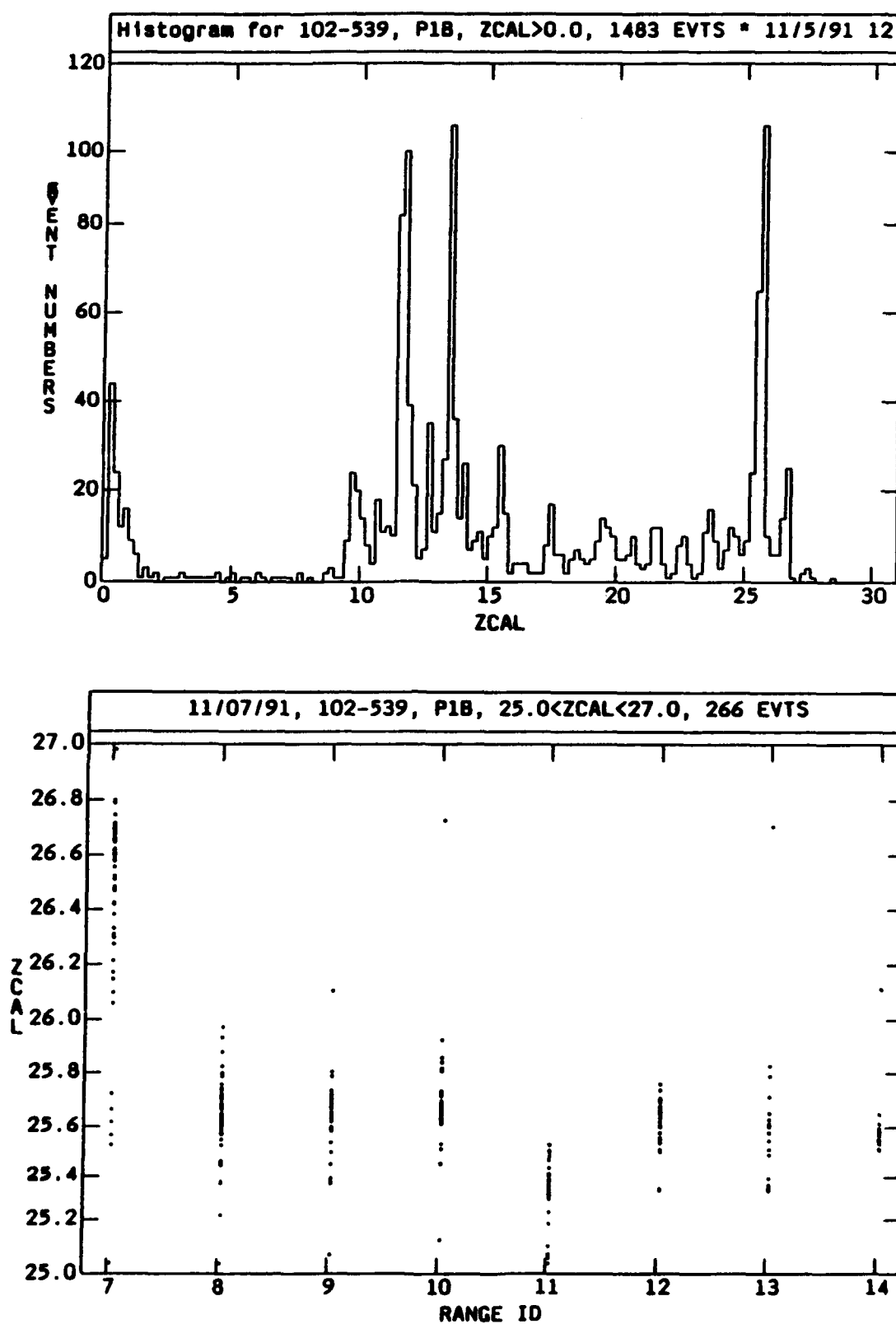


Figure V.11. The charge histogram for the cleaned events of Fig.7 (top) and the assigned charge by ID for the elements of the iron peak (bottom).

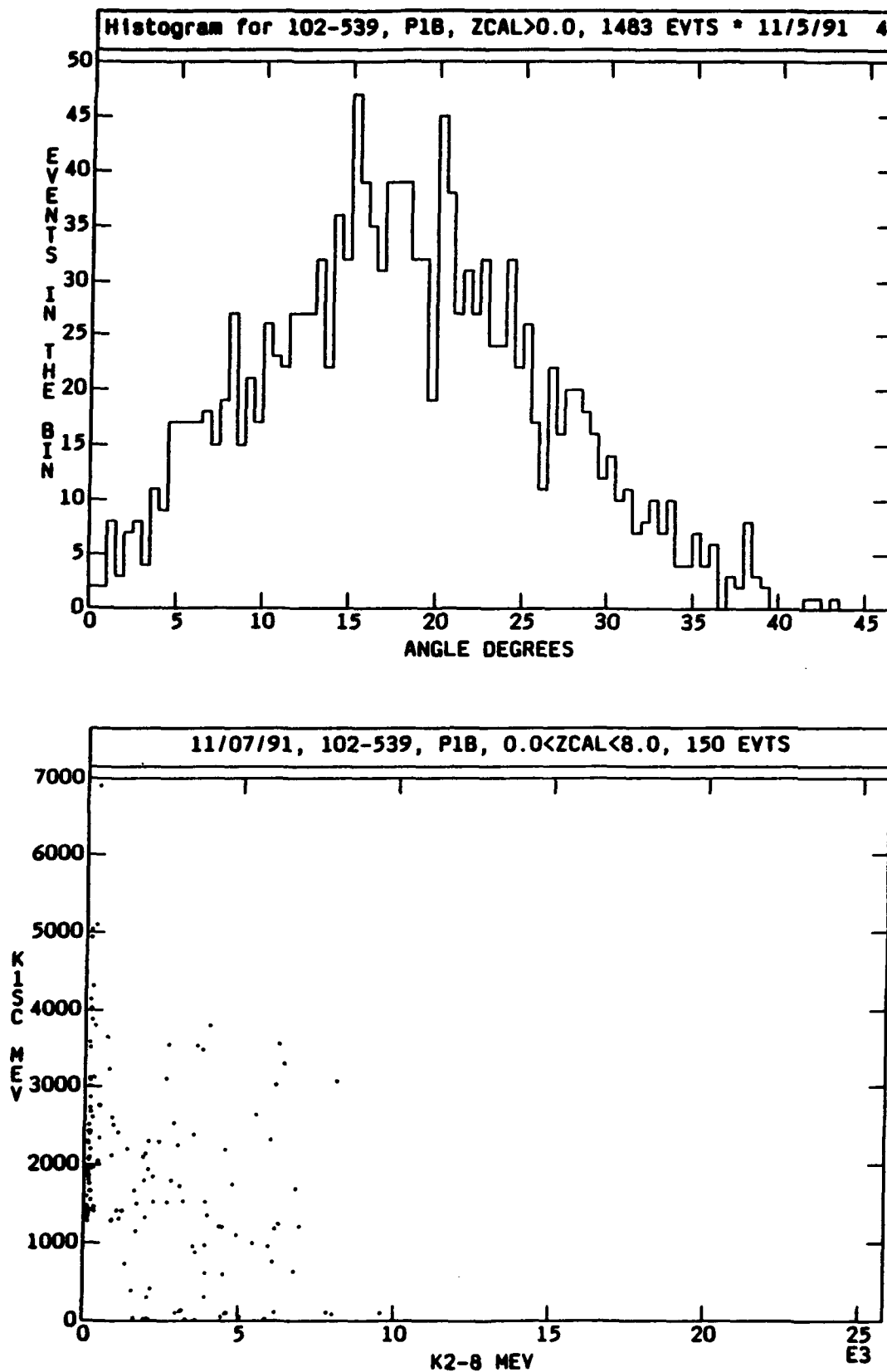


Figure V.12. The zenith angle distribution for the cleaned events (top) and the K1 versus K2-8 matrix for only the events with charge less than 9 (bottom).



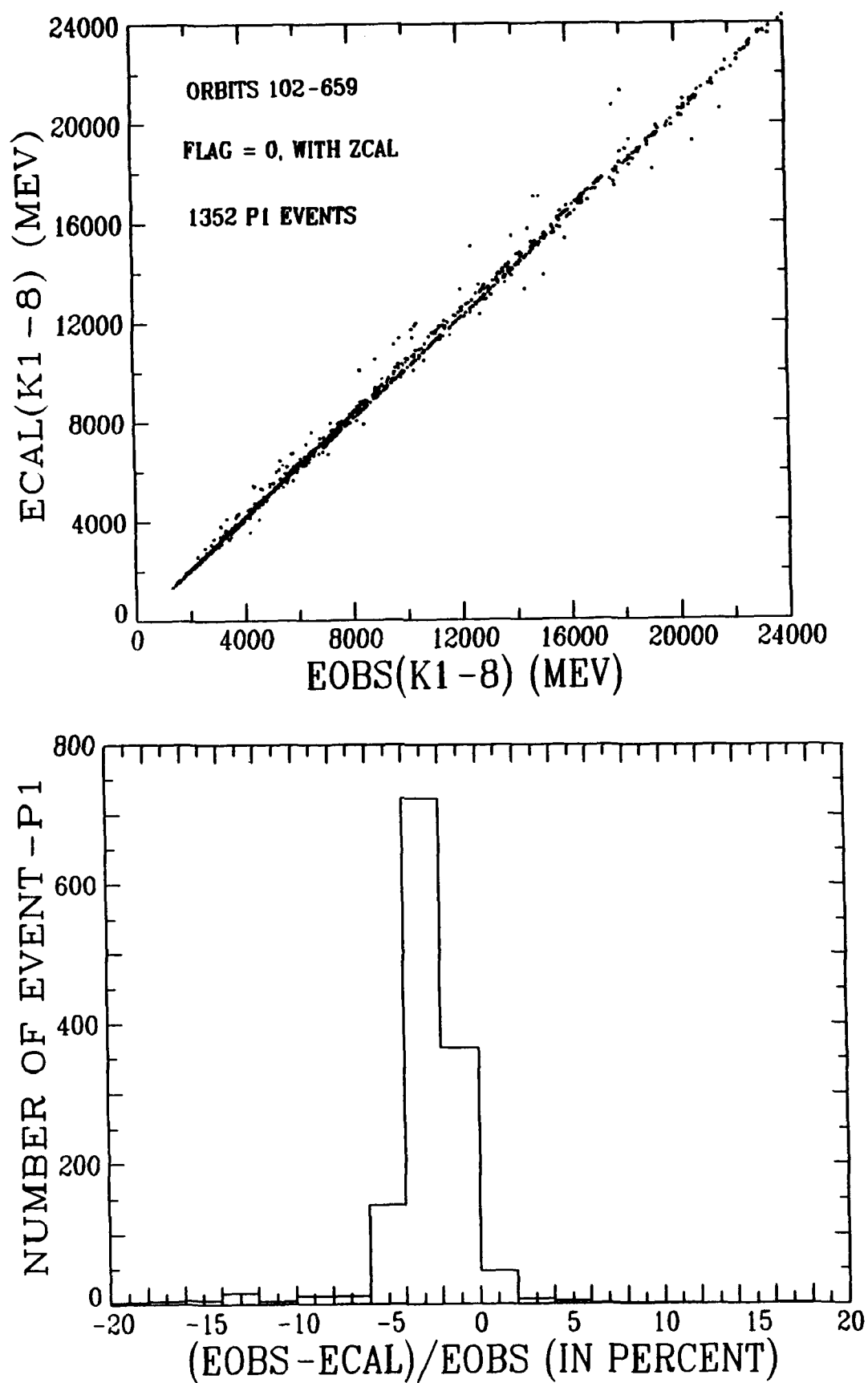


Figure V.13. Cross plot of the calculated and observed energy in detectors K1-K8 (top) and the histogram of the deviation between observed and calculated energies (bottom).

events far out on the tails which are obviously "wrong." However, the mean deviation is not centered at zero but shows that the calculated values are a few percent larger than the observations. This can account for the charges (ZCAL) not falling at the correct values in the histograms.

We have developed a procedure to calculate the RMS deviation of the observed energy from the predicted energy, detector by detector from D6 through the stopping detector. If this deviation is large compared to the mean, we assume that the initial charge assignment (ZCAL) may be in error. We then use the measurements to calculate a new charge (ZNEW) which minimizes the RMS deviation (DE) parameter. The top plot of Figure V.14 shows another cross plot of the calculated versus observed energy. Comparison with the top of Figure V.13 demonstrates that most of the "junk" has now been removed.

We can, however, go one step further. The distribution of the DE parameter is shown in the lower panel of Figure V.14. Even with the revised charge assignment, there remains a family of events separated from the main peak near the origin. This second group has DE values from ~1-3% with a long tail to large values. Such disagreements can result from nuclear interactions in the detectors which strip off only a single nucleon or, possibly, from timing glitches in the PHA circuitry. In any case, to get the cleanest sample of events, we can make a cut and only accept events with DE <1%. Again, the statistics suffer but we are now assured that we have a very good sample of events. This is illustrated in Figure V.15 which shows the measured charge histogram at the top compared to the theoretical expectation based upon Galactic Cosmic Ray Model calculations. The correlation is excellent and the charge peaks now fall at the correct values.

Turning next to the P2 events (~He-Ne), Figure V.16 shows plots of the P2 metal ( $Z > 2.5$ ) and the P2 Helium ( $1.5 \leq Z \leq 2.5$ ) derived counting rates. The presence of solar flares in the data is evident from the P2 Helium rate. Inclusion of solar flare periods is not advisable, since the high counting rates during the flares may affect the location of the different element tracks. Therefore, we developed a quiet-time data cut shown schematically at the top of Figure V.17 (c.f. Figure V.4). A plot of the charge versus incident energy for the P2 metal events is shown at the bottom of Figure V.17, and displays the expected behavior in which ~50% of Neon and smaller amounts of Na-Si are included in the P2 priority. This is an agreement with the pre-launch heavy ion calibrations as discussed previously. Note also that there are considerable events below  $Z=4$ , and these are presumably the tail of the abundant helium distribution, since  $Z=3$  and 4 are relatively rare in the cosmic rays. There are also events that fall between the charge bands which are potentially mis-assigned particles.

For the quiet periods, we applied a clean-up to the P2 metal events similar to that just described for P1 events. The result, for quiet orbits 251-400, is shown in the top plot of Figure V.18, which compares the measurements to the predicted "tracks" for a variety of elements. Note that most of the events now fall directly on the calculated lines, with only a few events in between the charge bands. For interest, we looked at the charge (ZCAL) distribution as a function of L-shell for the good P2 events, selected only for quiet orbits 251-400. This is shown in the lower panel of Figure V.18. There is a sharp cut-off at  $L \sim 3$  for all of the heavy ions ( $Z > 2$ ), as expected, but the Helium shows penetration below  $L=3$  to very low L-shells. This may imply that some of the helium is not fully stripped or that we are seeing a relatively high energy population of trapped helium ions. We will return to this point in the next section on preliminary results.

Since the ONR-604 instrument gives the arrival trajectory of each particle, we can unfold the geometry and, using a model for the quiet geomagnetic field, calculate the local pitch angle distribution of the particles. A sample of such a plot for the P2 metals is shown in Figure V.19 (top) and demonstrates that the local pitch angle distribution is peaked at  $0^\circ$  and  $180^\circ$ , i.e. along the magnetic field lines. The interpretation of this observation is under investigation. Finally, we show in the bottom panel of Figure V.19, the charge histogram for the "cleaned" P2 metal events from orbits

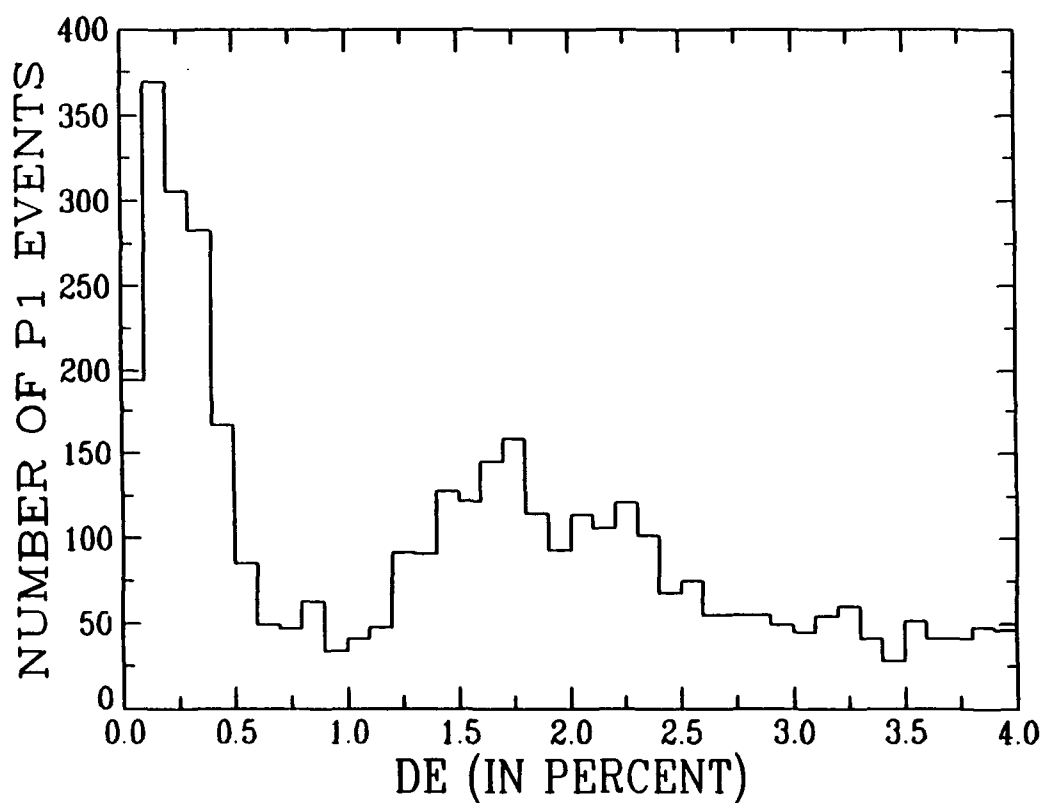
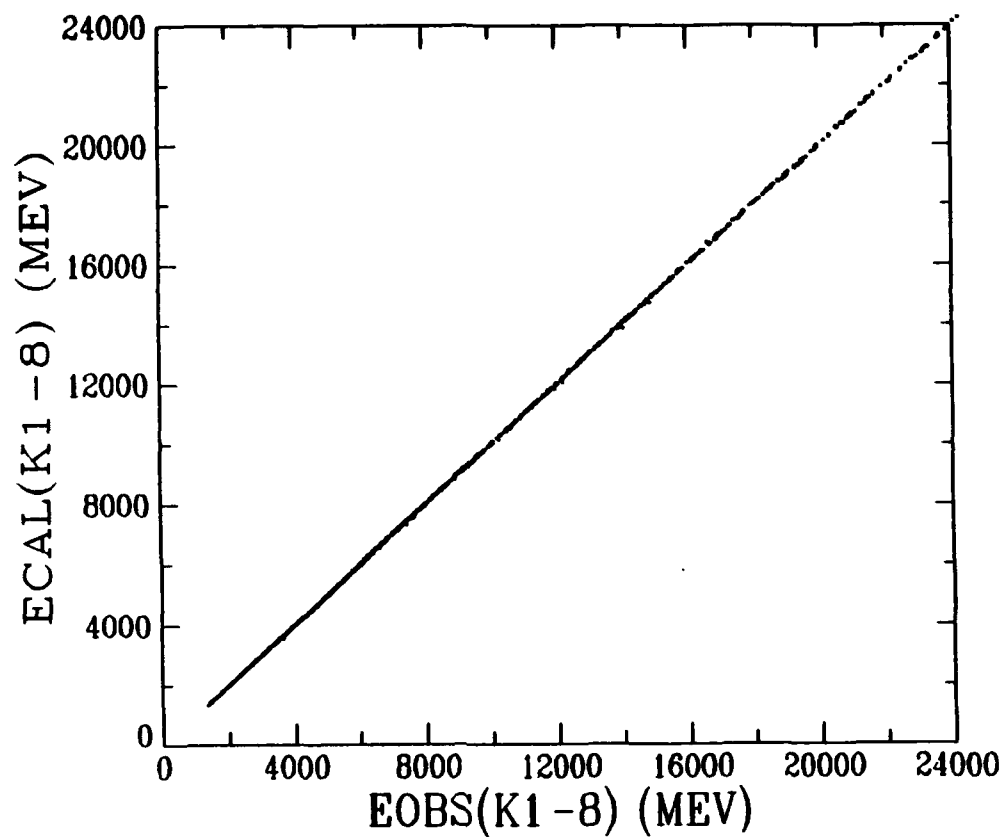


Figure V.14. Cross plot of the calculated and observed energies for detectors K1-K8 after correcting the charge assignments (top) and histogram of the DE parameter for a sample of events.

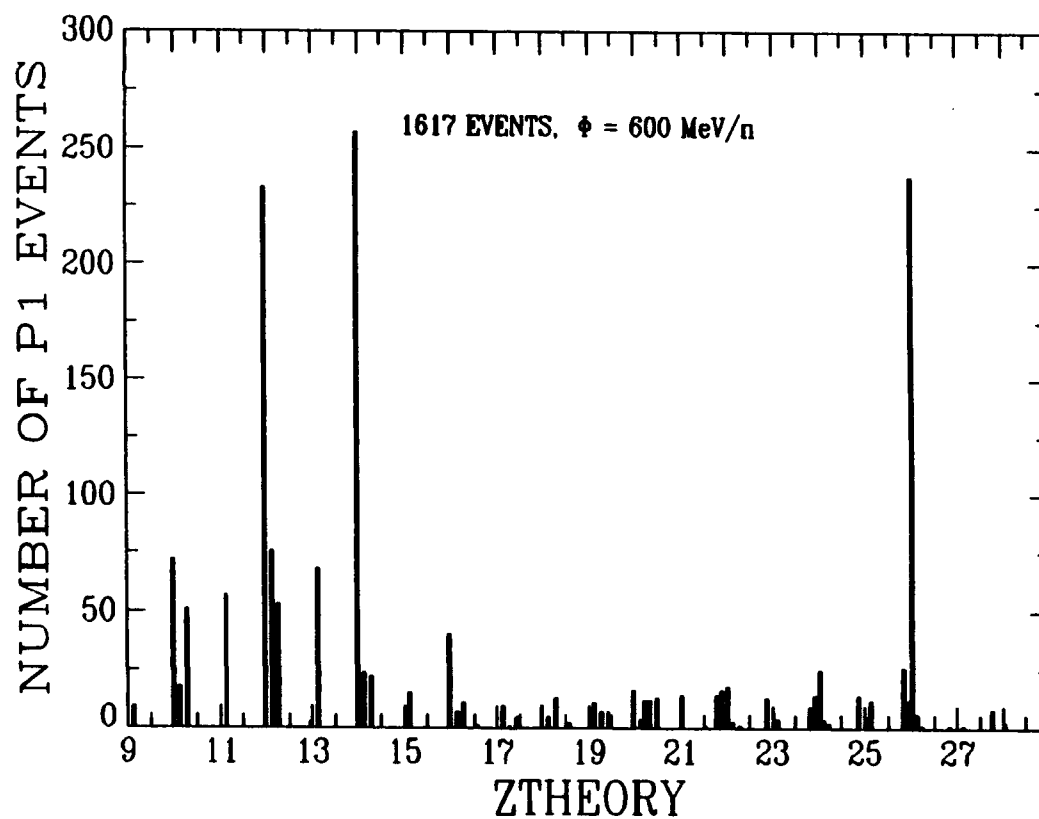
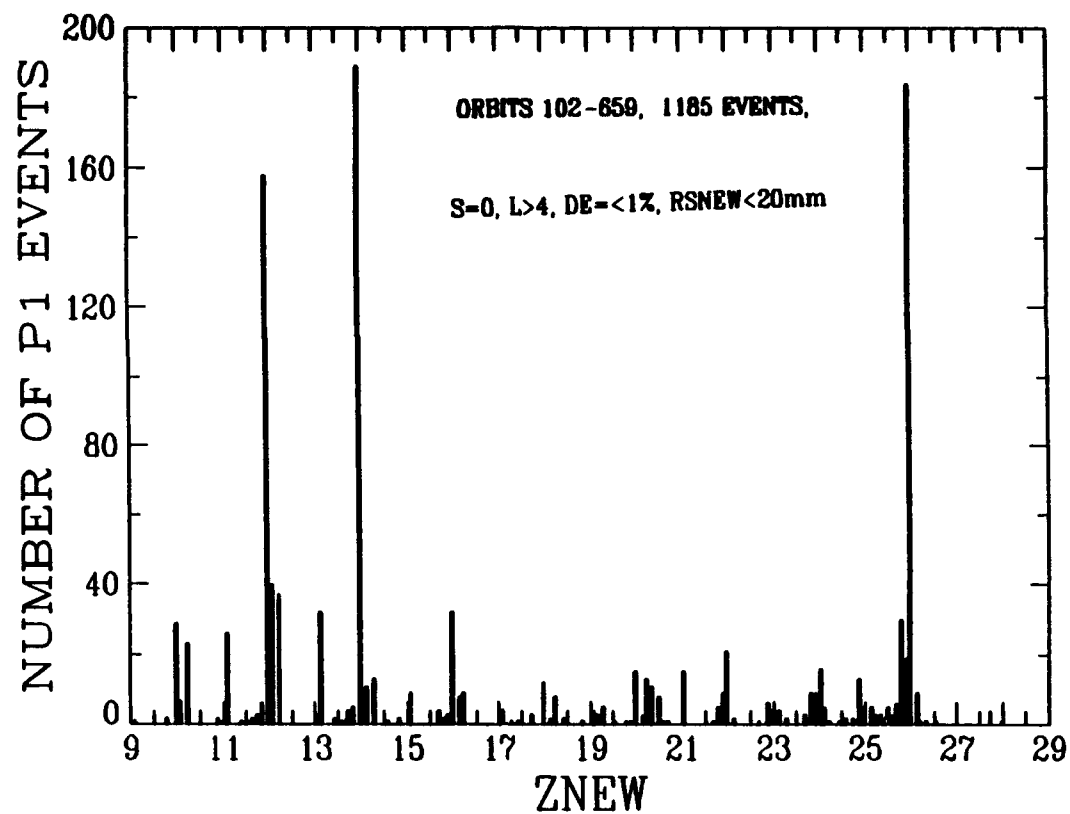


Figure V.15. Charge histograms for P1 events showing the measured distribution (top) compared to the expected distribution calculated from the Galactic Cosmic Ray Model (bottom).

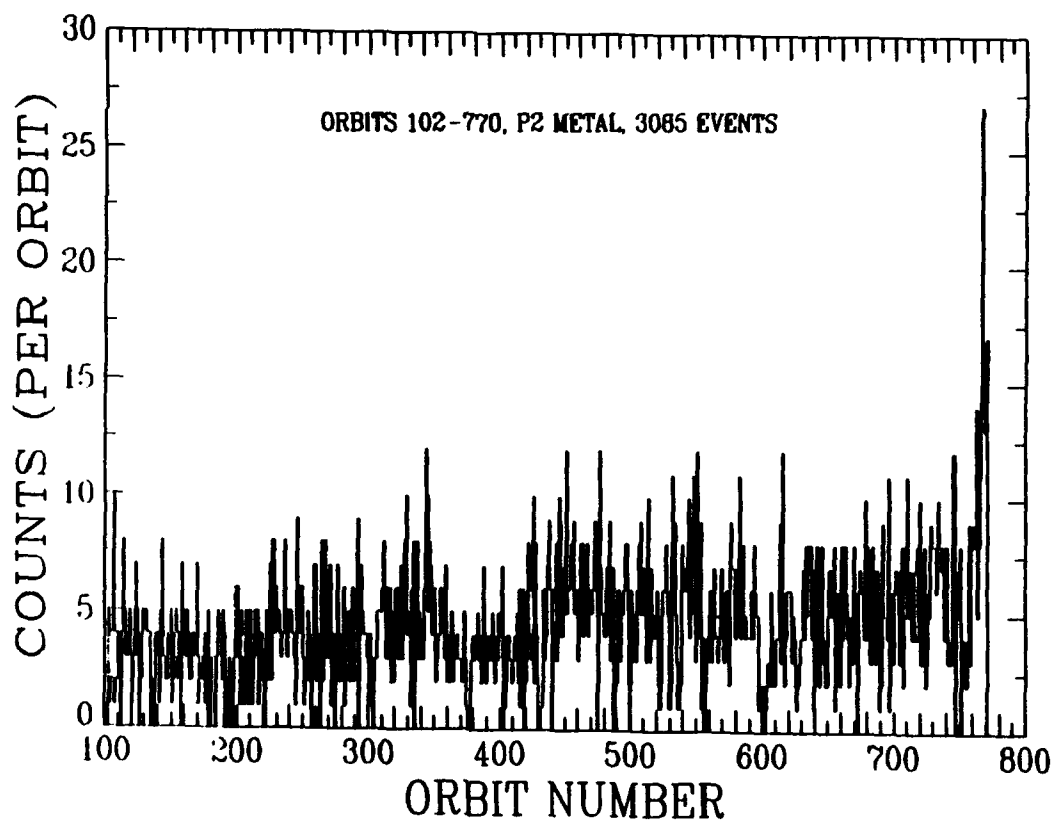
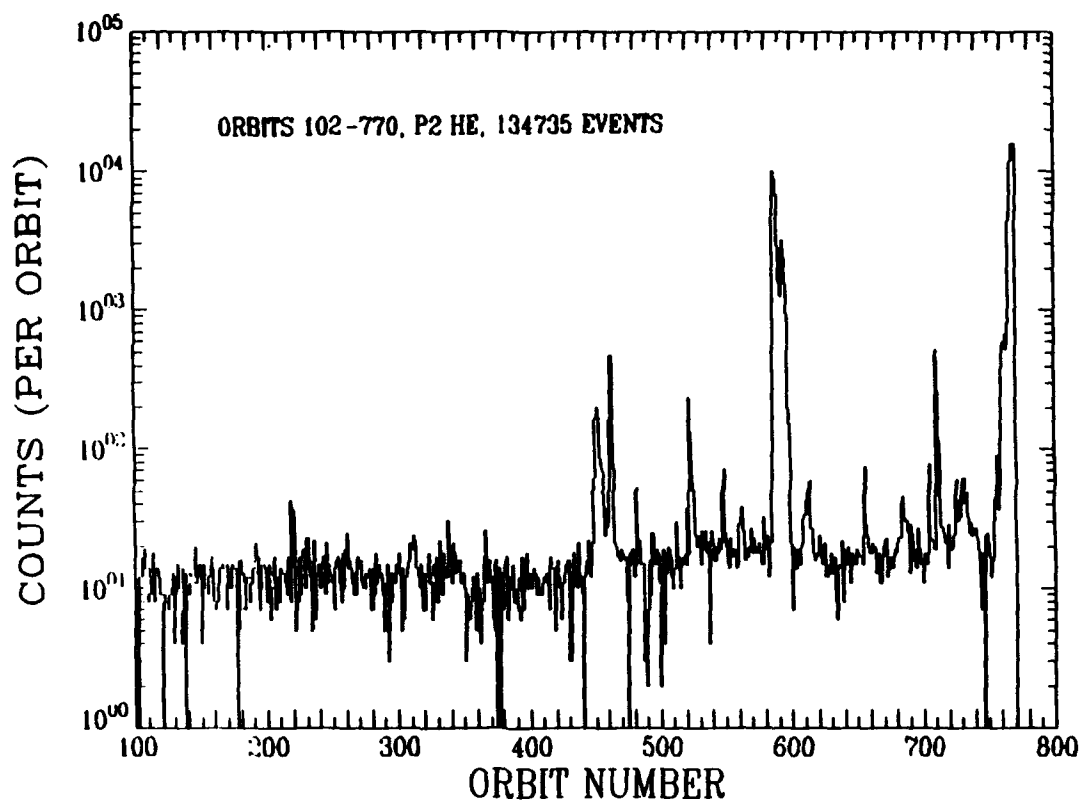


Figure V.16. Counting rates as a function of orbit for P2 metal (top) and P2 Helium (bottom). Note the logarithmic scale in order to include the large variation in the P2 Helium rate.

UNQUIET TIME (SHADED) DETERMINED FROM ONR-604, ORBITS 102-770

71

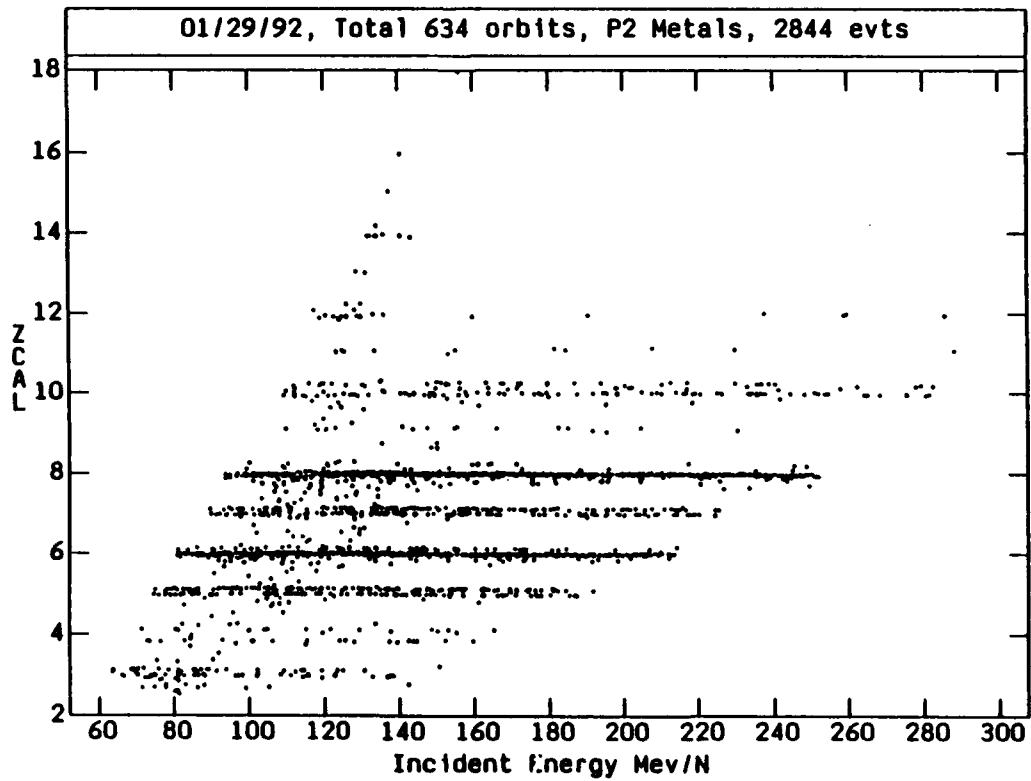
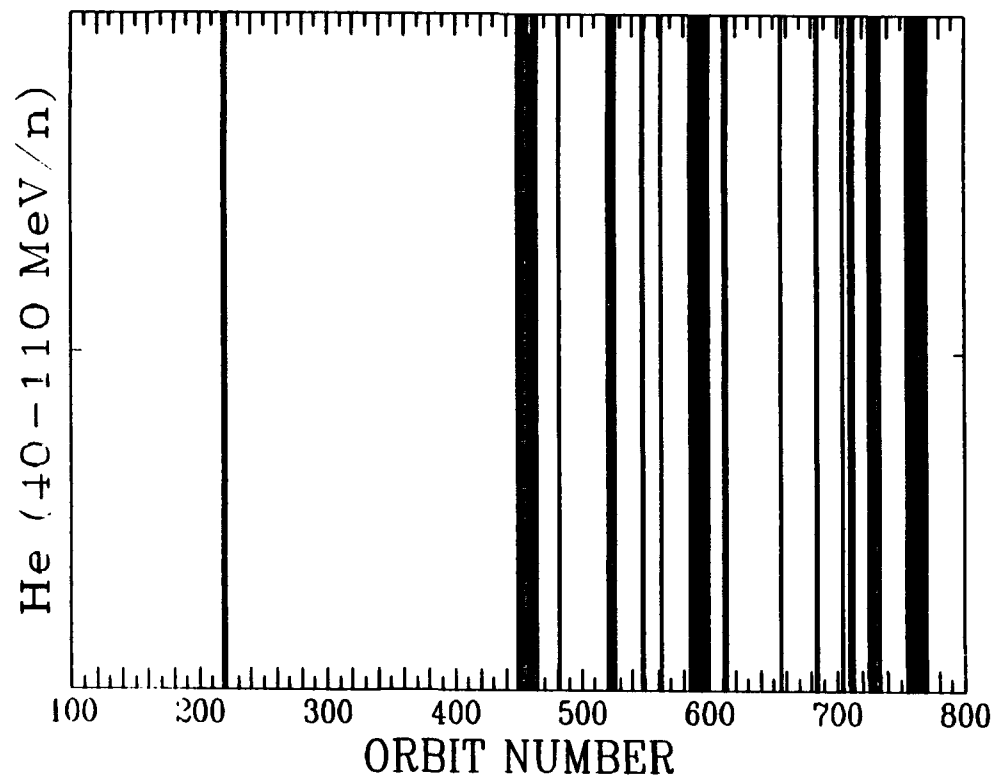


Figure V.17. Quiet-time periods (no shading) determined from the P2 Helium rate (top) and the charge (ZCAL) versus incident energy distribution for the P2 Metal events.

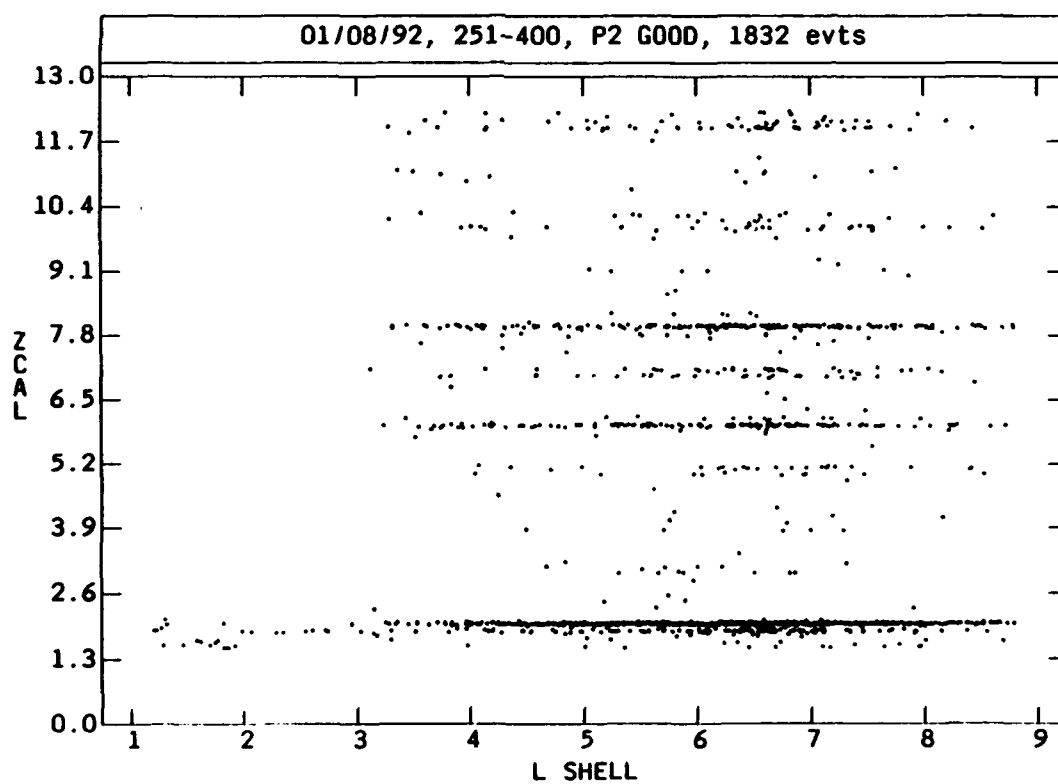
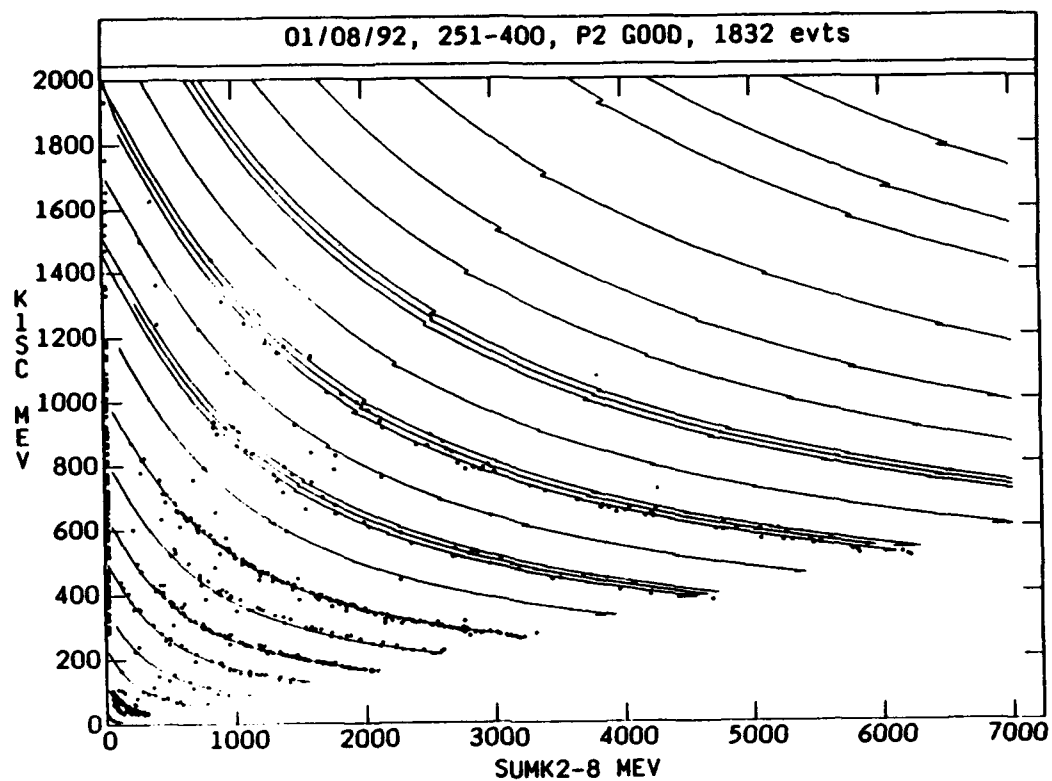


Figure V.18. Comparison of the observations to predicted locations of the different bands in the K1 versus K2-K8 matrix (top) and the L distribution of the different charges (bottom).

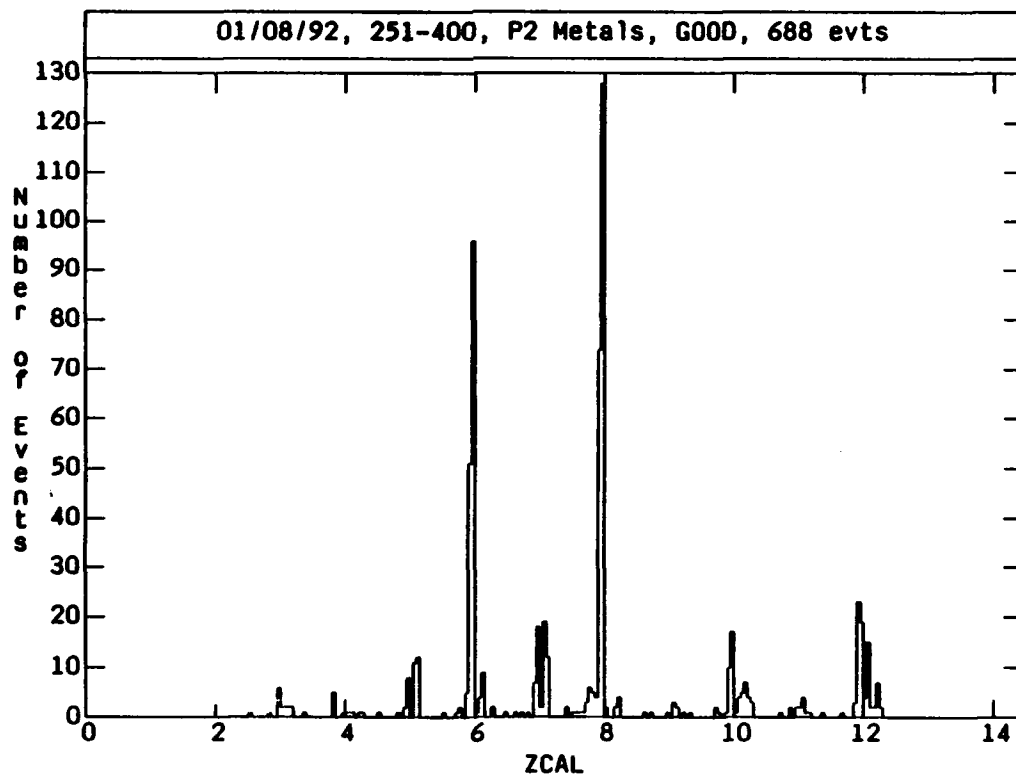
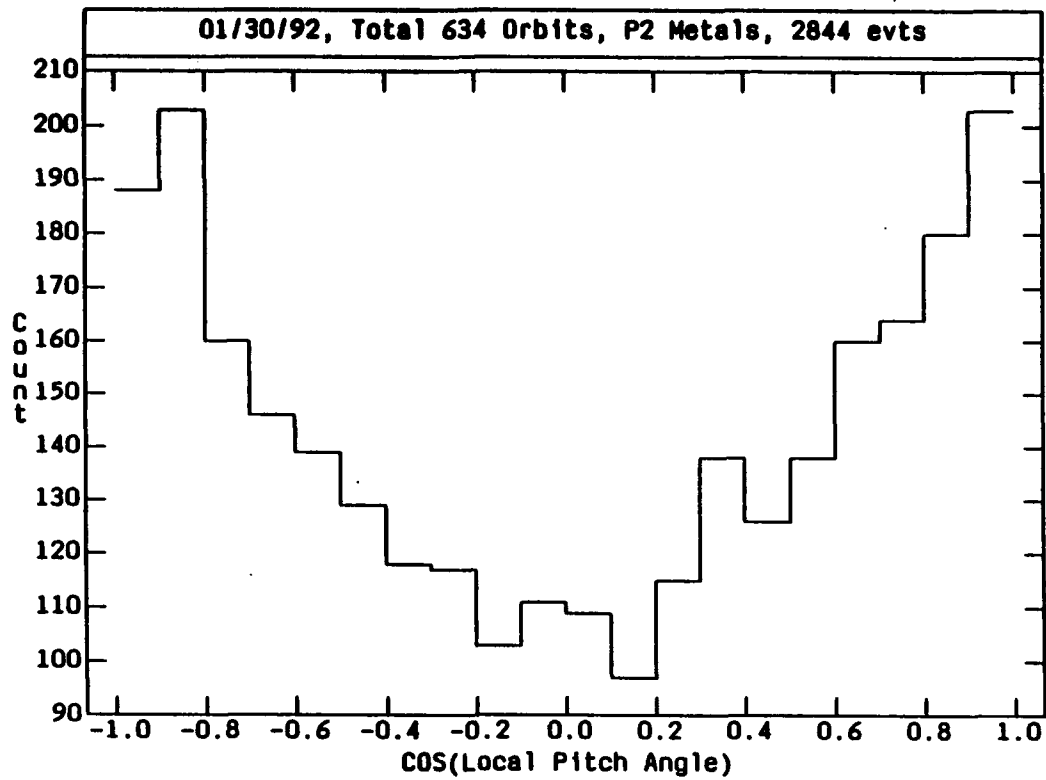


Figure V.19. The distribution of the cosine of the local pitch angle measured for P2 Metal events (top) and the charge histogram for a sample of fully cleaned P2 Metal events (bottom).



251-400. The histograms look remarkably clean and the charge peaks are well centered on the appropriate charge values.

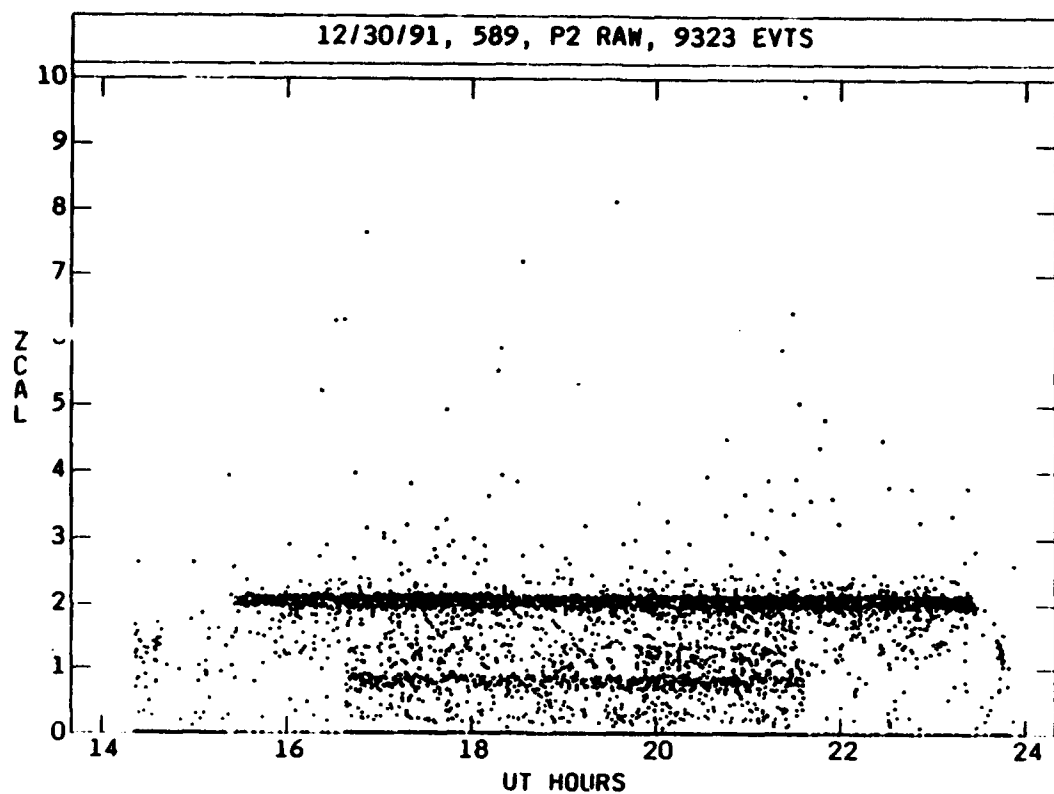
The Helium nuclei are a separate problem. The plot at the bottom of Figure V.18 indicated two distributions. Figure V.20 shows raw data from orbit 589, with the top plot presenting the charge (ZCAL) vs time while the bottom plot shows the K1 versus K2-K8 matrix of events with theoretical predictions for  $^3\text{He}$  and  $^1\text{H}$  shown as the solid lines. The top plot shows a strong helium line, a proton line plus significant events at  $Z=0$ . The problem is that there should be no protons among P2 events. The lower portion of the figure shows that the helium does follow the predicted track location but there is no obvious "track" for protons at the predicted location. The events below the helium track actually show a "smear" increasing in density toward the axes of the plot. Thus, all of these events below helium are proton or electron pile-up triggers.

Figure V.21 (top) shows the time history of the events recorded during orbit 589. Note the large spikes between hours 14-15 and 23-24 corresponding to passes through the inner belts. Comparison with the bottom plot, which shows the range ID distribution of the events, indicates that the inner belt triggers populate both positive and negative (unallowed) ID's. (For good P2 events only  $\text{ID} \geq 7$  meets the trigger logic condition.) Of interest is the number of negative ID's between 16-23 hours corresponding to the apogee portion of the orbit. Here the instrument is commanded into "proton mode" (at ~16.5 hours) which lowers the thresholds on the PSD detectors and allows additional "junk", presumably electrons, to trigger the instrument.

The clean up procedure for helium is again similar to the P2 "metal" procedures. All negative ID's,  $Z < 1.5$  and  $A=1$  events are removed. A stopping detector radius cut and a DE cut are also used. This reduces the 9323 initial events to 2994 events but does remove the inner belt triggers as shown at the top of Figure V.22. The charge histogram for these "Good He" events is shown at the bottom of Figure V.22. The peak is well defined but is not centered at 2.0. Note that there are still some events on the wings of the distribution. If we restrict the data further to  $\text{ID} \geq 8$ , only 617 events survive as shown at the top of Figure V.23. However, this dataset employs only the thick, 5 mm, detectors and, therefore, shows better resolution. Note that it is just possible to see the  $^3\text{He}$  emerging from this distribution, but more events are required to study the helium isotopes.

Finally, the bottom of Figure V.23 shows the L distribution for the "Good He" events. None of the helium here extends below  $L = 2.5$ . This orbit is part of the declining phase of a flare, so that much of the observed helium may be of solar origin. It will be necessary to use quieter periods to measure the galactic cosmic ray  $^3\text{He}/^4\text{He}$  ratio.

There remain the P3 events which contain the proton data as well as whatever is not included in P1 and P2. The P3 events are dominated by low energy events triggering D1D2D3S, (see Table 4.1), for which there is a large solid angle. In addition, the accelerator calibration demonstrated that an electron background (source runs) could cause P3 triggers and such events are evident in the flight data. Performing the background evaluation and "cleaning" the P3 events to obtain a good proton track is one of the tasks remaining in the ONR-604 analysis.



75

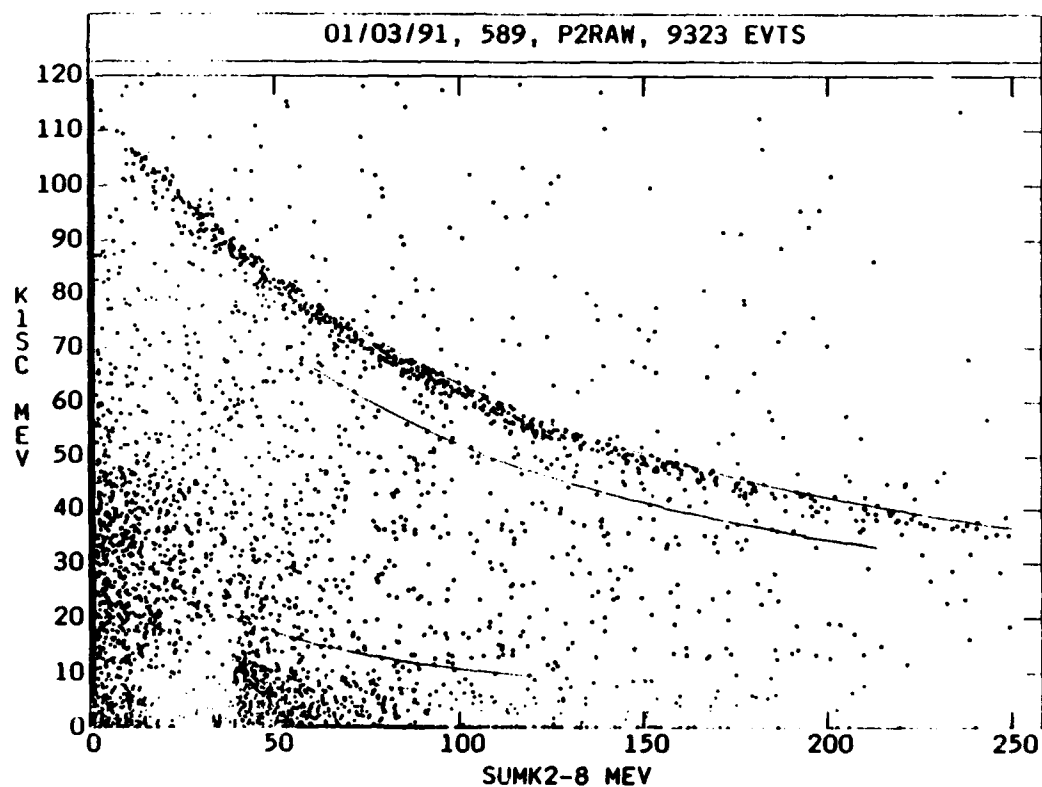


Figure V.20. Raw data from Orbit 589. The top plot shows the first order charge assignment as a function of time during the orbit. The bottom plot shows the K1 versus K2-K8 matrix with the predicted positions of H and He isotopes indicated.

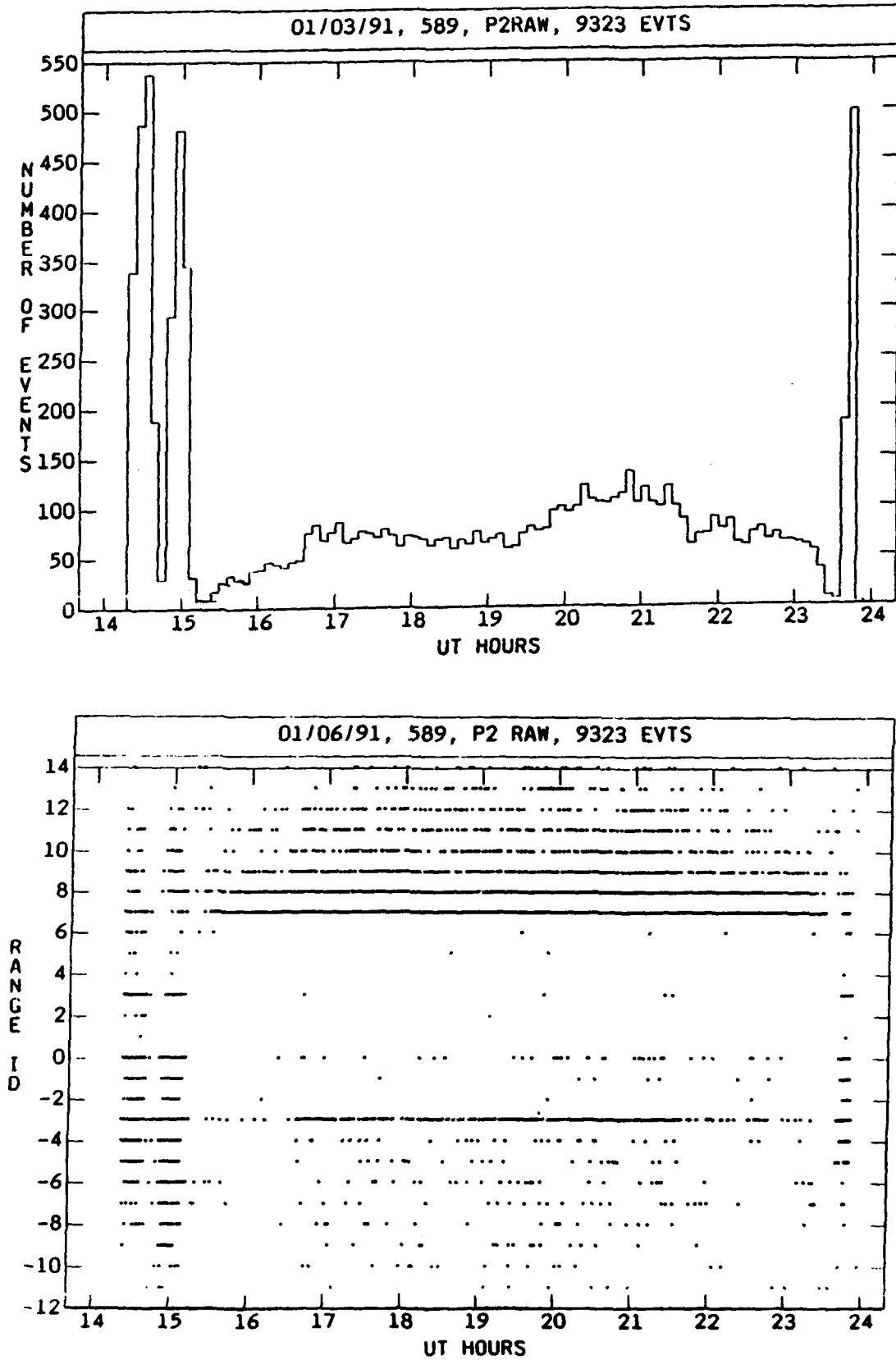


Figure V.21. Time history of the event rate recorded during orbit 589 (top) and the ID distribution of the events as a function of time (bottom).

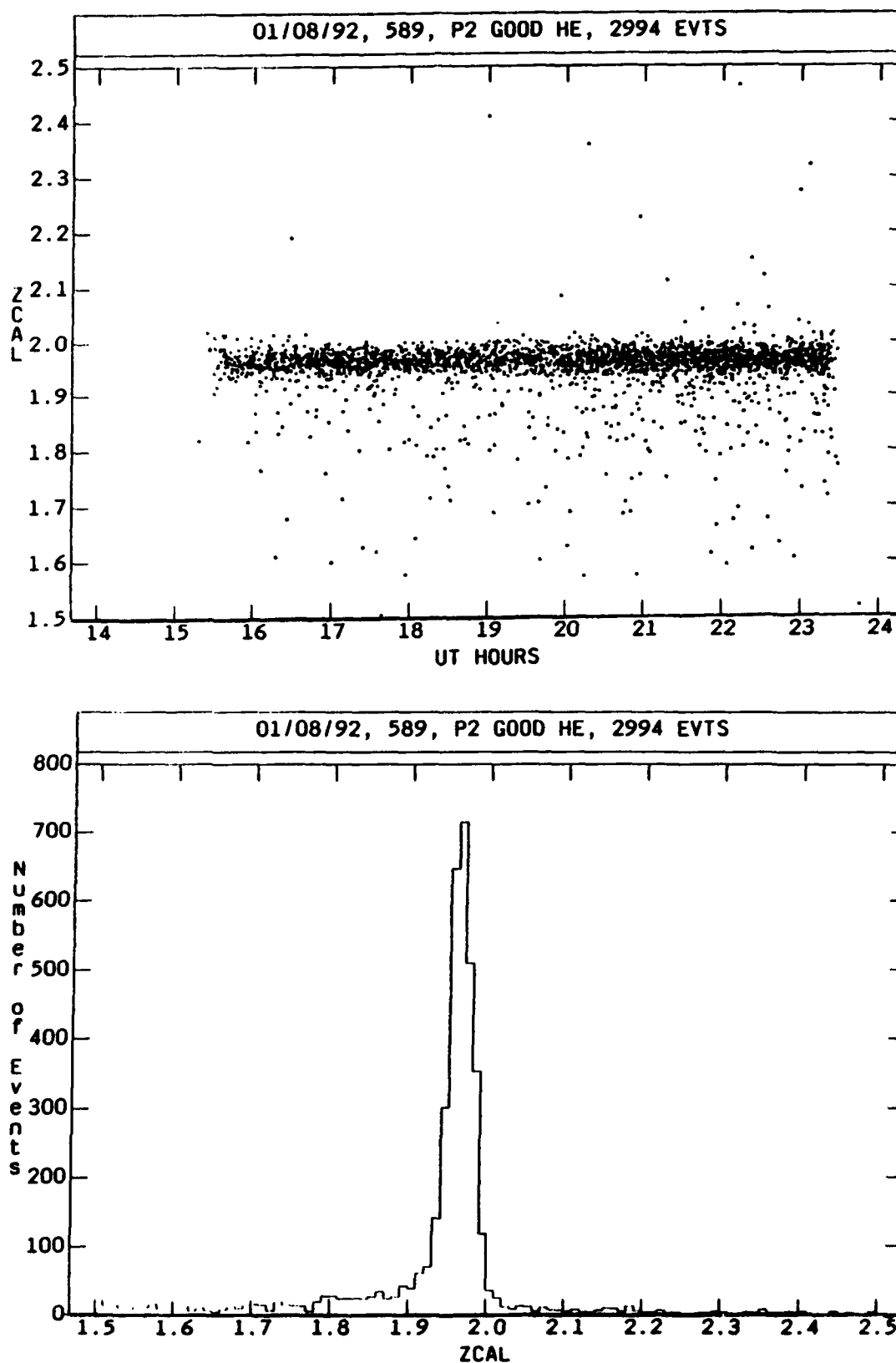


Figure V.22. The resulting "Good He" events showing the final charge values as a function of time (top) and the charge histogram for the events (bottom).

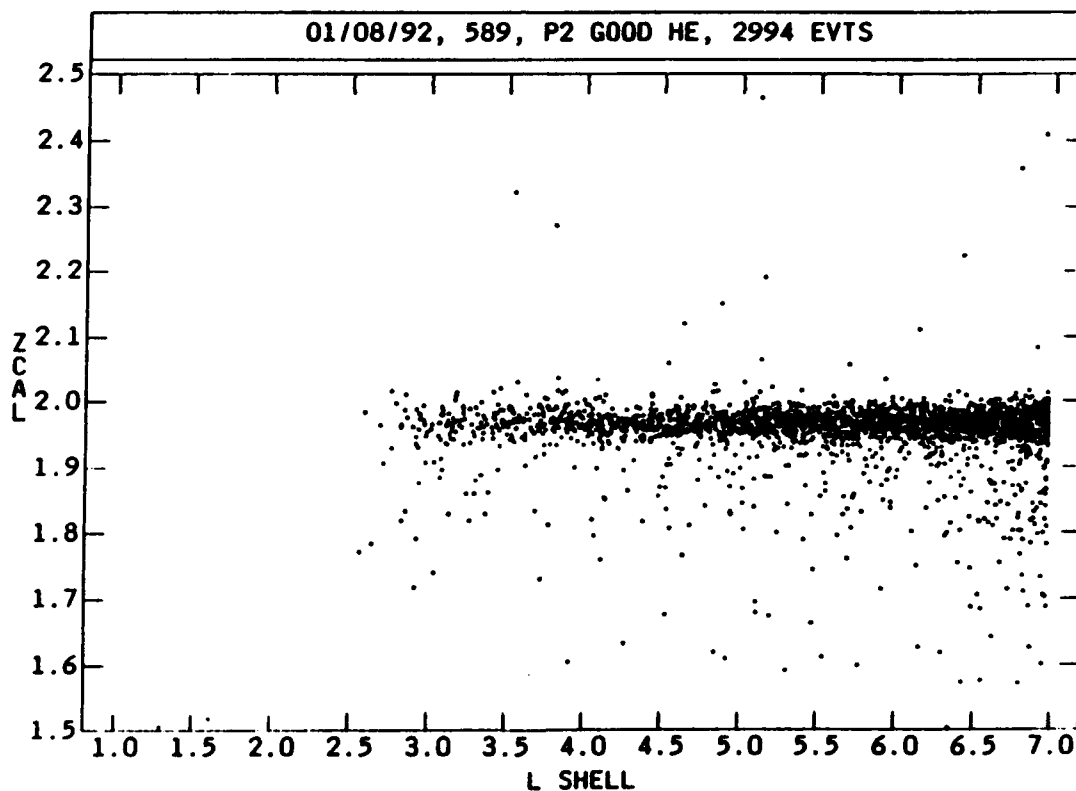
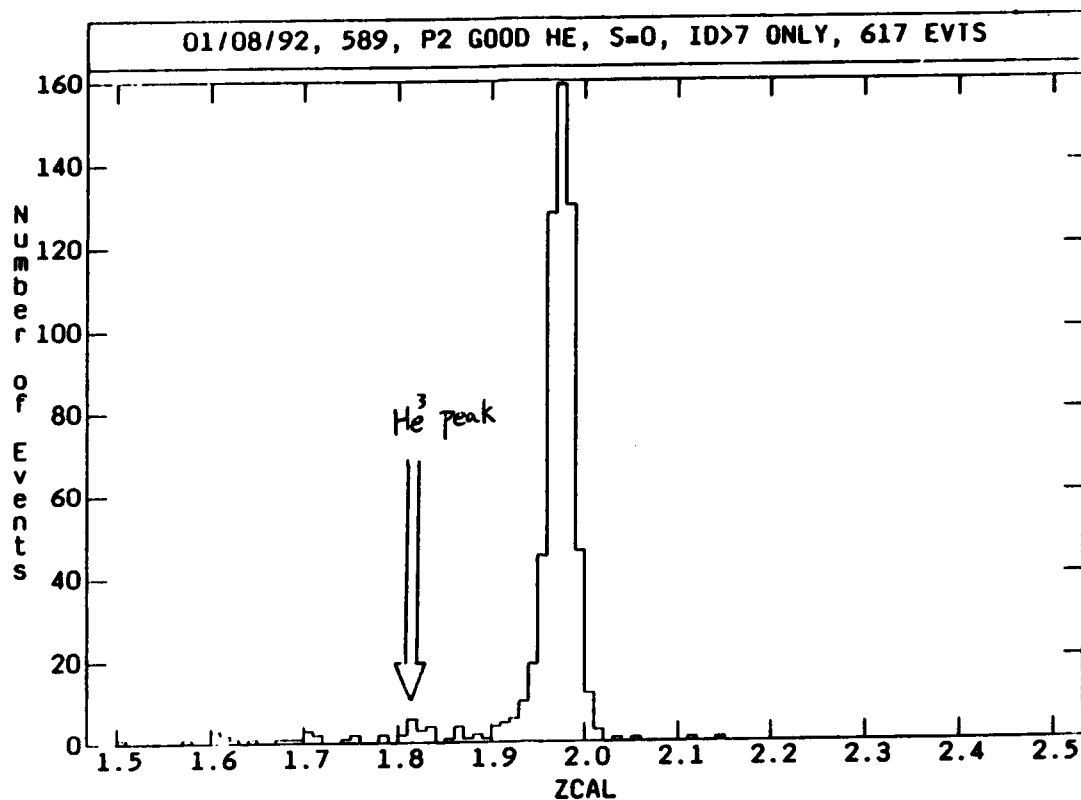


Figure V.23. Charge histogram restricted to ID > 7 (617 events) showing location of the  $^3\text{He}$  peak (top) and the L distribution of the "Good He" events (bottom).

## VI. Summary of Preliminary Results

Along with the data reduction and processing and the software development for ONR-604, we have begun some detailed analyses of the data. We have been working closely with the Chicago group, with John Cooper, now at Hughes STX Corporation assigned to the NSSDC at GSFC, and with David Chennette at the Lockheed Palo Alto Research Laboratory. Below we summarize some of the results to data from the ONR-604 analysis.

### A. March, 1991 Solar Flare

The March 1991 flare period initiated major changes in the Earth's magnetosphere (Blake et al., 1992). We began looking at this period when other CRRES instruments showed interesting behavior, and ONR-604 was asked if they also observed similar effects. The March flare, starting ~orbit 585 (see Figure V.2) produced an increase of ~two orders of magnitude in the P2 rate, but is hardly observable in the P1 data. This indicates that the flare is dominated by helium and  $Z=1$  particles. Figure VI.1 shows the P1, P2 and P3 rates, plus the instrument command state, for 21 March, a quiet orbit preceding the flare. This is to be contrasted with Figure VI.2 which shows a similar plot for 23 March (orbit 587). Note the P3 rate at apogee is saturated. Similar effects are seen in the ONR-604 singles rates (Figure VI.3) and in the coincidence counting rates (Figures VI.4, VI.5 and VI.6). Note the step in the P3 rate in Figure VI.2 when the instrument transitions to "proton mode." A similar step is observed in some of the singles rates and in the D4-A coincidence rates, all of which are 2-3 minute averages. The singles rates also show a modulation effect, probably due to the spacecraft spin rate, but this has not been confirmed. The scintillator, S, rate in Figure VI.3 saturates at just below  $10^5$  counts per second, about the maximum that the electronics should be able to count.

The basic readout period for many of the rates is 4.096 seconds (S is 65 seconds) so that considerably higher time resolution is possible. We can follow the progress of the flare in considerable detail. Figure VI.7 shows the expanded (high time resolution) plot of the P1, P2, P3 and S (scintillator) counting rates. The flare onset, during perigee of orbit 584 is observed, we believe, through the flare gamma rays that triggered the scintillator, as indicated by the arrow. Fortunately, the satellite was near perigee so that the signature is not hidden by the inner belt counting rates. This gamma ray spike is coincidental with the x-ray arrival at GOES, so that we have a "start" time marker in the data. The charged particles begin to arrive during orbit 585 increasing the raw counting rates. At orbits 587-588 we observe something interesting. On the in-bound pass (Figure VI.8) a "spike" is observed at ~0345 on 24 March. Following perigee on the outbound pass (Figure VI.9) this "spike" has broadened to a "hump" whose intensity in P3 is at the same level as the inner belt. This may be the result of the solar flare blast wave hitting and compressing the Earth's magnetosphere and forming a new "pseudo-belt" in what is nominally the slot region. Note that the "modulation" in the rates for this new belt is significantly greater than for the inner belt, suggesting that these particles are highly anisotropic in either time or space.

ONR-604 is in heavy ion mode at these times. Thus, P3 is not sensitive to protons, but will record either multiple-particle pile-up events or very low energy helium. The P2 rate also sees the "spike" and the "hump" albeit at reduced intensity. P2 is sensitive to helium and heavier particles. Thus, it is possible that ONR-604 is observing helium nuclei injected by the blast wave into the inner magnetosphere. On-the-other-hand, P2 shows a larger signal in the inner belt, which we suspect is due to electron/proton pile-up in the detectors. This new "hump" may very well be the same type of pile-up event.

To investigate this possibility further, we have focused upon the spike region, orbit 587, 0319-0359 in Figure VI.8. Figure VI.10 (top) shows the ID distribution for all of the events that were pulse height analyzed during the interval. Negative ID's indicate an illegal bit pattern and are not

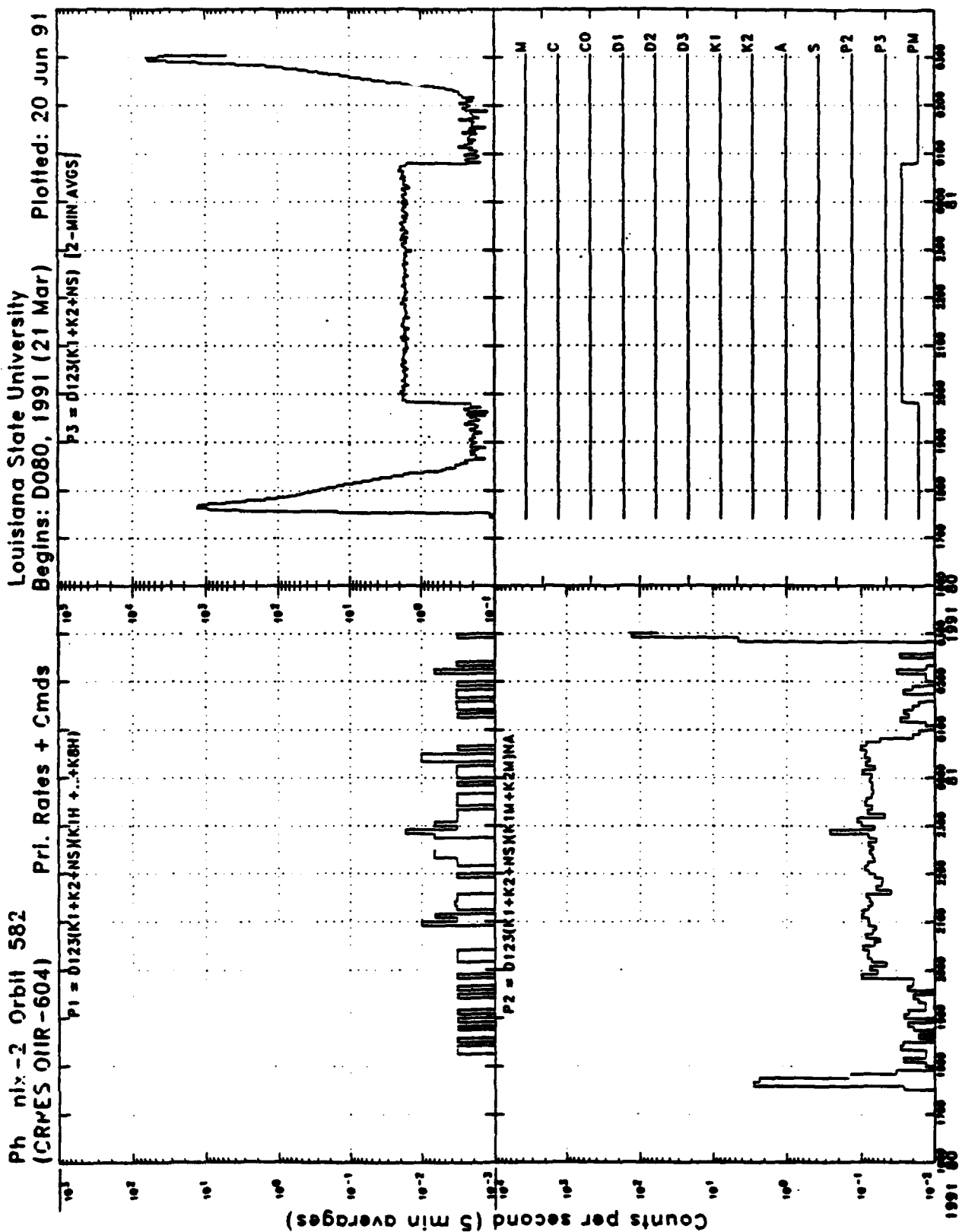
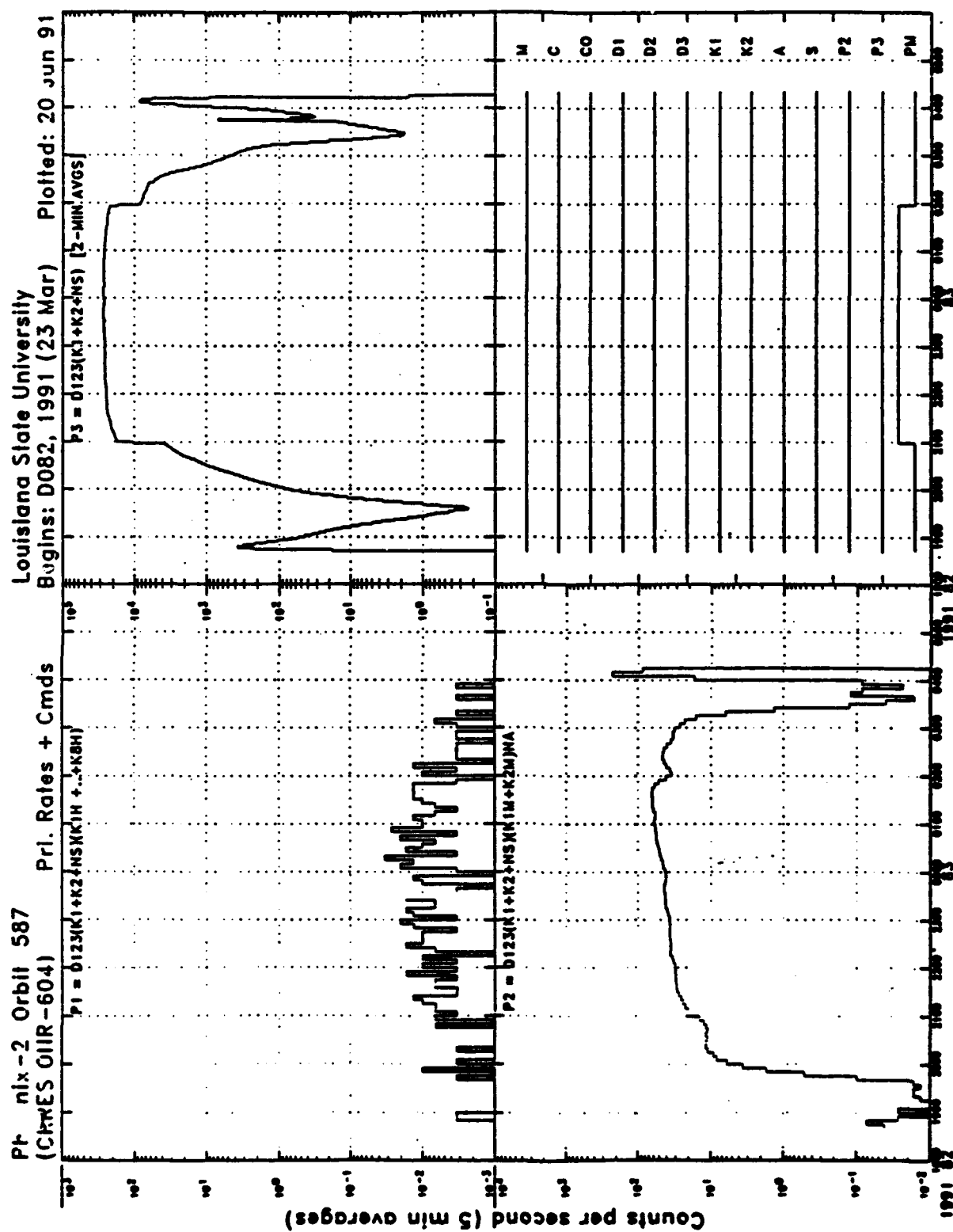


Figure VI.1. P1, P2, P3 and instrument command state for a "quiet" orbit (582) preceding the March flare.



**Figure VI.2** Same as Figure VI.1 except for orbit 587 during the March flare.



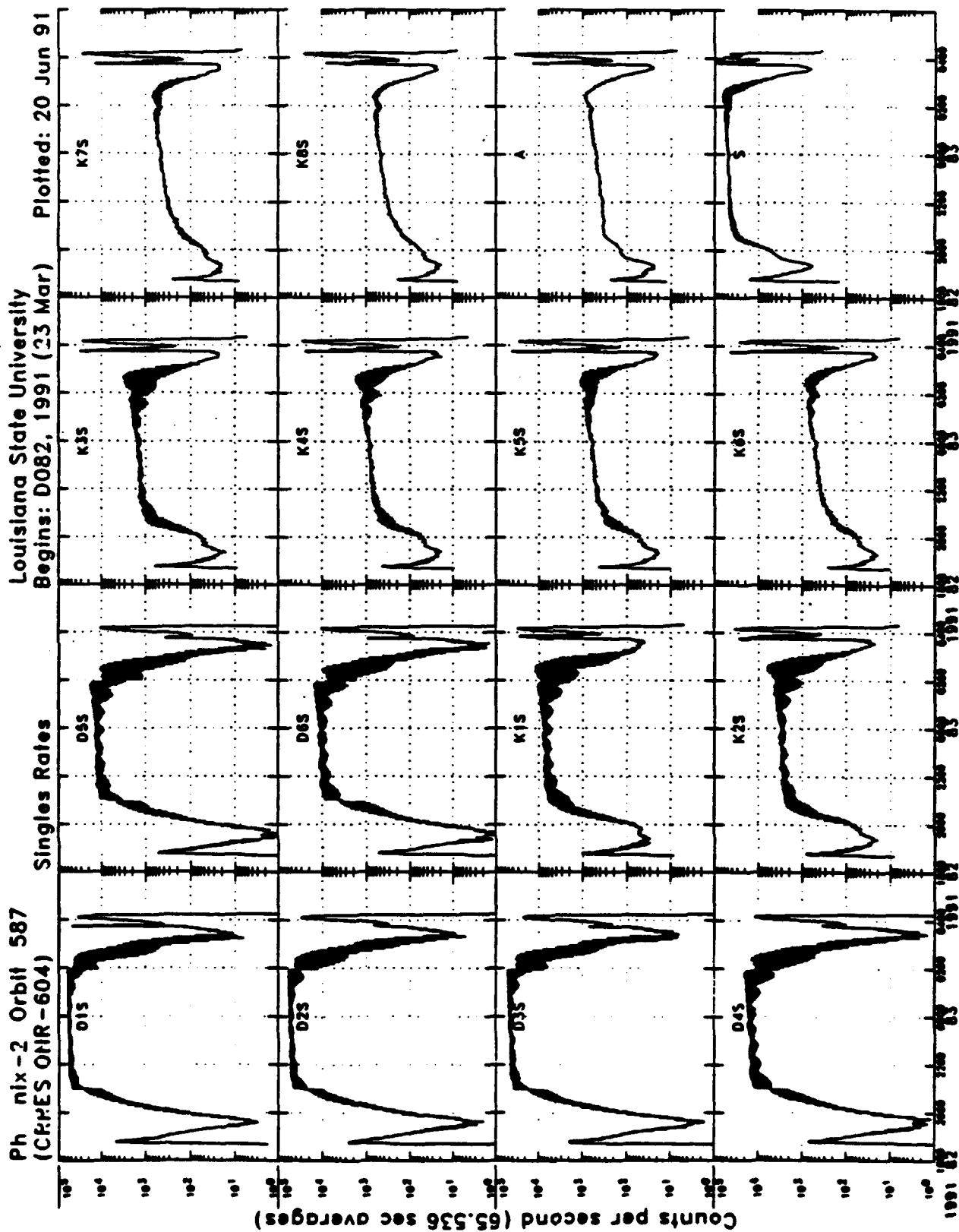


Figure VI.3. ONR-604 singles counting rates for orbit 587.

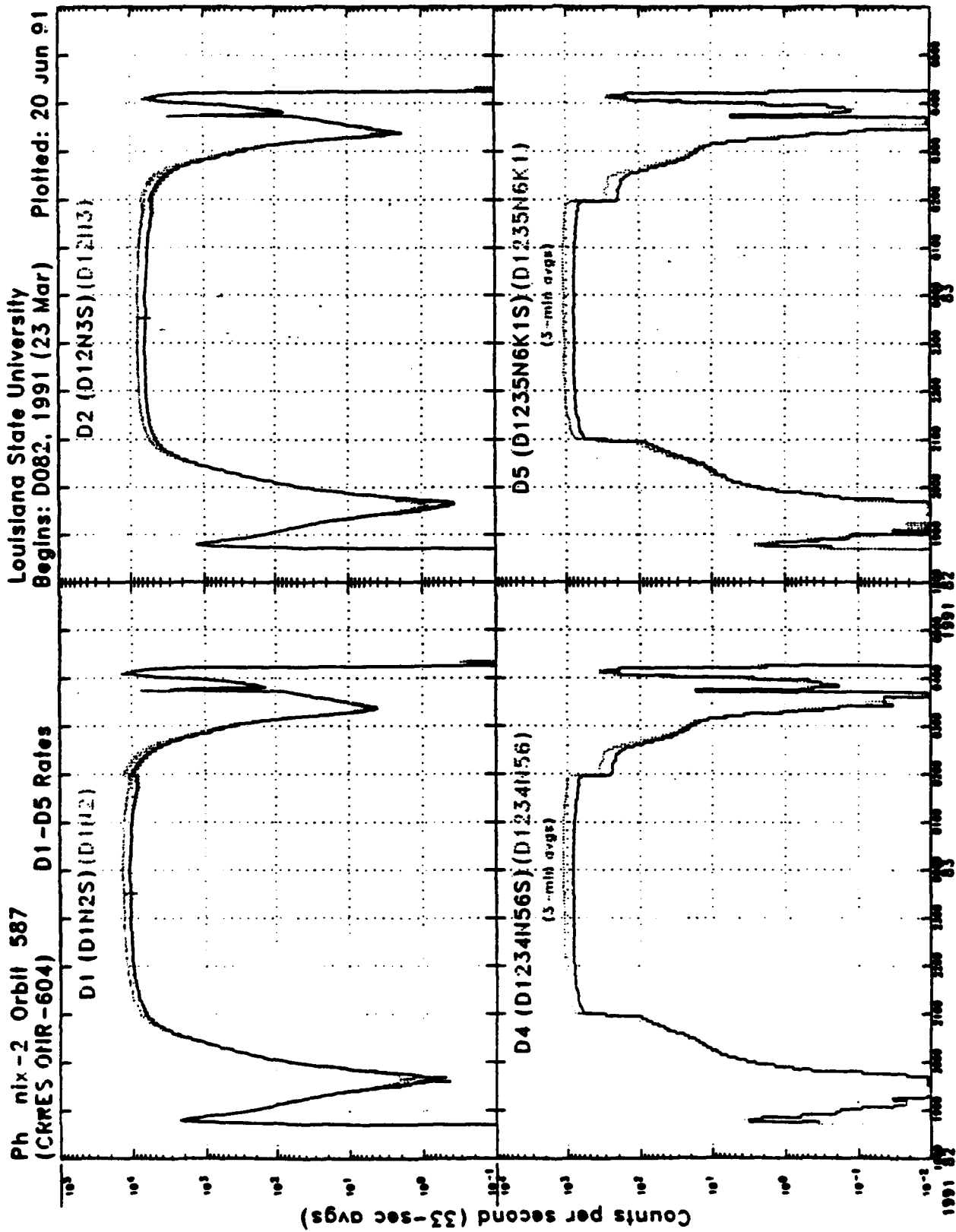


Figure VI.4 ONR-604 coincidence counting rates D1-D5 for orbit 587.

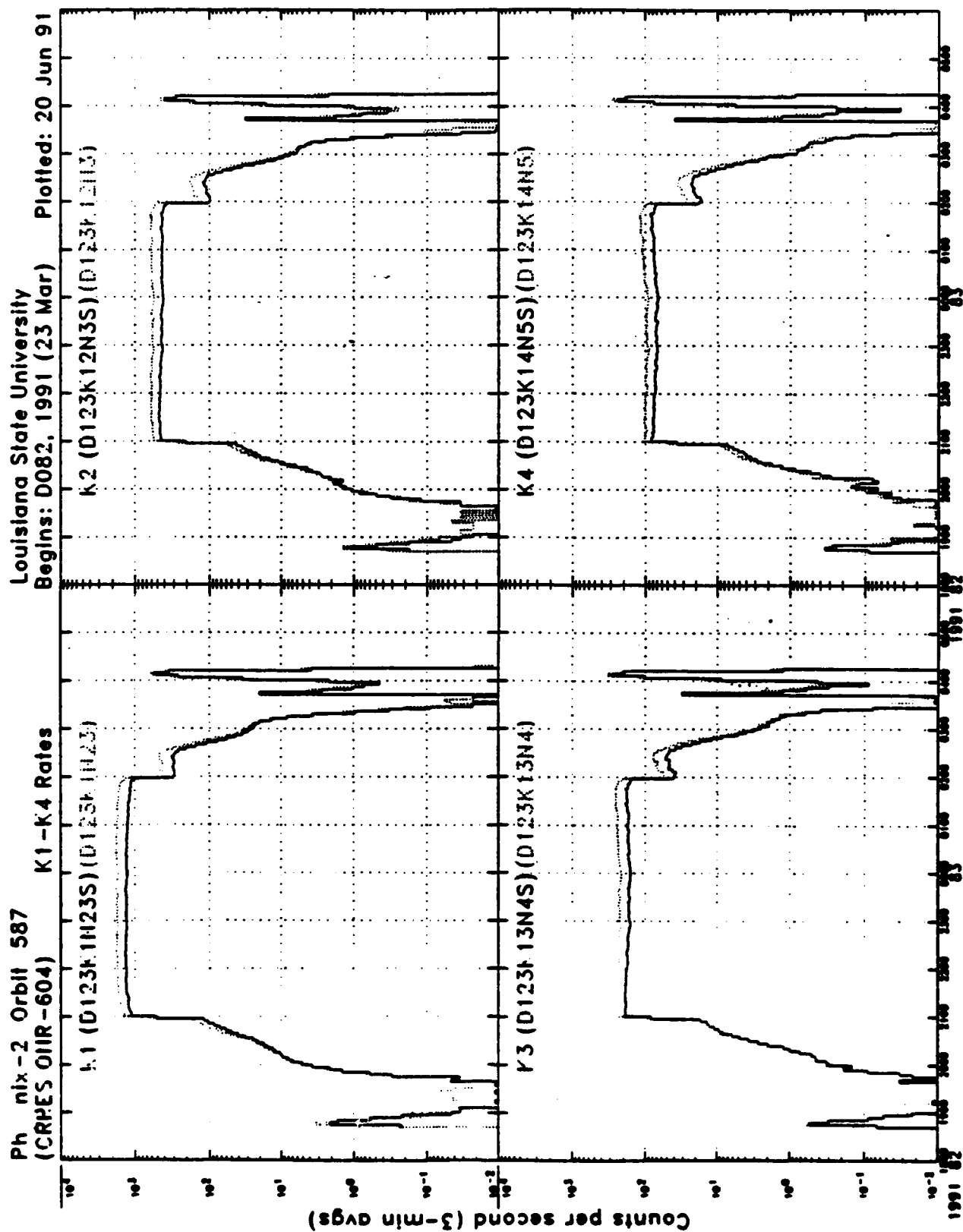


Figure VI.5. ONR-604 coincidence counting rates K1-K4 for orbit 587.

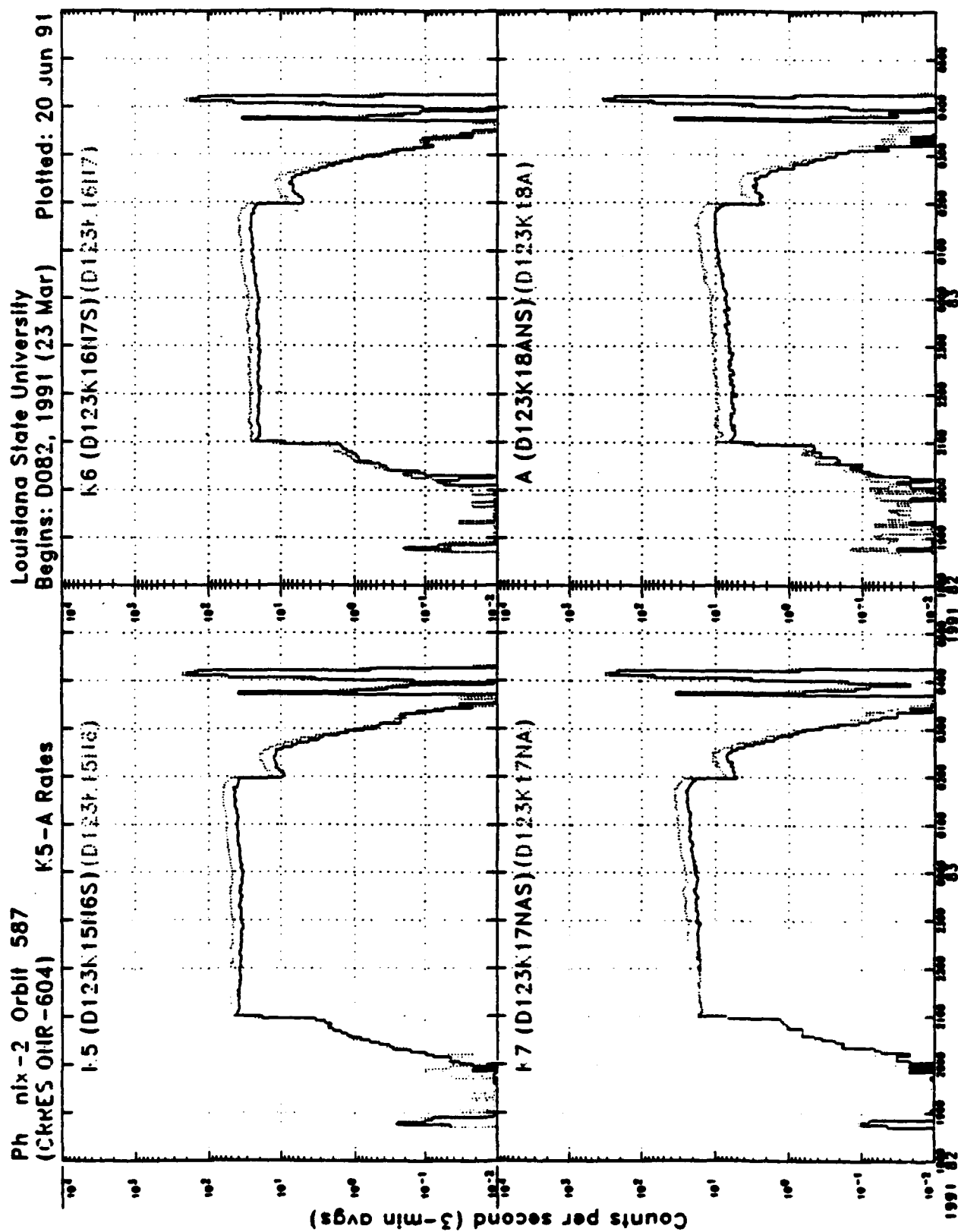


Figure VI.6 ONR-604 Coincidence counting rates K5-A for orbit 587.

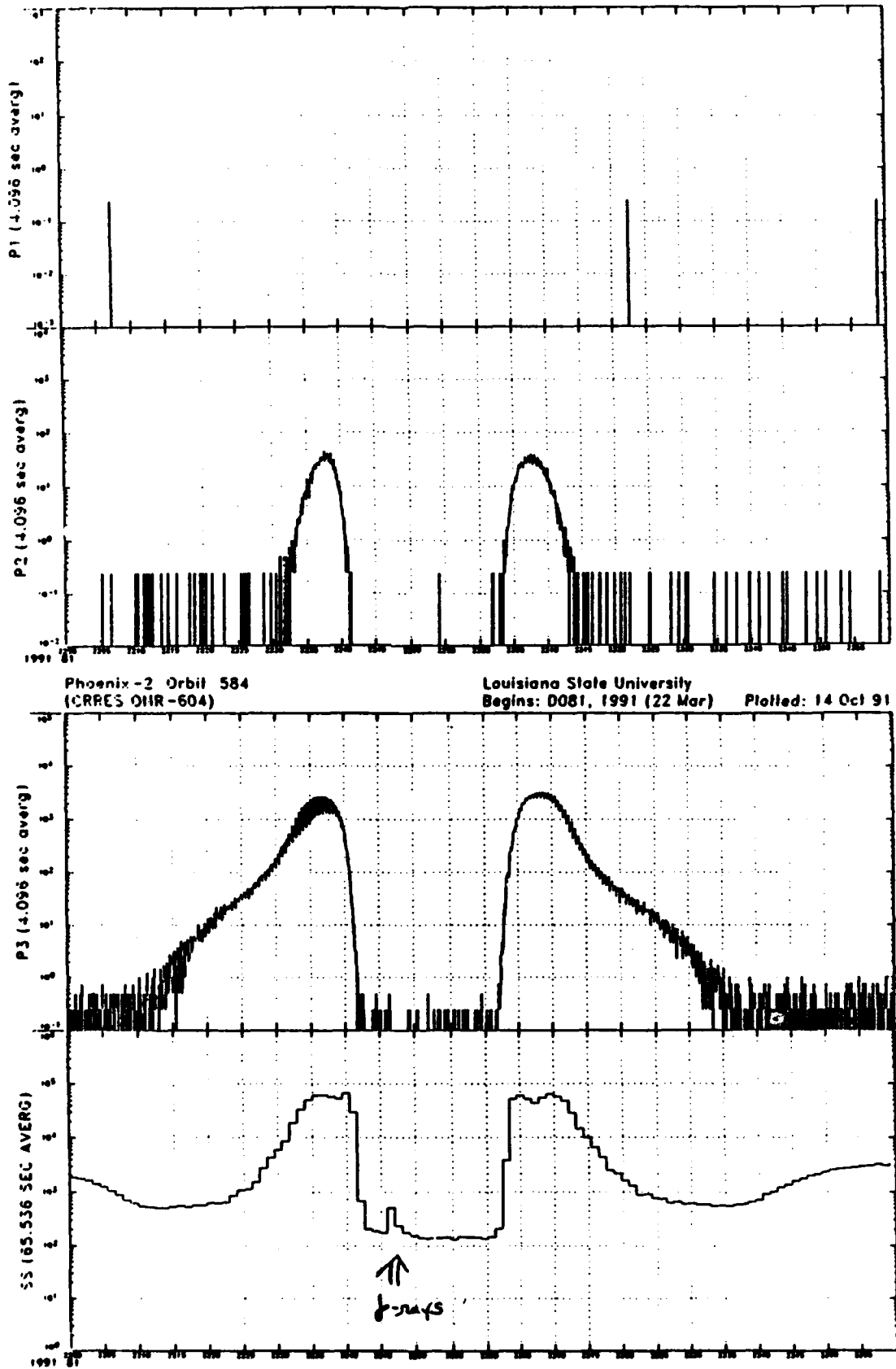
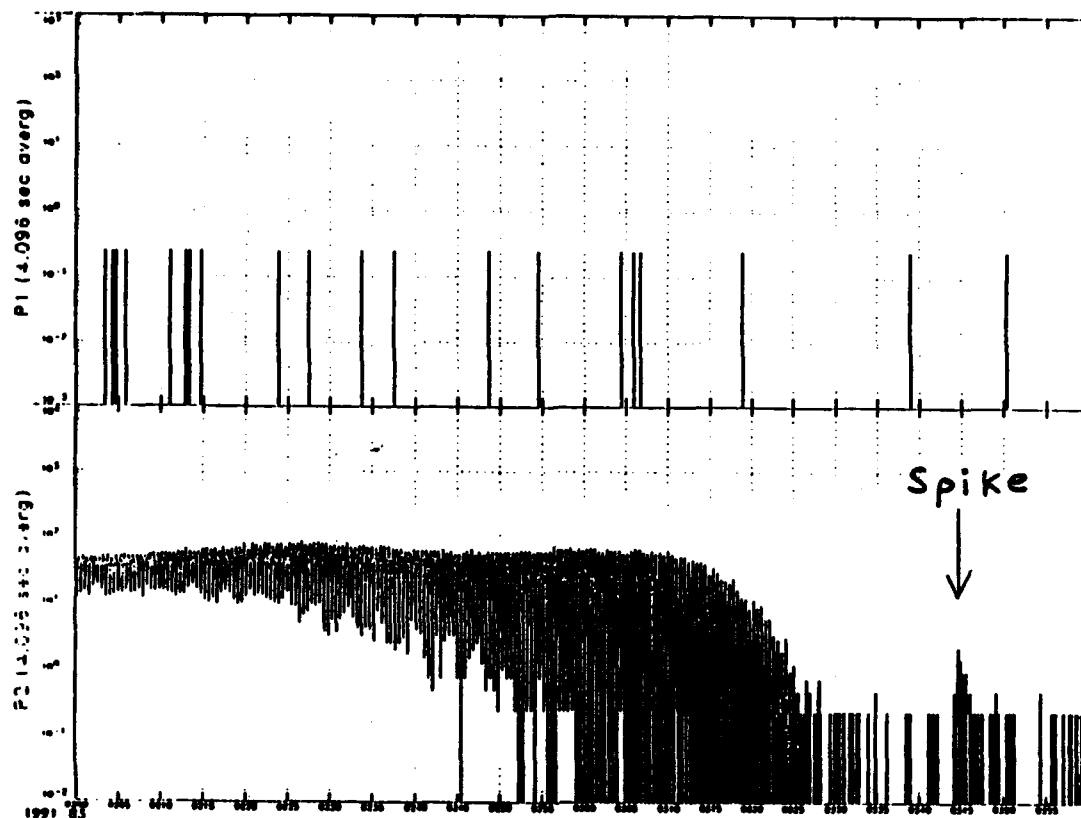


Figure VI.7 P1, P2, P3 at SS rates shown at maximum time resolution for orbit 584 indicating the onset of the flare.



Phoenix-2 Orbit 587  
(CRRES ONR-604)

Louisiana State University  
Begins: D083, 1991 (24 Mar) Plotted: 14 Oct 91

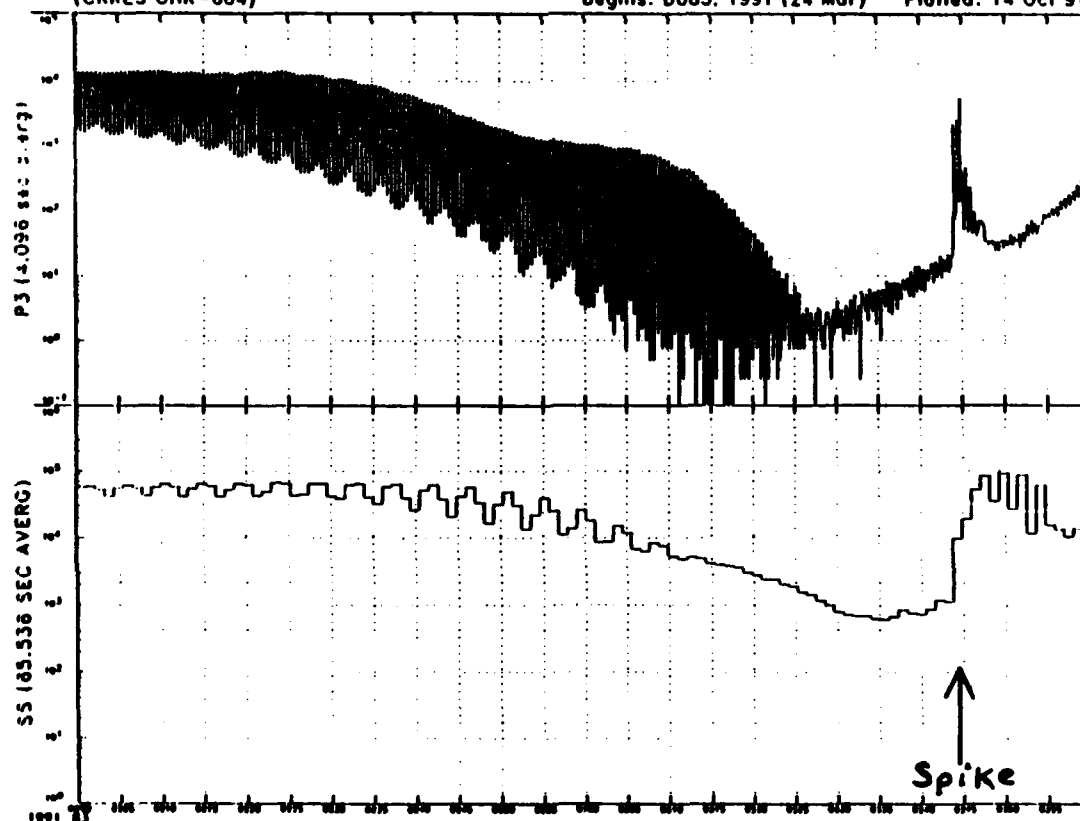


Figure VI.8 Same rates as Figure VI.7 except for orbit 587 just before perigee.

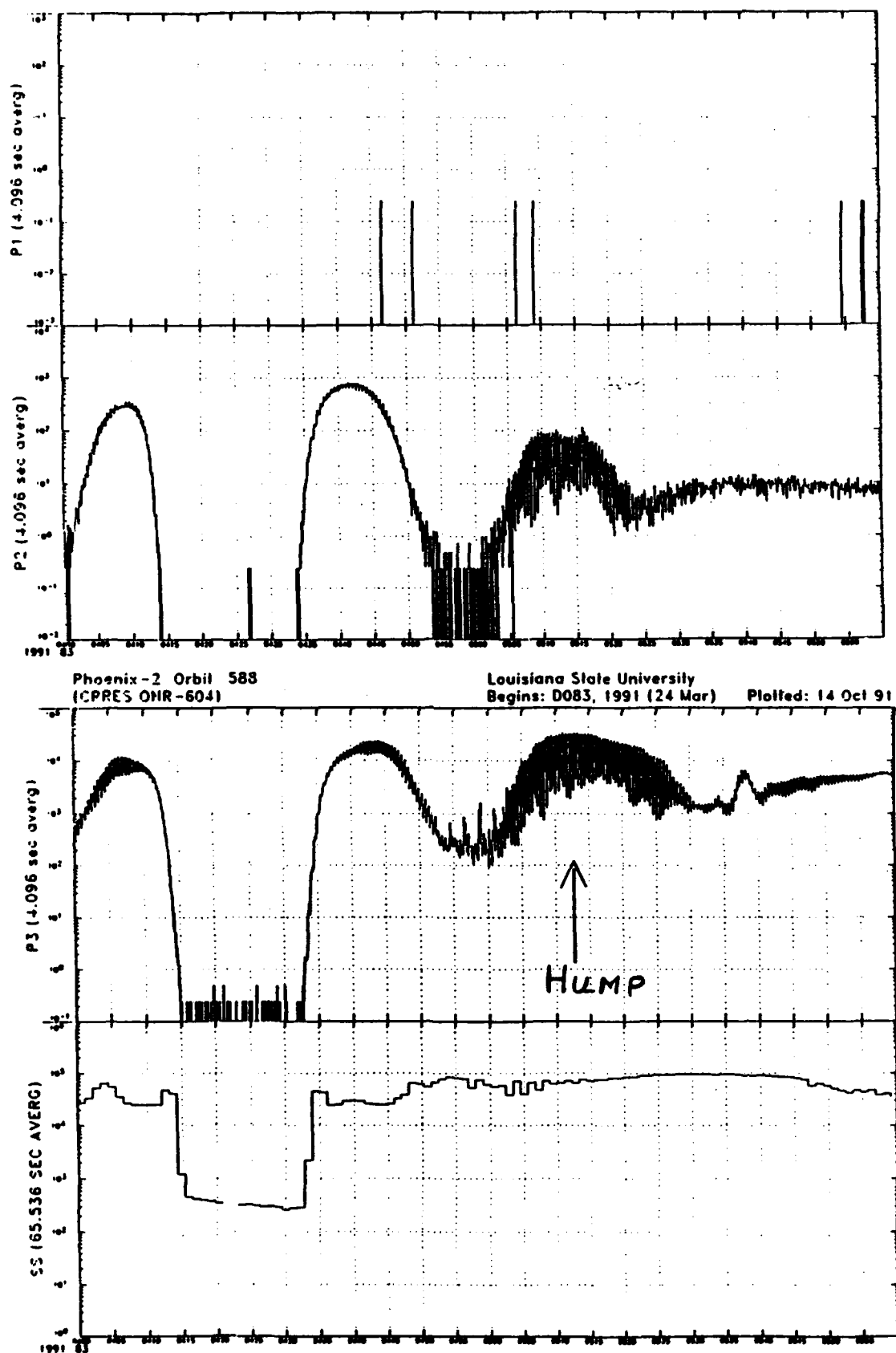


Figure VI.9 Same rates as Figure VI.7 except for orbit 587 just after perigee.

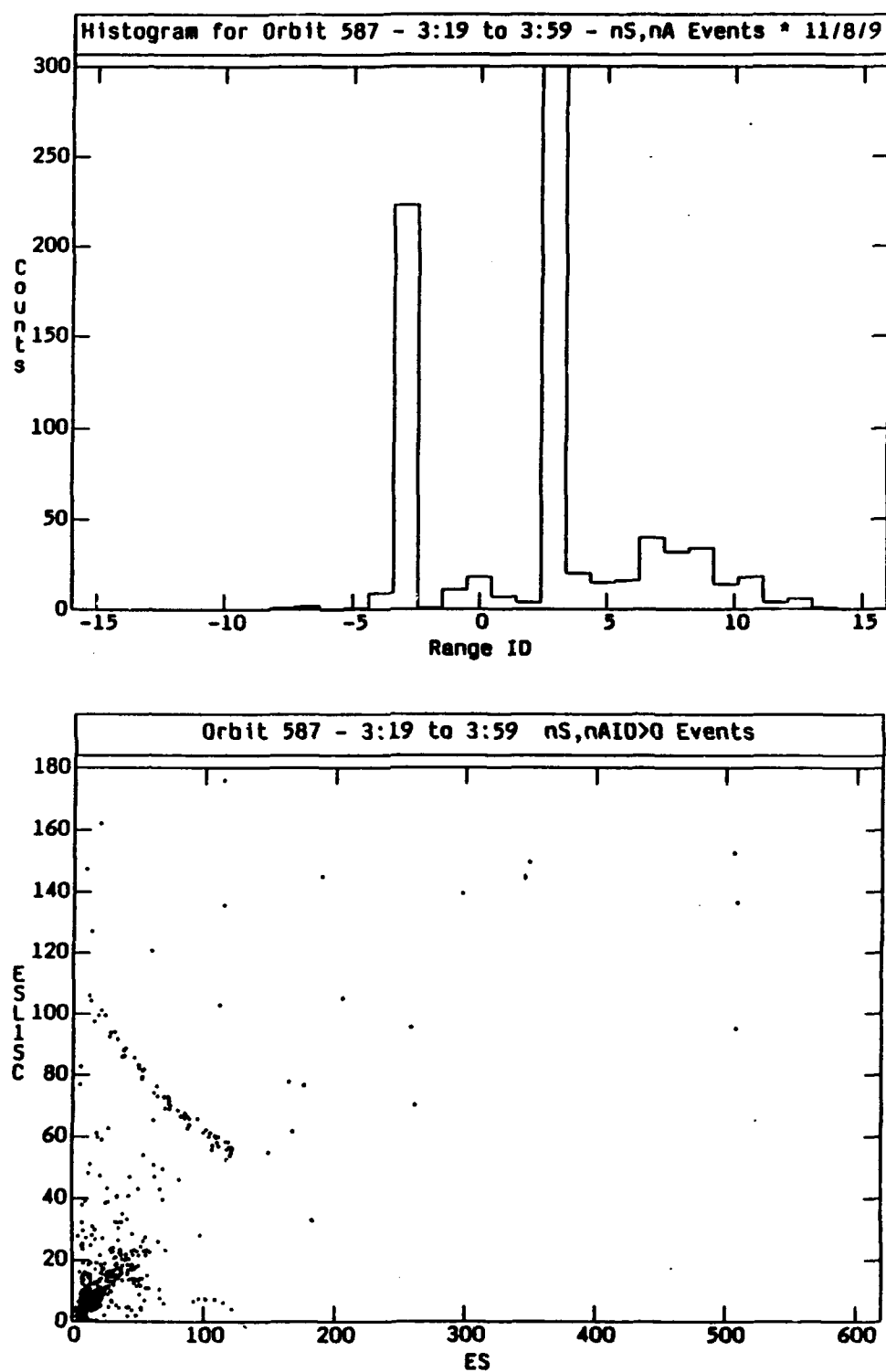


Figure VI.10 The range ID distribution (top) for events pulse height analyzed in the interval of the "spike" in Figure VI.8. The matrix of energy deposits in the stopping detector versus the preceding detector for the set of events with ID > 0 (bottom).



considered further. Most of the events are ID=3 which corresponds to  $D1 \cdot D2 \cdot D3 \cdot \overline{D4}$ , and requests a large solid angle. (P2 events should not normally be ID=3 events.) The ID's >6 correspond to particles penetrating into the stack of 5 mm thick detectors which constitute valid P2 events. Figure VI.10 (bottom) shows the result of plotting the signal in the last fired detector (ES) versus the signal in the preceding detector (ESL1SC). All of the ID=3 events are located in the black blob near the origin which corresponds to Z=1 pile-up events, as expected.

There is, however, a "track" in Figure VI.10 (bottom) extending from just above 100 on the y-axis to just above 100 on the x-axis. Eliminating the ID >7 events and expanding this plot yields Figure VI.11. Here the events for which P2 was triggered are circled, and most of the "track" is found to be P2 events. This track is located approximately where helium should be (from the pre-launch calibration data). Thus, we believe that some of the events are valid helium nuclei.

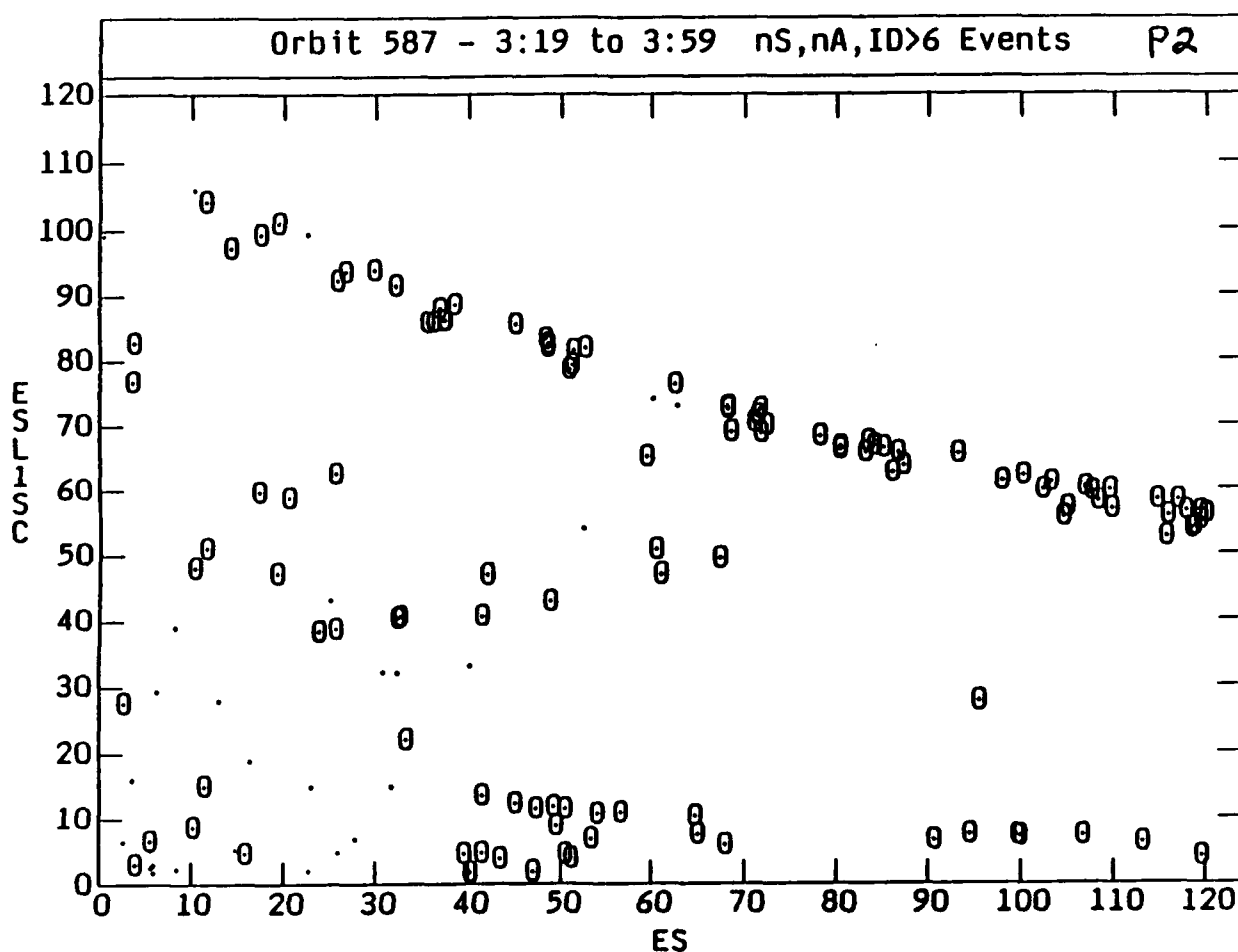


Figure VI.11. Pulse height analyzed events from the "spike" region. P2 events are circled. The track is at the expected location for helium in P2.

An alternate approach is to compare flare and non-flare time periods. This is done in Figure VI.12 where the ID distribution is shown for orbits 551-555, a pre-flare period, orbits 586-590, encompassing the flare and orbit 588 restricted only to the "slot" region. The top plot represents the expected ID (=Range) distribution for a galactic-cosmic ray spectrum while the center plot indicates a much steeper energy spectrum. The "slot" region shows a distribution closer to the steep flare spectrum. This distribution is most consistent with a low energy dominated population, and not with galactic cosmic rays. However, these particles could be either solar flare or pre-existing "trapped" helium nuclei.

This, however, does not answer the question about the composition of the spike seen in the P2 and P3 rates at ~0345 on 24 March 1991 during orbit 587. For all pulse-height analyzed events between 0319 and 0359 in orbit 587, Figure VI.13 shows a plot of the signal in the detector preceding the stopping detector as a function of time for both ID > 0 (top) and ID > 6 events (bottom). From the helium calibration and the helium observed at  $L > 6$ , valid helium events in ID  $\geq 7$  should have ESL1SC values between ~55 and 120, and such events are evident in the Figure. (Note that most of the events show very small signals, consistent with proton/electron pile-up triggering the pulse height analysis.) If we focus only on the higher energy events, those penetrating to the thick solid state detectors (K1, K2,...), as shown in the lower plot, the helium-like events are still present.

The interesting observation is that these helium-like events occur mainly between 0320 and 0330, not at 0345 which is the location of the counting rate spike! The period 0320-0330 corresponds to the outer edge of the inner belt during orbit 587. This would suggest that these events are "trapped" or "quasi-trapped" particles and are not necessarily associated with the flare population which is "flooding" the magnetosphere at higher L shells. If this conjecture is true, then we expect that such a "trapped" component should be present during non-flare periods. To prove this, it is necessary to look at a long quiet period of time.

### B. Quiet-time Helium

The helium nuclei can be used as tracers of the heavy ion component. Thus, understanding the behavior of the helium is an important first step in the overall analysis. From the P2 helium plot (Figure V.2), quiet times were selected. These are indicated in Figure VI.14 (top) as the missing orbits. Note that there is an interesting band of measured events at  $L=2$  in this plot. Another measure of "quiet" is the state of the geomagnetic field. This is indicated in the lower part of Figure VI.14 as a histogram of  $K_p$  values. For the full time interval, the average  $K_p$  was about 3 with few periods at the highly disturbed ( $K_p \geq 5$ ) level. A total of 800 orbits is included in the analysis involving ~8800 good helium events (after clean-up, as described in the previous section).

Figure VI.15 shows the L distribution of the helium events at the top. The peak at  $L \sim 2$  is evident along with a hint of another peak at  $L \sim 1.3$ . If the quiet-time helium sample is actually from galactic cosmic rays, then the  $^3\text{He}/^4\text{He}$  ratio near apogee should be the well-known GCR value. This test is performed in the lower part of Figure VI.15 which shows the mass histogram for the helium events recorded at  $L > 6$ . There is good isotope separation, and a ratio of  $^3\text{He}/^4\text{He} = 0.105 \pm 0.005$  is obtained, in good agreement with previously published values for the cosmic rays.

For the remainder of this analysis, we focus only on the  $^4\text{He}$ . The L versus incident energy distribution of the helium events is shown in figure VI.16 (top) and is converted to a relative energy spectrum for different L regions in the lower part of the figure. The important point here is the comparison between low-L and high-L events. At high-L, the particles cover the full energy range for helium, but the low-L events are confined to the lowest energies. Converting to a relative (not normalized) flux indicates that the low-L component has a very steep spectrum compared to the

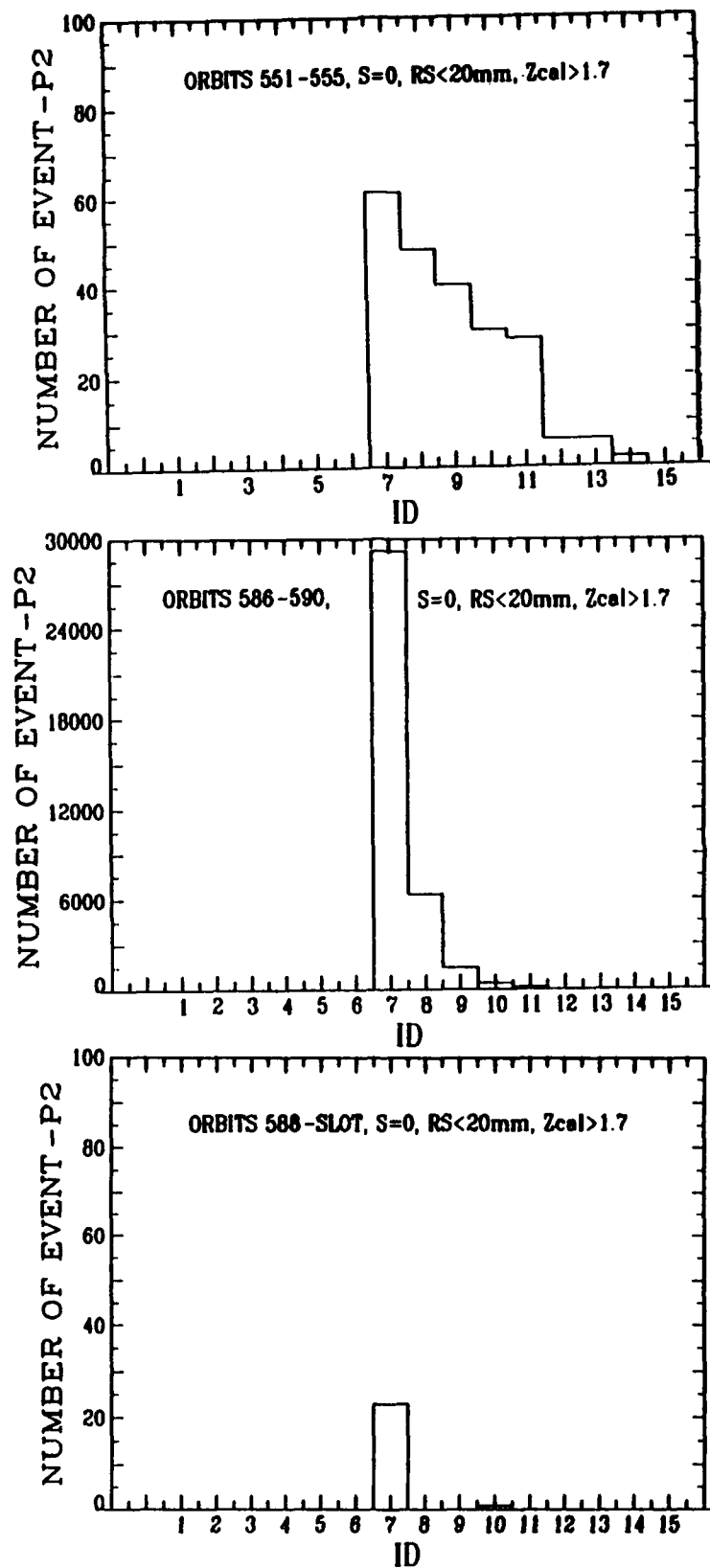


Figure VI.12. ID distributions for Helium events from (top) orbits 551-555, a quiet period, (middle) orbits 586-590, during the March flare, and (bottom) orbit 588 restricted to the "slot" region.

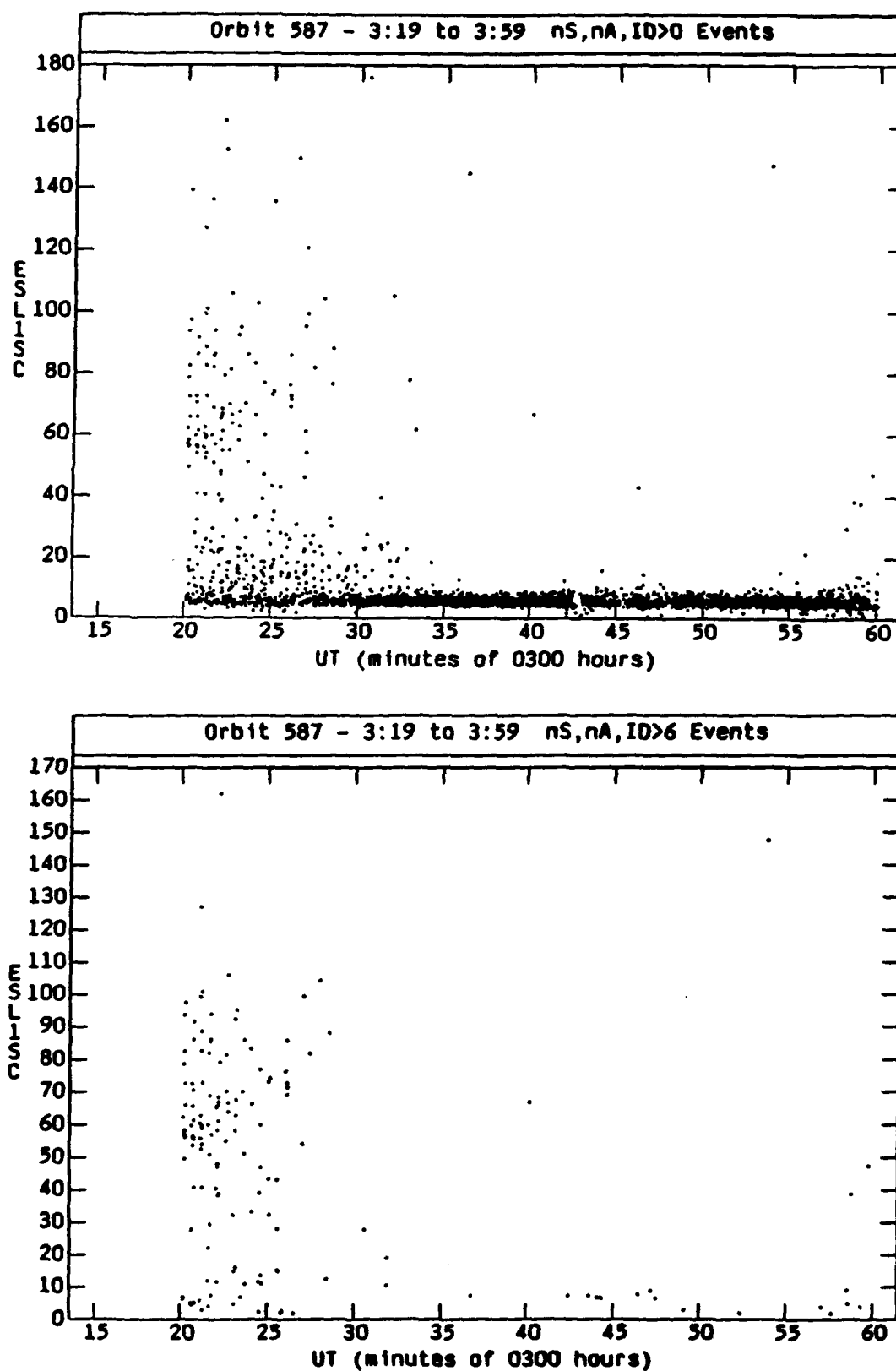


Figure VI.13. Pulse-height analyzed P2 events from 0320-0359 of 24 March during the flare. Plotted is the energy in the detector before the stopping detector versus time. The top plot is for all positive ID's while the bottom is restricted to ID>6.

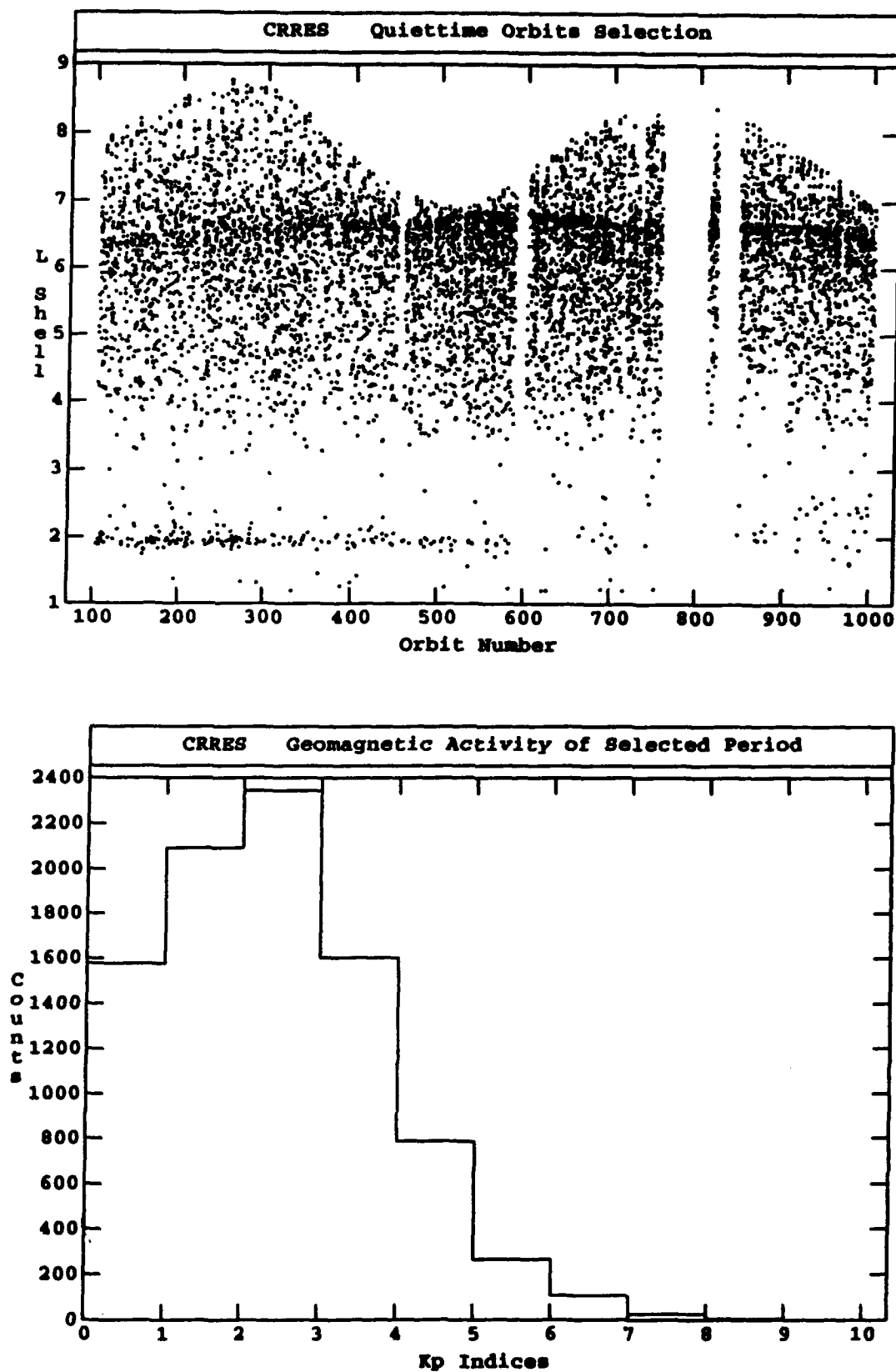


Figure VI.14. L shell versus orbit plot (top) for the events selected for quiet-time analysis. Histogram of reported  $K_p$  values (bottom) for the selected time interval.

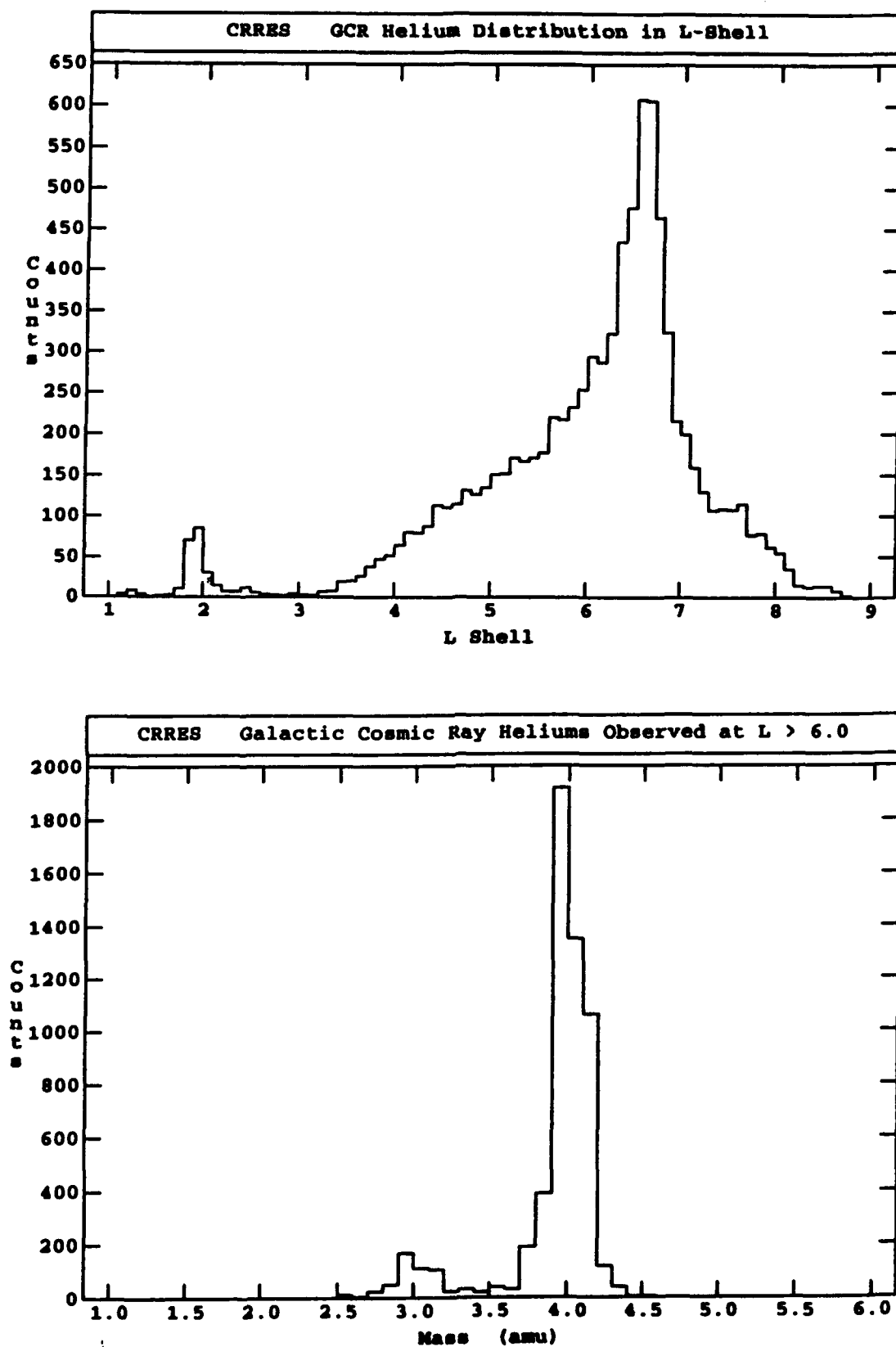


Figure VI.15. The L distribution (not normalized for relative coverage time) for the helium events (top) and a mass histogram for the helium observed at high L values.

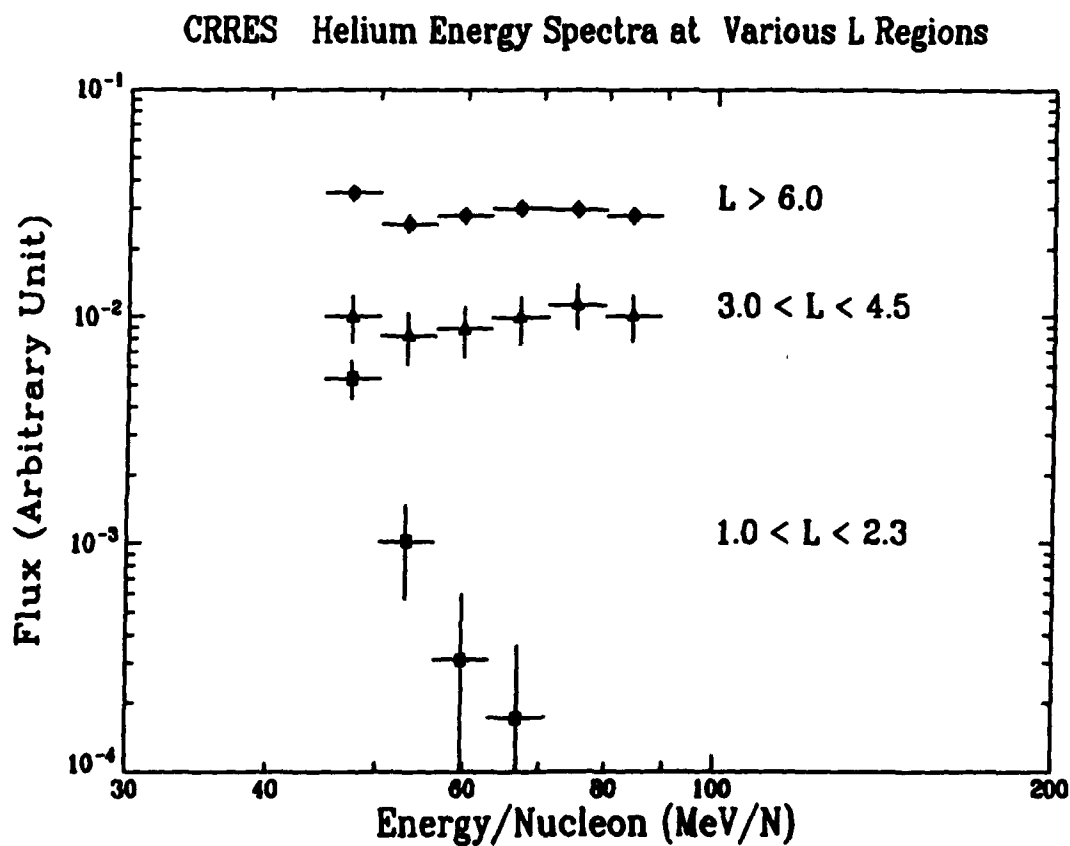
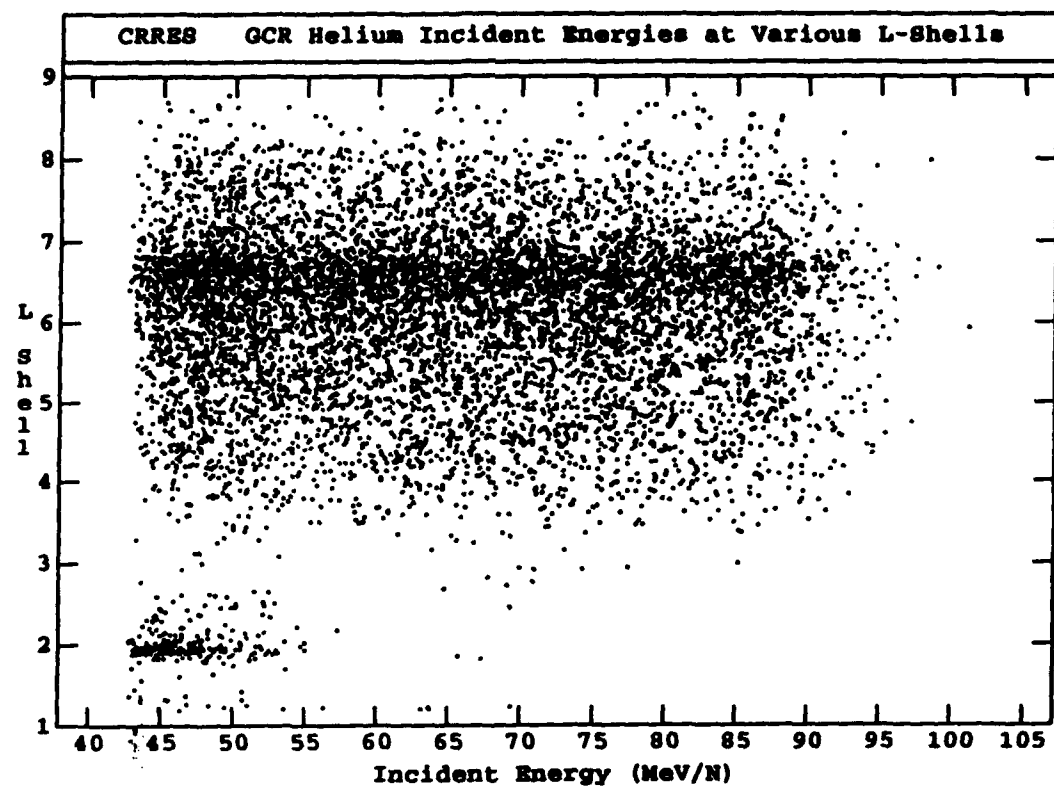


Figure VI.16. L versus incident energy plot (top) for the helium events and unnormalized helium energy spectra (bottom) for events from different regions of L space.

events observed at higher-L values. This would indicate that we are observing the high energy tail of a "trapped" helium population.

Note also that there is little difference in the spectra for  $L > 6$  and  $3 \leq L \leq 4.5$ . This may imply that there is relatively free access for the GCR helium down to about  $L=3$  with little or no geomagnetic shielding effect. This needs to be studied further since one would expect, from simple dipole models, that geomagnetic effects should become important at  $L \sim 4$ . It will be necessary to subdivide the  $3 \leq L \leq 4.5$  bin to determine if there is, in fact, a geomagnetic cut-off effect.

Another test for the origin of the helium ions is to look at the particle's pitch angle distribution. This can be done since the ONR-604 instrument contains a trajectory measuring system. By knowing the instrument mounting relative to the spacecraft axis, the spin rate and the attitude of the spacecraft as a function of time, each event can be mapped onto the magnetic field direction for the instantaneous location of the spacecraft. The magnetic field direction is taken from the Tsyganenko field model, corrected to a value of  $K_p = 3$ . Figure VI.17 shows the local pitch angles for each of the helium events at the top. CRRES also contained a magnetometer from which measured B values can be obtained. Using the calibrations provided by the AFGL group, we have looked at the pitch angles determined with respect to the measured field direction. These are compared to the Tsyganenko values in the lower part of Figure VI.17. Note that the vast majority of the data points fall along the  $45^\circ$  line, showing that, for quiet times, the Tsyganenko model is in good agreement with the measured field values.

The top portion of Figure VI.17 indicates that there is a difference between the low-L and high-L events in the distribution of pitch angles. This is illustrated in Figure VI.18 which compares the high-L distribution (top) to the low-L results (bottom). Note that the  $L > 6$  events are nearly field-aligned while the low-L events are peaked around pitch angles of  $90^\circ$ . This latter is exactly what would be expected for a "trapped" population. Particles with lower pitch angles find themselves in the loss cone leaving only those around  $90^\circ$  to be trapped or quasi-trapped. Unfortunately, the statistics do not permit a study of the time-dependence of the low-L component in order to investigate the possible sources of these particles.

However, the preliminary results on quiet-time helium do show evidence for a "trapped" component at high energies, 40-70 MeV/nucleon. Both the energy spectrum and the pitch angle distribution are consistent with a magnetospheric origin for these particles. Note that the location in L for these events is very close to that seen for the helium in the inner magnetosphere during the March flare. What remains is to determine the absolute flux of the particles and to study the probable access modes for such events. Further, the small peak near  $L = 1.3$  should also be investigated. An interesting diagnostic for the origin of these particles could be the isotopic ratio,  $^3\text{He}/^4\text{He}$ , as a function of L shell.

### C. Particle Access and Charge States

We have continued the analysis started with the ONR-602 experiment on "sub-cutoff" particles with the new data provided by ONR-604 on CRRES. We have looked initially at a sample of P1 and P2 events heavier than helium. For each particle, the arrival direction, incident energy and charge are used to trace the particle from its observation point out of the magnetosphere. The tracing code is a modification (TRAJT87) of the earlier IGRF-based code TRAJ developed by Shea and Smart at PL/GD to support usage of empirical models of the external (Tsyganenko, 1987) and internal (IGRF-1980) geomagnetic fields. The Tsyganenko model is an empirical representation of magnetic field measurements in the outer magnetosphere and magnetotail region to  $70 R_E$  from the Earth. TRAJT87 numerically traces the ion trajectory backward along the detected incidence direction at the measured energy and an assumed atomic charge  $Q \leq Z$ . If the



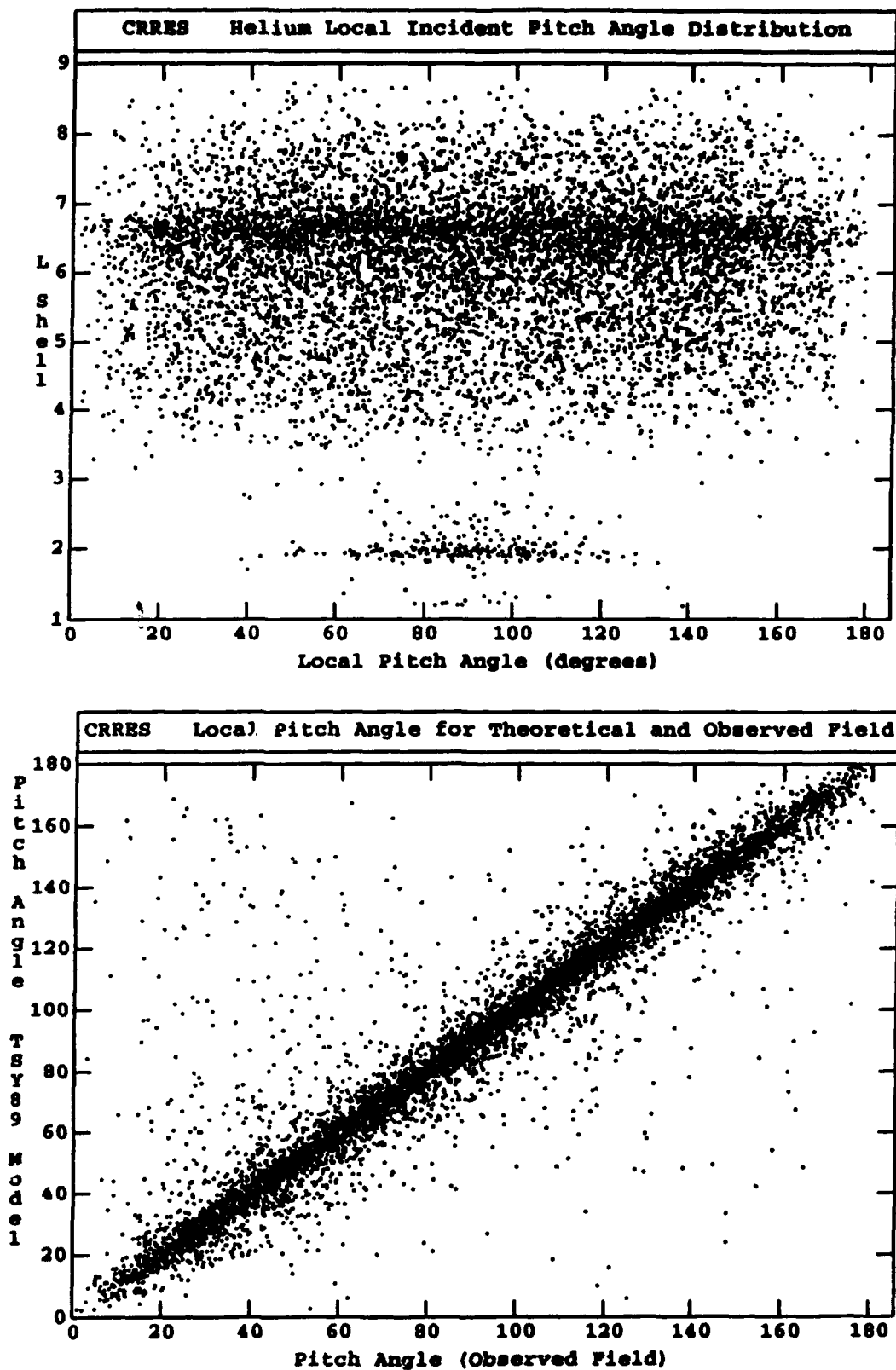


Figure VI.17. Local pitch angle versus L shell (top) for the helium events and a comparison between pitch angles determined with the Tysganenko model and with the magnetometer data (bottom).

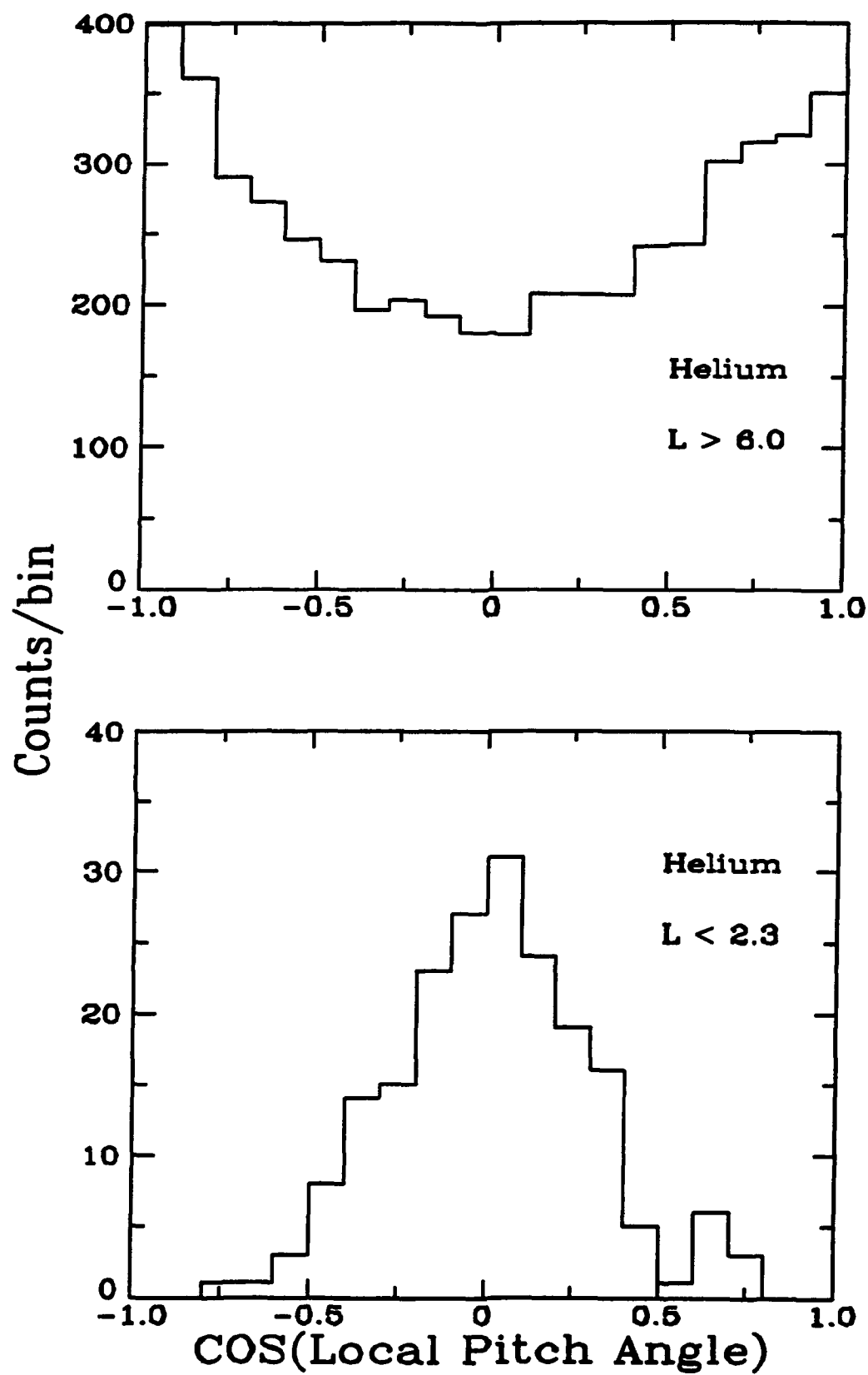


Figure VI.18. The pitch angle distributions for helium nuclei observed at (top)  $L > 6$  and (bottom)  $L < 2.3$  during quiet times.

calculation allows the ion to escape the magnetosphere at  $25 R_E$  from the Earth within a fixed number of trajectory steps as a fully striped ion of nuclear charge  $Z$ , the ion is deemed to be above the cutoff for penetration to the satellite from interplanetary space; if no escape occurs, the effective charge  $Q$  is decremented in unit intervals and the particle tracing is repeated until escape occurs or until  $Q < 1$ .

Figure VI.19 shows histograms of the results for 5633 events in the analysis. The open histogram shows all events while the shaded histograms show events with  $Z-Q=1$  and  $Z-Q \geq 2$ . Given the uncertainties in both the measurements and the magnetic field models, it is difficult to prove that  $Z-Q=1$  events are real. However,  $Z-Q \geq 2$  should not result from the uncertainties. We note that  $Z-Q \geq 2$  accounts for  $<1\%$  of the total number of events. Within the low statistics, the charge distribution of the  $Z-Q \geq 2$  events mirrors the parent distribution. In many cases the  $Q$  values differ from the measured charge  $Z$  by 4-8 units, and it is difficult to account for these events other than as genuine "sub-cutoff" particles.

Figure VI.20 shows the event statistics for the different  $Z-Q$  values. As a cross-check on the results, the calculations have been re-done with a simple centered dipole magnetic field model, which yields larger numbers of potential sub-cutoff events, as shown in the figure. This implies that the additional field components, e.g. the ring currents, included in the Tsyganenko field model do make a significant contribution at  $L < 5$ . Further, it argues that the current analysis is a conservative approach to the problem.

Another diagnostic for the origin of particles observed by CRRES is the particle pitch angle distribution, which can be determined because ONR-604 contains position sensing detectors. The conventional expectation for angular distributions of cosmic rays at energies above the local rigidity cutoff is that such distributions should reflect the anisotropy or isotropy of the particles outside the magnetosphere (e.g., with respect to the interplanetary magnetic field, IMF). Anisotropic flows of solar energetic ions from the IMF across the magnetopause into the magnetosheath and magnetotail regions may produce spatially varying windows of solar ion access into the polar cap region, particularly during onset of impulsive flare events, as was discussed earlier based upon ONR-602 results. More isotropic intensities of galactic cosmic rays in the IMF are assumed to propagate downward above local cutoffs into the inner magnetosphere. Since the magnetic fields are relatively weaker in the outer magnetosphere near and beyond CRRES's apogee distance, it is expected that measurements at apogee should reflect the galactic ion isotropy in interplanetary space. Alternatively, the fact that our heavy ion sample from CRRES/ONR-604 measurements consists of many ions whose gyroradii in magnetotail fields of order 10-20 nT could be contained within the tail lobe region might suggest that this region may produce some channeling effects during cosmic ray entry into the magnetosphere.

Our sampling of incidence direction distributions for high energy, heavy ions indicates the presence of significant field-aligned anisotropies even for quiet-time cosmic rays. Figure VI.21 shows directions of arrival (i.e., incidence from) in the local zenith and azimuth angle system for geographic coordinates. Zero zenith angle corresponds to incidence from the radial or zenith direction and 180 degrees to the downward or nadir direction, while zero and 180 degrees azimuth angle are for incidence from the north and south directions in geographic coordinates, and 90 and 270 degrees are for arrival from east or west, respectively. In these coordinates there are clear "hot spots" in the incidence distributions which correspond approximately to the north and south directions, along with a large population of other ions dispersed over a wide range of incidence angles. Since the local magnetic field along the CRRES orbit is nearly dipolar, and the dipole axis is tilted only eleven degrees from the geographic north-south axis, the north-south anisotropy maps to a bidirectional pitch angle distribution with peak flux along the field line and lower intensities at larger pitch angles.

# ONR-604 MEASUREMENTS OF HEAVY IONS

P2 & P1 Metal Ions in Orbits 102-1000

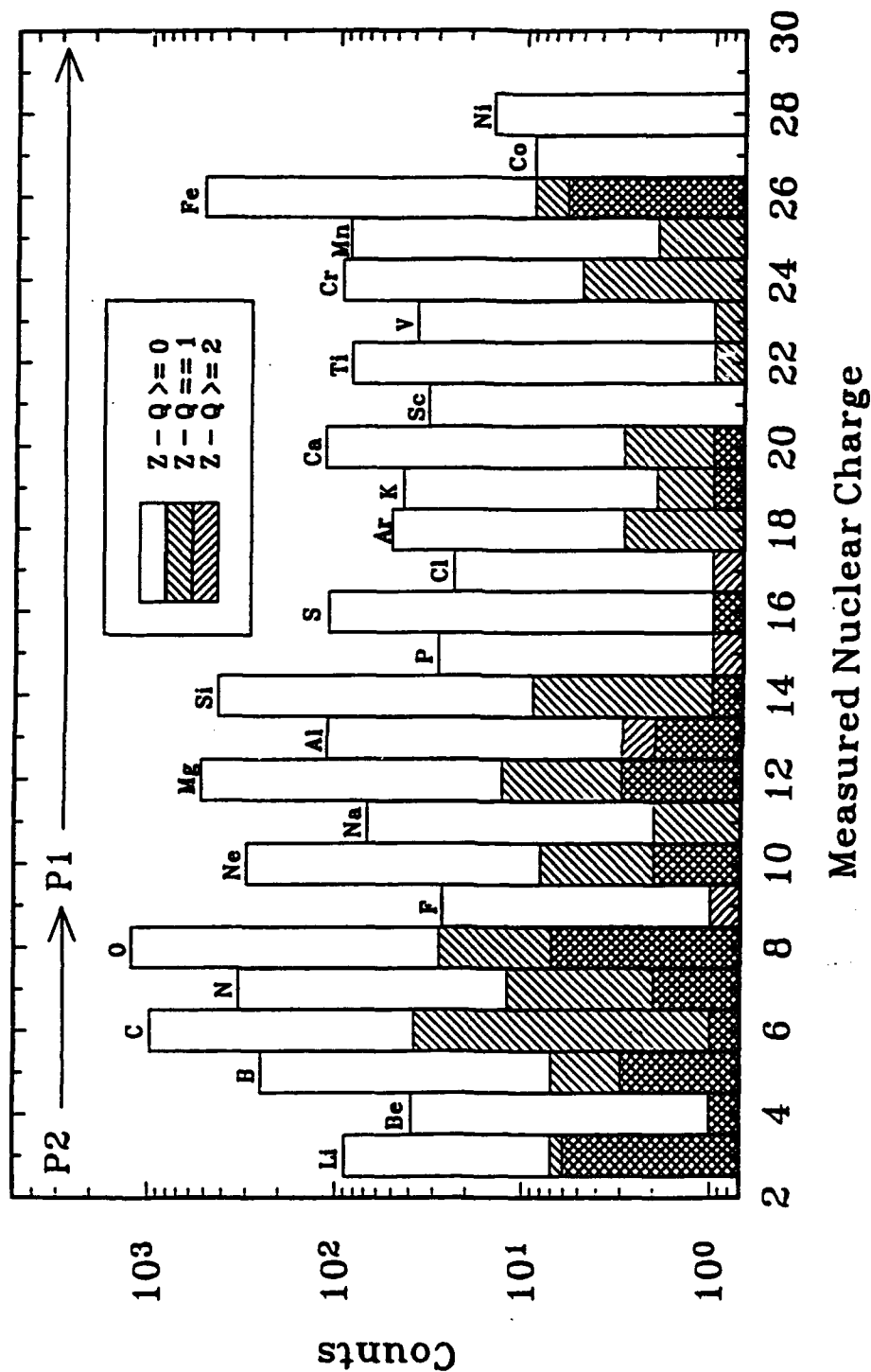


Figure VI.19. Charge histogram for all events (open) and for events with  $Z-Q < 0$ .

# ONR-604 MEASUREMENTS OF HEAVY IONS

P2 & P1 Metal Ions from Orbits 102-1000

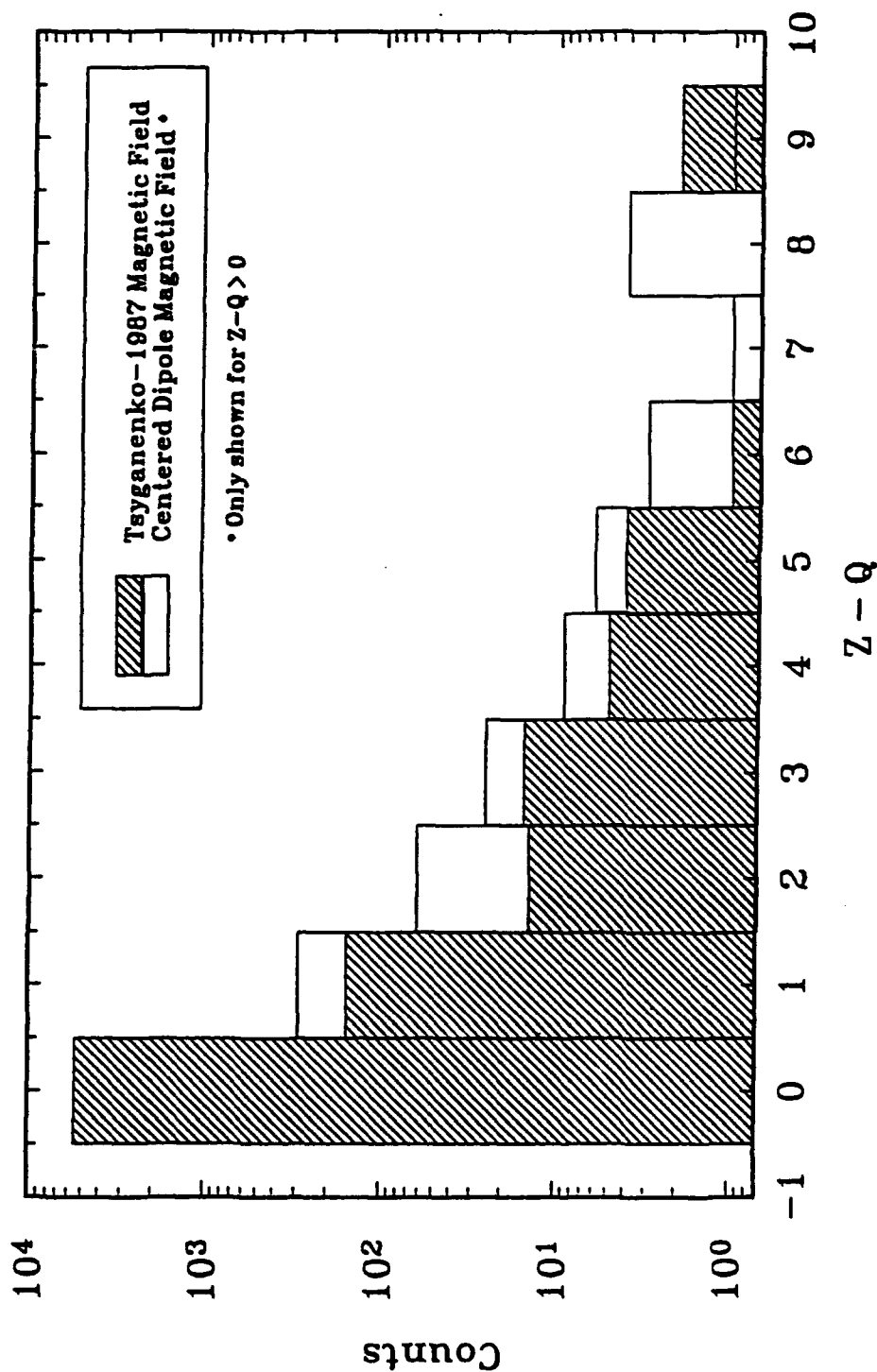


Figure VI.20. Distribution of  $Z-Q$  values for the events based upon the Tsyganenko and upon a centered dipole magnetic field model.

# ONR-604 MEASUREMENTS OF HEAVY IONS

P2 & P1 Heavy Ions From Orbits 102-1000

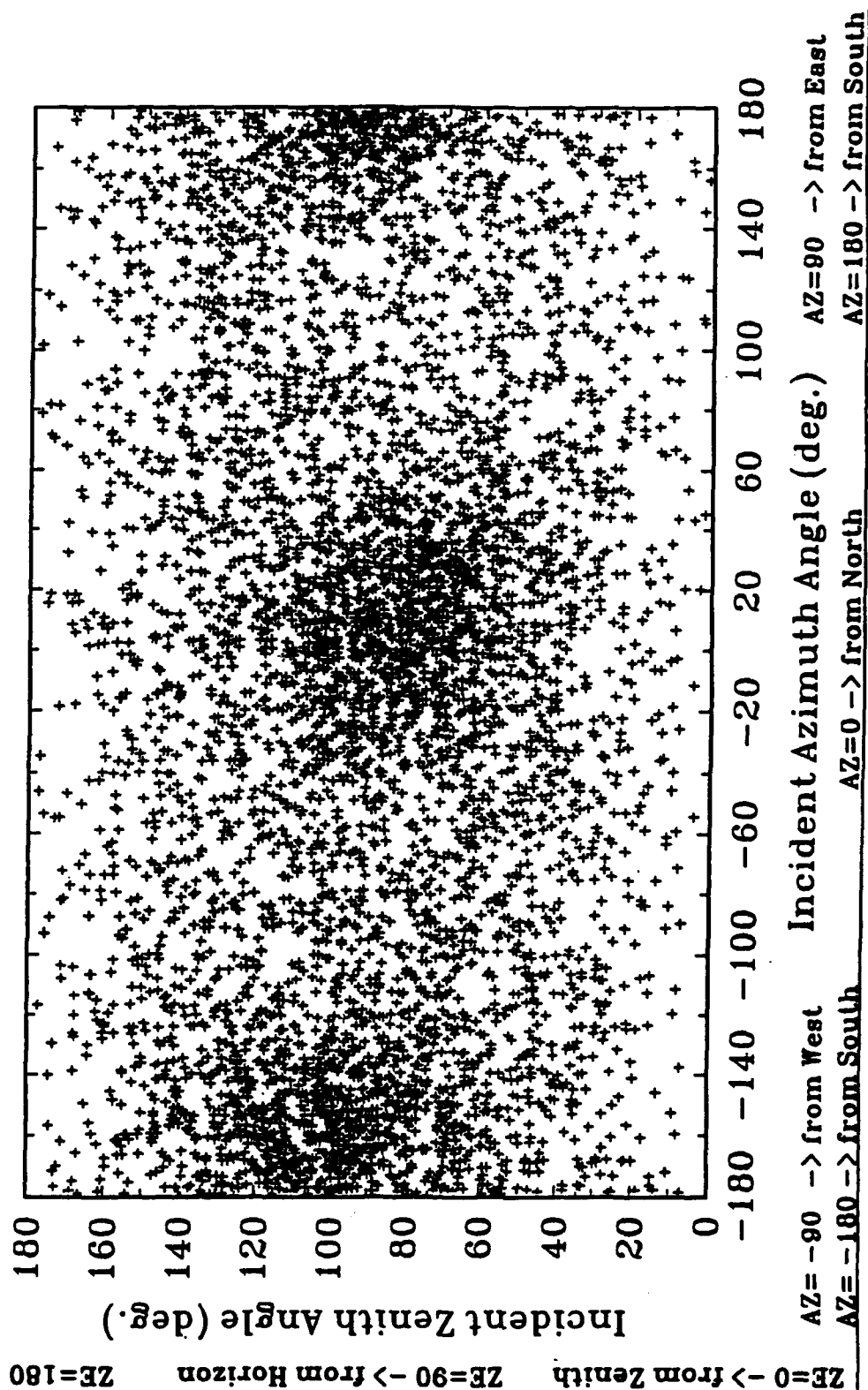


Figure VI.21. Arrival directions for the events plotted as local zenith versus local azimuth angles.

The latter point is illustrated in Figure VI.22 which shows histograms of event counts in equal bins of the cosine of the local pitch angle as determined by two different field models and by the CRRES magnetometer dataset. The directional event fluence increases by almost a factor of two from large to small pitch angles with insignificant variations between the different determinations of the magnetic field. Note that Figure VI.22 does not include the angle dependent geometry factors of the instrument or corrections (small) for instrument live-time as a function of pitch angle. Neither of these are expected to change the qualitative conclusion from Figure VI.22, namely that the events being observed have a large field aligned component. What remains is to understand this effect in terms of the particle energies, charges and time histories. Here the helium events, which show a similar effect (discussed in the preceding section), may provide the means for unraveling some of the questions.

Returning to the sub-cutoff events, Figure VI.23 shows another view of the local pitch angle distribution with the results for the  $Z-Q=1$  and  $Z-Q\geq 2$  events indicated. The statistics are meager, but the  $Z-Q=1$  events tend not to show the excess near  $\pm 1.0$  of the parent distribution. For the  $Z-Q\geq 2$  events it is difficult to draw any firm conclusions. For a "quasi-trapped" origin for the sub-cutoff ions, one would expect the loss cone to be relatively empty. For ions detected at  $0-30^\circ$  magnetic latitude and assuming sources at about 1500 km altitude, the loss cone is less than about  $6^\circ$  in local pitch angle, or cosine values  $>0.99$ . Such a depletion would not be observable in the histogram of Figure VI.23. Thus, we cannot rule out an origin arising from charge stripping of cosmic rays in the high altitude atmosphere. The problem is getting the particles through the magnetosphere to the atmosphere at the observed energies or accounting for sufficient energy loss to bring the events to within the observable (by ONR-604) energy range.

As was stated earlier, this is not a new problem. Measurements on other low altitude spacecraft have also seen sub-cutoff ions. A summary of some of the measurements is shown in Figure VI.24 where the Sc-Cr/Fe ratio is plotted as a function of energy. The group of data points at low energy that show ratios at or above 1.0 are measurements made on spacecraft within the magnetosphere. (The remaining data points are from satellite experiments in interplanetary space.) One of the reported characteristics of the sub-cutoff population is a high secondary to primary ratio for elements below iron. From Figure VI.19, we observe a ratio for  $0.78 \pm 0.39$  for  $Z-Q=1$  events and a ratio  $<0.2$  for the  $Z-Q\geq 2$  sample. Our results are most consistent with the galactic cosmic ray results at 0.5-0.6 but cannot, with present statistics, rule out the higher values reported by the other experiments. This is a particularly intriguing problem that will require additional work to resolve.

# ONR-604 MEASUREMENTS OF HEAVY IONS

P2 & P1 Metal Ions From Orbits 102-1000

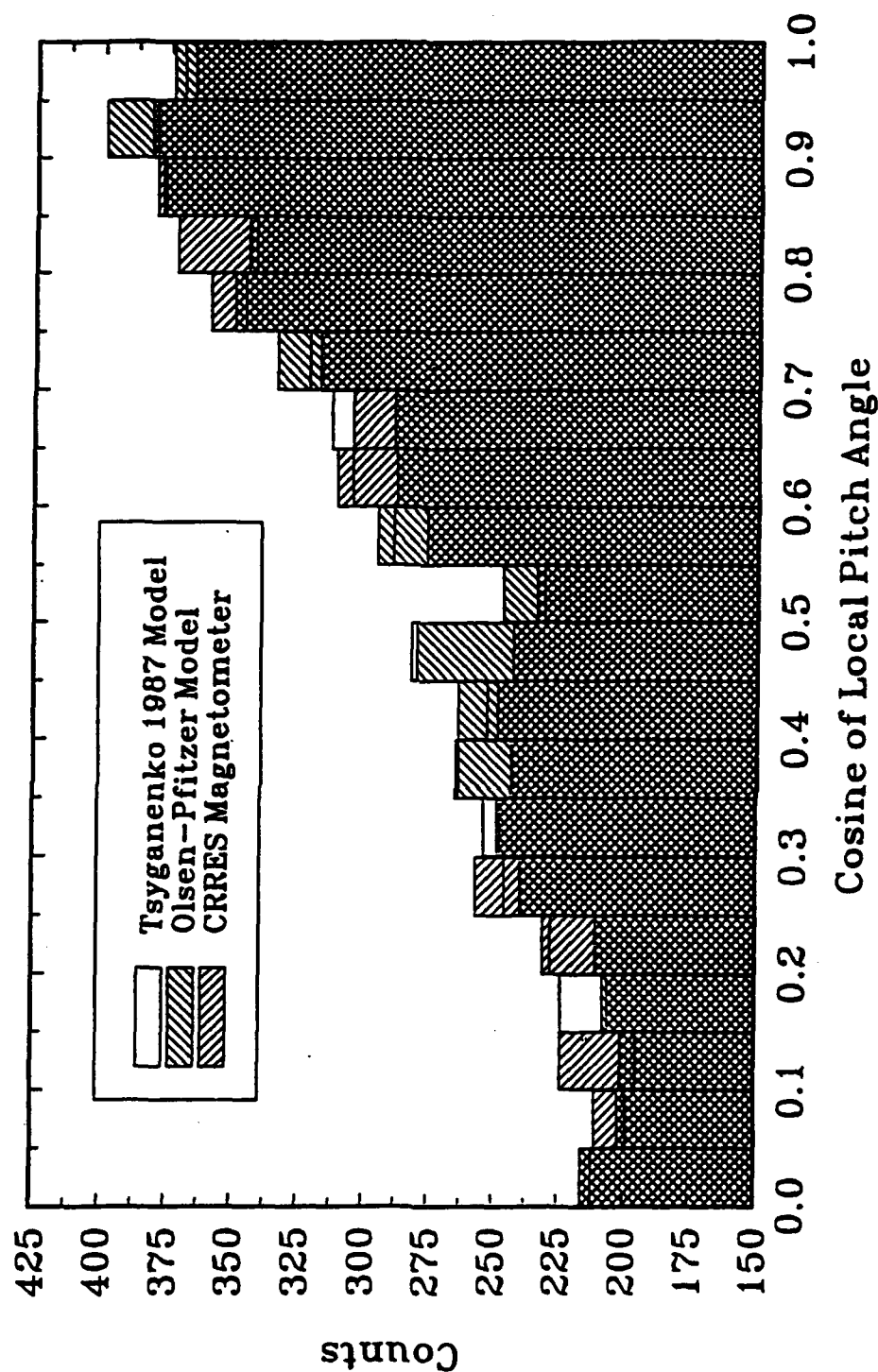


Figure VI.22. Pitch angle distribution (in cosine) for the events determined by two different magnetic field models and by the experimental data from the CRRES magnetometer.



# ONR-604 MEASUREMENTS OF HEAVY IONS

P2 & P1 Heavy Ions From Orbits 102-1000

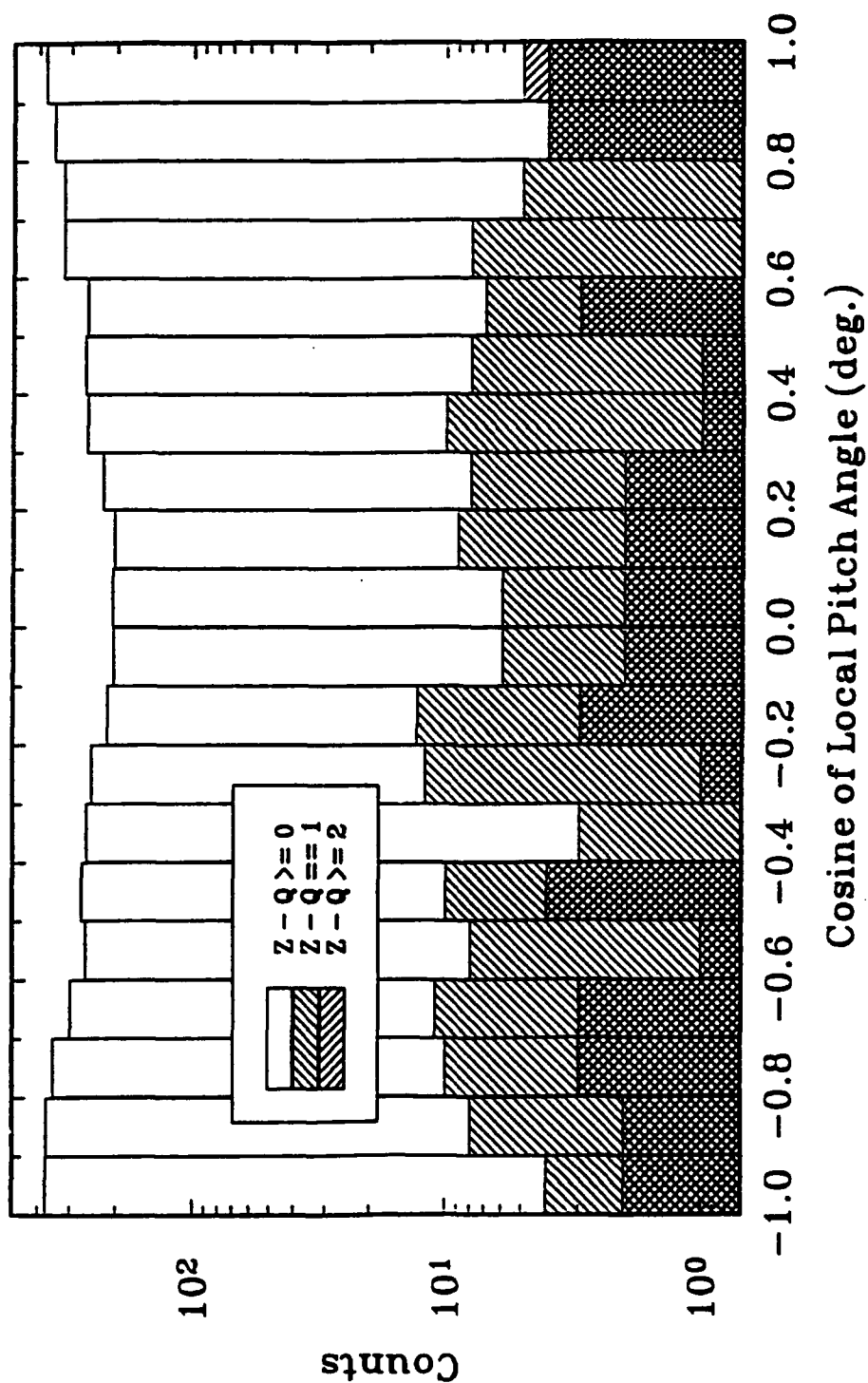


Figure VI.23. Pitch angle distributions for the heavy ion events identifying the  $Z-Q=1$  and  $Z-Q \geq 2$  components.

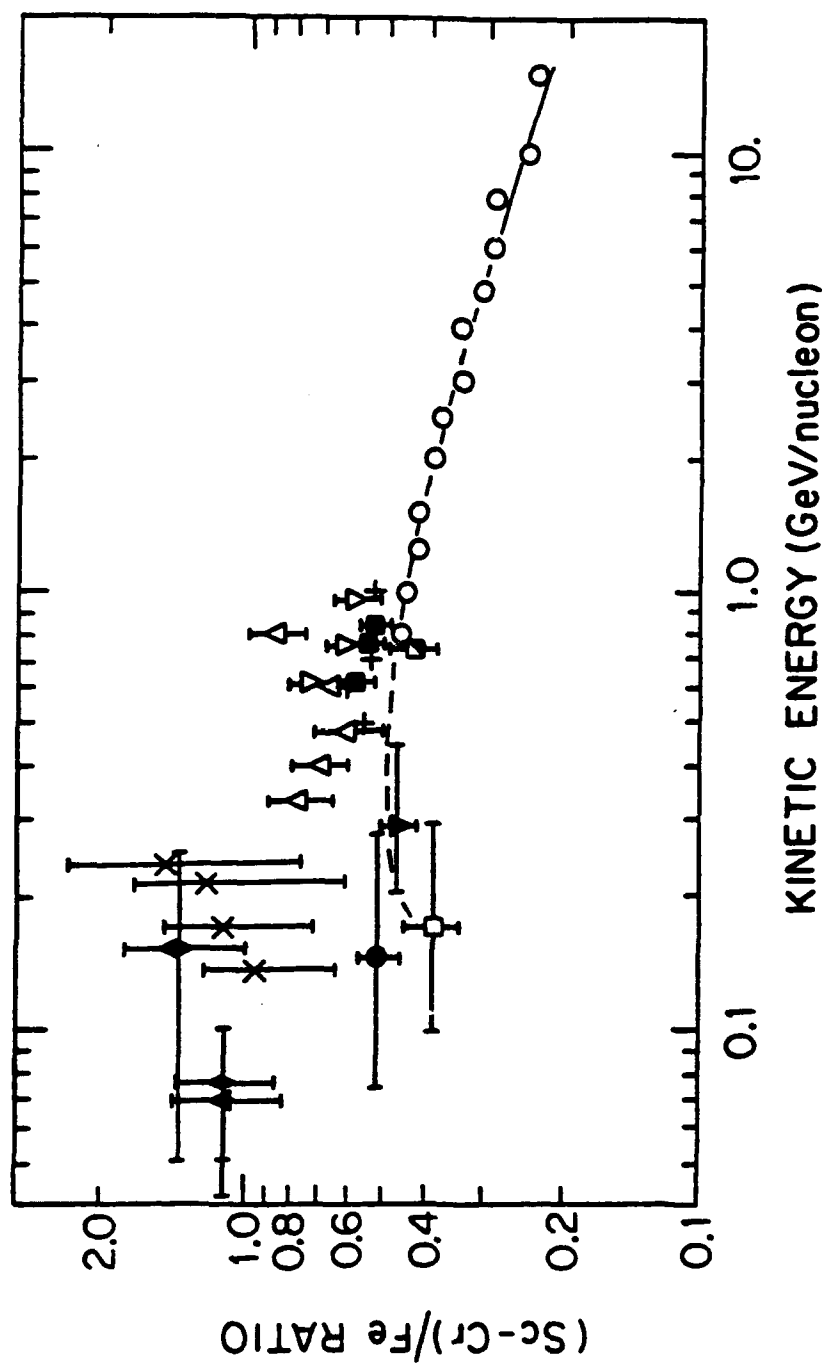


Figure VI.24. The Sc-Cr/Fe ratio as a function of energy compiled from the literature.

## VII. Modeling the Environment: Single Event Upsets

### A. Overview

The heavy ion radiation environment encountered in near-Earth space consists of three major components: (a) galactic cosmic rays (GCR), (b) solar energetic particles (SEP), and (c) trapped magnetospheric particles. The first two of these arrive at the Earth from outside our immediate geospace environment and are termed "interplanetary" while the last resides within the Earth's magnetosphere, and is termed a "local" component. The interplanetary particles encompass a wide range in both energy ( $E > 500$  keV) and charge ( $1 \leq Z \leq 92$ ). Some of these particles penetrate the Earth's magnetic field and form part of the radiation environment in which spacecraft must operate.

For electronic components located within a spacecraft, there is a large radiation dose (depending upon the actual orbit) contributed by protons and electrons plus radiation effects due to the heavy ion component. This latter is particularly important because of the ability of a single heavy nucleus to affect ("upset") microelectronic circuitry (Binder et al., 1975) particularly low power memory chips (Kolasinski, et al., 1979). Even though the relative abundance of heavy ions is small, compared to protons, the heavy ion efficiency is high since the effects are caused directly by the passage of the particle through the device. An important objective of the overall CRRES program is to investigate the effects of the space radiation environment on modern microelectronic components, in particular the ability of single, intensely-ionizing particles to upset the logical state of a single bit in a digital microcircuit, causing a single event upset (SEU). The MicroElectronics Package (MEP) onboard the CRRES satellite measured SEU rates in a large sample of digital components.

The parameter of interest to the device physicist is the Linear Energy Transfer (LET) spectrum of the incident radiation field. Calculating an LET spectrum requires knowledge of the relative abundances (composition) and energy spectra of all of the particle species. For CRRES this involves both GCR and SEP events.

It might, at first, seem best to employ the measurements from the particle sensors on CRRES directly to determine the radiation environment. This is not practical for several reasons: (1) the total flux of particles is so low that accurate measurements of all particle species will take a long time to accumulate; (2) a thorough analysis of the data to determine accurate abundances of each individual element will be time-consuming; (3) the CRRES sensors can only measure about half of the integral flux during quiet periods because they do not measure all of the highest energy particles; and most importantly, (4) the scientific research in cosmic ray physics over the past 30 years has established, accurately, relative abundances and energy spectra for most of the elements. A galactic cosmic ray model should take full advantage of this accumulated knowledge and use contemporary measurements most efficiently to accurately define the cosmic ray intensities over the energy ranges where temporal variations are large and not easily predicted in detail.

A description of GCR based upon the well-established physical principles of propagation and solar modulation that control and determine the time- and energy-dependent GCR intensity at earth is possible. Such a model would incorporate observations obtained over the past two decades of space research. The CRRES particle sensor datasets are not a significant improvement over the existing GCR database in terms of composition, characteristics of energy spectra, or range of intensity variation. The CRRES particle data do not provide information that changes the known qualitative features of the interplanetary high energy heavy ion environment, but are of crucial importance in obtaining quantitative agreement for the exact conditions during the CRRES mission. In this sense, CRRES provides the normalization of the time-dependence of the GCR intensity. The time variation, of course, is caused by the solar activity cycle and its modulating affect on the GCR.

Solar flares are also a time-varying phenomenon, following, roughly the solar activity cycle. However, flares also vary in major ways from one event to the next. Thus, there is not the broad database and physical understanding for SEP's that there is for the GCR.

In order to describe, quantitatively, the heavy ion environment in near Earth space, it is necessary to model the GCR and SEP components separately. For the galactic cosmic rays the model must describe the level of solar modulation and the presence of any "anomalous" components. For the solar flare component, the parameters will define the occurrence of the flares, its peak flux, total fluence, composition characteristics, and the form of its energy spectrum. We have been developing such models, with reference to the ONR-604 data from the CRRES mission. This development is a joint effort between the ONR-604 team at the University of Chicago and D. Chenette at the Lockheed Palo Alto Research Laboratory. The details of the analysis and the results to date are described below.

## B. The CRRES Environment

The CRRES spacecraft was launched during a period near the maximum of the solar activity cycle, as was illustrated in Figure V.4 (top), which showed the last four solar cycles as seen by ground based neutron monitors. Note that 90-91 was a period in which the neutron monitors reached their lowest level, compared to previous solar cycles. This low level indicates very strong solar modulation for the cosmic rays. Referring to Figure V.4 (bottom), CRRES was launched just after the minimum in the neutron monitor rate, and was on an increasing intensity curve (recovering towards solar minimum conditions) until late March 1991 when the flare activity halted the recovery. However, the time period between ~1 Sept. 90 and 1 March 91 appears to be a relatively quiet period and was selected as the first six month period for GCR analysis, without the need to worry about SEP events.

Figure VII.1 shows the selected period in more detail. Compared are the P2 and P3 rates for Apogee ( $L > 6.5$ ) and for all proton mode data (PM, at bottom), the GOES proton counting rates P5 (39-82 MeV) and P3 (8.7-14.5 MeV) and Climax neutron monitor and IMP-8 proton quiet times (top). Note the ONR-604 P2 rate which appears relatively constant. No major heavy ion flares occurred during this period. The ONR-604 P3 ( $L > 6.5$ ) rate, however, does show some proton or electron events. These are correlated, for the most part, with the low energy proton increases seen in the GOES P3 channel. The larger events are discernible in the GOES P5 rate as well. When the ONR-604 rates are plotted for all proton mode data (bottom two plots), the P3 rate shows considerable activity while P2 remains relatively constant. The extra spikes in P3 are, presumably, of magnetospheric origin. Only near apogee can the ONR-604 counting rate for P3 be used to trace the interplanetary proton component.

Figure VII.2 (top) shows the number of P1 events recorded and the L distribution of P1 events (bottom) as a function of orbit for a portion of the dataset. The 22-24 March flare period starts at orbit 584, for which no noticeable increase is observed. There is a gradual increase in the overall rate which is consistent with the decreasing modulation shown by the neutron monitors. Most of the events occur at  $L > 5$  with a band at  $L = 6.5$  which is the location of the geomagnetic equator. The CRRES orbital plane and the geomagnetic equatorial plane are effectively aligned at ~orbit 500. What is interesting is that there are a handful of events observed at low L values. These are most likely high energy GCR events but could also be pseudo-trapped particles or sub-threshold events, as have been reported by others (Oschlies et al., 1989; Durgaprasad et al., 1990; Adams et al., 1991).

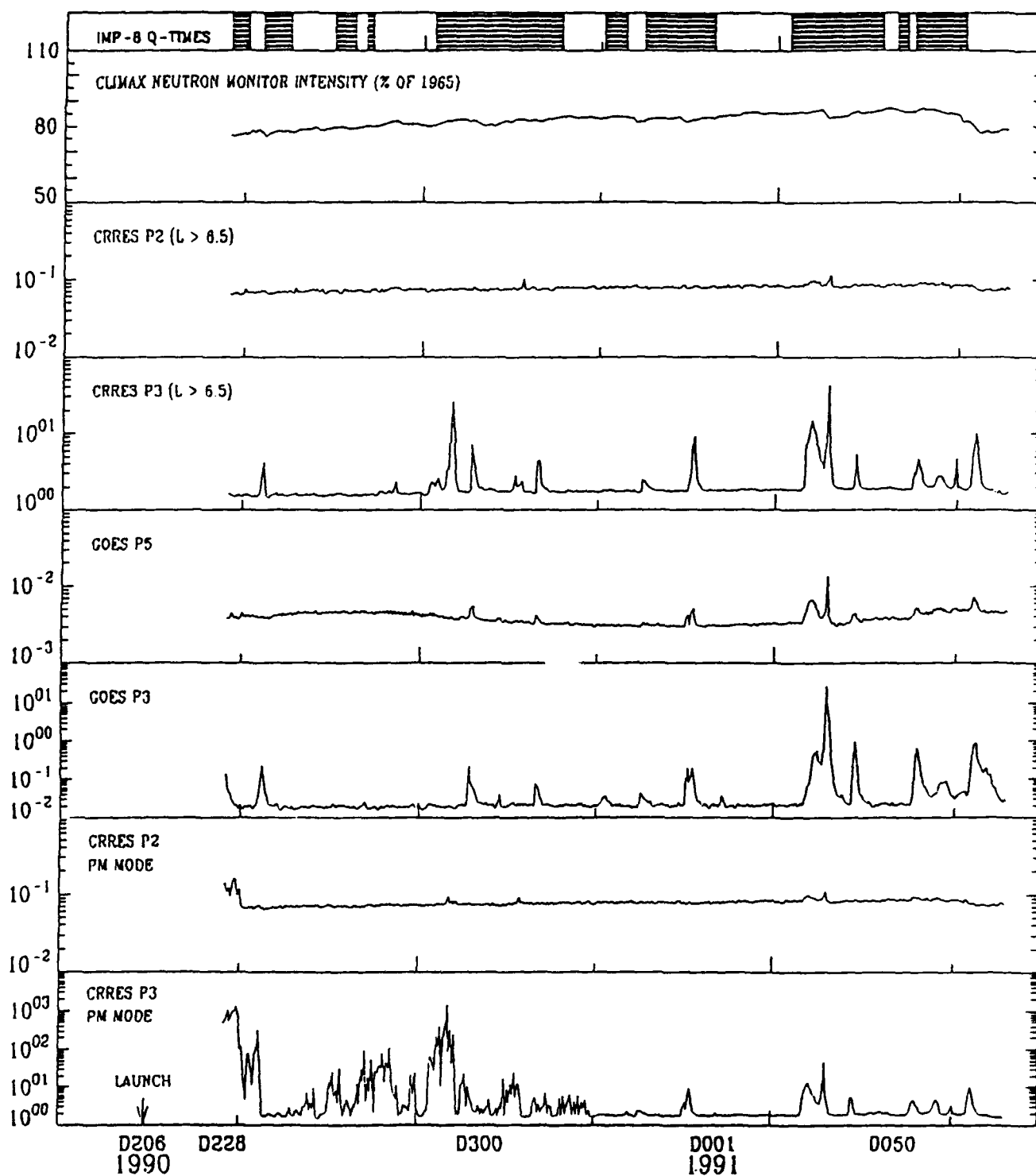


Figure VII.1. The first part of the CRRES mission comparing ONR-604 and GOES rates plus IMP-8 and neutron monitor data.

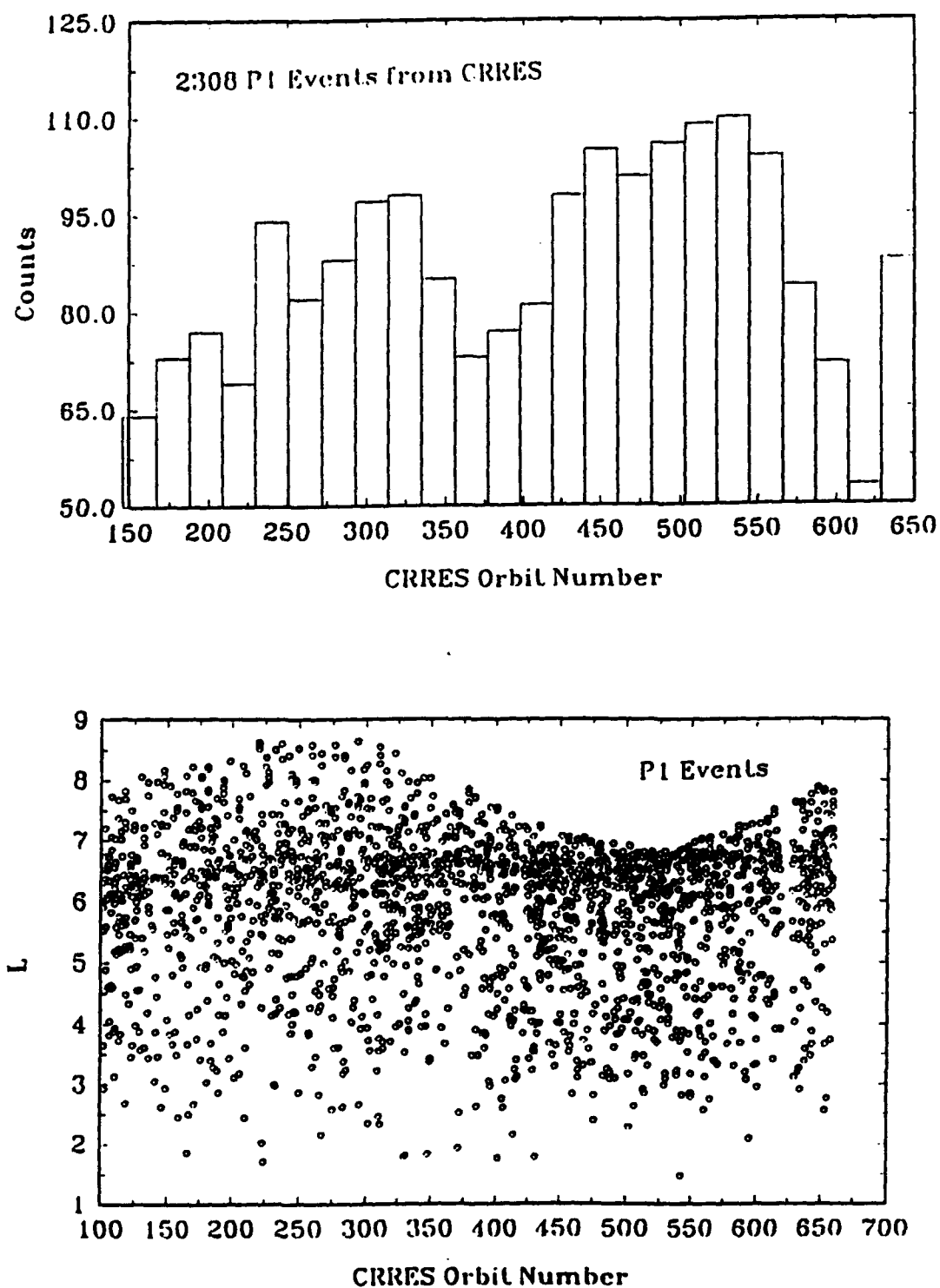


Figure VII.2. The number of P1 events (top) and the L distribution of the events (bottom) as a function of orbit for the first part of the CRRES mission.

### C. Solar Modulation

It is well known (see reviews by Jokipii 1971, Fisk 1979, McKibben, 1986) that at energies below a few GeV per nucleon the intensity and the spectral shape of the cosmic rays arriving at the orbit of Earth are significantly modified by solar modulation. The cosmic rays diffuse into the heliosphere against the outward-flowing solar wind, carrying frozen-in interplanetary magnetic field, which convects the cosmic rays out of the heliosphere. In this process, the cosmic rays lose energy to the expanding field (adiabatic deceleration), and their energy spectrum is modified.

A spherically symmetric model of solar modulation has been developed (Parker 1965; Jokipii 1971; Urch and Gleeson 1972; Fisk 1979) which explains most of the gross features of the modulation process. This model includes the effects of diffusion, convection, and adiabatic deceleration (but not drifts due to the gradient and curvature of the magnetic field) and assumes that these three physical processes are in equilibrium in the heliosphere. Quantitatively these effects are represented by a Fokker-Planck equation in which the parameters are the solar wind velocity, the diffusion coefficient and the radius of the heliosphere, with the cosmic-ray differential energy spectrum in local interstellar space as a boundary condition.

Evenson et al. (1983) (see also, Garcia-Munoz et al., 1986), solving this equation numerically, have analyzed the simultaneous modulation of electrons, protons, and helium nuclei over the 1965-1979 period involving more than one solar cycle. They find that in general the model fits the data quite well. In this model the degree of modulation at a heliospheric radius  $r$  is given by the modulation parameter

$$\phi(r) = \frac{1}{3} \int_r^R \frac{V(r')}{K(r')} dr', \quad (1)$$

where  $V(r')$  is the solar wind velocity,  $K(r')$  is the radial part of the diffusion coefficient, and  $R$  is the radius of the heliosphere. An insight into the physical meaning of  $\phi$  is obtained from the "force-field" approximation (Gleeson and Axford 1968) in which  $\Phi$  corresponds to a "potential energy," that in the particular case in which the diffusion coefficient is proportional to particle rigidity takes the simple form

$$\Phi = |Ze| \phi(r), \quad (2)$$

where  $Ze$  is the particle charge. This potential energy has been identified as the mean energy loss that the particles experience in penetrating the heliosphere to a radius  $r$ . The parameter may be expressed in rigidity or energy units, connected through,

$$\Phi \text{ (MV)} = \frac{A}{Z} \Phi \text{ (MeV/nucleon)}.$$

The modulated nucleonic differential energy spectra obtained by the numerical solution of the Fokker-Planck equation are almost completely determined by the value of the modulation parameter  $\phi$ . Combinations of the parameters  $R$ ,  $r$ ,  $V(r)$ , and  $K(r)$  giving the same value of  $\phi$  will lead to modulated nucleonic spectra which are very nearly equal to each other (Urch and Gleeson 1972). Therefore, values of the modulation parameter  $\phi$  can be used to specify different levels of modulation.

Figure VII.3 (from Garcia-Munoz et al., 1987) shows the time dependence of the modulation parameter used by Evenson et al. (1983) for 1973-1980, compared with the time dependence of the Climax Neutron Monitor count rate (given as the percent decrease below the 1954 solar minimum level). The period 1974-1978, corresponding to solar minimum conditions, was characterized by a

nearly constant level of solar modulation for which the average value of the modulation parameter was about  $\phi = 490$  MV, or  $\Phi = 245$  MeV per nucleon for  $A/Z = 2$  particles. This time period, during which much cosmic ray data was recorded, becomes a baseline to which more recent data, in particular the CRRES results, can be compared.

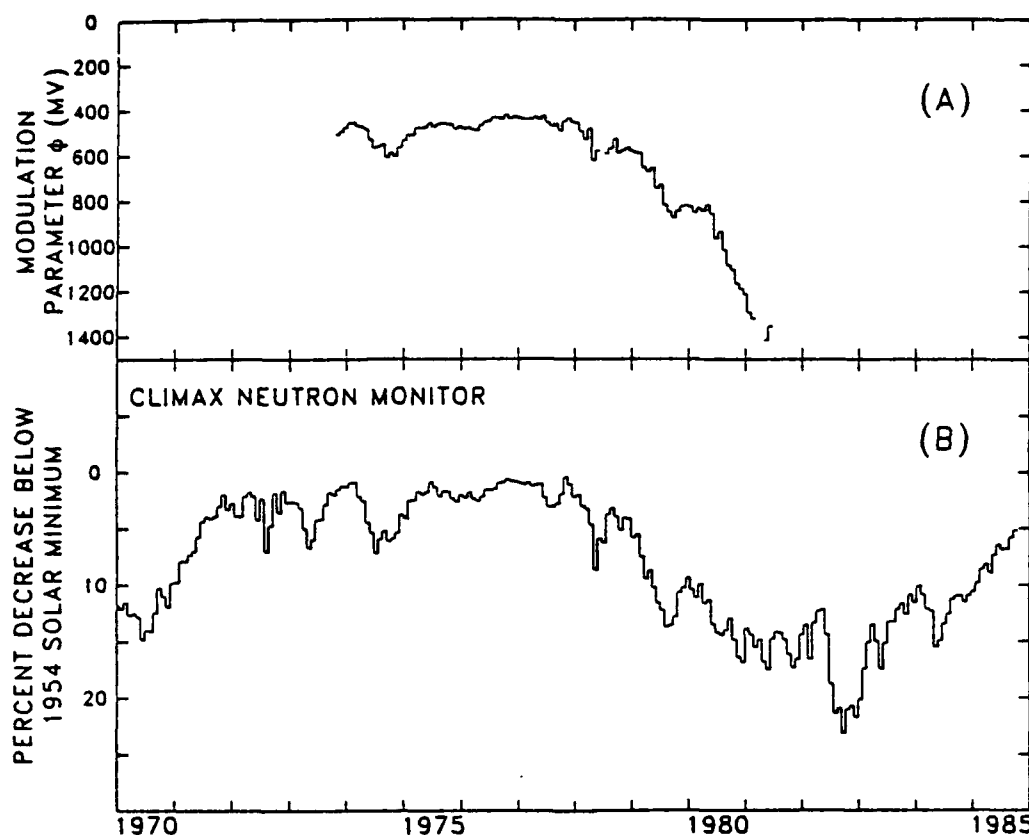


Figure VII.3. The modulation parameter  $\phi$  (MV) for 1973-1980 determined by Evenson et al. (1983) from the flux of 70-95 MeV/nucleon Helium compared to (B) the Climax Neutron Monitor rate.

There are several approaches to determining the solar modulation level for a specific time period during the CRRES mission:

- (a) Demodulation of CRRES elemental spectra
- (b) Demodulation of IMP-8 elemental spectra
- (c) CRRES Heavy Ion Rate Modeling
- (d) Neutron Monitor Correlation

The normalization procedures and background subtraction methods for ONR-604 have not yet been completed, so that actual flux values, which could be fit by the solar modulation model described above, are not available. However, IMP-8 can be used in the same way, and some preliminary IMP-8 data has been provided by Chicago. Technique (d) exploits the correlation shown in Figure VII.3, developed for the previous solar cycle. It is not known whether the same correlation holds for the present cycle, and this approach remains to be investigated. What we have concentrated upon initially was method (c), which will be described below, and using IMP-8 data for validating or comparing the results obtained.



The ONR-604 P1 and P2 rates are dominated by heavy ions -- Mg - Fe for P1 and He - O for P2. Both rates respond mainly to GCR and are relatively insensitive to magnetospheric populations, at least during the apogee portion of the orbit as was indicated by Figure VII.1. Thus, using the instrument description and operating modes described previously, it should be possible to calculate the expected priority rates for any given particle spectrum outside the spacecraft.

What has been done is the following. For each element, the energy range appropriate to a given logic condition is determined. Then the geometry factor is calculated as a function of energy (range) as illustrated in Figure VII.4. Any incident spectrum can then be integrated over the appropriate energy range, folding in the geometry factor, to predict the number of events per second. Repeating the process for all of the elements within a particular logic condition (such as P1), and summing the results, gives a calculated rate (counts/second) to compare to the flight data.

The input spectra for such a calculation are the differential energy spectra outside the instrument, i.e. at the CRRES orbit. These are obtained by folding the interplanetary spectra with the geomagnetic transmission function (Figure VII.5). For data limited to the apogee portion of the orbit (proton mode for ONR-604) there is little geomagnetic inhibition except at the lowest particle energies. The interplanetary spectra are calculated by modulating the spectra in local interstellar space (LIS) to the orbit of Earth. In this process  $\Phi$  is the parameter, so that the calculations can be performed repeatedly for a variety of values of  $\Phi$ . The value of  $\Phi$  that gives calculated rates in accord with the data is then the appropriate level of modulation for the time interval being studied. (The determination of the LIS spectrum is described in the next section.)

Figure VII.6 shows an example of the results from such a study for P1 and P2 rates. Plotted at the left are calculated counting rates for:  $P1 = P1\bar{S}$ ,  $P1^* = P1\bar{S}A$ ,  $P2 = P2A\bar{S}$ ,  $P2^* = P2A\bar{S}$  ( $Z > 2$ ), which corresponds to particles not entering or leaving the sides of the experiment and, except for P1, stopping in the detector stack. The curves are the result of many calculations, each for a different level of modulation, shown on the horizontal axis in units of MeV/nucleon. Solar minimum conditions exhibit a residual modulation level of  $\sim 250$  MeV/nucleon, so the lower values of  $\Phi$  will not be applicable, while previous solar maximum conditions have given  $\Phi$  values of 600-800 MeV/nucleon. The  $P1^*$  and  $P2^*$  rates respond principally to low energy (stopping) Mg-Fe and C-O nuclei, respectively, and are slightly more sensitive to changes in  $\Phi$  than is P1, which includes penetrating particles as well. The P2 rate is shown for comparison but is not used since the helium region of P2 events shows some background contamination.

The equivalent counting rates must be obtained from the pulse height analyzed events, since the hardware logic circuitry does not conform to any of the conditions specified above. Each event is read from tape and its discriminator bit pattern is compared to the conditions described previously. In the case of  $P2^*$ , a preliminary charge assignment of  $ZCAL > 2.8$  is required as well. Each event meeting the criteria is counted over a specific active time interval to obtain the "measured" counting rate. These are shown, for P1,  $P1^*$  and  $P2^*$ , at the right side of Figure VII.6. Note that the three rates, when extended to the appropriate curve, all give a relatively consistent value for the solar modulation parameter,  $\Phi = 550 \pm 50$  MeV/nucleon.

While Figure VII.6 shows a consistent result for  $\Phi$ , it remains to be demonstrated that this value is correct. Such a validation can be provided by IMP-8 data (in the absence of normalized CRRES spectra) since the IMP-8 instrument is well understood and has been utilized for many years in such studies. Figure VII.7 (top) shows IMP-8 oxygen spectra provided by M. G. Munoz for the late 1990-early 1991 period, as well as for previous periods, to be used in comparative studies. Beginning with a model for local interstellar spectra, the lower set of curves in Figure VII.7 (bottom) shows the solar modulation prediction compared to the IMP-8 data. A best fit value of  $650 \pm 30$  MeV/nucleon ( $1300 \pm 60$  MV) is obtained, somewhat above the values for  $\Phi$  inferred from the priority rate analysis. Assuming that the IMP-8 level is correct, then there must be a problem with

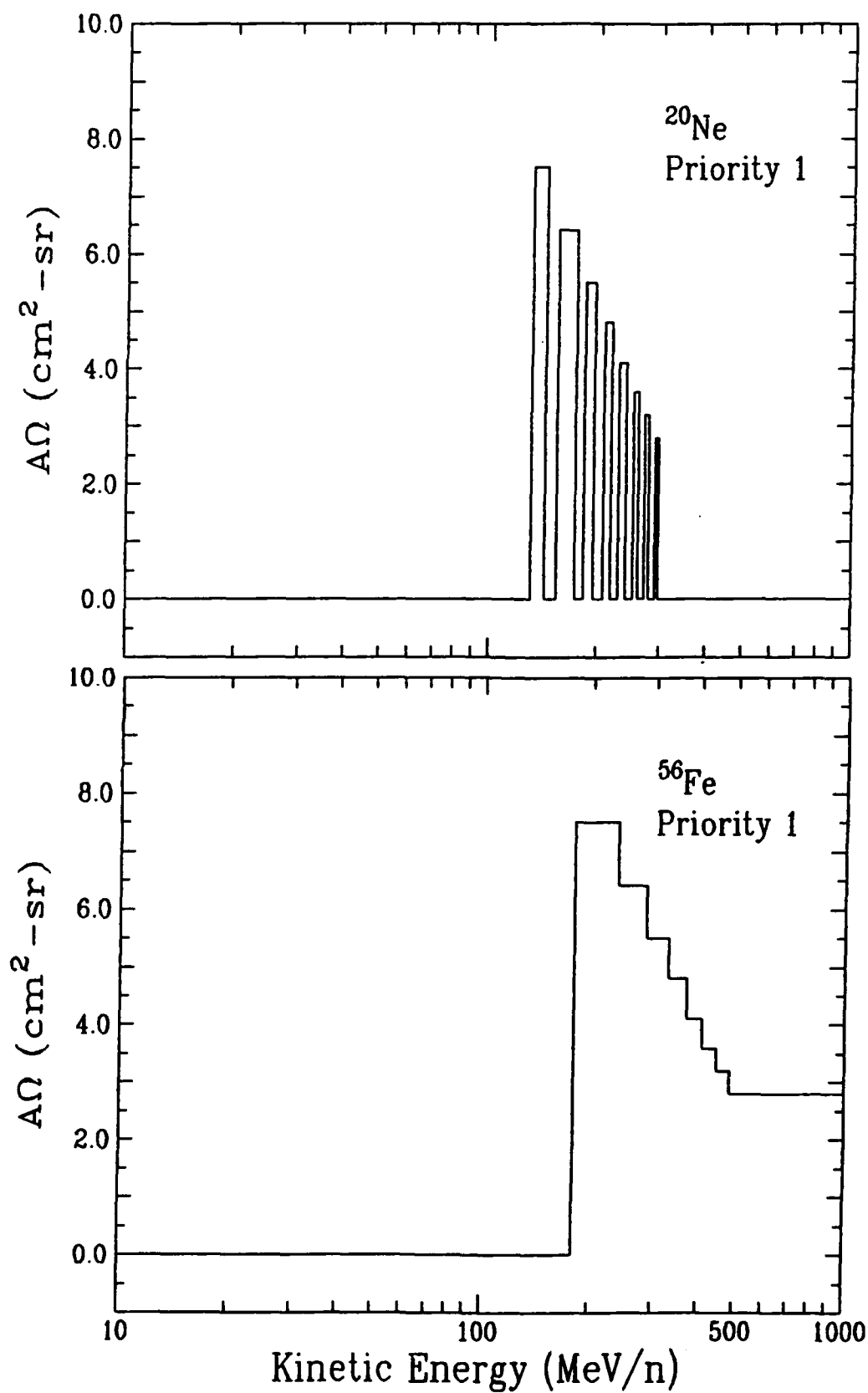


Figure VII.4. Geometry factor for  $^{20}\text{Ne}$  and  $^{56}\text{Fe}$  in priority 1 as a function of the particle's incident energy.

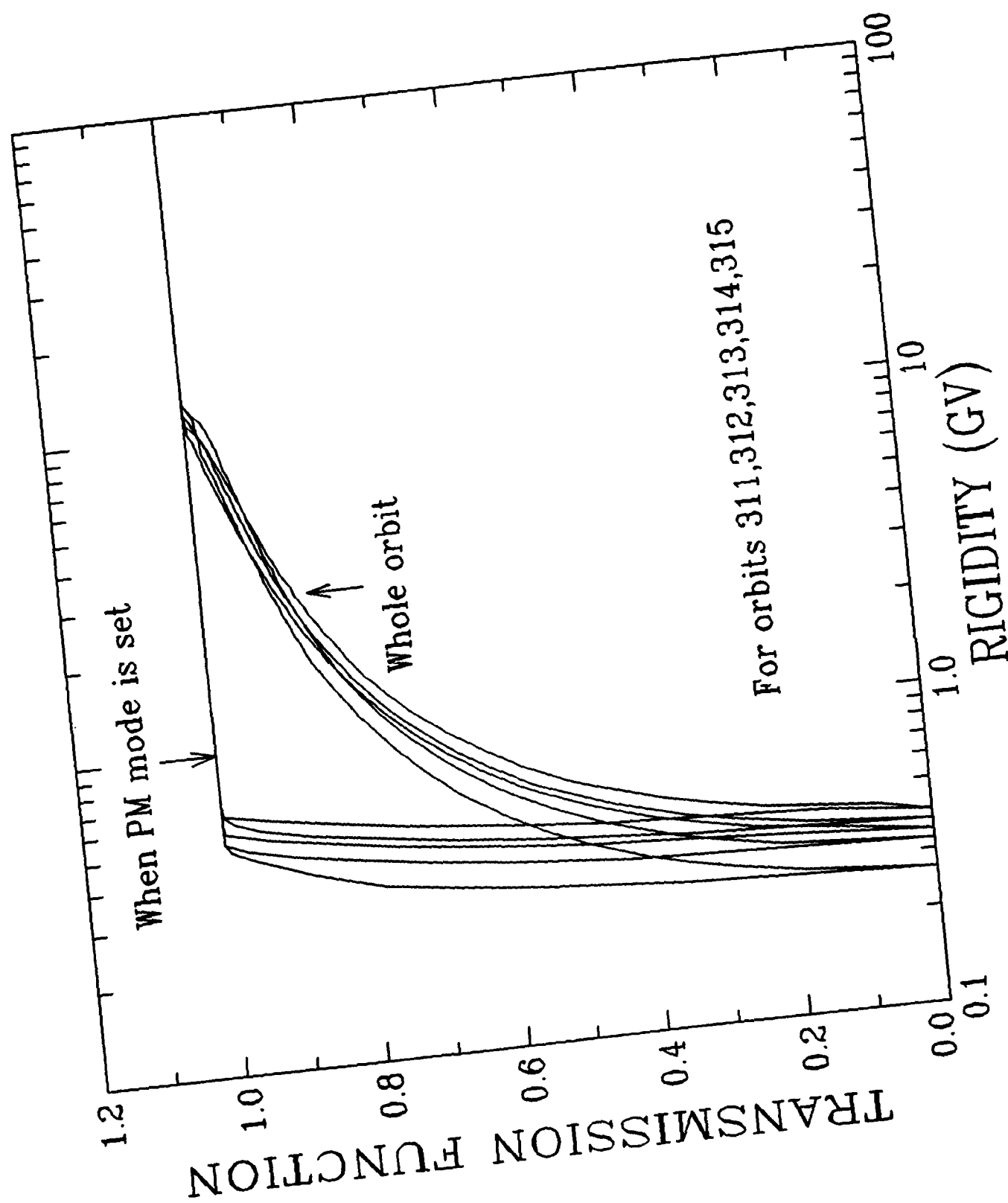


Figure VII.5. Geomagnetic transmission function for several CRRES orbits.

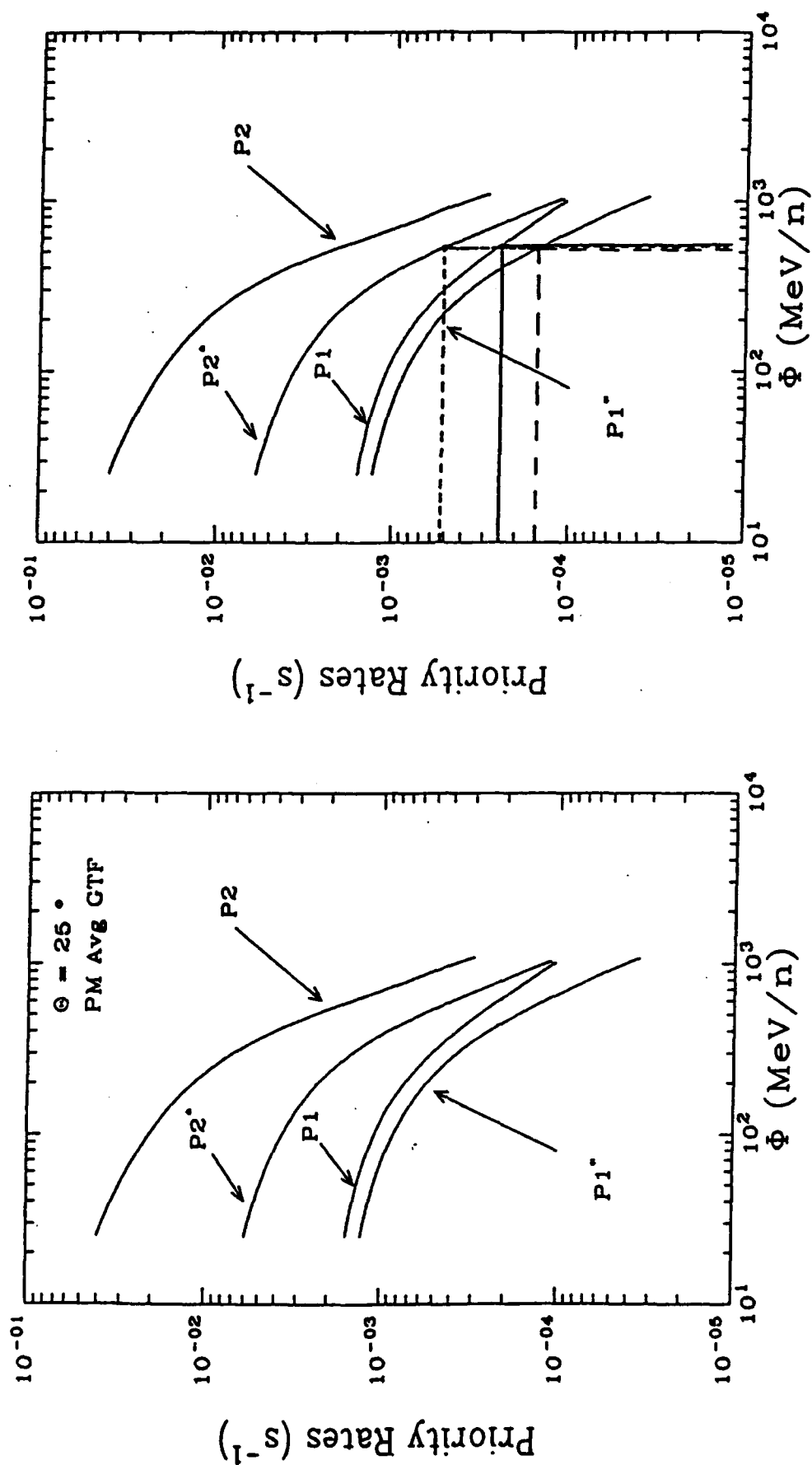


Figure VII.6. Calculated priority counting rates for ONR-604 (left) and comparison of the calculations to the data (right).

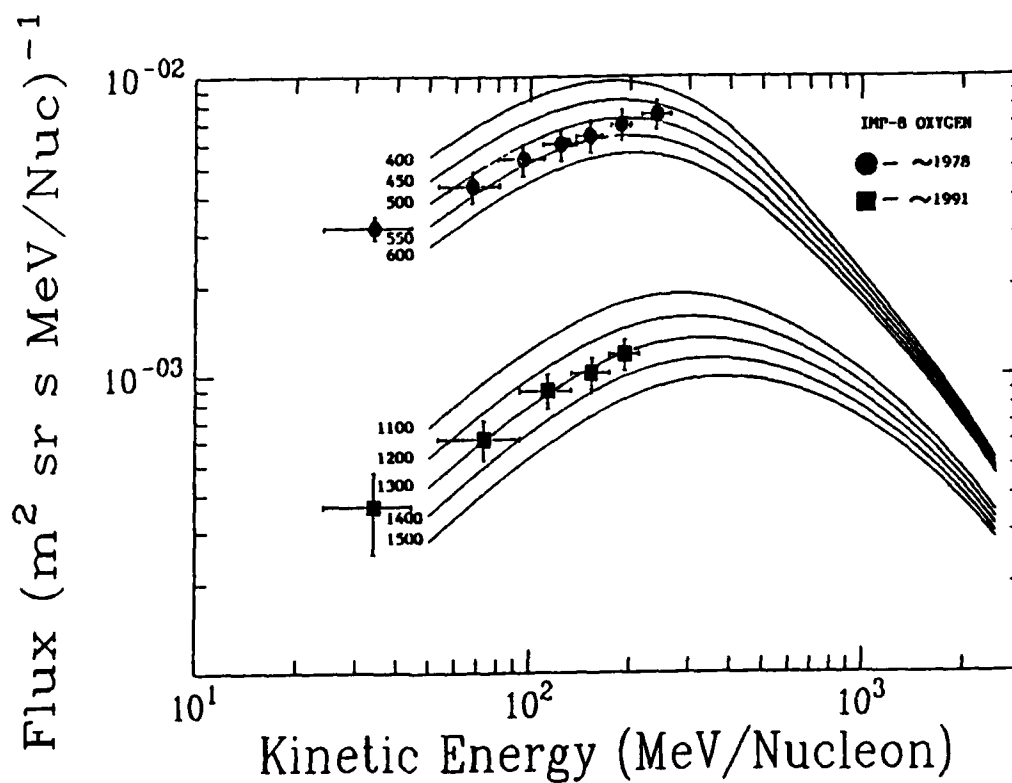
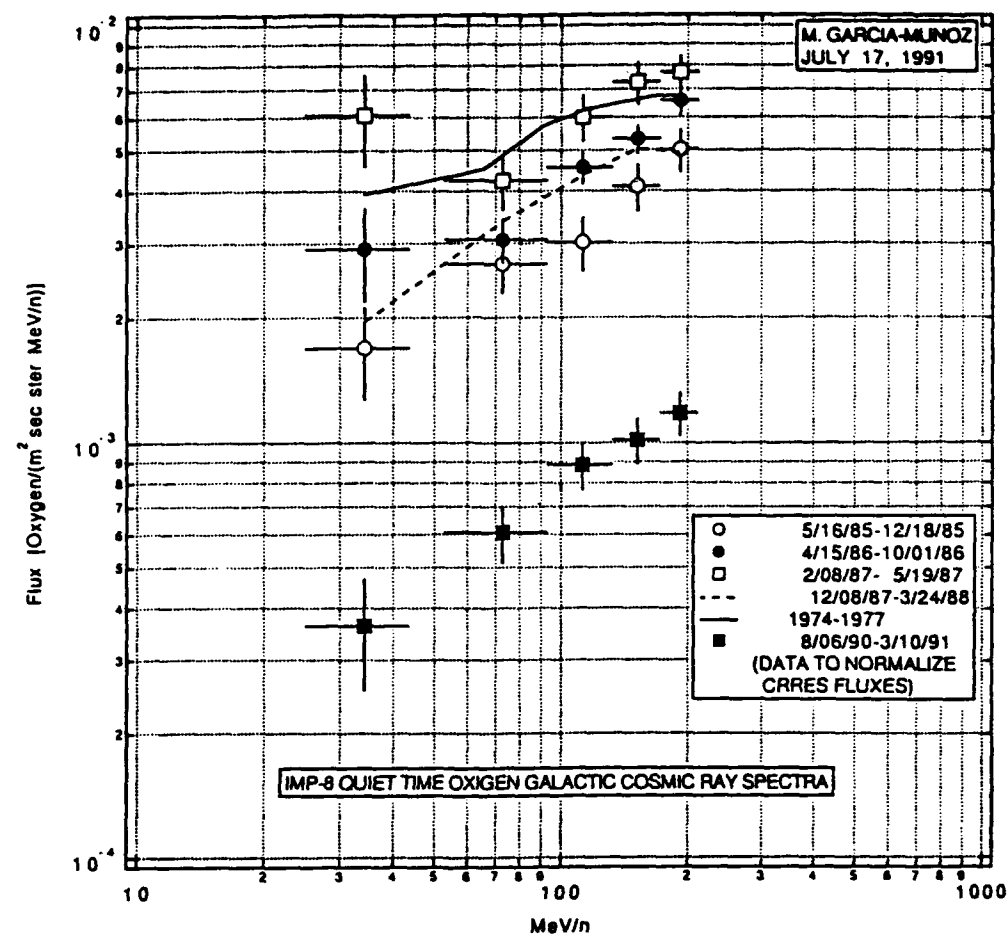


Figure VII.7. IMP-8 quiet time Oxygen spectra from University of Chicago (top) and solar modulation predictions for the 1978 and 1991 spectra (bottom).

the rate model or with the ONR-604 data itself. Alternatively, the local interstellar spectra may not be the most applicable, and this would affect the curves

The geomagnetic transmission function has been checked, as has the energy dependent acceptance, and no major uncertainties have been found. Since the rate analysis shows a lower value of  $\Phi$ , the measured counting rate should be lower to bring the inferred  $\Phi$  values into agreement. This might indicate a residual background among the P1 and P2 events which has not been removed by the strict logic cuts employed. Further investigation will be required to try to resolve the apparent discrepancy.

#### D. Galactic Cosmic Rays

For the past several decades the composition and energy spectrum of Galactic Cosmic Ray (GCR) nuclei have been measured by a number of satellite experiments and ONR-604 represents the latest, current technology instrument in this series. Thus, there is a wealth of previous measurements which can be used as a baseline. In fact, ONR-604 will not provide measurements over the full charge and energy range required, so the baseline dataset will be needed to set and/or constrain the parameters of the analytic model.

The current GCR baseline database contains close to 1000 data points from more than 50 literature references and covers the most important elemental ratios and spectra. The database was initially developed in the early 1980's and a majority of the measurements available then were made during the extended solar minimum period of 1972-1978. Since then relatively few, new missions have been flown and the statistics collected during the current solar cycle have been hampered by the two relatively deep solar maximums bracketing a rather narrow solar minimum period (c.f. Figure VI.4).

A portion of the energy spectra measurements is shown in Figure VII.8, for He, C and Fe, with curves from initial GCR Model calculations. These results used a calculated local interstellar spectrum (LIS) modulated by the technique described earlier with solar minimum conditions corresponding to the 1972-1978 period ( $\Phi = 490$  MV). The LIS was calculated using a computer program that is based upon the weighted-slab GCR interstellar propagation technique (Fichtel and Reames, 1968) and which is fully described in Garcia-Munoz et al. (1987). In essence, this technique starts with a set of relative abundances of elements and isotopes at the GCR source, assumes a common source energy spectrum, as well as a particular interstellar medium (ISM) composition and density, and then calculates new abundances and spectra for a series of discrete ISM slabs. This calculation includes the effects of production and loss of species via nuclear interaction, radioactive decay ( $\beta^+$ ,  $\beta^-$ , and K capture), electron capture and loss, and ionization energy loss. These "slab results" are then integrated over an assumed pathlength distribution (PLD) to obtain the LIS.

One might note at this point that the "Slab Calculations" involve only atomic and nuclear effects which can, in principal, be measured in the laboratory, while the PLD involves the astrophysical details of GCR interstellar propagation and must be either theoretically derived or obtained from the GCR data. Thus, obtaining a good representation of the Galactic Cosmic Rays is actually a multi-parameter problem and it is important to use laboratory measurements, GCR data and other astrophysical information to constrain as many of these parameters as possible. For example, of particular importance are the nuclear interaction cross sections, but only a few interaction channels have been measured over the energy range required by the cosmic ray problem (Guzik, 1990). Therefore, there is a heavy reliance on calculated cross sections (e.g. Silberberg and Tsao, 1990) but these can differ from measured values by up to 60% (Webber, Kish and Schrier, 1990). Constraining the Model parameters is, thus, a complex process involving direct laboratory measurements, semi-empirical calculations and good judgment. Considerable effort was required to establish the parameter database for the initial GCR calculations, and additional effort will be

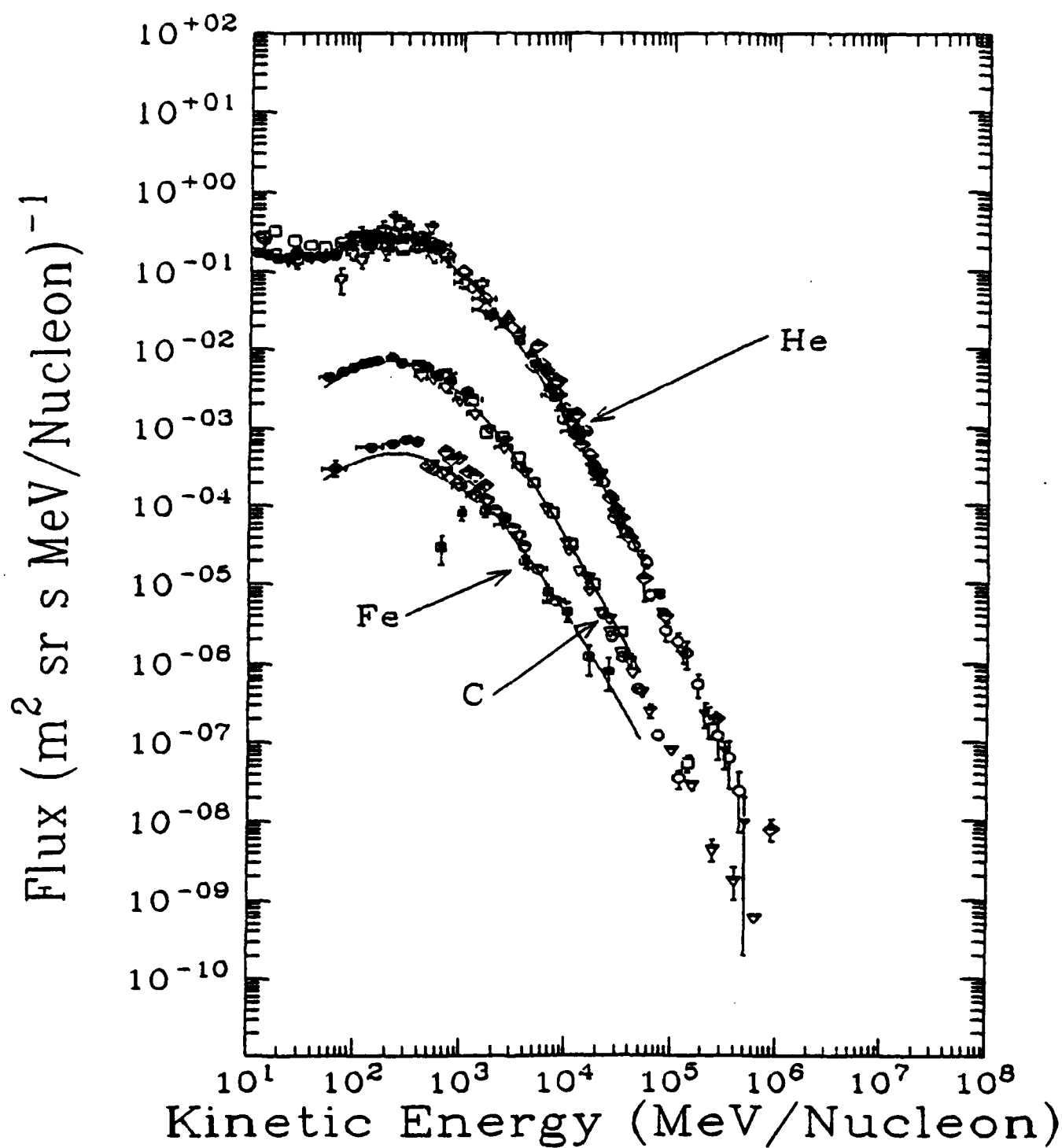


Figure VII.8. Measurements of GCR energy spectra for He, C and Fe from the database with initial model predictions shown by the curves.

required to maintain this database as new laboratory measurements or other constraints become available.

The PLD used for the results shown in Figure VII.8 is an exponential distribution of pathlengths with a mean that is a decreasing power law in total energy. This distribution, referred to as the Power-Law Exponential (PLEXP), is consistent with a homogeneous model of cosmic ray propagation which allows a small, but increasing "leakage" from the "galactic" confinement volume with increasing energy. These results appear to fit the data quite well. Helium, Carbon, and Iron, however, are "primary" species. That is, their relative abundance in the measured GCR is dominated by their abundance at the source and is not significantly affected by the "secondary" component generated by the nuclear fragmentation of heavier species. Therefore, primary species reflect conditions at the cosmic ray source rather than conditions during GCR propagation. Pure secondary species, which have a negligible source component, are very sensitive to the exact form of the PLD. In fact, by examining ratios of secondary to primary elements the PLD parameter in the GCR Model can be constrained.

Figure VII.9 (top) shows measurements from the GCR database for the B/C secondary to primary ratio, along with the GCR Model results using the PLEXP PLD (long dashed curve). For energies greater than 1 GeV/nucleon the prediction represents the data, but overestimates the measurements for lower energies. Thus, while the Model may correctly predict the primary spectra it will overpredict the flux of secondary GCR at 100 MeV/nucleon by ~60%. An alternative PLD referred to as the Double-Sided Power Law (DSPL) pathlength distribution is shown as the solid curve in the figure and provides a much better fit to the ratio. The DSPL has, in essence, the same form as the PLEXP for high energy (>1 GeV/nucleon), but for low energy the exponential mean is a decreasing function of decreasing energy. Such a PLD may be consistent with propagation models which involve a "galactic wind" that flows outward from the galactic plane in a fashion similar to the solar wind which flows outward from the Sun (Garcia-Munoz et al., 1987).

Further details of the PLD can be constrained by requiring multiple secondary to primary ratios widely separated in charge to be fit simultaneously. Figure VII.9 (bottom) shows the collection of data for the ratio Sub-Fe/Fe where the "Sub-Fe" group includes the elements Sc, Ti, V, Cr and Mn. The DSPL result which fit the B/C ratio is shown as the solid curve and is quite likely low of the data for energies less than ~1.0 GeV/nucleon. This discrepancy has been used to argue that the PLD must be depleted of short pathlengths (Garcia-Munoz et al., 1987). Since the Iron group species have a larger total nuclear interaction cross section, and hence a shorter mean interaction length, than the Carbon group nuclei, the iron secondaries will be more sensitive to the short pathlength characteristics of the PLD. By removing or "truncating" the short pathlengths from the PLD the calculation will cause more Iron nuclei to interact and raise the Sub-Fe/Fe ratio (dashed curves in Figure VII.9 bottom) while not affecting the prediction for B/C (short dashed curve in Figure VII.9 top).

The spectra calculated using these various PLDs are shown in Figure VII.10. The solid curves are the same as in Figure VII.8 (i.e. using the PLEXP), the short dashed curves are results using the DSPL and the long dashed curves result from a "truncated" PLD. For Helium and Carbon the three PLDs yield almost identical results, but the differences are apparent in the low energy (<700 MeV/nucleon) Iron spectrum. As energy deposit is proportional to  $Z^2/E$  an error made in calculating the low energy Iron spectrum may translate into a relatively large uncertainty in the Linear Energy Transfer (LET) spectrum.

In fact, the accuracy to which the PLD can be determined and, consequently, the spectra can be calculated, depends upon the accuracy of the other Model parameters. For example, while the solid curve in the bottom portion of Figure VII.9 (no truncation) appears to underpredict the low energy data, it can be argued that the dashed curves (with truncation) are high for all energies. This could be due to having an incorrect source abundance for the Sub-Fe species in the Model, and reducing these



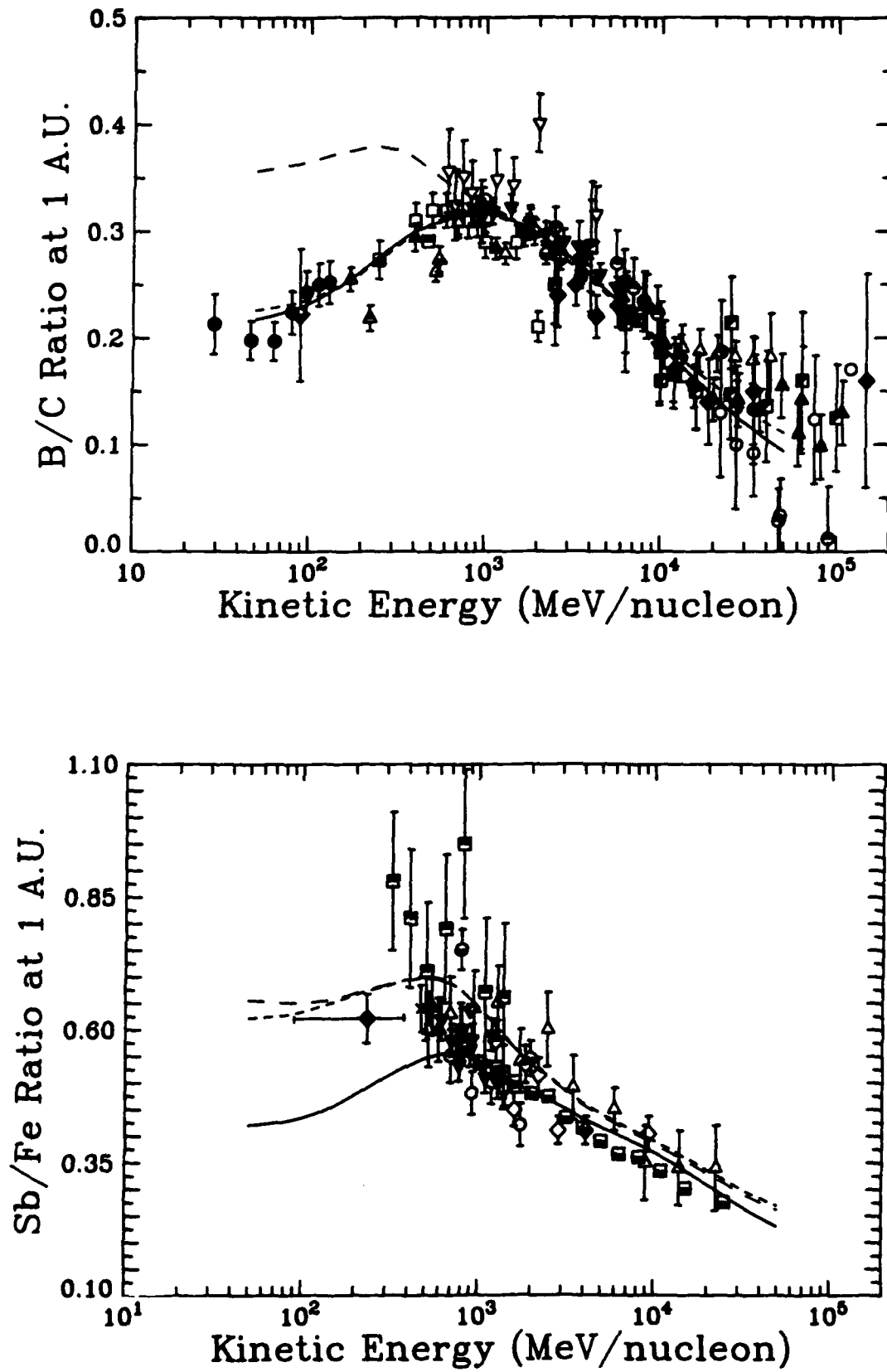


Figure VII.9. Measurements of the B/C ratio (top) and Sub-Fe/Fe ratio (bottom) compared to predictions of various propagation models (see text for details).

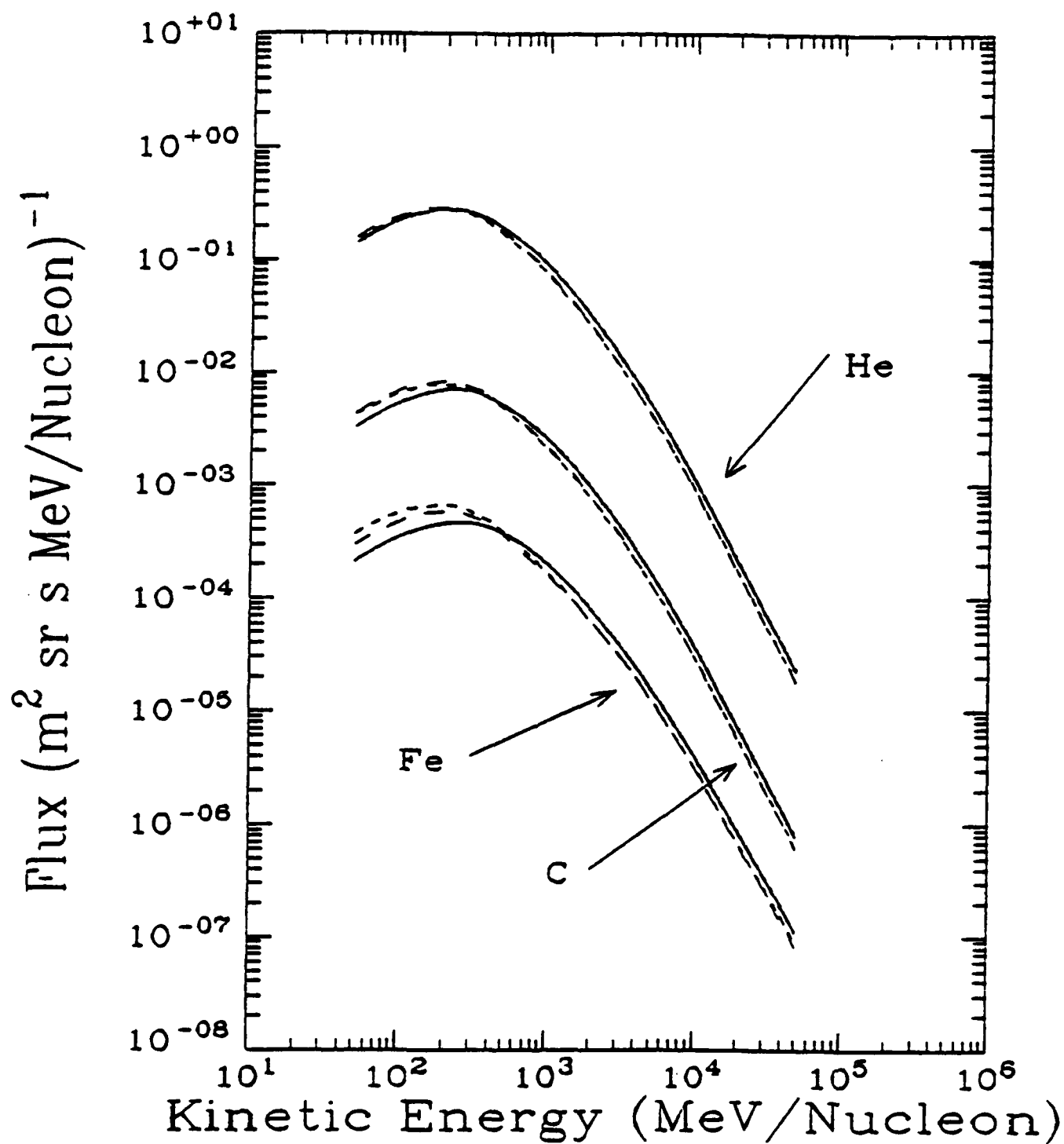


Figure VII.10. Spectra for He, C, and Fe predicted for various PLD's.

abundances would lower the dashed curves. In addition, PLD truncation is still controversial, and the case for truncation is based largely on the low energy IMP-8 measurement. The recent measurement by Ferrando et al. (1991) provides the only other data in the IMP-8 charge and energy range. Their value for Sub-Fe/Fe is about 30% less than the IMP-8 measurement and is in good agreement with the solid curve (no truncation). As discussed above, however, it is not immediately clear whether the Ferrando et al. measurement made with an instrument onboard the Voyager 2 spacecraft at 22 AU can be so directly compared with the IMP-8 data made in the vicinity of Earth. Finally, the nuclear interaction cross sections for the production of Sub-Fe species from Iron are also largely unmeasured and, thus, the Model uses mostly calculated cross sections. If these cross sections are increased in value then the solid curve would move up and it may be possible to fit the Sub-Fe/Fe and B/C data simultaneously without requiring a truncated pathlength distribution.

Refining the GCR Model and evaluating the consequences of these uncertainties is a time consuming process involving multiple calculations. First and alternate set of input parameters, such as the source abundances, source spectra or nuclear cross sections, must be determined from the literature, derived or calculated. Next the "Slab Calculation" program, which takes roughly 10 to 12 CPU hours on an IBM 3090, must be run with the new inputs. Using these new slab results the PLD parameters must be adjusted so that the B/C and Sub-Fe/Fe data are simultaneously fit. The final results of this process are then compared with the spectra and ratio measurements from the baseline database. If further adjustments are still called for then the process begins again. Usually 3 to 4 iterations through this loop and several months of effort are needed to achieve an additional level of refinement in the GCR Model.

### E. LET Spectra

The preceding sections have discussed the needed inputs for the GCR portion of an Interplanetary Heavy Ion model and the current state of the analysis. While it is still premature to try to specify a definitive environment model, a preliminary "working" prediction can be made. Since the time period of interest (1 Sept. 90 - 28 Feb. 91) contains no large solar flares, a flare component need not be considered. Thus, this period is dominated by the Galactic Cosmic Rays.

Using the PLEXP spectra in Local Interstellar Space and a modulation level of  $\Phi = 625$  MeV/nucleon (from IMP-8) the calculated spectra of cosmic rays at the orbit of Earth is illustrated in Figure VII.11 for the elements H, He, O and Fe. To investigate the effect of these particles on microelectronic components, it is necessary to calculate the integral Linear Energy Transfer (LET) distribution for different levels of shielding. This has been done for shielding thicknesses of 50, 100, 200, 400, 800 and 1600 mils of Aluminum for a grid of different thresholds. The results are shown graphically in Figure VII.12. These preliminary results can be utilized by the investigators for the CRRES microelectronics package.

What has not been completed is a study of the variation in spectra or LET distributions introduced by the uncertainty in the level of solar modulation or the different LIS spectra that were described above. Such a study will indicate the range of possible variation about the "working" values, and will allow a "user" of these results to estimate the uncertainties in his analysis. The study of these variations will be one of the next tasks undertaken.

Finally, the solar energetic particles must be considered, since their effects could be dominant during highly disturbed periods such as March and June, 1991. A beginning has been made on developing a SEP model, and this will be completed in the near future.

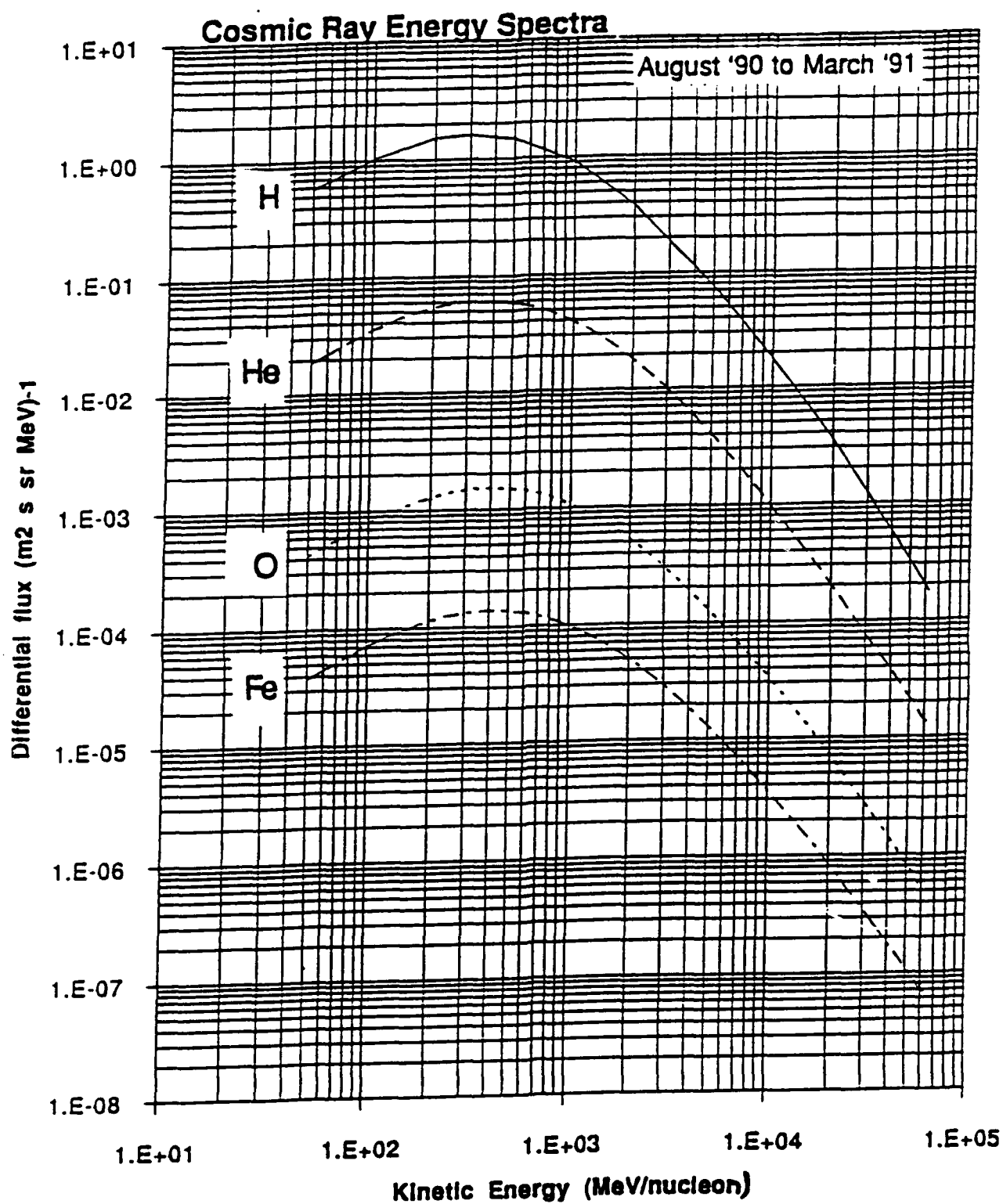


Figure VII.11. Calculated spectra at Earth orbit for H, He, O and Fe for the time period 9/1/90 - 2/28/91

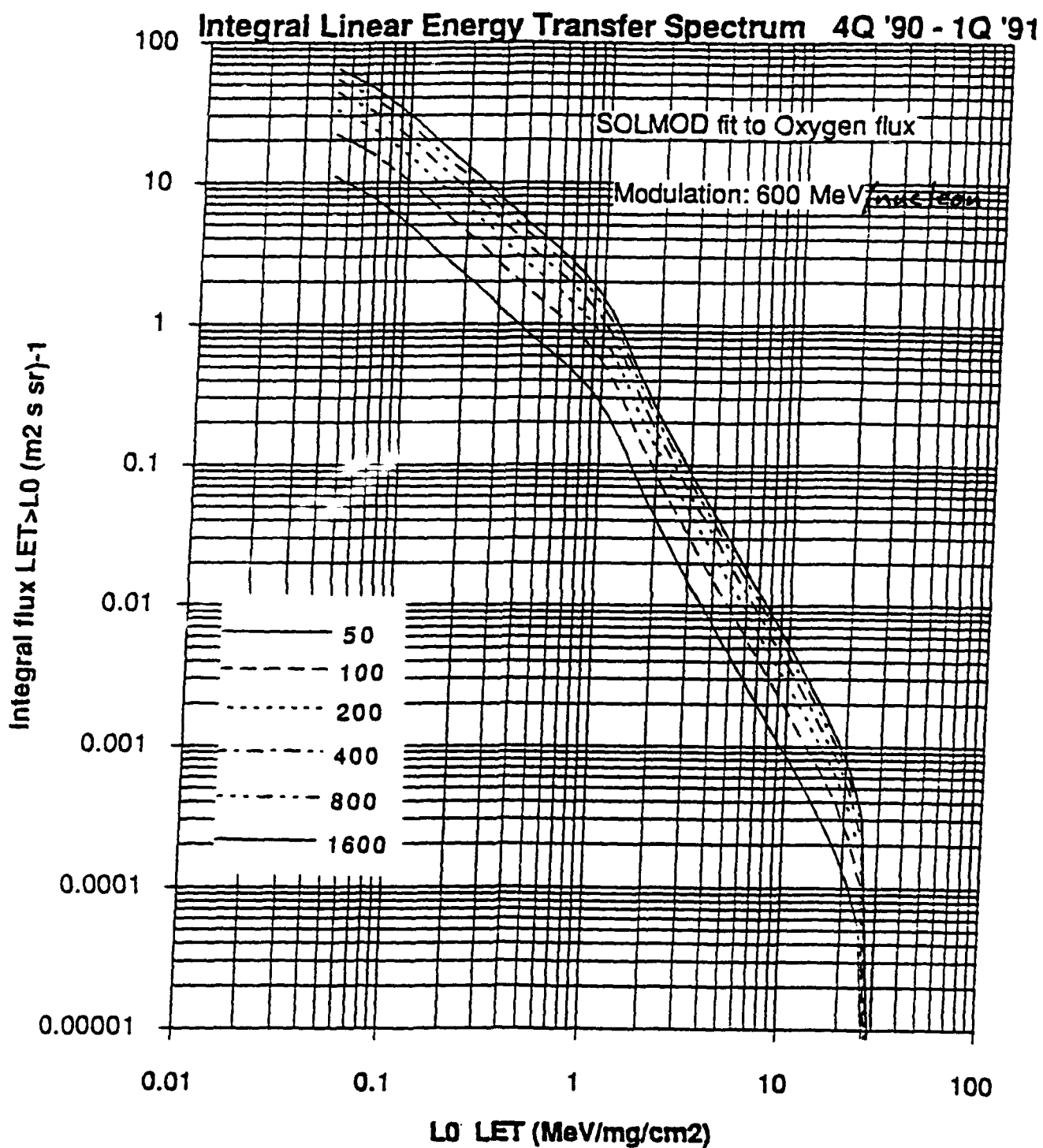


Figure VII.12. Predicted LET spectra behind various levels of shielding.

# VIII. Bibliography

- Adams, J. H., Jr., Silberberg, R. and Tsao, C. H., (1981), NRL Memorandum Report 4506, Naval Research Laboratory, Washington, DC.
- Adams, J. H., Jr., and Partridge, K., (1982), NRL Memorandum Report 4846, Naval Research Laboratory, Washington, DC.
- Adams, J. H., Jr., Garcia-Munoz, M., Grigoriv, N. L., Klecker, B., Kondratyeva, M. A., Mason, G. M., McGuire, R. E., Mewaldt, R. A., Panasyuk, M. I., Tretyakova, Ch. A., Tylka, A. J. and Zhuravlev, D. A. (1991), *Ap. J. Letters*, 375, L45.
- Akasofu, S.-I., Lin, W. C. and Van Allen, J. A. (1963), *J.G.R.* 68, 5327.
- Binder, D., Smith, E. C., and Holman, A. B. (1975), *IEEE Trans. Nucl. Sci.*, NS-22, 2675.
- Biswas, S., Durgaprasad, N., Mitra, B., Singh, R.K., Dutta, A. and Goswami, J. N. (1990), 21st ICR Conference Papers, (Australia; University of Adelaide), 3, p.23.
- Blake, J. B., Kolasinski, W. A., Fillius, R. W. and Mullen, E. G. (1992) *Geophys. Res. Letters*, 19, 821.
- Bruckner, G. J., Chater, W. and Kolasinski, W. A. (1980), *IEEE Trans. Nucl. Sci.*, NS-27, 1490.
- Durgaprasad, N., Mitra, B., Singh, R. K., Biswas, S., Dutta, A. and Goswami, J. N. (1990), in 21st ICR Conference Papers, (Australia, University of Adelaide), 3, p. 389.
- Engelmann, J. J., Ferrando, P., Soutoul, A., Goret, P., Juliusson, E., Koch-Miramond, L., Lund, N., Masse, P., Peters, B., Petrou, N. and Rasmusen, I. L. (1990), *Astron. and Astrophys.*, 233, 96.
- Evenson, P., Garcia-Munoz, M., Meyter, P., Pyle, K. R. and Simpson, J. A. (1983), *Ap. J. Letters*, 272, L15.
- Ferrando, P., Lal, N., McDonald, F. B. and Webeer, W. R. (1991), *Astronomy and Astrophysics*, 247, 163.
- Fichtel, C. E. and Reames, D. V. (1968), *Phys. Rev.*, 175, 1564.
- Fisk, L. A. (1979) in Solar System Plasma Physics, Vol. 1, ed. E. N. Parker, C. F. Kennel, and L. J. Lanzerotti (Amsterdam: North Holland), p. 179.
- Garcia-Munoz, M., Meyer, P., Pyle, K. R., Simpson, J. A. and Evenson, P. A. (1986), *J.G.R.*, 81, 2858.
- Garcia-Munoz, M., Simpson, J. A., Guzik, T. G., Wefel, J. P. and Margolis, S. H., (1987), *Ap. J. Suppl.*, 64, 269.
- Gleeson, L. J. and Axford, W. I. (1968), *Ap. J.*, 154, 1011.
- Guenzer, C. S., Allas, R. G., Campbell, A. B., Kidd, J. M., Petersen, E. L., Seeman, N. and Wolicki, E. A. (1980), *IEEE Trans. Nucl. Sci.*, NS-27, 1485.

- Gussenhoven, M. S., Mullen, E. G. and Sagalyn, R. C. (1985) Air Force Geophysics Laboratory Report AFGL-TR-85-0017 (ADA 160504), Hanscom AFB, MA, 185 p.
- Guzik, T. G. (1988), Solar Physics, 118, 185.
- Guzik, T. G. (1990), in Particle Astrophysics: The NASA Cosmic Ray Program for the 1990's and Beyond, eds. W. V. Jones, F. J. Kerr, J. F. Ormes, (AIP Conference Proceedings 203: American Institute of Physics, New York, NY), p. 275.
- Guzik, T. G., Miah, M. A., Mitchell, J. W. and Wefel, J. P. (1989), J.G.R., 94, 145.
- Hamm, R. N., Turner, J. E., Wright, H. A. and Ritchie, R. H. (1979), IEEE Trans. Nucl. Sci., NS-26, 4892.
- Imhof, W. L., Reagan, J. B. and Gaines, E. E. (1971), J.G.R., 76, 4276.
- Iverson, W. R. (1979), Electronics (November), p. 44.
- Jokipii, J. R. (1971), Rev. Geophys. Space Phys., 9, 27.
- Kolasinski, W. A., Blake, J. B., Anthony, J. F., Price, W. E. and Smith E. C. (1979), IEEE Trans. Nucl. Sci., NS-26, p. 5087.
- Lamport, J. E., Mason, G. M., Perkins, M. A. and Tuzzolino, A. J. (1976), Nucl. Instr. and Methods, 134, 71.
- Lamport, J. E., Perkins, M. A., Tuzzolino, A. J. and Zamow, R. (1980), Nucl. Instr. and Methods, 179, 105.
- May, T. C. and Woods, M. H. (1979), IEE Trans. Elect. Dev., ED-26, 2.
- McKibben, R. B. (1986), in The Sun and the Heliosphere in Three Dimensions, ed. R. G. Marsden, (Dordrecht, The Netherlands; D. Reidel Publ., Co.), p. 361.
- McNulty, P. J., Farrell, G. E., Wyatt, R. C., Rothwell, P. L., Filz, R. C. and Bradford, J. N. (1980), IEEE Trans. Nucl. Sci., NS-27, 1516.
- Oschlies, D., Beaujean, R. and Enge, W. (1989), Ap. J., 345, 776.
- Parker, E. N. (1965), Planet. Space Sci., 13, 9.
- Petersen, E. L. (1980), IEEE Trans. Nucl. Sci., NS-27, 1494.
- Shea, M. A. and Smart, D. F. (1975), Air Force Geophysics Laboratory Report AFGRL-TR-75-0185, Hanscom AFB, MA.
- Silberberg, R. and Tsao, C. H. (1990), Phys. Reprints, 191, (b), 351.
- Simpson, J. A., Wefel, J. P. and Zamow, R. (1983), "Proceedings of the 18th International Cosmic Ray Conference," (Bombay, India; Tata Institute of Fundamental Research), 10, p. 322.

Simpson, J. A., Munoz, M. G., Perkins, M. and Wefel, J. P. (1985), in CRRES/SPACERAD Experiment Descriptions, eds. M. S. Gussenhoven, E. G. Mullen and R. C. Sagalyn, Air Force Geophysics Laboratory Report AFGL-TR-85-0017 (Hanscom, AFB, MA), p. 163, ADA160504.

Tsyganenko, N. A. (1987), Planet. Space Sci., 35, 1347.

Urch, I. H. and Gleeson, L. J. (1972), Astrophys. Space Sci., 17, 426.

Webber, W. R., Kish, J. C. and Schrier, D. A. (1990), Phys. Rev. C, 41, 566.

Ziegler, J. F. and Lanford, W. A. (1979), Science, 206, 776.